The Synthesis and Characterisation of Ceramic Composites and A-Site Deficient Perovskites as Dielectrics for Multi-Layer Ceramic Capacitors.

James Henry Killeen

A thesis submitted in partial fulfilment of the requirements for the degree of

Doctor of Philosophy

The University of Sheffield

Functional Materials & Devices

School of Chemical, Material & Biological Engineering

Supervisors: Professor Derek C. Sinclair, Dr. Julian S. Dean

October 2024

Acknowledgements

My first thanks go to my supervisors, Professor Derek C. Sinclair and Dr Julian S. Dean. Their knowledge and expertise is something I couldn't have gained from any book or publication, and without them this thesis would never have been possible. Their guidance, teaching and patience has allowed me to develop into the scientist I would never have imagined four years ago, for which I cannot thank them enough.

I would like to extend my appreciation to Maureen Strawhorne and Dr Graham Dale, as well as the rest of the research and development team at Kyocera-AVX Coleraine. Their expertise regarding functional ceramics and MLCCs is second to none, and the provision of this expertise in many engaging and enjoyable meetings has been invaluable. I would like to thank the EPSRC and Kyocera-AVX for their funding of my studentship, allowing me to develop into the scientist I am today, and providing me with the opportunities to develop professionally.

I would like to thank Dr Lewis Owen for his training regarding Rietveld refinements, as without him I would have had little chance in taming GSAS-II. Thank you to the Henry Royce Institute for Advanced Materials for funding the EPMA, and thanks to Mr Stuart Creasey-Gray for assisting in the measurement, analysis and understanding of data, without whom I would have simply been looking at a series of nice colours. A thank you to Professor Antonio Feteira and Muhammad Wasim at Sheffield Hallam University for their assistance and insight regarding the P-E testing of my samples.

To the Functional Materials and Devices group at Sheffield, I thank you for your constant support and encouragement, insight and expertise which has helped me enormously over my four years. This thank you extends to members past and present, including Dr Linhao Li, Dr Ge Wang, Dr Zhilun Lu and Dr George Kerridge for training me on a variety of techniques before which I was completely unaware existed. A special thanks must go to Kerry Mclaughlin, Dr Jessica Andrews, Dr Tom Hooper, Dr Jordan Canton, Sadi Ege Parim and Erin Carroll. This is not just for the incredibly useful knowledge and years of lab experience I was able to absorb, but for making my journey at Sheffield as fun and memorable as it has been. I have loved every minute of my PhD, especially those chaotic L09 based minutes, which is in no small part down to the amazing people I have been able to work with.

Finally, but not least, my greatest thanks must go to my family, without whom I would not have been able to achieve what I have. To Mum, Dad, Georgina, George, Daniel and Daisy, thank you for all your constant love and support. I would never have gotten this far without you.

Abstract

This thesis will regard two differing mechanisms for the enhancement of temperature stable dielectrics in $NaNbO_3$ related compositions, with the aim of synthesising dielectrics meeting X7R and X8R rated Temperature Coefficient of Capacitance (TCC) and/or dielectrics with prospective use for energy storage applications. The first of these mechanisms will be the formation of $Na_xBa_{1-x}Nb_xTi_{1-x}O_3$ (XNNBT) based ceramic-ceramic composites with 3-0 dimensional interconnectivities between its $BaTiO_3$ (BT) matrix phase and homogeneously distributed relaxor NNBT secondary phases. The formation of this composite is based on the ability to retain compositional heterogeneity post sintering due to the thermodynamic stability of relaxor components of the NNBT solid solution. X7R rated TCC is achieved for a BT-60NNBT composite with a 80:20 wt.% phase fraction, with a room temperature permittivity magnitude over 2000 and tan δ <0.05 across a -150 to 400 °C temperature range. This TCC specification can be extended to X8R rating with the doping of 7 mol% Ca onto the A site of the BT matrix pre sintering. These B(Ca)T-60NNBT ceramic-ceramic biphasic composites exhibit a linear electric field dependence of polarisation, with moderate energy storage efficiencies ~ 77 % and W_{rec} ~ 0.56 Jcm^{-3} when 2 wt.% glass sintering additive is used. The formation of the composite is reproducible from hand-mixing of its component phases to ball milling of larger batches, whilst X8R TCC rating can be replicated with a ball milling of a stoichiometric mix of NN, BT and BCT commercial nano-powders.

The second mechanism for enhancing temperature stability of $NaNbO_3$ dielectrics is the increase in A site vacancy concentration through aliovalent La^{3+} A site doping, along the $NaNbO_3$ – $La_{1/3}NbO_3$ solid solution, $La_xNa_{1-3x}NbO_3$ (XLNN). X-ray Diffraction and Analytical Scanning Electron Microscopy analyses verify A-site vacancies to form as charge compensating defects, accommodated through a series of compositionally driven phase transitions induced by the competing influence and variation in the cooperative tilt network of the $[NbO_6]$ octahedra, cationic displacements and ordering of A-site species. A range of dielectric behaviours is observed across the solid solution. For 7.5LNN and above, an order-disorder transition in Nb displacements induces a suppression in TCC from that associated with $NaNbO_3$, with dielectric behaviour retained. TCC is, however, unsatisfactory for X7R or X8R rating. Mixed Na^+/n-type conductivity is induced for 15LNN and above, which is optimised in 25LNN, with a conductivity 8.0 x 10^{-5} Scm^{-1} at 400 °C. The $La_{1/3}NbO_3$ end member shows comparable mixed ionic-electronic conduction, where the ionic species is undetermined. Linearisation of polarisation electric field dependence occurs above the order-disorder transition at ~ 7.5LNN, for which an energy storage efficiency ~ 72 % and recoverable energy density ~ 0.4 Jcm^{-3} is achieved for 10LNN. The solid solution offers a range of properties suitable for diverse dielectric and non-dielectric applications.

1 Introduction

1.1 Introductory Remarks

Multilayer ceramic capacitors (MLCCs) represented a market value of ~ 15 billion USD in 2023[1,2], with most forecasts unsurprisingly projecting annual growth with an increase in circuitry integration demanded by the automotive, aerospace and domestic sectors (to name a few). The growth of the hybrid electric vehicle (HEV)/Electric vehicles (EV) market in particular is a major influence on this increasing demand. Such vehicles regularly contain more than 10,000 MLCCs, each used within circuitry to control the various electrical subsystems contained within. These range from AC-DC and DC-DC conversion systems, as well as battery monitoring systems and power management systems. A schematic overview of some of these electrical subsystems within EVs is shown in figure 1.1 [3].

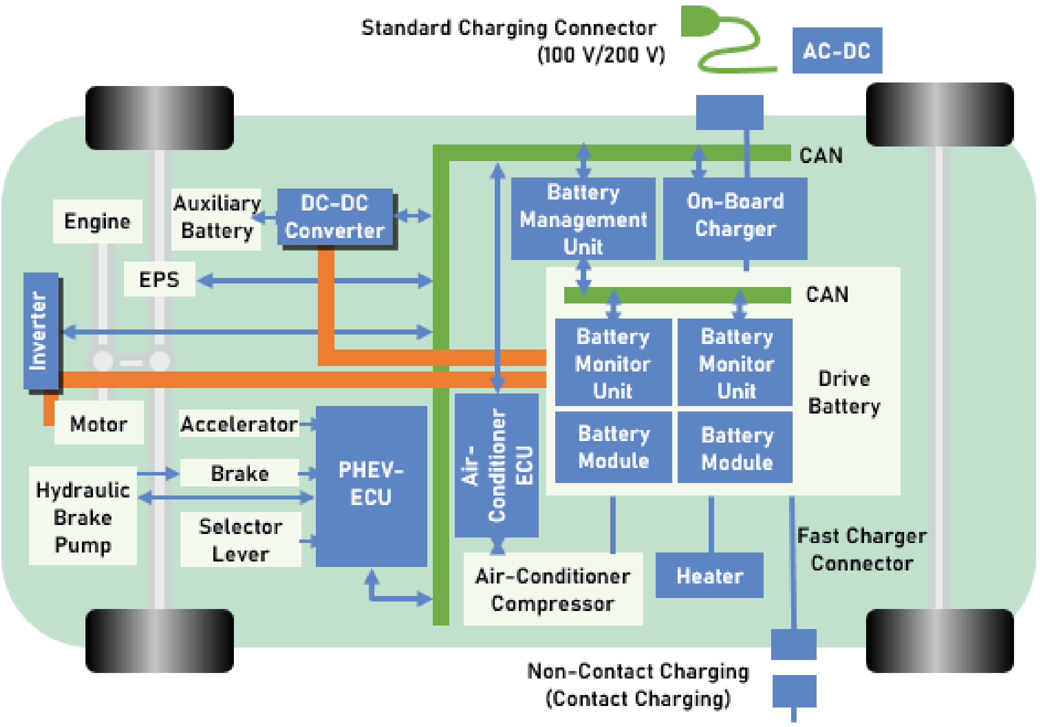

Figure 1.1: The electrical subsystems common within EVs, where MLCC integration is frequent Reformatted from [3].

MLCCs are inherently volumetric efficient, particularly with respect to conventional parallel plate capacitors, a consequence of the parallel lamination of 'n' parallel plate capacitors with thin dielectric layers. This allows for the provision of a specific capacitance with smaller dielectric surface areas, reducing associated capacitor case sizes and facilitating increasingly miniaturised circuitry. Such miniaturisation allows weight reductions in EVs, important for range maximisation, or alternatively facilitates more complex circuits containing an increasing number of MLCCs (or alternate components) per unit size, with improved circuitry performance.

However, the variable ambient conditions EVs and integrated circuitry are exposed to, combined with operational heating effects such as joule heating, induce a range of operating temperatures the capacitors are exposed to. It is fundamental that the capacitance variation is known with temperature to ensure the electrical subsystems contained within the vehicle operate optimally and safely. Furthermore, it is preferential that the capacitance variation with temperature is minimal. This would maintain circuitry output over a range of operating conditions, whilst negating the need for additional capacitor integrations and increasingly complicated designs to offer an auxiliary output when the operating temperature changes. Capacitors do exist with very small capacitance variation, built with 'Class I' dielectrics where variability is so low it is quoted in the parts per million per degree [4]. These class I dielectrics, by virtue of their crystal structures, offer an inherently low polarisability and the capacitors they constitute have a low capacitance. Although this suffices for some applications, such as filters, a higher capacitance is often necessary, and more temperature dependent 'class II' dielectrics are necessary. Materials engineering is necessary to enhance the thermal stability of these class II dielectrics without compromising the higher capacitance magnitudes desired.

Appropriate materials selection and compositional engineering should be utilised to facilitate the continued MLCC miniaturisation and performance enhancement. A dielectric composition that offers high intrinsic relative permittivity, typically above 1000 or close to 2000, that is stable over a wide operating temperature range and with sufficiently high dielectric breakdown strength to facilitate thin dielectric layers, ~ 1 µm or less, is the ideal component for a class II dielectric. Appropriate doping strategies on pre-existing dielectric materials and compositional modulations could provide novel solutions to the provision of temperature stable dielectrics for MLCC applications.

1.2 Aims & Objectives

This thesis aims to produce a dielectric composition suitable for class II dielectric MLCCs. This composition should yield a high room temperature permittivity, in excess of 1000, that varies no greater than ± 15 % between at least – 55 and 125 °C. This temperature dependence of permittivity is referred to as its ‘temperature coefficient of capacitance’ (TCC), introduced in section 2.2.5. Alpha numeric coding systems describe the maximum permittivity (capacitance) variation across a defined temperature range, with this aforementioned stability desired described as ‘X7R’ rating. The thesis is prospectively aimed at then extending the upper bound of this permittivity stability to 150 °C, meeting X8R rated TCC specification. The dielectric losses need to be low combined with a reasonable dielectric breakdown strength.

This thesis will utilise a bi-phasic ceramic-ceramic composite architecture, with associated 3-0 physical connectivity, to achieve this dielectric thermal stability specification. This composite system will utilise materials considered independently unsatisfactory for X7R or X8R rated TCC dielectrics, from the $NaNbO_3$-$BaTiO_3$ (NNBT) solid solution, that offer otherwise interesting and useful dielectric responses that could be useful when electrically connected in a composite arrangement. Alterative bilayer architecture had previously achieved X7R rating with the same materials, showing potential dielectric use if arranged appropriately. There were, however, considerable drawbacks through the need for configuration of physical interfacial diffusion barriers, imparting undesirable manufacturing complexities. A bi-phasic ceramic-ceramic composite system instead identifies a route to utilise the good dielectric properties of the NNBT solid solution whilst remaining non-disruptive to and compatible with current manufacturing tape casting procedures.

The thesis will also examine the response that A-site vacancies introduced into the perovskite crystal structure can impart upon the dielectric response of a material, specifically relating to TCC stabilisation and linearisation of the polarisation response upon an applied electric field. The former would make a composition suitable for temperature stable capacitors, such as X7R or X8R rated class II dielectrics considered for the ceramic composite system discussed in results chapters 1 through 3. The latter is considered for capacitors for high recoverable energy density applications, where often a multitude of dopant ions are introduced into $NaNbO_3$-based materials to achieve linearisation of the polarisation response in an applied electric field. A-site vacancies are introduced into $NaNbO_3$ through aliovalent La^{3+} A-site doping and forms results chapter 4.

1.3 Thesis Structure

The thesis will begin from chapter 2 as a ‘Basic Concepts’ chapter. This contains a basic description of the fundamental theory utilised within the rest of the thesis, including basic crystallography and the structurally imparted properties of a crystalline material, including the polarisation response which are so fundamental to dielectrics for capacitors. Chapter 3 contains the ‘Experimental Methodology’, outlining the theory and specifics of the structural and electrical characterisation techniques used to analyse the materials.

Results Chapters 1 through 3 will explore the NNBT based ceramic-ceramic composite systems for dielectric use. Chapter 1 outlines the ability to form an NNBT based ceramic composite system that satisfies X7R rated TCC. Results Chapter 2 focuses on extending this TCC specification to X8R rating, whilst Results Chapter 3 describes the industrial scalability of the composite systems.

Results Chapter 4 outlines the role of A-site vacancies in the $La_{1/3}NbO_3$ – $NaNbO_3$ perovskite solid solution on the dielectric response and TCC, whilst also comparing A-site vacancies on enhancing the linearisation of the polarisation response for energy density capacitor applications. These will be followed by chapters based on an overall discussion of the results, conclusions and further work.

2 Basic Concepts

2.1 Basic Crystallography

A crystalline substance is one that exhibits a long range, periodic ordering of its component atoms across three dimensional space. This array of atoms is by definition a lattice, a regular and finite array of points in space where each lattice point shares an identical environment [5–7]. That is, each lattice point shares an equivalent spatial distribution and orientation of surrounding lattice points [5]. Crystal lattices, due to their regularity and periodicity, exhibit translational symmetry. This means a select repeating unit of the lattice, such as the unit cell which is considered the smallest repeating unit that encapsulates the total three dimensional symmetry of the lattice, can be translated by a specific vector across the lattice and situate itself into an environment identical to the one it left. A primitive unit cell is shown in figure 2.1, owing to the fact it is composed of a single lattice point.

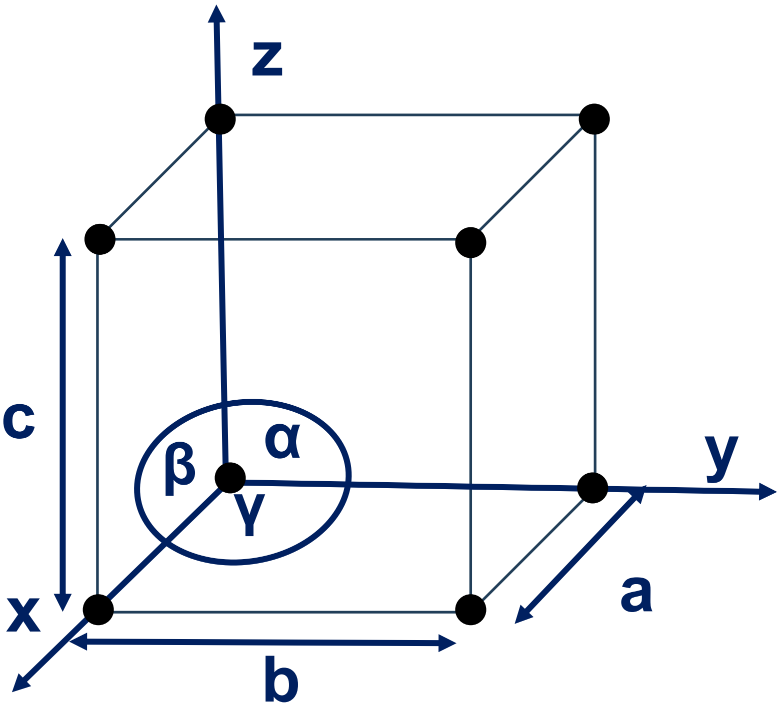

Figure 2.1: The unit cell for a primitive lattice, showing cartesian coordinates, associated a, b, c lattice parameters and α, β, γ angles. If all lattice parameters are equal and the internal angles are 90 °, the cell is primitive cubic. Other primitive unit cells are a distortion of this cell where lattice parameters and associated interplanar angles are able to vary.

The unit cell can be defined by the lengths of the orthogonal axes/vectors that connect its lattice points – unit cell lengths a, b and c - as well as the angles between these axes - α, β and γ. The relationship between these cell lengths and angles are shown in figure 2.1. The unit cells representing the lattice fall into one of seven crystal systems depending upon the relationship between these unit cell lengths and angles, table 2.1:

Table 2.1: The seven crystal systems and their associated lattice parameter/angle relationships.

Triclinic	$a \neq b \neq c$, $\alpha \neq \beta \neq \gamma$
Monoclinic	$a \neq b \neq c$, $\alpha = \gamma = 90\,°$, $\beta > 90\,°$
Orthorhombic	$a \neq b \neq c$, $\alpha = \beta = \gamma = 90\,°$
Trigonal	$a = b \neq c$, $\alpha = \beta = 90\,°$, $\gamma = 120\,°$
(Rhombohedral)	$a = b = c$, $\alpha = \beta = \gamma \neq 90\,°, < 120\,°$
Tetragonal	$a = b \neq c$, $\alpha = \beta = \gamma = 90\,°$
Hexagonal	$a = b \neq c$, $\alpha = \beta = 90\,°$, $\gamma = 120\,°$
Cubic	$a = b = c$, $\alpha = \beta = \gamma = 90\,°$

These cells are not always primitive, such as the one shown in figure 2.1. For non-primitive unit cells, different body types refer to the arrangement of additional lattice points. Body centring (I) is where an additional lattice point is located at the centre of the unit cell, face centring exhibits an extra half a lattice point at the face centres (F), and base centring (C) has an extra half a lattice point at the cell base and its adjacent face. A finite number of permissible spatial configurations of the lattice points within the unit cell are found for crystalline materials, being a combination of these crystal systems and body centring types. 14 of these lattice types were derived by Bravais, hence referred to as Bravais lattices. These 14 lattice types are shown in figure 2.2.

Crystal lattices are not always constituent of the same atom. It is important to distinguish that a lattice point does not have to be an atom, but rather a defined point in space that manifests the periodicity of the lattice. A motif is a better description of the environment the lattice point represents, and can be an atom, a cluster of atoms or a molecule for example [5,6]. The motif will have an associated symmetry, and so will the unit cell as it is constructed from these motifs. Symmetry is best defined as operations, induced by symmetry elements such as mirror planes, rotational axes, glide planes or screw axes, that act upon the cell and render it unidentifiable from the original spatial arrangement. A series of symmetry elements that act through a single point in the unit cell collectively describe the point group of that cell. There are 32 point groups for a three dimensional lattice, and combined with the 14 Bravais lattice types permissible, result in 230 possible space groups that a real, three dimensional crystal structure can exhibit. These space groups describe the overall three dimensional symmetry and spatial arrangement of the motifs and thus describe the crystal structure in its entirety.

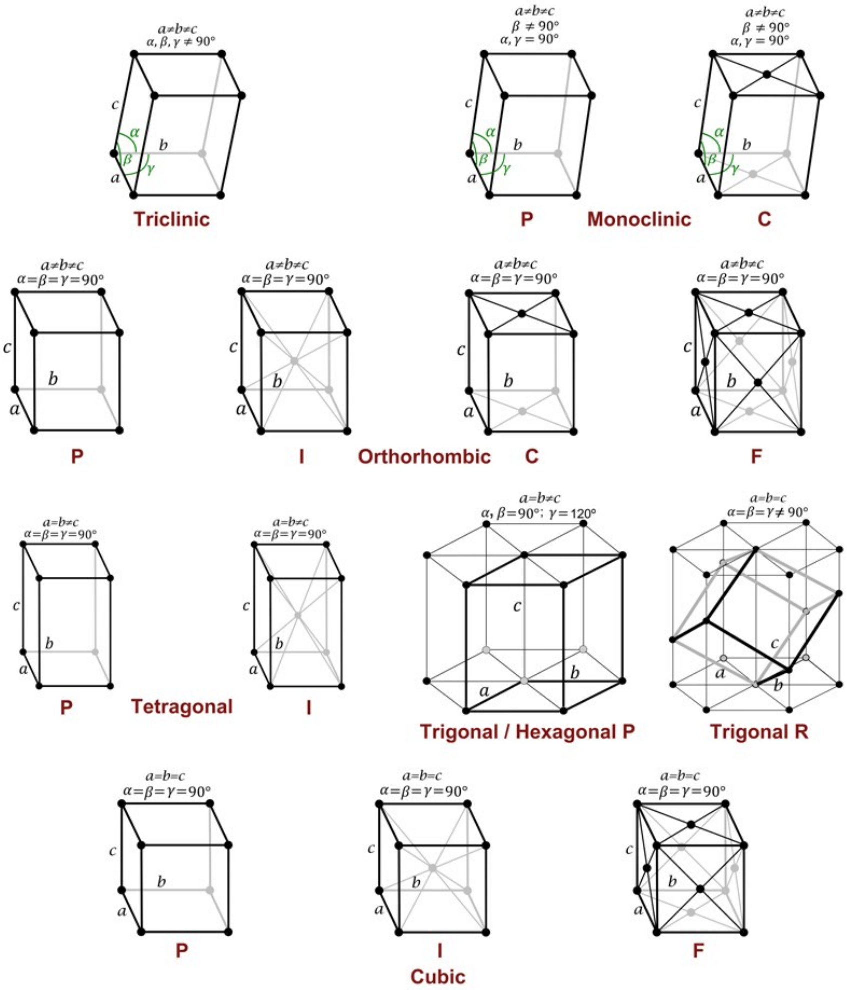

Figure 2.2: The 14 Bravais lattices, with lattice parameter and angular relationships. Reformatted from [9]

Crystal lattices are best described by the symmetry that it exhibits, for it is this symmetry that yields many of the consequent properties inherent of the crystal. The 230 space groups that describe this lattice symmetry are denoted using Hermann-Mauguin nomenclature, an alpha numeric code that describes the Bravais lattice type as the first digit, (P, I, F, C and R, for rhombohedral) followed by a shortened form of the symmetry elements that are sufficient to describe the total three dimensional symmetry of the structure [8,9]. These are the generator symmetry elements, named so for all other symmetry elements present within the cell can be generated from these. For example, 2 perpendicular mirror planes will generate a two-fold rotational symmetry axes. These are ordered according to viewing directions unique to a crystal system. Other space group notations are used, including Schoenflies notation, however Hermann-Mauguin notation is often preferred due to the ease at which translational symmetry elements can be included when transitioning from point group symmetry (2 dimensions) to space group symmetry (3 dimensions).

2.1.1 Miller Indices

Lattice planes and directions can be specified by means of Miller indices. These three digit indices are given as (hkl) values for planes and [hkl] values for directions, and are commonly used in structural analysis techniques such as diffraction where reference to specific lattice planes becomes important for their unique and varied responses when perturbed by an input signal. (hkl) references a plane that intercepts the x, y and z axis at $\left(\frac{a}{h},\frac{b}{k},\frac{c}{l}\right)$, where a, b and c are the unit cell lengths along these cartesian axes. Figure 2.3 shows the (100), (210) and (111) planes and the corresponding coordinates of interception along the unit cell lengths. (100) intercepts the x axis at one unit cell length ‘a’, whilst remaining parallel to both the y and z axes. It never intercepts these axis and so its k and l Miller indices are zero. For (210), the coordinates of x, y and z axes

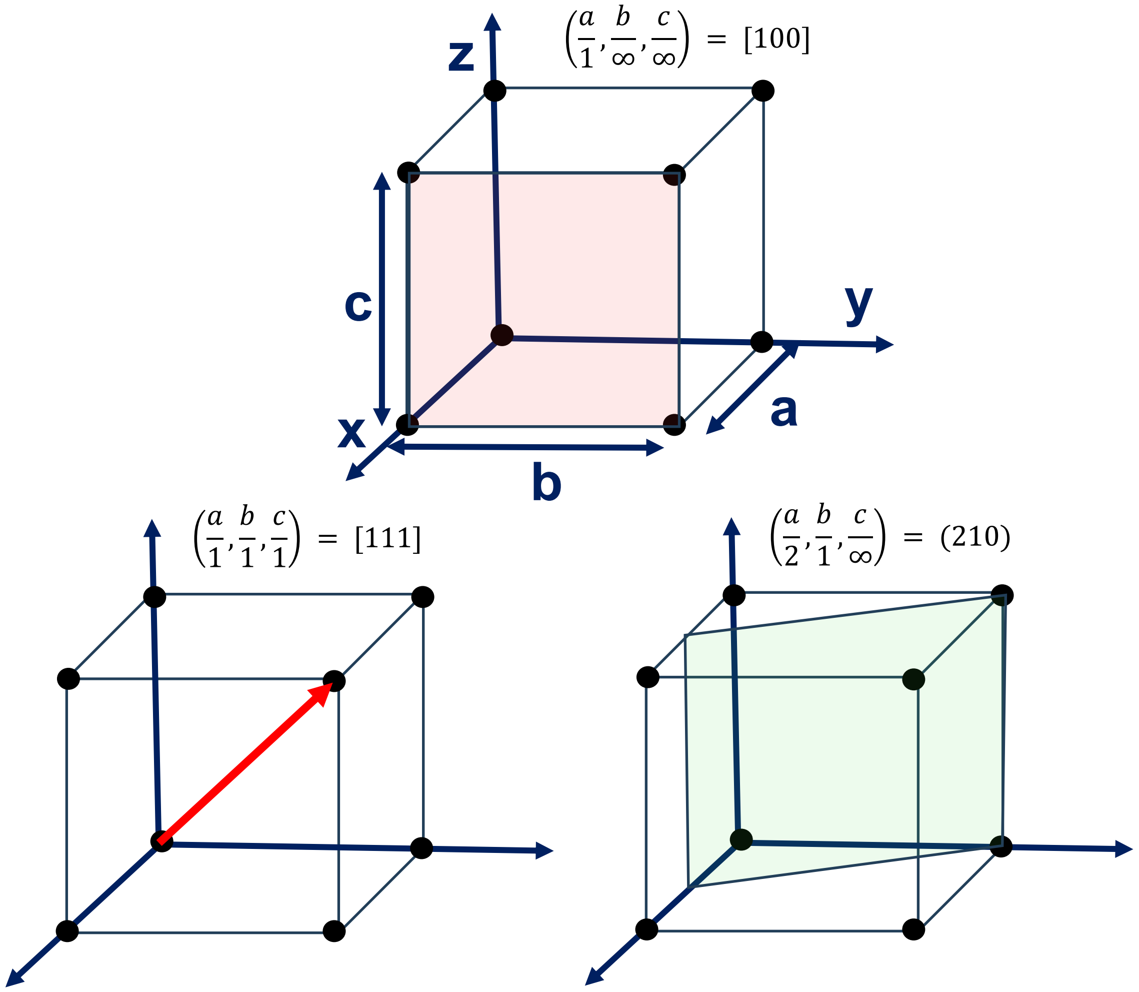

Figure 2.3: Visualisation of (100) and (210) planes and a [111] direction, and how the Miller indices (hkl) originate from the axial intercepts between the planes/vectors and the unit cell.

intercept are $\left(\frac{a}{2}, \frac{b}{1}, \frac{c}{\infty}\right)$ and so its Miller indices become (210). The same process can be repeated for the [111] vector.

2.2 Symmetry Dependent Behaviour

2.2.1 Piezoelectrics, Pyroelectrics and Ferroelectrics

As described, the symmetry of a three dimensional crystal structure falls into one of 32 different point groups or crystal classes. Of these 32 crystal classes, 11 are centrosymmetric, i.e. having a centre of symmetry. Stress application imparts an equal and opposite displacement of the ions constituting the crystal structure, with no net dipole moment formed. For the remaining 21 non-centrosymmetric crystal classes, 20 exhibit polarity when stress is applied as the displacement of charge is no longer equal and opposite [5,6,10,11]. The cubic class 432 is the only non-centrosymmetric crystal class to not exhibit this response, as polarisation along its <111> axes are symmetrically related and cancel out. The effect of a net dipole moment being imparted upon stress application is termed the piezoelectric effect. This dipole moment induced is linear and reversible with stress [10]. The converse effect can be observed where strain is imparted upon these 20 non-centrosymmetric crystal classes by the application of an electric field.

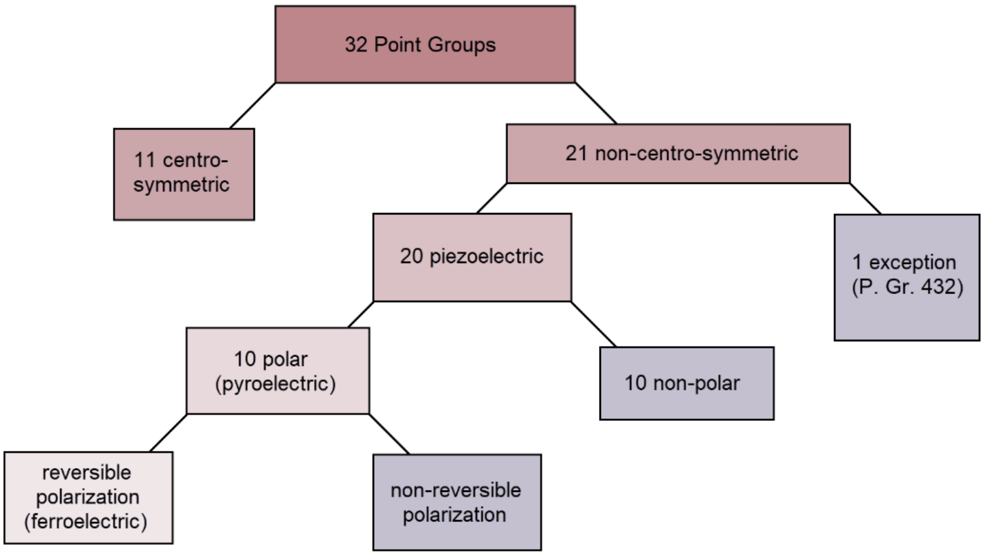

Figure 2.4: The relationship between the symmetry dependent piezoelectric, pyroelectric and ferroelectric properties of the 32 point groups. Reformatted from [11]

Of these 20 crystal classes, 10 exhibit a unique polar axis, a temperature dependent spontaneous dipole moment, and are considered pyroelectric classes. A material that has two or more stable orientations of this spontaneous dipole moment at null electric field, where the vector of polarity can be reoriented upon application of an electric field, are termed ferroelectric materials. The relationship between each of these symmetry dependent behaviours are shown in figure 2.4 [11].

2.2.2 Ferroelectric Domains

If a ferroelectric crystal structure was to polarise along one of its available polarisation vectors, the energy associated with the consequent depolarising field would be relatively large. In order to minimise the associated electrostatic (and elastic) energy constraining the material, different areas of the structure polarise uniformly along one of the available polarisation vectors forming a ferroelectric domain [10,12–14]. Multiple domains, each of differing but reorientable polarisation vectors, nucleate throughout the crystal structure, separated by domain walls of unique properties, such as thicknesses and energies, according to the transition between neighbouring polarisation vectors. A single domain state is unfavourable since the energy associated with the crystal surfaces would be greater than the energy associated with ferroelectric ordering, so much so that ferroelectric ordering would cease to exist [10,12].

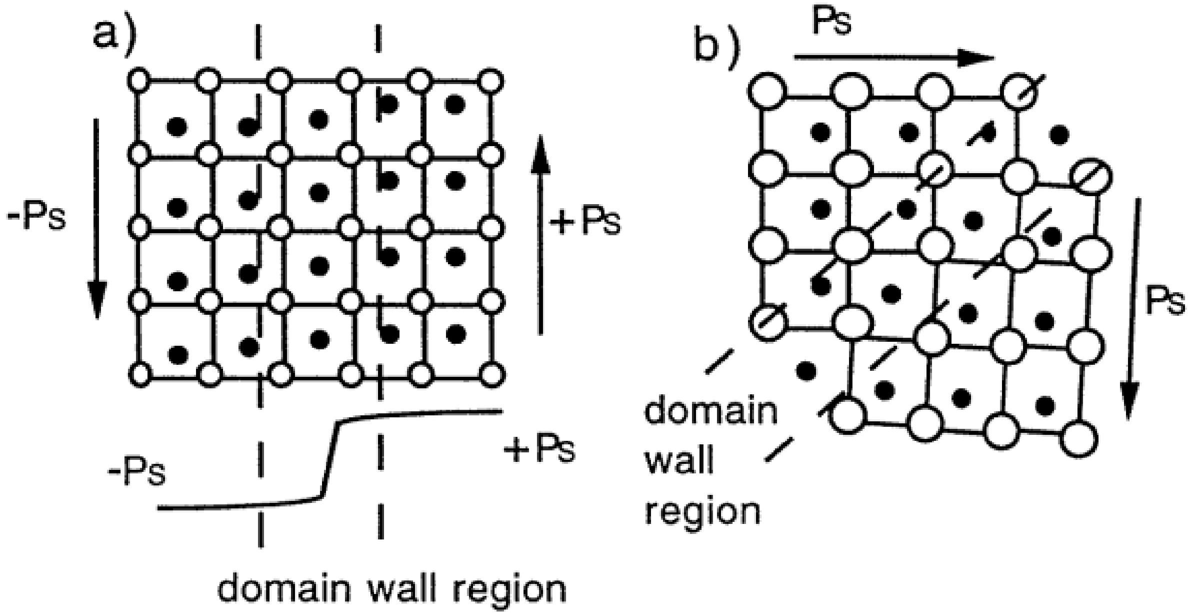

Figure 2.5: The formation of 180 and 90 ° domain walls, seperating adjacent domains with spontaneous polarisation vectors P_S. These domain walls form to minimise the electrostatic and elastic energy of a ferroelectric crystal. Reformatted from [12].

In tetragonal $BaTiO_3$, where the 6 polarisation vectors exist along the <001> axes, 90 ° and 180 ° domains are able to form within the crystal structure referring to the 90 and 180 ° relative orientation of polarisation vectors between neighbouring domains. A schematic showing 90 and 180 ° domain walls is shown in figure 2.5 [12]. These different domain wall formations offer different energetically minimising properties. 180 ° domains seek to minimise the depolarisation field due to the antiparallel arrangement of neighbouring polar axes, whilst 90 ° domains minimise the elastic energy imposed by the straining associated to the <001> dipole moments formed within a domain [12]. The orientation of domains changes according to crystal symmetry and for the low temperature rhombohedral polymorph of $BaTiO_3$, due to the polar vector occurring along the <111> axes, 71, 109 and 180 ° domain walls are found to exist instead [12].

Ferroelectric domains walls are typically a few unit cells wide, however the width and associated energies are dependent on their type (the angle subtended between neighbouring polarisation vectors). 90 ° walls are typically thicker but lower in associated energy with respect to 180 ° domain walls, for example. This wall energy typically originates from depolarisation fields associated with the divergence of the polarisation vector across the wall, misorientation between neighbouring dipole moments/polar vectors either side of the wall and the straining/elastic contributions [10].

2.2.3 Electric Field Dependence of Polarisation

The principle of electrostriction is applicable to all crystal structures and indicates dipole moment formation and consequent polarisation under the application of an electric field, as positive and negative ions of the crystal structures are displaced conversely [10]. The behaviour and rate of polarisation change under electric field application is however sensitive to the crystal symmetry and the dynamics of polarisation incurred, including the correlation lengths of polar ordering. This results in variable hysteresis effects and consequent polarisation-electric field (PE) loops. The exact shape and dimensions of these loops are of course material dependent, but fall into similar profiles according to the whether the dielectric material is paraelectric with a linear polarisation response, ferroelectric, relaxor-ferroelectric or antiferroelectric. These produce the characteristic responses shown in figure 2.6 a) through d), respectively.

The hysteresis induced upon electric field application is greatest for a ferroelectric material, and is incurred by the energy lost due to the polarisation dynamics associated with domain reorientation (domain wall mobility), including those of irreversible nature. In ferroelectric (tetragonal) $BaTiO_3$, loss is typically incurred from the mass reversal of 180 ° domains [15] near the coercive field, with energy transferred as heat throughout the crystal structure [13]. 90 °

domain walls are typically moved at higher fields towards the polarisation saturation, and are the first to relax upon subsequent field reduction for electrostrictive purposes. Smaller losses are incurred at lower fields from domain wall vibration (with energy transferred as acoustic plane waves that propagate throughout the structure) and low scale domain wall translations, however these impart little macroscopic effects on the surrounding domain structure [13], with the minor/Rayleigh loop this would form not visible on figure 2.6 b).

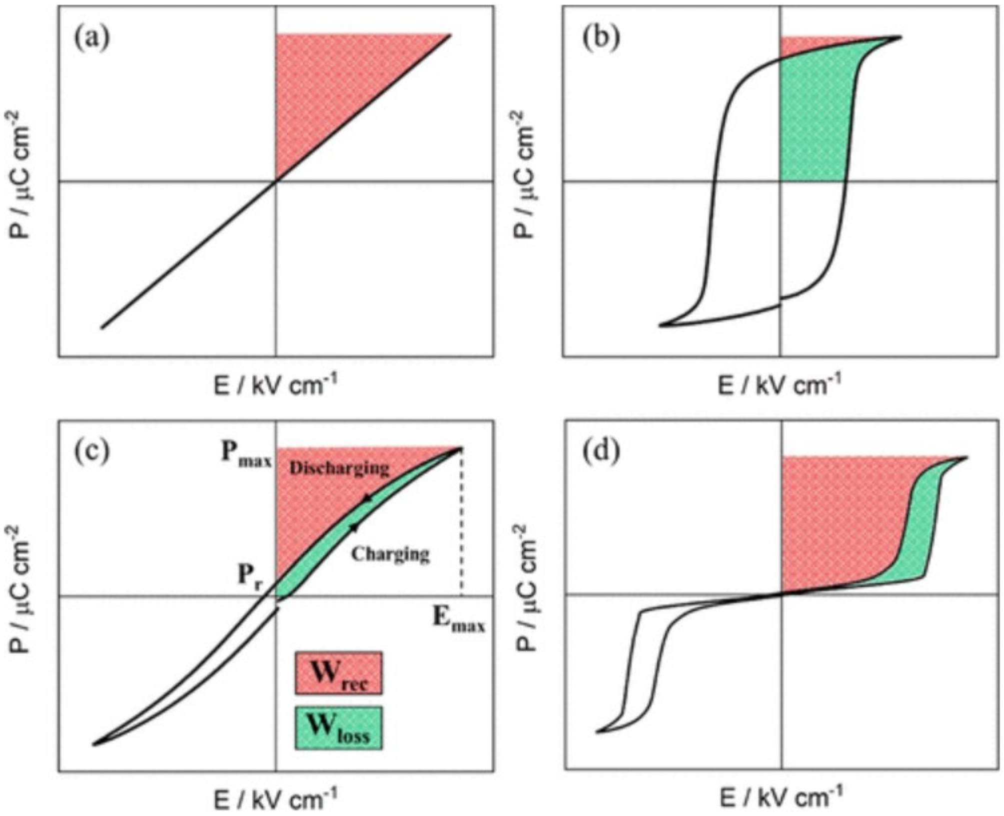

Figure 2.6: The P-E hysteresis typical of four different dielectric materials with different intrinsic polarisation behaviours: a) linear b) ferroelectric c) a relaxor-ferroelectric d) anti-ferroelectric. Reformatted from [19].

Upon field reversal, a finite negative electric field, the coercive field, is required to achieve a complete net polarity reversal as some of the domain walls become pinned. The recoverable energy density stored within the dielectric as a result of its polarisation is calculated as the integral of equation 2.1 [16–18].

$$W_{rec} = \int_{P_r}^{P_{max}} E\, dP \tag{2.1}$$

Where 'P_{max}' is the maximum polarisation observed and 'P_r' is the remnant polarisation, observed when the electric field is reduced to 0 kVcm^{-1}. It is equivalent to the area shaded in red in figure

2.6. The irrecoverable energy density is shaded green in figure 2.6 and given by the integral of equation 2.2.

$$W_{rec} = \int_{0}^{Pmax} E\, dP \tag{2.2}$$

The result of long range polar domains forming induces higher maximum polarisation magnitudes, but also induces the higher losses and polarisation saturations that are deleterious to the magnitude of recoverable energy density achievable. Reducing the scale of polar order reduces the maximum polarisation achievable for the dielectric, but linearises the electric field dependency. The energy storage efficiency, the ratio between the recoverable to irrecoverable energy density stored within the capacitor upon polarisation, consequently improves. Should the dielectric resist electric field induced dielectric breakdown, such as through smaller volumes and an associated statistical reduction in breakdown nucleating flaws (pores or cracks for example) or higher densities, the lack of polarisation saturation incurred provides a route to high recoverable energy density with high associated storage efficiency. Increasing amounts of literature are dedicated to the linearisation of materials with nominally high intrinsic polarisation, to maximise the efficiency and recoverable energy density achievable in a miniaturised MLCC chip. The overall intention of this research is then to shift MLCCs from typical power electronics (to which they are useful for their short charge/discharge times) to applications that can utilise both storage and power, such as pulse-power applications[19].

2.2.4 Polarisation & Dielectric Permittivity

When a crystal is subjected to an electric field, dipole moments are formed across a range of length scales. A dipole moment (μ) is the separation of charge (q) over a finite length (d) [13]:

$$\mu = q \cdot d \tag{2.3}$$

The polarisation of a dielectric (P), an electronically insulating material, is then described as the total dipole moment formed per unit volume (V) [13]:

$$P = \frac{\mu}{\delta V} \tag{2.4}$$

Since this thesis is focused on dielectric materials, should they be located between two oppositely charged plates separated by a distance d, they are capable of separating charge in the formation of a parallel plate capacitor, just like a vacuum can. The electric field across a parallel plate capacitor separated by a vacuum is based on the voltage (V) driven charge that is built up on these adjacent electrode surfaces, of area A with charge density σ, relative to the permittivity of free space ($\varepsilon_0 = 8.85 \times 10^{-14}$ Fcm^{-1}) [13]:

$$E = \frac{\sigma}{\varepsilon_0} = \frac{V}{d} \tag{2.5}$$

When a medium is placed between the parallel plates, the polarisation of the medium induced by the electric field influences the effective charge density seen by the plates. The total charge of the plates then becomes a function of the intrinsic polarisability of the material, a function of its crystal structure and component ions. This is described by its electric susceptibility, χ_e , and so the charge storage (Q/A) can be represented as [13]:

$$\frac{Q}{A} = (1 + \chi_e)\varepsilon_0 \frac{V}{d} \tag{2.6}$$

The function $(1 + \chi_e)\varepsilon_0$ is the permittivity of the medium, ε, and $(1 + \chi_e)$ is equal to the relative permittivity of the medium, ε_r, since it is relative to that of a vacuum. The capacitance of a vacuum parallel plate capacitor becomes [13]:

$$C_0 = \frac{A\varepsilon_0}{d} \tag{2.7}$$

and the capacitance of a parallel plate capacitor separated by a dielectric medium of relative permittivity ε_r, becomes:

$$C = \frac{A\varepsilon_0\varepsilon_r}{d} \tag{2.8}$$

Polarisation of a dielectric medium can be described by four general mechanisms, each providing a dipole moment and polarisation contribution over different length scales. Atomic polarisation occurs at the smallest length scale and is the response of an ion's electron cloud displacing relative to the nucleus. Ionic displacement of the cation and anion sublattices also occur but over a slightly larger length scale. Dipole moments that are present within the structure will also reorientate, particularly so for ferroelectric materials that exhibit a spontaneous and unique dipole moment. Finally, on the largest length scale are space charge effects, the accumulation of charge at a potential barrier. These polarisation processes and their associated length scales are visualised in figure 2.7 [13]. The length scales that these polarisation processes act over impart the frequency dependence of polarisation observed under an applied ac electric field.

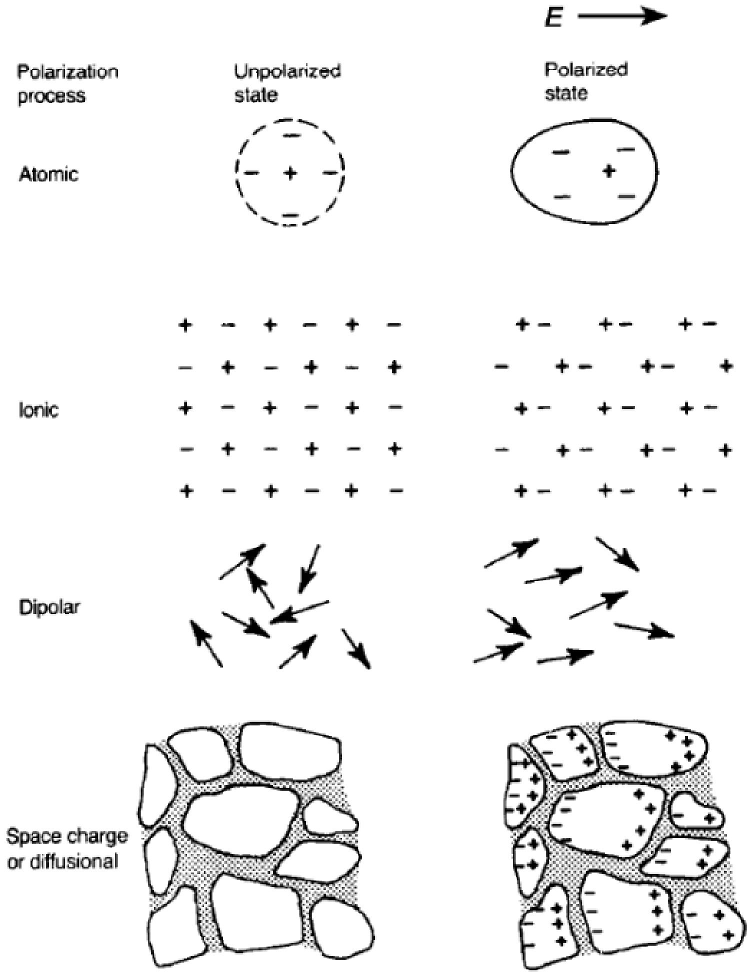

Figure 2.7: Four fundamental polarisation mechanisms of a material under the application of an electric field. The length scale of the dipole moments formed increase moving from atomic to space charge mechanisms. Reformatted from [13].

Polarisation processes that occur over the largest scales will be 'relaxed' out at comparatively lower electric field frequencies compared to mechanisms of polarisation over the smaller length scales. Relaxation of the polarisation simply refers to the inability for that polarisation mechanism to respond to increasing frequencies and produce the associated charge separation for dipole moment formation. When the polarisation mechanism is relaxed out, it no longer contributes to the overall polarisation of the sample. The frequency dependence of the aforementioned polarisation mechanisms is shown in figure 2.8. The relaxation of space charge and dipolar mechanisms with increasing frequency occurs first and second, respectively. Ionic and atomic polarisation mechanisms instead show a resonance effect rather than the relaxation effect described.

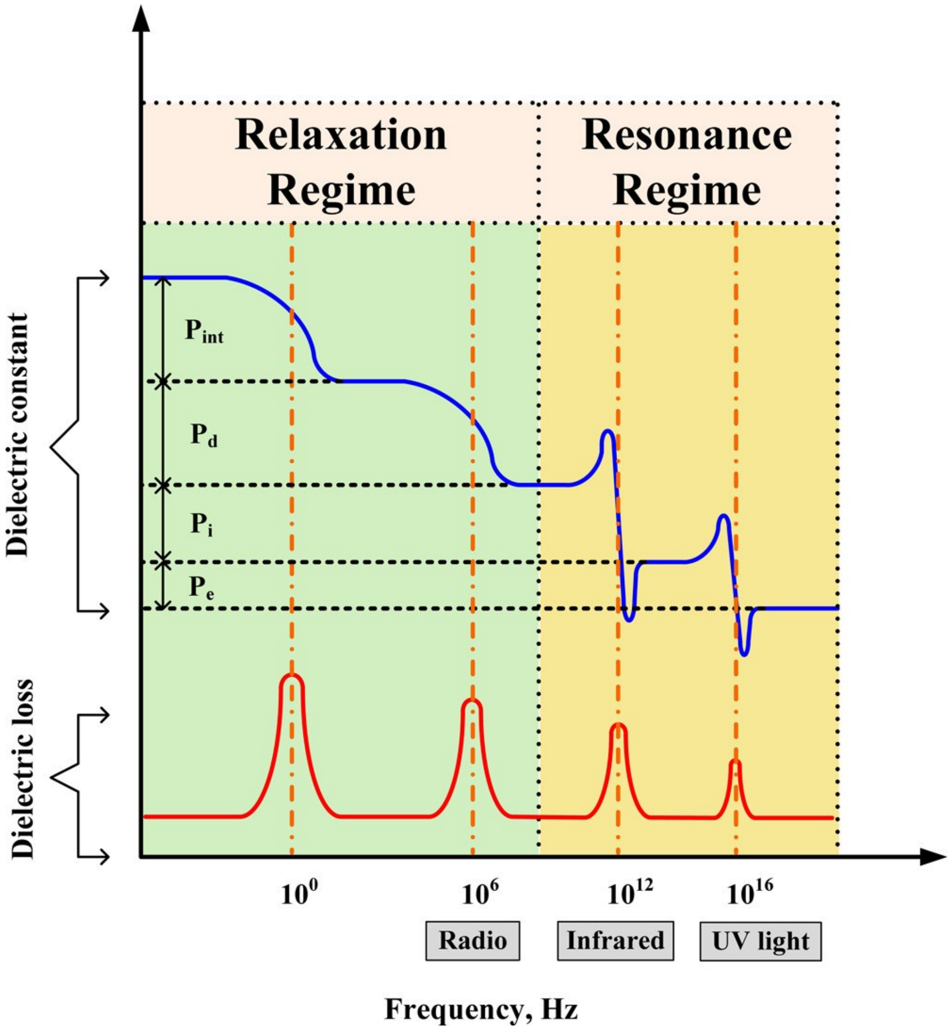

Figure 2.8: The relaxation and resonance effects of the four main polarisation mechanisms with increasing frequency, in terms of permittivity and dielectric loss. P_{int} refers to interfacial (space charge) contributions, P_d dipolar contributions, P_i is ionic polarisation and P_e is electronic (atomic). Reformatted from [222]

2.2.5 Temperature Coefficient of Capacitance

Since permittivity is a property inherent to the crystal structure of a material, a temperature dependence of permittivity results. The temperature coefficient of capacitance, TCC, is a measure of how much the permittivity (capacitance) varies with respect to the room temperature equivalent (25 ^{0}C), equation 2.9.

$$TCC\ (\%) = \frac{\varepsilon(T) - \varepsilon(25\ °C)}{\varepsilon(25\ °C)} \times 100 \tag{2.9}$$

For class II dielectrics used within MLCCs, permittivity variation with temperature can be quite considerable unlike class I dielectrics. It is necessary to know how this permittivity varies with temperature to ensure the capacitance output of the device is sufficient to fulfil its intended role. The Electronic Industries Alliance (EIA) has standardised the permittivity variation of a dielectric (capacitance variation of a capacitor) with temperature, based on the calculated TCC, according to the following alpha-numeric coding system:

Table 2.2: The alpha-numeric coding system used to specific TCC associated with a capacitor across a defined operating temperature range

First Character		Second Character		Third Character	
Letter	Lower Temperature Bound (°C)	Digit	Upper Temperature Bound (°C)	Letter	Maximum TCC Tolerance (%)
X	- 55	2	+ 45	D	± 3.3
Y	- 30	4	+ 65	E	± 4.7
Z	+ 10	5	+ 85	F	± 7.5
		6	+ 105	P	± 10
		7	+ 125	R	± 15
				S	± 22
				T	+ 22 / - 33
				U	+ 22 / - 56
				V	+ 22 / - 82

For X7R rated dielectrics, a maximum TCC variation of ± 15 % is observed between -55 and 125 °C. For X8R rated dielectrics, a maximum TCC variation of ± 15 % is observed between -55 and 150 °C

2.3 Perovskites

The ideal aristotype perovskite structures exhibited by compounds such as $SrTiO_3$ are related to the mineral perovskite $CaTiO_3$, existing with a unit cell formula ABX_3 (where X is typically an O^{2-} anion, but metal-halide perovskite families exist where a halide anion replaces the oxygen)[7,20–25]. This ideal structure is cubic with an associated Pm3m space group. Paradoxically, the mineral perovskite $CaTiO_3$ exhibits orthorhombic symmetry (space group Pbnm) distorted away from this ideal high symmetry aristotype phase. The perovskite structure is composed of larger A-site cations located in a 12 fold cubo-octahedral anion coordination at the cell centres whilst the comparatively smaller B-site cations are 6-fold anion coordinated at the cell corners within corner sharing BO_6 octahedra. An example of this structure is shown in figure 2.9.

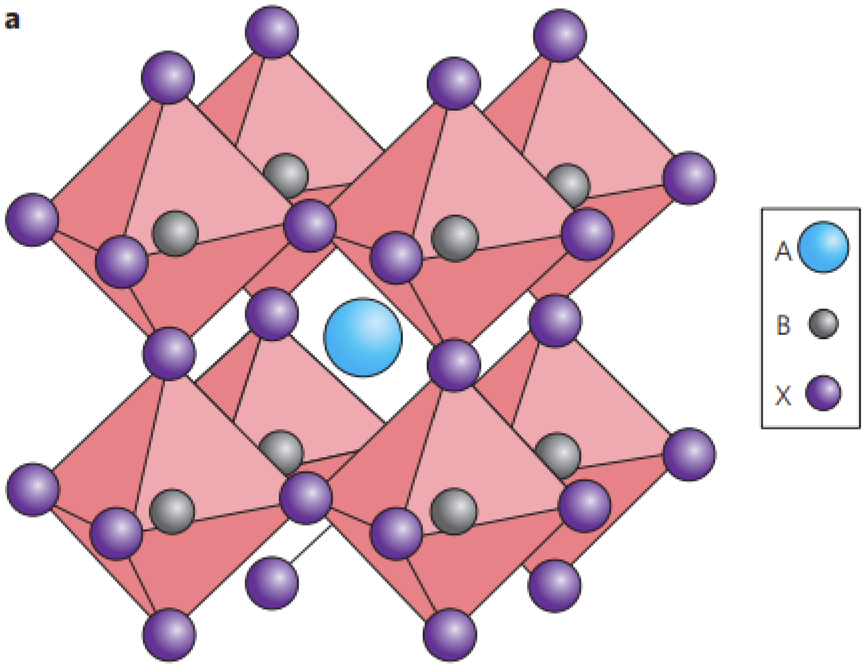

Figure 2.9: The idealised cubic unit cell of the ABO_3 perovskite. The blue sphere represents the body centred A cation. The grey spheres represent the corner occupying B cations, whilst the purple spheres represent the corner sharing oxygen or halide anions. Reformatted from[21]

The ideal perovskite can also be considered as a cubic close-packed structure, where the oxygen and A site ions are stacked in cubic close-packed layers along the cubic [111] direction, and B site ions occupy one quarter of the octahedral sites that are consequently formed [23]. In the ideal structure, the B-O distance is equal to a/2 (with a being the cubic unit cell parameter), whilst the A-O bond distance is equal to $a/\sqrt{2}$ [24]. A relationship between the atomic radii of the A, B and O ions is also held – $r_A + r_O = \sqrt{2}(r_B + r_O)$ [24](where $r_{A,}$ r_O and r_B are the atomic radii of the A, O and B ions, respectively).

In reality few perovskite oxides exist with this cubic structure at room temperature, although most of them tend towards this at elevated temperatures (or in the paraelectric state for a ferroelectric material). Goldschmidt introduced a tolerance factor (t) as a measure of distortion away from the idealised cubic structure (and thus it can be used to quantitatively predict the crystal structure of the perovskite compound based on the ionic radii)[26]:

$$t = \frac{\mathrm{rA} + \mathrm{rO}}{\sqrt{2}(rB + rO)} \qquad (2.10)$$

Materials with a tolerance factor of 0.9-1.0 generally exhibit the ideal cubic structure (however strictly speaking cubic symmetry is attained with t=1), whilst a tolerance factor of 0.71-0.9 results in a distorted perovskite structure with tilted BO_6 octahedra. A tolerance factor greater than unity (1) or below 0.71 may result in the formation of non-perovskite structures [26,27].

2.4 Multi-Layer Ceramic Capacitors

A Multilayer Ceramic Capacitor (MLCC) is effectively a parallel lamination of ‘n’ parallel plate capacitors, where ‘n’ is equal to the number of insulating dielectric layers separating ‘n+1’ overlapping internal electrodes. Each of these dielectric layers acts as a conventional parallel plate capacitor and so the total capacitance of the MLCC becomes a parallel summation of these ‘n’ independent capacitors:

$$C = \frac{n\varepsilon_0\varepsilon_r A}{d} \qquad (2.11)$$

where C is the device capacitance, n is the number of dielectric layers, ε_0 is the permittivity of free space, ε_r is the relative permittivity of the dielectric, A is the cross-sectional overlap area of adjacent internal electrodes and d is the thickness of the dielectric layers. A schematic of this serial connectivity of internal dielectric layers is shown in figure 2.10. MLCCs have an inherent advantage on miniaturisation with respect to monolithic parallel plate capacitors hence finding integration in vast numbers within common electrical circuitry.

The capacitance of the MLCC can be maximised through the use of a dielectric layer with as high of a relative permittivity as possible, with its layers as thin and cross sectionally large as possible, and with layers as frequent as possible. In reality, not all are achievable and the demand for miniaturisation sets constrains on the size of these layers and how numerous they are. The need for optimisation of material properties, specifically dielectric response, then supersedes device design. Maximising permittivity without compromising the temperature stability is a frequent

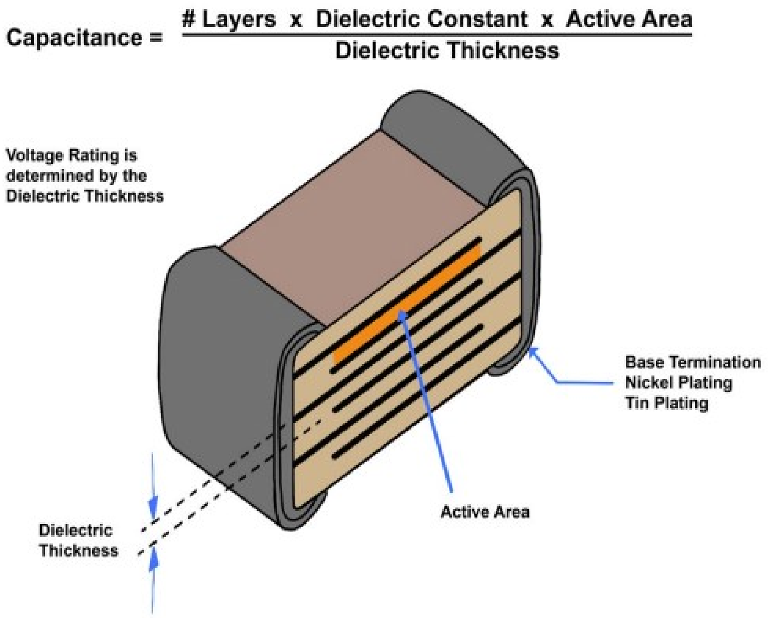

Figure 2.10: A schematic representing the lamination of ‘n’ internal parallel capacitors in an MLCC. Reformatted from [3]

challenge, one that shall be covered within this thesis. $BaTiO_3$, a prototypical ferroelectric below its Curie temperature (T_c ~ 130 °C) and a material that is commonly utilised within MLCCs, exhibits a large permittivity often in excess of 10,000 at T_c. Either side of this Curie temperature comes a sharp and large drop in permittivity. It is unrealistic to expect circuitry to be operated consistently around 130 °C to take advantage of this high permittivity. When its temperature stability is improved, often through chemical doping, the permittivity is consequently lowered. A fine balance is necessary to find materials that exist with a compromise of the two qualities. Of course, high capacitance is not always essential where thermal stability is crucially important, often for filter networks, timing circuitry or resonant applications, in which case class I dielectrics such as $CaZrO_3$ and TiO_2 in NP0’s can be utilised which have inherently lower permittivity’s but far superior thermal stabilities.

Although permittivity variation is expected across differing capacitor types, the dielectric should always exhibit low dielectric losses, i.e. minimal leakage current upon application of an electric field. The device build should also exhibit low losses, manifesting as a high insulation resistance. The dielectric should also be thermally and chemically compatible with the internal electrode materials, with base metal electrodes (BMEs) such as nickel or copper preferable for their low manufacturing costs. This is increasingly important as miniaturisation drives thinner dielectric layers and increasing electrode layer fractions within the capacitors. The dielectric will consequently need to be non-reducible for use of the BMEs, or re-oxidisable at lower temperatures post sintering.

While the exact details and formulations of MLCC manufacture typically varies according to the manufacturer, a similar tape-casting route to that shown in figure 2.11 is frequently used. This involves the milling of the dielectric formulation with necessary binders, flocculants and plasticisers to attain a green body strength and an associated tape flexibility for subsequent chip build. The slurry formed is cast as a wet film with a defined thickness. After drying, the electrodes are screen printed onto the layers, with the layers then orientated and laminated, cut and fired to densify and remove the organic constituents introduced in previous stages. The chips are then terminated and coated for environmental protection [28].

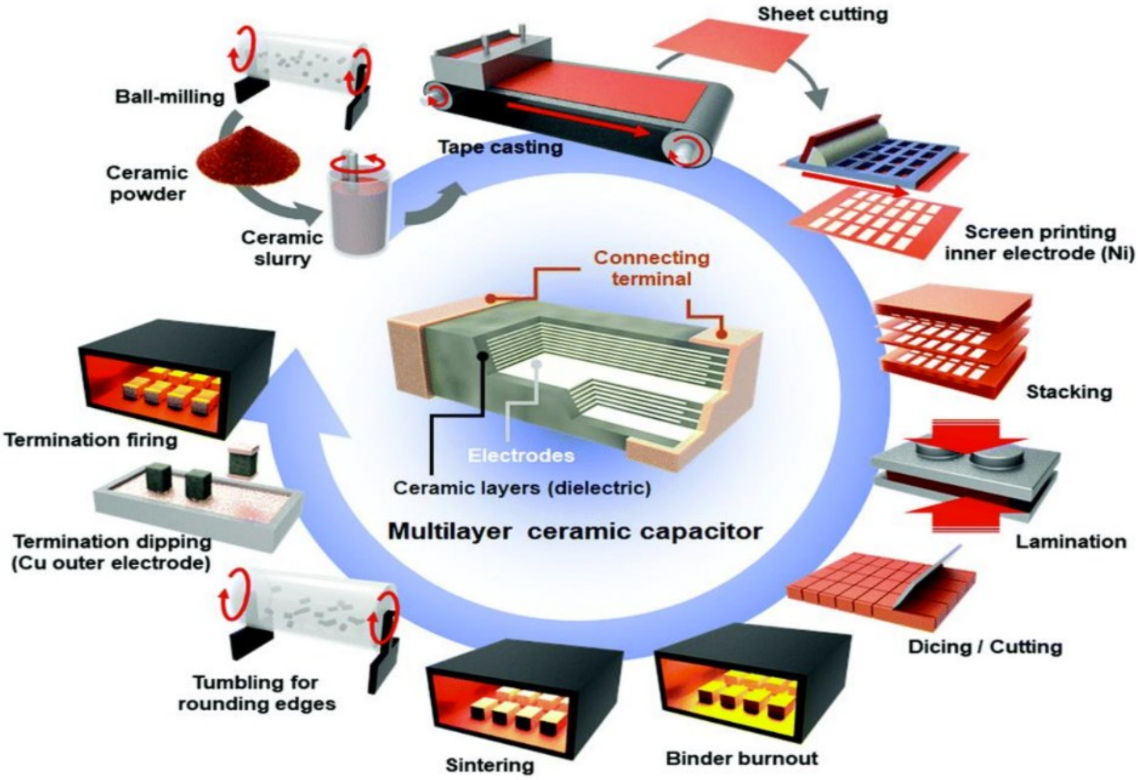

Figure 2.11: The typical tape casting process utilised for commercial MLCC manufacture. Reformatted from [28]

3 Literature Survey

3.1 $BaTiO_3$

First discovered in the 1940’s [29,30], $BaTiO_3$ is a prototypical ferroelectric perovskite until ~ 120-130 °C, whose (process dependent) dielectric behaviour promotes integration within most commercial class II MLCCs. $BaTiO_3$ is characterised by an exceptionally large relative permittivity, often in excess of 10,000, at its Curie temperature ~ 130 °C [31,32], manifesting a large change of order parameter as it undergoes a transition from its cubic paraelectric polymorph to its tetragonal ferroelectric analogue. This relative permittivity response is shown in figure 3.1.

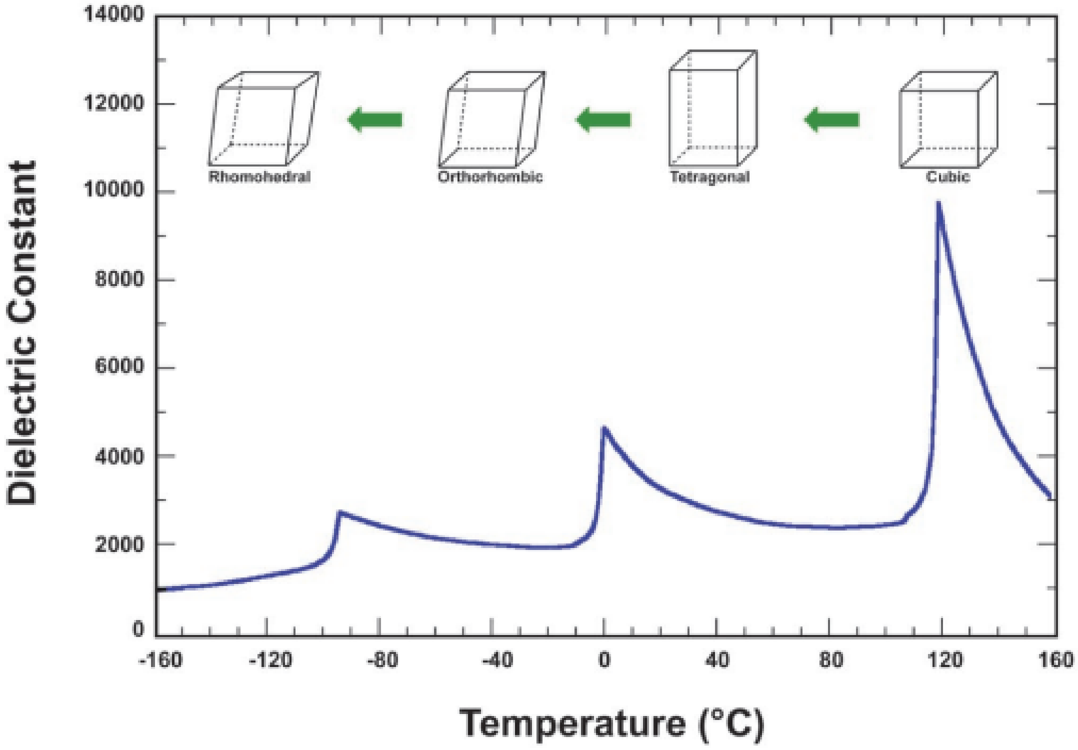

Figure 3.1: The relative permittivity response of $BaTiO_3$. Reformatted from [32]

This is one of three sequential phase transitions that occur between its cubic paraelectric polymorph and three, lower symmetry distorted ferroelectric polymorphs upon cooling, each driven by a reorientation of the associated polar axes that arises as the Ti displaces away from its centralised coordination within the $[TiO_6]$ octahedra [33]. The sequence of crystal systems, from cubic to tetragonal, orthorhombic and rhombohedral [25,33], as well as their associated transition temperatures, are shown in figure 3.2 (reformatted from [13]). The anomalies recognisable in figure 3.1 correspond to the transition between each of its ferroelectric polymorphs and the change in vector associated with the reorientable polar axes.

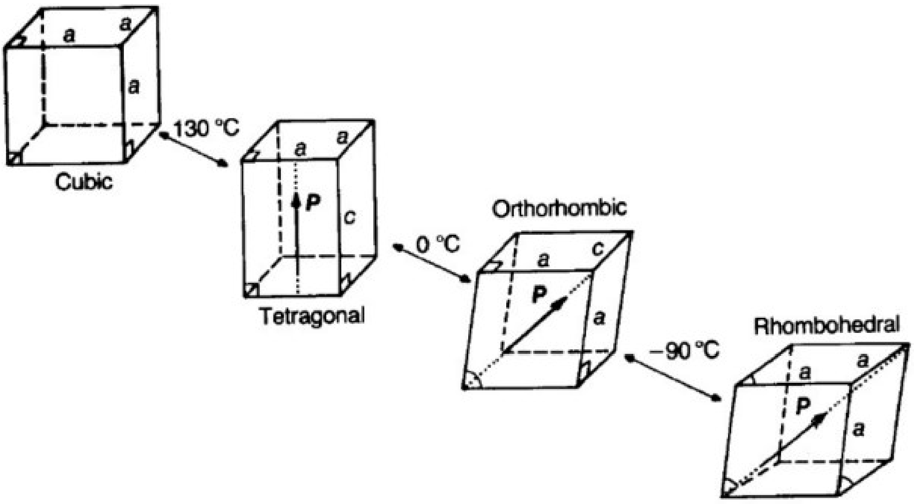

Figure 3.2: A schematic showing the symmetry loss upon cooling as $BaTiO_3$ transitions through 3 ferroelectric phase transitions. Reformatted from [13]

The nature of these ferrodistortive transitions in $BaTiO_3$ have long been considered displacive in type, driven by the condensation of a ‘soft-mode’. This is a transverse optic phonon mode whose frequency reduces to zero upon cooling to the Curie temperature, imparting dynamical instability within the lattice and freezing out with associated intraoctahedral Ti displacements. These Ti displacements are described as the eigenvectors of this high temperature soft mode [34,35]. Some early neutron spectrometry and infrared reflectivity studies [34,36]that supported this theory in other ferroelectric titanates, namely $SrTiO_3$, were, however, not so supportive for $BaTiO_3$. This system was instead viewed as somewhat more complicated, and newer X-ray fine structure analysis has even suggested a more order-disorder type ferroelectric transition in $BaTiO_3$ instead [37].

$BaTiO_3$ is an electrical insulator when processed in air, useful for dielectrics, although n-type semi-conductivity can be induced when sintered under low pO_2 atmospheres (> 1200 °C) [38]. Consequently, when heating semiconducting $BaTiO_3$ within a finite temperature range exceeding the Curie temperature, an increase in resistivity by several orders of magnitude in a positive temperature coefficient of resistance (PTCR) response is observed, shown in figure 3.3. A double Schottky barrier is formed between an insulating grain boundary/interfacial layer with high acceptor density (segregated acceptor ions and/or adsorbed oxygen) and n-type semiconducting grains [39–41]. The resulting space charge layer promotes band bending towards the interface, with an additional energy requirement necessary for the excitation of valence electrons into the conduction band, thereby inducing the observed sharp PTCR effect. Towards elevated temperatures, the Fermi energy level shifts closer to the conduction band with a smaller

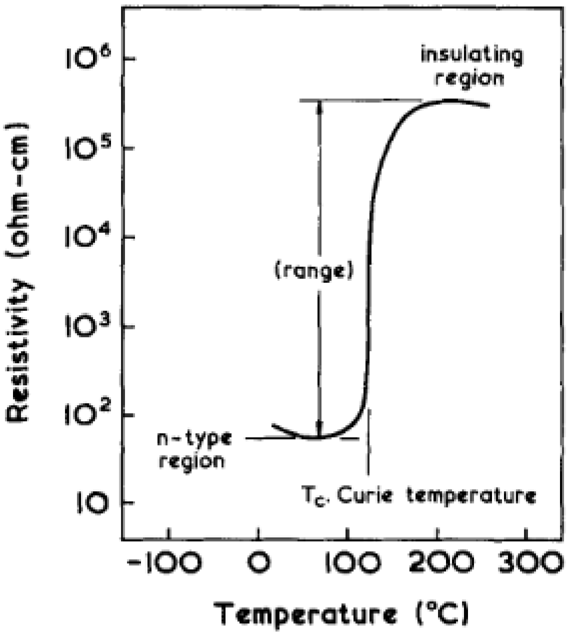

Figure 3.3: The positive temperature coefficient of semiconducting n-type $BaTiO_3$ with insulating, reoxidised grain boundaries. Reformatted from [41].

associated band gap, sufficiently close enough for a statistically appreciable number of electrons to be promoted into the conduction band, inducing a consequential reduction in the associated barrier height and retaining negative temperature coefficient of resistance behaviour once more. It is only after the Curie temperature is exceeded within these polycrystalline $BaTiO_3$ specimens that the PTCR effect is observed, since in the ferroelectric state the spontaneous polarisation of the bulk compensates the charge build up at the interfaces [42,43]. This PTCR effect is understandably processing dependent. Controlling the microstructure, sintering atmosphere and cooling rates have a significant impact on the resistivity variations observed. Reoxidation of the grain boundaries in particular is of significant importance in optimising this effect [44], with the formation heterogeneous oxygen concentrations interpretable as forming a heterogeneous electrical microstructure from impedance spectra when air or argon cooled atmospheres are utilised during sintering, limiting complete grain reoxidation [45].

For PTCR samples, donor doping of $BaTiO_3$ is often utilised to enhance the n-type semiconducting behaviour of the grain cores and increase the Schottky barrier height for a larger resistivity increase. La^{3+} dopes preferentially onto the A site of $BaTiO_3$ [46–49]as a consequence of its relatively large ionic radius, too large for B site coordination, and results in an enhancement of n-type conductivity for small doping concentrations < 1 at%. An optimal conductivity is achieved between 0.3 – 0.5 at% doping, used for commercial PTCR formulations [50], as shown in figure 3.4.

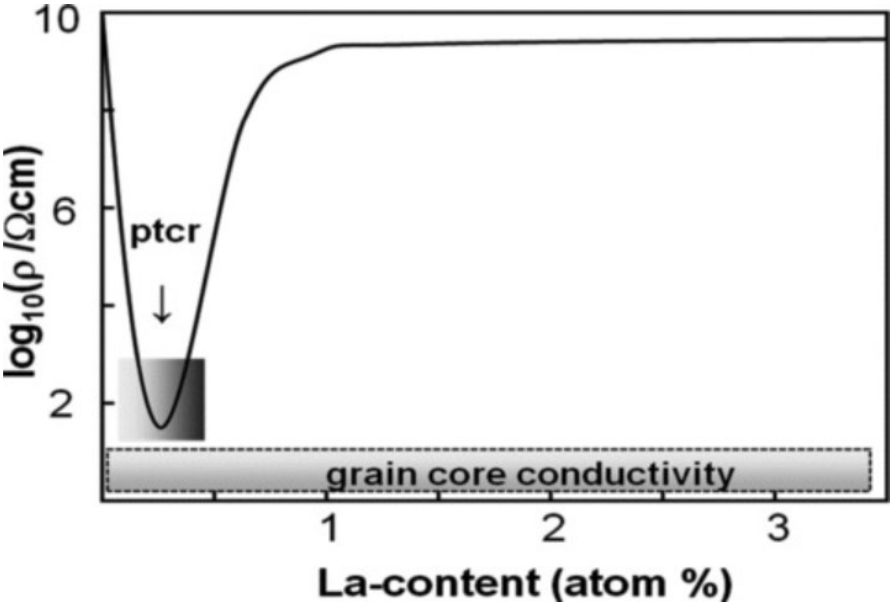

Figure 3.4: The change in resistivity of polycrystalline A site La^{3+} doped $BaTiO_3$. The minimum resistivity is utilised for commercial PTCR ceramics, at 0.3-0.5 mol% doping concentrations. Reformatted from [50].

Above this, the resistivity begins to increase once more, previously considered to be the transition between doping mechanisms from electronic to ionic compensation [51–53]. It has since been shown that ionic compensation, specifically the formation of V_{Ti}'''', is the most energetically favourable compensation mechanism [50]until the ~ 25 mol % solution limit. It is the loss of the resulting under-bonded oxygen from V_{Ti}'''' clusters that yields the n-type semi-conductivity forming $Ba_{1-x}La_xTi_{1-x/4}O_{3-\delta}$ [50]. The change in (re)oxidation rates/kinetics with increasing La^{3+} content influences the increase in resistivity towards higher La^{3+} concentrations as opposed to a change in doping mechanism [45,54]. The doping concentration is also dependent upon the temperature range the PTCR effect is intended for, given the ~-24 °C/mol% T_c reduction induced by the La^{3+} A site doping [47].

Regarding $BaTiO_3$ integration into MLCCs as dielectrics, the need to lower manufacturing costs with the use of base metal electrodes (BMEs), such as Ni or Cu that are lower in cost compared comparatively more inert Pt or Ag-Pd electrodes, comes with a necessity to sinter under a reducing (low pO_2) atmosphere to inhibit oxidation of these electrode materials [28,55]. As previously discussed, such low pO_2 atmospheres will readily reduce Ti and induce n-type semi-conductivity undesirable for dielectrics [38,56], as in equation 3.1 and 3.2:

$$O_O^X \rightarrow \frac{1}{2}O_{2(g)} + V_O^{\cdot\cdot} + 2e' \tag{3.1}$$

$$2Ti_{Ti}^X + 2e' \rightarrow 2Ti_{Ti}' \tag{3.2}$$

Often, acceptor doping is used to form non-reduceable dielectrics to inhibit this Ti reduction under such low oxygen partial pressure environments, forming oxygen vacancies in the process. These oxygen vacancies do, however, prove deleterious to the mean time to failure and ageing of the dielectric under progressive voltage loading conditions. It is oxygen vacancy migration to the cathode which has long been considered to encourage premature dielectric breakdown in MLCCs [57–60], shown schematically in figure 3.5, accumulating and decreasing the energy barrier for electron 'injection' the cathode, a Schottky emission process. Simultaneous with this increasing conduction is Joule heating, which can accelerate the breakdown process [61]. The defect chemistry of undoped $BaTiO_3$ is often driven by the presence of impurity ions within the material, which act often as acceptor type dopants based on the abundance of lower valence ions, giving $BaTiO_3$ its inherent pO_2 dependence (n-type at lower pO_2 and p-type at higher pO_2) [62]. Table 3.1 reveals an example of impurity elements found within undoped $BaTiO_3$ via spark-source mass spectrographic analysis.

Table 3.1: Impurity ions and their associated concentrations (by weight), found within polycrystalline undoped $BaTiO_3$ *[62]*.

Impurity	Concentration, ppm (by weight)
Carbon	0.5
Nitrogen	0.4
Magnesium	1.1
Aluminium	2.2
Phosphorus	2.3
Calcium	7.4
Iron	7.9
Arsenic	2.2

In polycrystalline $BaTiO_3$, Schottky barriers form at the grain boundary ~ 200 nm in length [63], often with segregated acceptor solutes at the interface [64], shown in figure 3.5, and impede mobility of the $V_O^{\cdot\cdot}$. It is this mechanism that enhances the electric field induced breakdown resistance and facilitates the improvement in time to failure of the dielectric [57,63,65]. Rare earths (REs) such as Dy or Ho that are intermediate in size compared to other cations of the series are able to dope onto both the A and B site, and are termed as amphoteric dopants for this ability to act as a donor or acceptor dopant in $BaTiO_3$ depending upon its coordination [66]. It is for this reason, and its intrinsic capability of reducing oxygen vacancy formation during processing, that time to failure and ageing is minimised upon such RE doping, especially compared to rare earths of differing radii. Increasing the grain boundary density via reduced grain sizes has also been

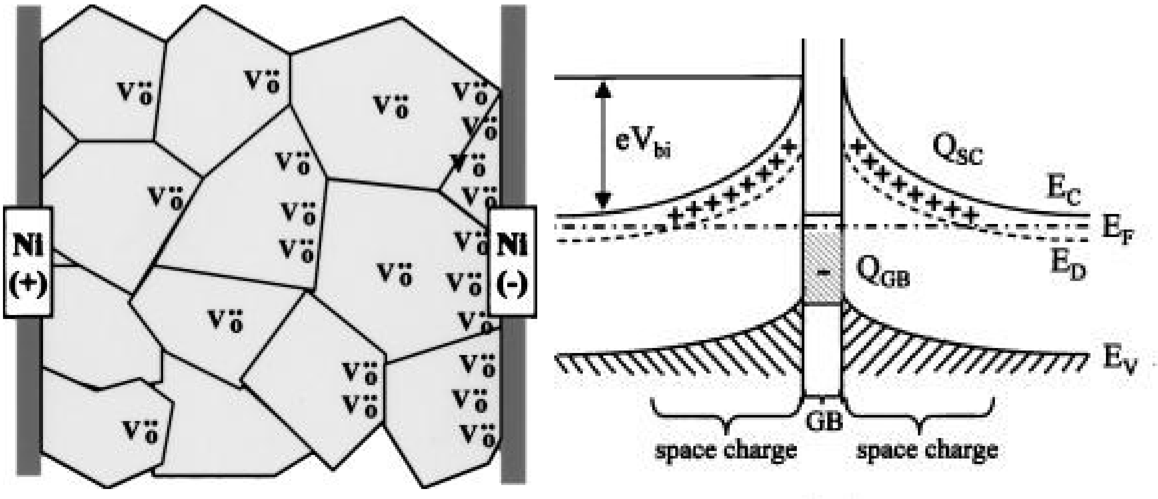

Figure 3.5: left) A schematic of the electromigration of oxygen vacancies through $BaTiO_3$ layers within Ni-MLCCs towards the cathode. Right) a) shows symmetric band bending and DSB formation in non-degraded MLCCs. Reformatted from [57].

found to assist breakdown resistance, with studies of acceptor doping of Al for Ti in $BaTiO_3$ finding a significant change in the characteristic time to breakdown depending upon grain size, with it being 500 times larger for fine grained samples with respect to the coarse grained equivalent [65] for the same doping concentration of 0.1 mol %. There is, however, a well characterised relationship between the permittivity response of $BaTiO_3$ and grain size, shown in figure 3.6.

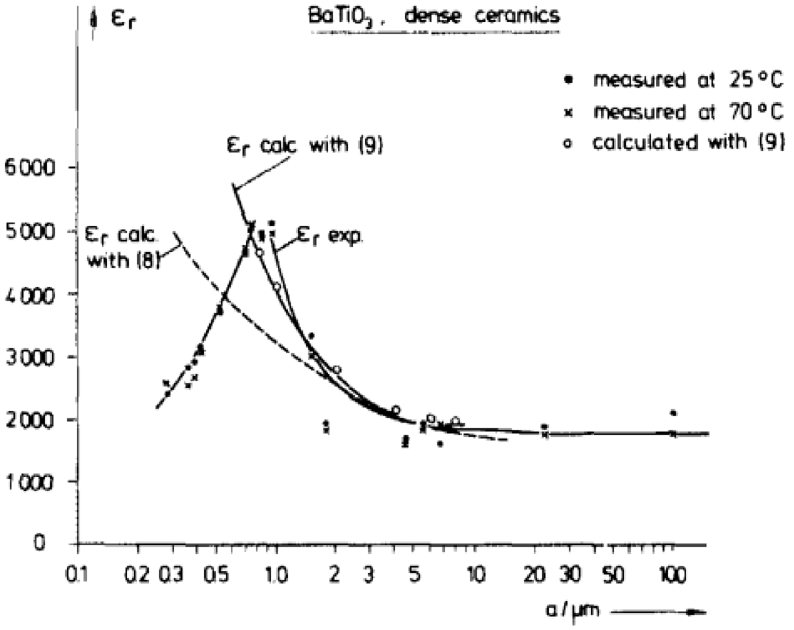

Figure 3.6: The grain size dependence of maximum relative permittivity for $BaTiO_3$. Reformatted from [68].

The permittivity maximum increases with decreasing grain size, optimising at ~ 1 µm[67–72], below which further reductions impart a decrease in the magnitude of the permittivity maximum.

This needs to be considered when dielectric layers are designed, for grain boundaries are necessary for breakdown resistance yet too small of a grain size introduces a decrease in the permittivity. The increase in permittivity at fine grain sizes towards ~ 1 µm was attributed to a reduction in the 90 ° domain width and an increase in the density of the corresponding domain walls, visually observed from SEM and TEM [68,69]. These more numerous 90 ° domain walls offered a higher mobility and greater extrinsic, vibrational contribution to reorientation under applied electric fields [68,70,73], supported by more recent in-situ XRD analysis [70] (where intensity variations between (200)/(002) split peaks reveals the changing domain texture of the ceramic, based on the changing volume fraction of domains during poling [74]). There is also a consideration that the straining associated around the domain wall could influence local symmetries, as XRD patterns previously revealed a more pseudo-cubic peak splitting upon reducing grain size as a result of the orthorhombic consistency within the tetragonal bulk [68]. This would make sense with the associated tetragonal-orthorhombic transition temperature having been observed to shift to higher temperatures with reducing grain size. This strain is then suggested to be capable of enhancing the intrinsic lattice displacement contribution to polarisation [69].

The permittivity is also dependent on the Ba/Ti ratios utilised during synthesis, with secondary phase Ba_2TiO_4 forming when the ratio is below or above 1. However, the mechanism by which this secondary phase forms is significant with respect to the dielectric response observed. For Ti excess, a liquid eutectic forms, with liquid phase sintering encouraging abnormal grain growth with this secondary phase forming predominantly around the grain boundaries. This essentially creates a serial connection between two polarising phases, decreasing the overall maximum permittivity observed for the phase mixture (with respect to nominal $BaTiO_3$) in proportion to secondary phase thickness. For Ba excess, Ba_2TiO_4 forms during sintering within grain centres. The resulting interfacial strain is compensated by the increase in 90 ° domain wall density, offering an enhanced extrinsic contribution to permittivity and increasing the maximum observed relative permittivity [75].

Although the insulating behaviour observed in $BaTiO_3$ is fundamental for dielectric utilisation in capacitors, when looking at figure 3.1 it becomes clear that the temperature variance of permittivity is significant and unsuitable for temperature stable dielectrics. Many of the dopant ions [76–79], including the aforementioned REs [80–82], segregate within the grain in the formation of a compositionally heterogeneous core-shell microstructure. This is often via liquid phase mechanisms where dissolution and reprecipitation occurs[78,79,83], or via thermodynamic inhibition of dopant diffusion kinetics [81,84], or both [85]. Mg, for example, is frequently used for its lack of homogenisation and couples to REs to form shell configurations

[80–82]. Core-shell formations are often necessary for X7R or X8R $BaTiO_3$ dielectric use (although this thesis will show alternative composite structures utilising $BaTiO_3$ related materials), relying on the limitation of long-range ferroelectric ordering amongst the $BaTiO_3$ cores by the shells. This lowers the permittivity magnitude associated to the core $BaTiO_3$'s ferroelectric-paraelectric transition, becoming similar in magnitude to the shell-related permittivity contribution that is observed at a temperature. The overall effect is a flattened permittivity response, shown in figure 3.32 section 3.8. This 'composite' type behaviour will be reviewed subsequently in section 3.8, showing how these macrostructures are desirable for TCC stabilisation in commercial MLCCs.

3.1.1 Ca-doped $BaTiO_3$

Although much of the aforementioned doping of $BaTiO_3$ regards aliovalent donor or acceptor doping, isovalent doping of $BaTiO_3$ has considerable effects on the dielectric properties of $BaTiO_3$. Sr A-site doping of $BaTiO_3$ was one of the earliest examples of such isovalent doping systems, with a monotonic reduction in T_c with increasing Sr content associated to a size effect of the smaller $Sr_{(XII)}^{2+}$ (1.44 Å) substitution for larger $Ba_{(XII)}^{2+}$(1.61 Å) [86]. This is analogous to the effect of hydrostatic pressure, which has previously been shown to result in a progressive decrease in the T_c of $BaTiO_3$ (a consequence of decreasing potential wells for Ti displacements) [87,88]. Ca induces a comparable reduction in tolerance factor upon A site doping, with an ionic radii of 1.34 Å (compared to 1.61 Å of Ba^{2+}) [86] in this 12 fold coordination environment, yet exhibits a different dielectric response to the Sr doped analogue.

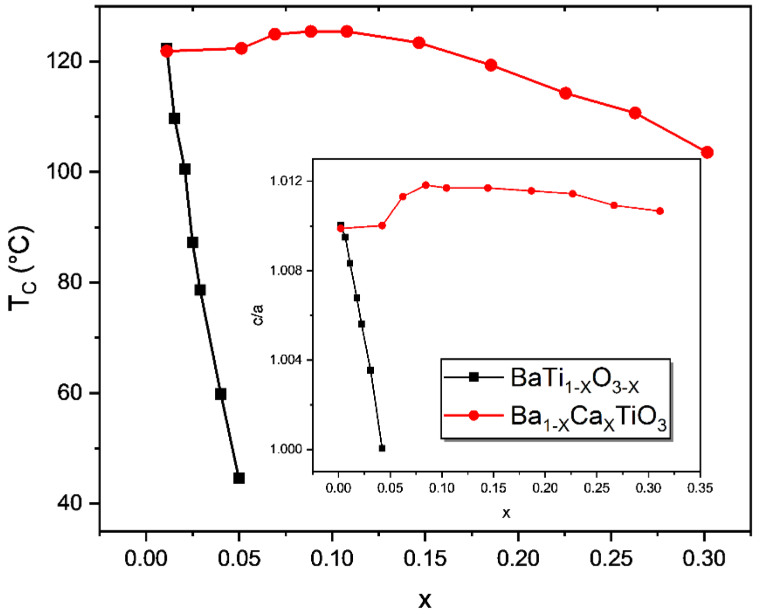

Figure 3.7: The effect of isovalent A site substitution of Ca onto the A site of $BaTiO_3$ (red) and the aliovalent acceptor doping of Ca onto the B site of $BaTiO_3$ (black) on Curie temperature. Reformatted from [94].

For this Ca doped system, a 20-25 mol% Ca solubility limit has been proposed based on the variance of lattice parameters from a linear Vegard's law type dependence above this concentration [89–92]. Preliminary reports noted a relative invariance of T_c with increasing Ca content, as opposed to a decrease of T_c, despite observing a monotonic reduction in the tetragonal-orthorhombic transition temperature [91,93]. Mitsui and Westphal [92]were the first to report on a now commonly observed increase in T_c with Ca A-site doping. This increase in T_c was small, extended to a maximum of 136 °C at 8 mol% substitution, hereafter a progressive decrease in T_c followed until the solid solution limit was exceeded [92,94]. This effect is shown in figure 3.7. The report was also the first in observing a monotonic decrease in the orthorhombic-rhombohedral transition temperature with Ca substitution, equivalent to the known reduction in the tetragonal-orthorhombic transition temperature [92].

The proposed mechanism behind the variability in alkaline earth metal effects on the T_c of $BaTiO_3$ was attributed to a competing effect between the size effect and bond strain induced at the A-site between itself and the surrounding coordination environment [95]. In the case of Ca, the size effect of the smaller Ca ion and a compressive strain it introduces upon the cells (that would cause cell contraction and thus inhibit the B site cation's ferrodistortive behaviour) is dominated by the strain which mediates off centring of the Ca cation, shown in figure 3.8. This Ca displacement can couple to (and favour) the intraoctahedral [TiO_6] distortions that attain the ferroelectric behaviour of $BaTiO_3$ based materials [88,96,97]. More recent simulations [98] are complimentary to this straining theory, with results implying the structural relaxations are a product of Ca preferentially attaining a lower coordination due to its insufficiently small size relative to the cubo-octahedral A site of Ba. This under-bonding of Ca cannot be compensated through distortions of the rigid [TiO_6] octahedra, and so displacement is necessary. Some, although not all, sites displace preferentially along the [001] direction essentially becoming 8-anion coordinate [98]. As discussed, this ferroelectric relaxation of within the [CaO_{12}] units is combinatorial or even influential to that within the [TiO_6] octahedra. From Cohen's description of ferroelectricity [88] in $ATiO_3$ perovskites, Ti-O hybridisation reduces local repulsion forces within the octahedra and drives these Ti displacements. The A-site cation can influence bond strains and thus bond lengths by its hybridisation with surrounding oxygen, which can also in turn change the electronic ground state and Ti-O interactions/displacement. Levin et al attributed a similar effect in $Ba_{1-x}Ca_xTiO_3$, with a degree of covalency between the equatorial oxygen and Ca influencing the hybridisation between the Ti-O and driving correlated displacements of Ca and Ti [96]. In this way, these Ca displacements couple to that of Ti, enhancing the intrinsic dipole formation and increasing T_c. The percentage of Ca ions undergoing this structural relaxation increases with Ca content, and thus so too does the T_c of BCT materials to a maximum of 8 mol% substitution. The rate of increase in Ca relaxations does begin to decrease, and consequently above this maximum the cell contraction will begin to dominate the strain effect, hence inducing the loss in T_c towards higher doping concentrations [98].

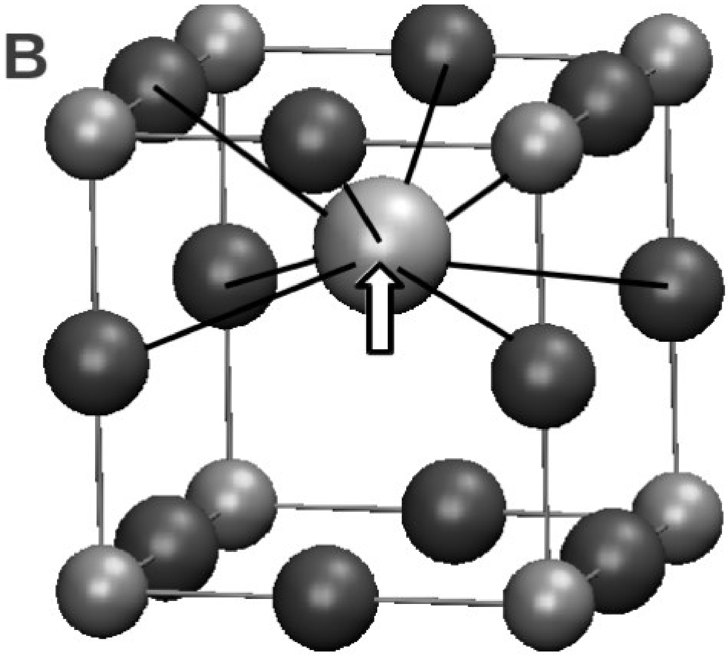

Figure 3.8: The ferroelectric relaxations of Ca (central large sphere) predicted for A-site doping of $BaTiO_3$, with Ca displaced along the [001] direction (indicated by the arrow, comparable to Ti) to reduce its coordination and alleviate bond strain. Reformatted from [98].

The effect of Ca on T_c is simultaneously influenced by the ability for Ca to be octahedrally coordinated in the B-site sublattice in an acceptor doping mechanism of $BaTiO_3$, $BaTi_{1-x}Ca_xO_{3-x}$. This is understood to have a solution limit of around 4 mol% [94,99]. Clear from figure 3.7, T_c

reduces monotonically with Ca doping onto the Ti site of $BaTiO_3$. Zhuang et al [99] proposed this octahedral coordination of Ca reduced T_c on account of the compressive stress it imparted into its neighbouring cells, deleterious to their polarisabilities (with reducing c/a lattice parameter ratios) and associated macroscopic correlations. With the formation of $V_O^{\cdot\cdot}$, given the importance of hybridisation between the Ti and O, the long-range correlation of B site cation displacements is likely to be interrupted and contribute to the reduction in T_c. The effect was more pronounced with a combined occupation of A and B sites. 1 mol% Ca B site occupation into a $Ba_{0.95}Ca_{0.05}TiO_3$ sample was able to reduce T_c by ~35 °C [99]. B site occupation has, however, been suggested to be useful for improving the compatibility of BT-based dielectrics in the low pO_2 sintering conditions necessary for processing of BME MLCCs [100]. However, a larger tan δ (associated to oxygen ion mobility) [94]above an ever-reducing T_c makes B site coordination unfavourable for X7R or X8R temperature stable dielectrics. Although use of acceptor dopants such as these for low pO_2 sintering is not relatively novel, it was also proposed that the A-site occupation of Ca would even also be useful for low pO_2 processing as it was experimentally considered to increase the enthalpy for reduction whilst inhibiting the formation of charge compensating $V_O^{\cdot\cdot}$ that are deleterious to the voltage stability of the ceramic dielectric [101].

3.2 $NaNbO_3$

Structural studies on alkali niobates, specifically $NaNbO_3$ (as well as $KNbO_3$) began with Vousden [102], following reports of observed 'ferroelectricity' comparable to that exhibited by the then recently characterised $BaTiO_3$ [14,103]. However, the Curie temperature corresponding to the permittivity maxima in $NaNbO_3$ exists at considerably higher temperature with respect to $BaTiO_3$, ~ 360 °C compared to ~ 130 °C. The dielectric response of $NaNbO_3$ is shown in figure 3.9. It was initially considered that these niobates must be 'pseudo-isomorphous' to $BaTiO_3$ as a result of similarities in the high permittivity dielectric response, with multiple structurally related anomalies manifested. Vousden's [102] early analysis of x-ray diffraction imagery coupled with optical studies, specifically comparing the extinction of the incident polarised light with that of orthorhombic $BaTiO_3$, associated not only an orthorhombic room temperature symmetry, but a sequence of phase transitions at -173 °C and 300 °C. Here, $NaNbO_3$ was proposed to transition from the orthorhombic to the tetragonal state, and to the cubic perovskite prototype structure at higher temperatures ~600 °C. Such a series of transitions was clearly comparable to that of $BaTiO_3$, but was missing the low temperature rhombohedral phase.

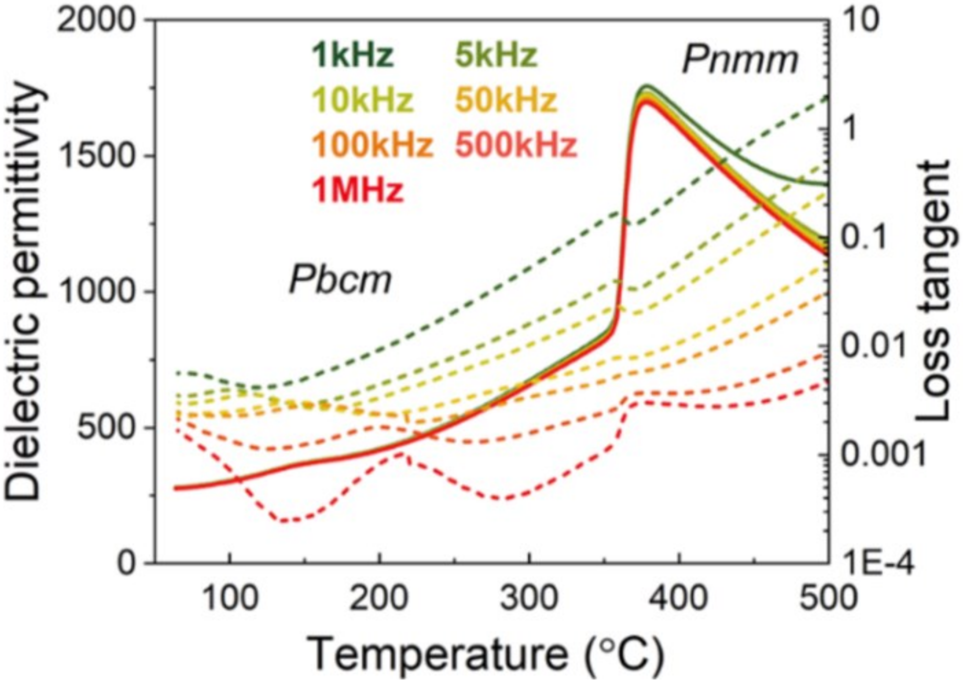

Figure 3.9: The relative permittivity (solid) and dielectric loss (dashed) of $NaNbO_3$ with Antiferroelectric Pbcm symmetry at room temperature. Reformatted from [108]

This was premature, however, and was perhaps a result in the relative boom in the (re-)characterisation of materials observed with ferroelectric (or antiferroelectric) behaviour that occurred at the time. A non-polar room temperature space group was instead subsequently proposed by Vousden after re-visiting the diffracted data [104], and after finding a lack of tetragonality due to the inequivalence in the intensity of what should have been symmetry related planes, intensity variations in the diffracted data were associated to the (relatively) heavily scattering Nb ion displacing off its ideal sites, moving along one of its orthorhombic axes. Non-polarity was proposed to be achieved through two possible mechanisms; randomisation of the Nb displacements along its orthorhombic a-axis, or antiparallel displacements of Nb ions amongst neighbouring pseudo-cubic cells such that the net polarisation over a more 'macroscopic' scale would become null [104]. This is the description Kittel gave for an antiferroelectric material [105]. This would extend the cell size introducing additional superlattice peaks into the diffraction pattern, which were considered too small in intensity to be discernible amongst the background data at that time. Here we see the first accurate description of the antiferroelectric room temperature orthorhombic polymorph of $NaNbO_3$ we consider to date, although the exact symmetry described by a $P22_12$ space group was not entirely correct. Instead, it was Megaw and Wells [106] who proposed the now routinely accepted orthorhombic Pbma (Pbcm) antiferroelectric space group as $NaNbO_3$'s virgin room temperature structure.

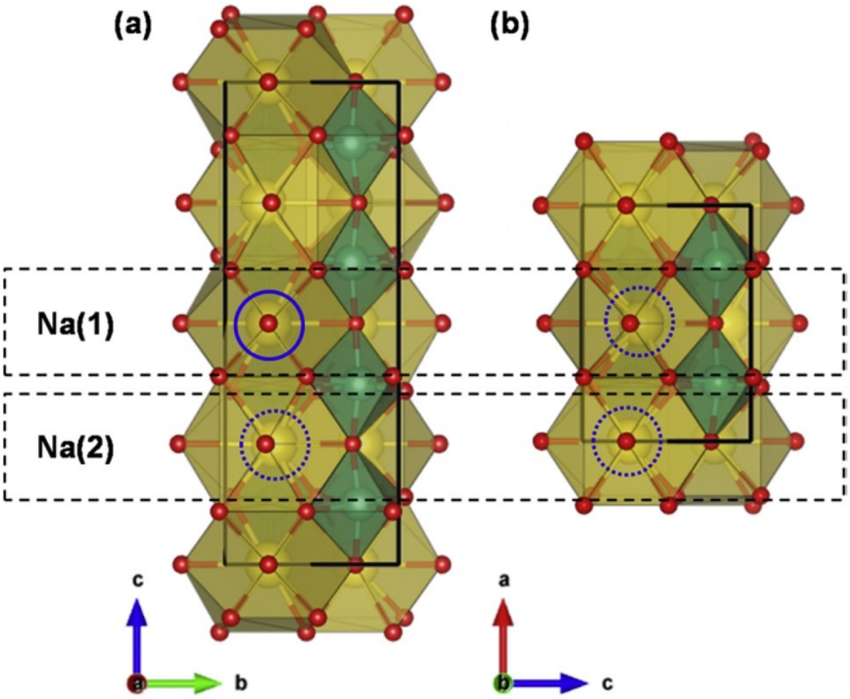

Figure 3.10: A comparison of the unit cells of the two room temperature polymorphs of $NaNbO_3$. a) antiferroelectric P phase and b) ferroelectric Q phase. Reformatted from [116]

This room temperature antiferroelectric phase, otherwise referred to as the 'P' phase, is visualised in figure 3.10. This polymorph can be described with a unit cell that consists of 8 $NaNbO_3$ formula units, with the orthorhombicity driven by a complex combinatorial effect of cation displacements, including the antiparallel intraoctahedral displacement of the Nb ions from their special positions, and sequential layering of in phase and antiphase octahedral tilting sequences (both dependant and independent based on the rotational axis considered) of these corner linked $[NbO_6]$ octahedra[107–109]. The resulting unit cell for the P phase relates to the ideal cubic perovskite unit cell (with lattice parameter $a_p \sim 3.9$ Å) by $a=\sqrt{2}\cdot a_p$, $b=\sqrt{2}\cdot a_p$, $c=4\cdot a_p$ [110].

It has been shown by Cross and Nicholson [111] that this antiferroelectric symmetry can be irreversibly transformed into a ferroelectric analogue through reorientation of the antiparallel Nb displacements via the application of a sufficiently high electric field[112]. Termed the 'forced ferroelectric', this 'Q' phase can be formed at field strengths around 50 $kVcm^{-1}$ [113], whilst electric fields as low as ~ 12$kVcm^{-1}$ were found capable of ~ 50 % phase transformation [114]. In this way, since the Nb displacements are now parallel (giving the polar ferroelectric symmetry), the unit cell halves in length, shown in figure 3.10. Field application isn't the only way to promote the Q phase formation in $NaNbO_3$. Reduced grain sizes have been suggested to promote Q phase formation [115,116], with a critical grain size ~ 0.27 µm promoting the antiferroelectric-ferroelectric transition. This is on account of the increasing internal stresses that occur with reduced grain size.

In reality, multiple studies have described the coexistence of both the P and Q phase at room temperature [117,118], with the proportion of each phase sensitive to the sample's thermal history [119]. Johnston et al [107] reported all solid state samples synthesised in their investigation (using various annealing rates, sintering temperatures and dwells) yielded mixed P and Q phase polymorphism at room temperature. The same study showed the Q phase fraction could be varied by up to 40 %; however, the P phase remained dominant with a minimum fraction ~ 50 %. The Q phase could only be isolated via a sol-gel synthesis route. It was also reported in this same study [107] that phase fractions were not reproducible for solid state synthesis. The choice of reagent also influences the polymorph stabilised, with P phase preferred when orthorhombic Nb_2O_5 was used for solid state synthesis as opposed to monoclinic or a mixed polymorph Nb_2O_5 [120]. It is logical that both polymorphs should coexist and are highly processing dependent, based on the small energy difference that separates the stability of each phase, ~ 2.3 meV/formula unit [121].

The octahedral tilts present in $NaNbO_3$ (and many perovskites symmetries in general) that facilitate symmetry reduction from its high temperature cubic aristotype phase can be described using notation introduced by Glazer [122]. This notation consists of three letters, each with an associated superscript. Each of these letters compare the magnitudes of tilt along one of the three pseudocubic tetrad axes ([100], [010] and [001]) of this pre-distorted, high temperature cubic aristotype symmetry. The superscript associated to the letter references the relative sense of octahedral tilts about the axes for successive/neighbouring octahedra projected along the axes. If neighbouring octahedra tilt about the axes in phase, with the same sense, the tilt is denoted with a '+' superscript. If the neighbouring octahedra tilt in opposing senses, this is denoted with a '-' superscript. No tilting about a particular axis is denoted with a '0' superscript. It is important that the distinction of phase is made for rotations along the axes, since octahedra in plane are geometrically constrained to tilt in the opposite sense due to the corner sharing nature of these octahedra. The influence of this geometric condition is that unit cell lengths become doubled along the axes perpendicular to the one for which the tilting occurs along. This titling relationship and the doubling of the lattice periodicity is visualised in figure 3.11

The magnitude of tilt is described using an ‘a’, ‘b’ or ‘c’ according to its comparability with tilt magnitudes about the other two tetrad axes. If all tilt magnitudes are equal about each of the axes, they each shall be denoted with an a, as in aaa. If tilts around [100] and [010] are equivalent but different to tilts about the [001] axes, the term aac is used. If tilts about each of the axes are different, abc is used. In total, Glazer described a total of 23 possible tilt systems within a perovskite structure [22], which has since been reduced to 15 possible systems based on a group theoretical analysis [123]. Based on the cell doubling introduced, tilting with different magnitudes and phases results in particular reflection conditions for diffraction techniques, with additional reflections occurring at the half integral reciprocal lattice planes [22]. These additional reflections can be indexed according to the tilt system that induced them, as tabulated in table 3.2. Antiphase tilts produce reflections that can be indexed with odd-odd-odd miller indices, whilst in phase tilts produce additional reflections of the even-odd-odd type[22]. Indexing superlattice reflections this way permits for the total tilt systems present in a distorted perovskite structure to be deduced.

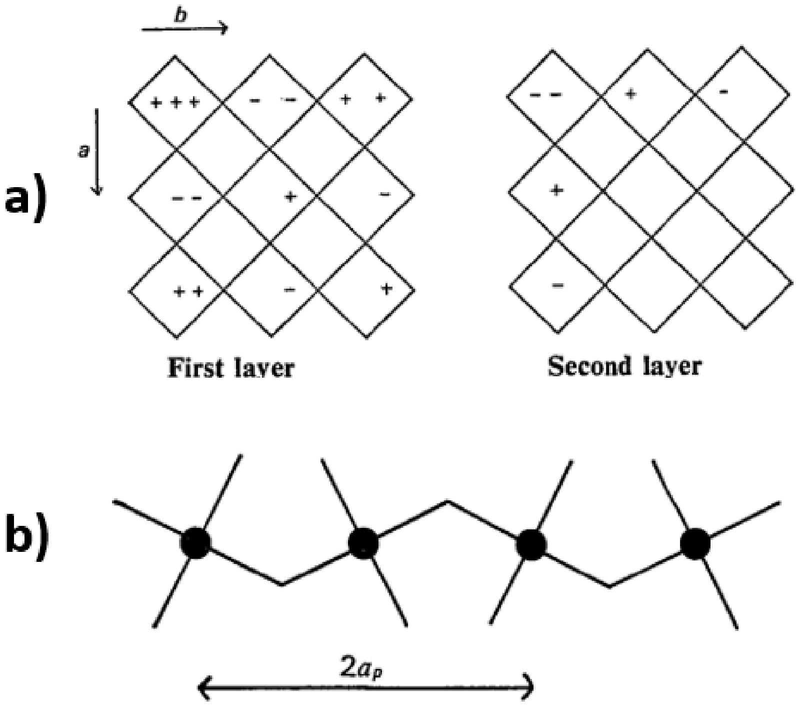

Figure 3.11: a) The relative octahedral tilt senses about each of the [100], [010] and [001] axes between successive ab planes. This reveals how neighbouring octahedra in plane are constrained to tilt in opposing senses. Reformatted from [122]. b) The effect these opposing tilt senses have on doubling the repeat unit length. Reformatted from [22].

Table 3.2: The miller indices that correspond to additional reflections introduced by in phase and antiphase octahedral tilts of varied magnitudes. Reformatted from *[22]*

Tilt	Reflection produced
a^+	even-odd-odd (k≠l) (e.g. 013)
b^+	odd-even-odd (h≠l) (e.g. 103)
c^+	odd-odd-even (h≠k) (e.g. 130)
a^-	odd-odd-odd (k≠l) (e.g. 113)
b^-	odd-odd-odd (h≠l) (e.g. 311)
c^-	odd-odd-odd (h≠k) (e.g. 131)

The tilting and cationic displacements that occur within the room temperature P and Q polymorphs are illustrated in figure 3.12. Sakowski-Cowley et al [110] reported the Nb ions to displace ~0.13 Å from the idealised centre of the octahedron within the O(3) and O(4) square plane, almost orthogonal to the [010] tetrad axis of the idealised symmetric octahedral unit. The resulting discrepancies between the equatorial Nb-O bonds due to this Nb displacement was surprisingly found to have little effect on the regularity of the octahedron, with edge lengths remaining fairly constant[110]. The Na(1) atoms displace ~ 0.4 Å away from the centre of the $[NaO_{12}]$ interstice [124], whilst the Na(2) cation remains relatively undisturbed. Tilting of the octahedra exist with at least two competing $a^-b^+a^-$, $a^-b^-a^-$ tilt sequences in alternating layer pairs, subtended at angles of ~8° and 9.5° to the x and y cell axes, respectively [110,125]. Figure 3.12 shows how these tilt sequences act over sequential [001] layers, with antiphase tilting about the [001] axes confined to layers 2 and 3, whilst in phase tilting about the same axes occurs for layers 1 and 4. For the ferroelectric Q phase, the Na(1) also displaces parallel to the next Na(1), causing

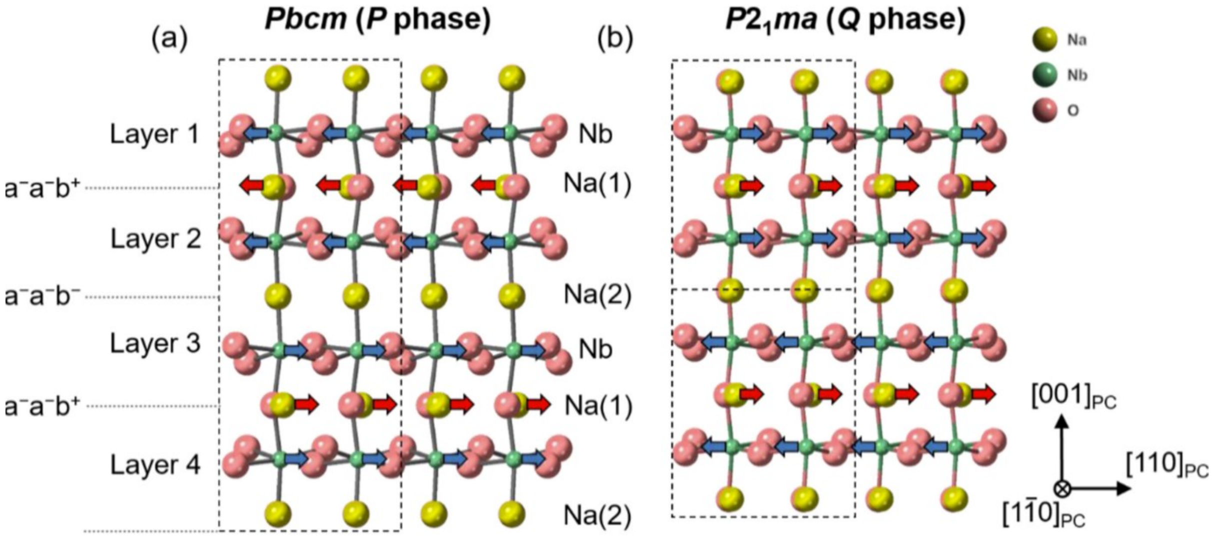

Figure 3.12: The cationic relative displacement directions and octahedral tilt sequencing of the two room temperature polymorphs of $NaNbO_3$ a) P phase Pbcm b) Q phase $P2_1ma$. Reformatted from [108].

the halving of the unit cell length. In the Q phase, only a single $a^-a^-b^+$ tilting sequence is evident [126].

The temperature driven polymorphism in $NaNbO_3$ is comparatively more complicated than that exhibited in the previously discussed $BaTiO_3$. The Cambridge crystallography laboratory [110,126–130]were the first to publish on the temperature induced polymorphism in $NaNbO_3$, finding symmetry reductions towards higher temperatures are mediated by tilt variations, whilst lower temperature phase transitions are instead driven by cationic distortions. Seven stable polymorphs exist between the range of ~ -100 to 640 °C [108,109], with their symmetries, associated transition temperatures and number of cationic distortions and tilt systems shown schematically in figure 3.13 below [108].

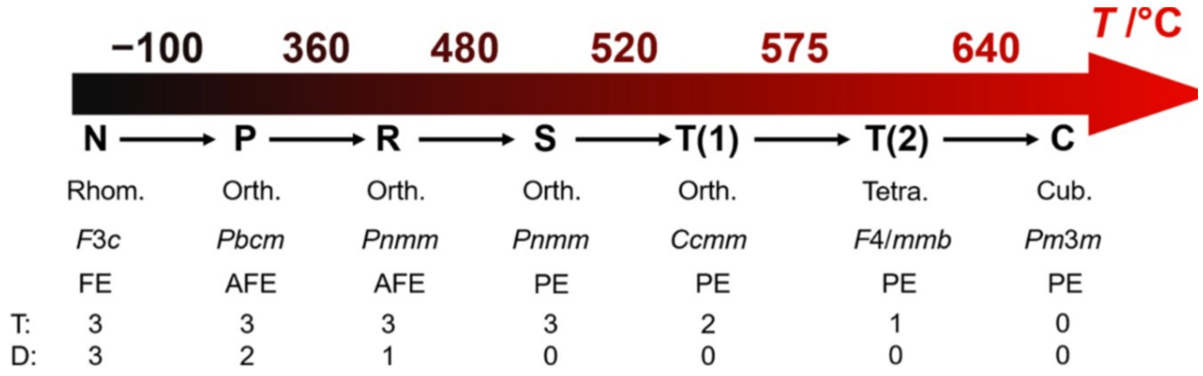

Figure 3.13: The phase transition sequence of NaNbO3 with temperature, showing the number of tilt systems present (T) and cationic displacements (D) associated with the lowering of symmetry. Reformatted from [108].

The dielectric response of $NaNbO_3$ is shown in figure 3.9. The large peak ~ 360 °C corresponds to the orthorhombic P → R transition. There is a dielectric anomaly manifested in the relative permittivity response of $NaNbO_3$ that is not characterised by one of the seven polymorphs shown in figure 3.13. This has been attributed to a second order transition [119,131] and the formation of an incommensurate structure involving the modulation of tilts about the [010] direction [132,133]. The TCC is noticeably large at 360 °C, hence why many studies (some of which will be discussed in the subsequent literature survey) utilise A or B site doping to reduce the thermal dependence of what is clearly a dielectric material, based on the tan δ response of figure 3.9 (after the relaxation of space charge).

3.3 $BaTiO_3$-$NaNbO_3$ Solid Solutions

Glaister [134] appears to have been the first to investigate the solubility of $BaTiO_3$ in $NaNbO_3$, $Na_xBa_{1-x}Nb_xTi_{1-x}O_3$ (XNNBT) (amongst a series of other $BaTiO_3$-ABO_3 systems). Compositions close to $NaNbO_3$ were synthesised via a solid-state reaction, finding an enhancement to the diffusivity of the dielectric response as the binary transitioned away from $NaNbO_3$. For the two compositions synthesised, 75NNBT and 80NNBT, both were comparatively more diffuse than $NaNbO_3$. For 75NNBT, the relative permittivity peaked at ~2500 and varied by a maximum of ~ -40 % across the X8R operating window, shown in figure 3.14.

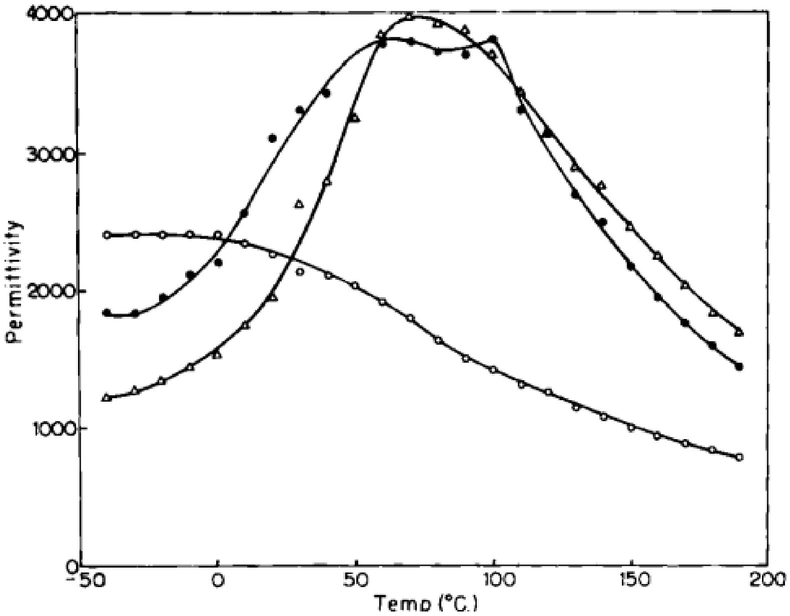

Figure 3.14: The first apparent report of relative permittivity for NNBT compositions. The open triangles are for 80NNBT, whilst the open circles are for 70NNBT. The solid circles are for 80NNBT with 1 mol% addition of MgF_2. Reformatted from [134].

This is of course insufficient for X8R class II dielectric rating, but represents a significant enhancement of the TCC away from an end member that yields TCC variations of the order of 10^2. Only a small domain of the solid solution was analysed yet TCC suppression of this order of magnitude was observed, whilst retaining a high relative permittivity magnitude only a fifth of the way across the $NaNbO_3$-$BaTiO_3$ binary. Such diffusivity in an equilibrated system is often associated with ferroelectric relaxor materials and the confinement of correlated polarity to reduced (often nano) length scales.

A similar enhancement in the diffusivity of dielectric response is observed via small $NaNbO_3$ doping into $BaTiO_3$, $0 \leq x$ (mol%) ≤ 10 [135–139], shown in figure 3.15 (a) and (b1). TCC stabilisation was initially ascribed to nano-size crystallite formation and uncompensated strain from the lack of 90 ° domain wall formation. Reports suggest $NaNbO_3$ additions as low as 4-6 [137,138]or even 2 mol% [136] are sufficient to induce a relaxor response within compositions of this range, based on associated frequency dependence and non-Curie Weiss type depolarisation above T_m. The permittivity responses of figure 3.15 a) and b1) are better defined as core shell type composite microstructures as opposed to intrinsic ferroelectric relaxors based on the presence of multiple temperature separated phase dependent permittivity anomalies. A comparatively $NaNbO_3$ rich shell may produce a low temperature permittivity contribution and a $BaTiO_3$ core may induce a permittivity response close to 120 °C.

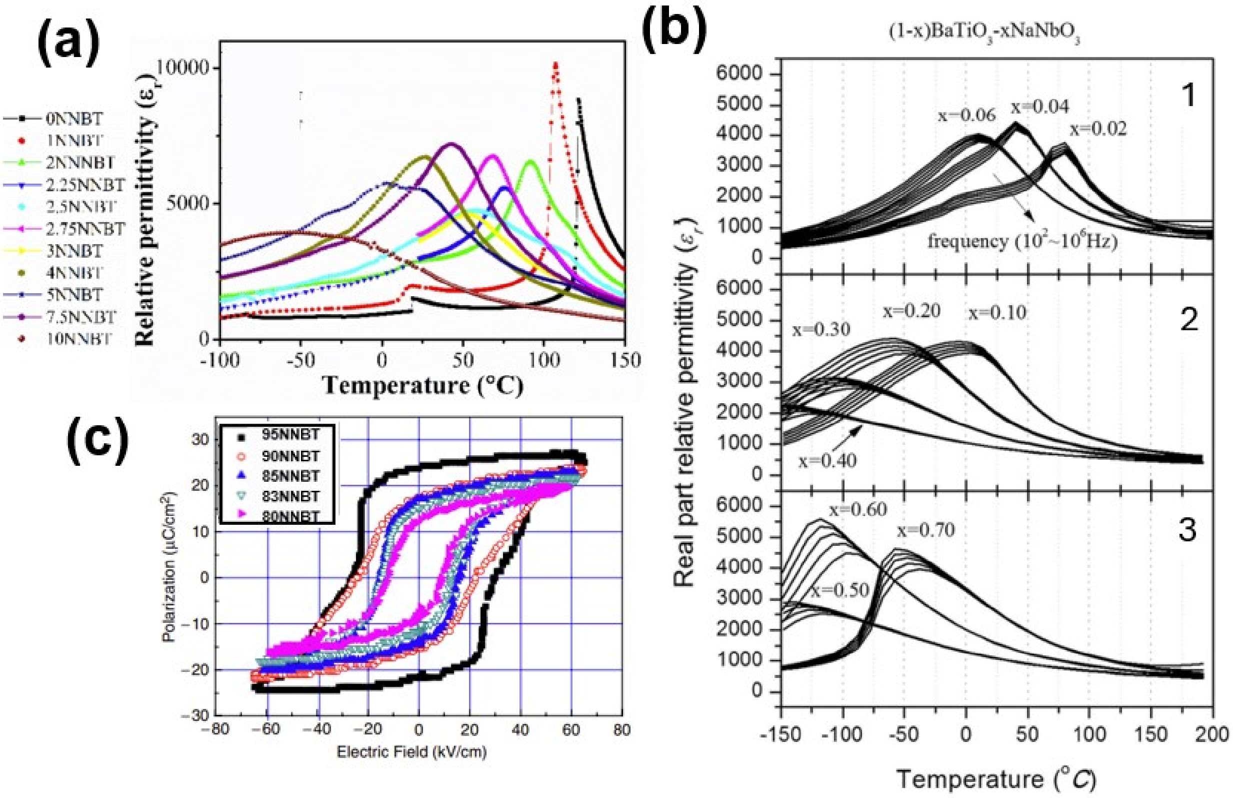

Figure 3.15: (a) The suppression of TCC variation for NNBT compositions close to the $BaTiO_3$ end member. Reformatted from [136] (b) The relaxor nature of NNBT compositions close to $BaTiO_3$(1) and as high as 70NNBT(3), reformatted from [137]c) the P-E hysteresis of NNBT compositions near to the $NaNbO_3$ end member, showing ferroelectric hysteresis. Reformatted from [138].

It is proposed that such core-shell formations occur as a result of the lower melting temperature of $NaNbO_3$ (~1410°C) with respect to $BaTiO_3$ (~ 1620 °C). Consequently, liquid phase sintering occurs and a $NaNbO_3$ coating of $BaTiO_3$ can occur, which can be quenched forming a shell surrounding the $BaTiO_3$ grain core [140,141]. More recent reports of a diffuse core-shell type response in NNBT compositions close to the $BaTiO_3$ end member have, however, been sintered at comparatively higher temperatures (1400 °C) for longer dwells (8 hours)[136]. This suggests this compositionally heterogeneous structure is not kinetically but thermodynamically stabilised. Perhaps the stabilisation comes from an entropic as opposed to enthalpic stabilisation, since an increase in configurational entropy would surely arise in the formation of a relaxor shell with greater macroscopic disorder than a lightly doped homogeneous ferroelectric ordered $BaTiO_3$

rich grain. An enhancement in electric field induced dielectric breakdown strength was proposed to occur for the antiferroelectric $NaNbO_3$ coating of the $BaTiO_3$ grains[140]; however, breakdown has only been shown to improve by ~ 5 $kVcm^{-1}$ compared to that of undoped $BaTiO_3$[142].

The entire solid solution was probed by Raevskii et al[143], with the first derivation of a phase diagram along this binary, figure 3.16. A xNNBT solid solution is able to form between these two end members, validated by XRD [138], as a result of the electroneutrality preserved by the equal and opposite 1+ oxidation state difference that exists between the Ba/Na and Ti/Nb host/dopant species at the A and B sites. The solid solution is self-compensating in this sense, with no necessity for electronic or ionic compensation should stoichiometry be preserved during synthesis. A compositionally driven tetragonal → pseudocubic → orthorhombic phase transition sequence is observed as NNBT transitions from $BaTiO_3$ to $NaNbO_3$ [136–138]. Compositions > 10NNBT induce the pseudo-cubic symmetry, whilst compositions of 80NNBT and above show the orthorhombic symmetry [138]. The symmetry of this orthorhombic phase is not well defined within literature, particularly relating to if P or Q phase stabilisation occurs. An increase in tolerance factor is expected with $BaTiO_3$ doping into $NaNbO_3$, due to the larger expansion of the $[AO_{12}]$ cuboctahedra expected relative to the contraction of the $[BO_6]$ octahedra (since the change in radii at the A site = 0.22 Å, the change in the radii at the B site = 0.035 Å) [86]. In other $NaNbO_3$ systems, an increase in tolerance factor upon doping favours stabilisation of the ferroelectric Q orthorhombic room temperature polymorph. Zeng et al [138]studied the diffraction patterns in this $NaNbO_3$ rich

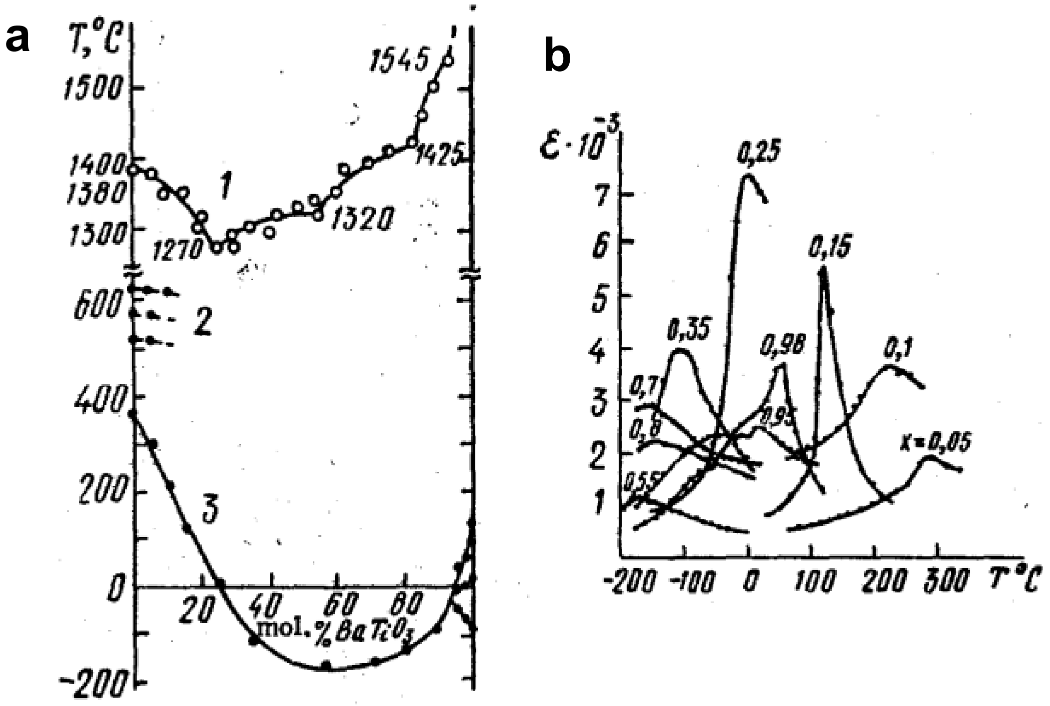

Figure 3.16: a) An experimentally derived phase diagram, showing the distribution of T_m with NNBT. b) relative permittivity spanning the width of the NNBT solid solution. Reformatted from [143]

region of the solid solution; however, they didn't differentiate between the exact symmetry stabilised, nor were the tilt and cation driven superlattice reflections between ~ 35 – 45 ° (Cu-Kα) studied. Based on the ferroelectric type loops in figure 3.15 c), it appears Q phase symmetry is favoured, although a degree of pinching in the 95NNBT sample may imply the retention of some antiferroelectricity that is subsequently converted to ferroelectric upon higher field applications. The relaxor state shows the loss of long-range structural order as pseudo-cubic macroscopic symmetry is observed. When probed via Raman spectroscopy, in-situ synchrotron XRD and EXAFS data, local tetragonality is found whose correlation scales can be forced into larger microdomains under an electric field [144].

Across the solid solution, the distinct ferroelectric - relaxor-ferroelectric transitions are somewhat conflicting but consistent in the observation of relaxor behaviour towards the solid solution centre, and the induction of such behaviour at lower doping concentrations at the $BaTiO_3$ end of the solid solution with respect to the $NaNbO_3$ end of the solid solution. Examples of this relaxor behaviour are shown in figure 3.15 b) and 3.16 (right), with frequency dependence, low T_m and broad permittivity responses. As previously discussed, low $NaNbO_3$ additions into $BaTiO_3$, < 10 mol%, are capable of inducing the relaxor transition. Abdelkefi et al claimed compositions retained this ferroelectric-relaxor until a transition to a ferroelectric phase occurred ~ 55NNBT [139,145]. However, work by Zampiere et al and Cwikiel et al still showed relaxor behaviour for 70NNBT [146,147], whilst Zuo et al showed a transition from this relaxor-ferroelectric state to the polar state at ~77NNBT [148]. Despite this, reports across the NNBT solid solution describe good dielectric properties with low associated tan δ (after space charge relaxation) across the X7R or X8R temperature bounds [136,149].

Through P-E hysteresis analysis, Zuo et al [148] revealed the relaxor compositions in the 75-85NNBT compositional range yield large hysteresis free electrostrictive strains, optimised with a electrostrictive strain coefficient (Q_{33}) ~0.046 m^4/C^2 for 75NNBT. This type of hysteresis free straining gives NNBT prospects as lead free high precision ceramic actuators where the frequency dependence of strain in the piezoelectric materials is unsuitable[148]. The slim polarisation hysteresis response also implies good energy storage efficiencies for these relaxor NNBT compositions, with high polarisability achieved suggesting good recoverable energy densities. It is consequently unsurprising that reports have since focused on NNBT-based compositions for energy density dielectric applications. Fan et al [150] revealed in an acceptor (1 mol%) Mg doped

10NNBT, a recoverable energy density of 3.4 Jcm^{-3} with an associated energy storage efficiency ~ 82.6% could be achieved, shown in figure 3.17.

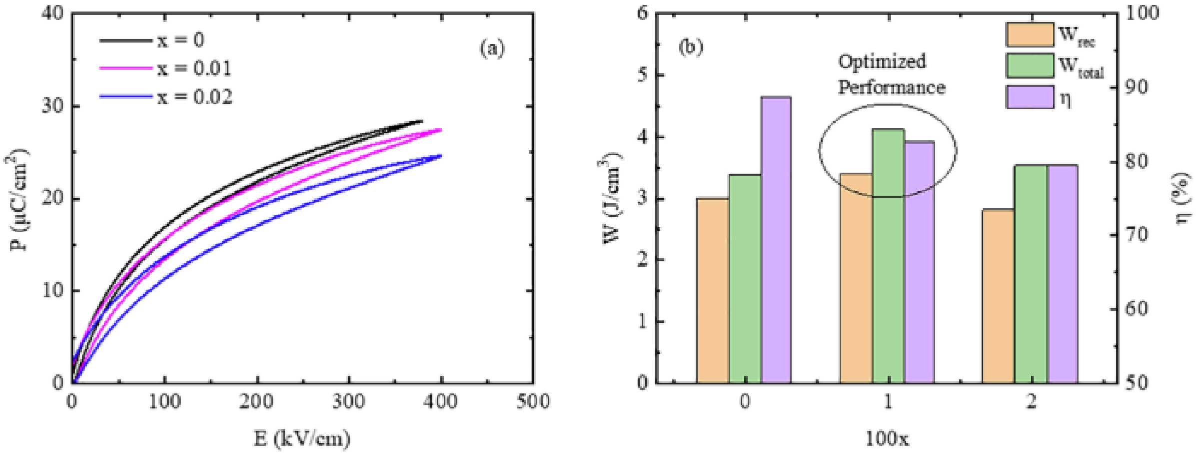

Figure 3.17: a) The slim hysteresis loops and b) high recoverable energy densities of Mg doped 10NNBT, with a maximum of 2 mol% acceptor doped Mg. 1 mol% Mg doping is optimal for recoverable energy density, as shown in b). Reformatted from [150].

This represents an alternative to Pb- or Bi-containing systems often used due to the inherent polarisability of these two cations, but undesirable for their toxicity and thermodynamic incompatibility with BMEs (specifically Ni), respectively. 10NNBT has been used as the foundation of other energy density dielectric studies, with even higher storage efficiencies achieved - near 90 % [151]. It must be noted, however, that multiple A (La^{3+}/Bi^{3+}) and B (Ta^{5+}/Mg^{2+}) site dopant species were incorporated, each for band gap and microstructural engineering purposes (for enhanced breakdown resistance). With numerous dopants present, it is inherently difficult to determine the significance of 10NNBT in the overall linearised polarisation response, since a number of species each with competing bonding requirements will inherently destabilise any long range polar ordering anyway, regardless of the NNBT composition utilised.

3.4 $La_{1/3}NbO_3$

$La_{1/3}NbO_3$, since its first report by Iyer and Smith[152] in the 1960s, has been well characterised as an A site deficient perovskite. Where oxides such as ReO_3 or WO_3 can be related to the perovskite structure as a distorted network of corner sharing [$(Re,W)O_6$] octahedra where the close packed A cation layers are completely vacant[153,154], $La_{1/3}NbO_3$ exists with 1/3 of the A sites La^{3+} occupied and 2/3 vacant. Diffraction experiments have revealed an orthorhombic room temperature structure equivalent to that shown in figure 3.18.

Clear superlattice reflections along the [001] axes reveal a doubling of the pseudo-cubic unit cell along this axes [155]. This doubling of the lattice periodicity is attributed to the ordering of A site vacancies and La^{3+} cations into alternating (001) planes, alternating between 2/3 La^{3+} occupation and complete A site vacancy, respectively. This orthorhombic (space group Cmmm) room temperature symmetry is evident from the relevant splitting of reflections and systematic absences/extinction conditions associated to a body centred lattice, specifically h+k=2n, directly observed from electron diffraction [155,156]. Previous studies [157,158] had suggested a 1x1x2 tetragonal unit cell at room temperature, such as that exhibited within its analogous $La_{1/3}TaO_3$ companion perovskite, where an equivalent ionic radius between the two transition metal cations within the octahedral coordination (0.64 Å [86])exists. Instead, this higher symmetry tetragonal state is not attained until ~ 200 °C [159] for $La_{1/3}NbO_3$, hereafter a second order transition to a tetragonal P4/mmm symmetry is observed as the octahedral tilts present in the orthorhombic room temperature polymorph are supressed and the lattice periodicity along the a and b axes is consequently halved. This polymorphism is like $La_{2/3}TiO_3$, another La-based A site deficient perovskite [160]. This transition temperature is comparatively lower than the same orthorhombic-tetragonal phase transition that occurs in isostructural $Nd_{1/3}NbO_3$ and $Pr_{1/3}NbO_3$, at ~ 650 °C [161]. This symmetry increase at 200 °C in $La_{1/3}NbO_3$ has been verified by group theoretical analysis [162], with P4/mmm the only possible symmetry Cmmm can be derived from

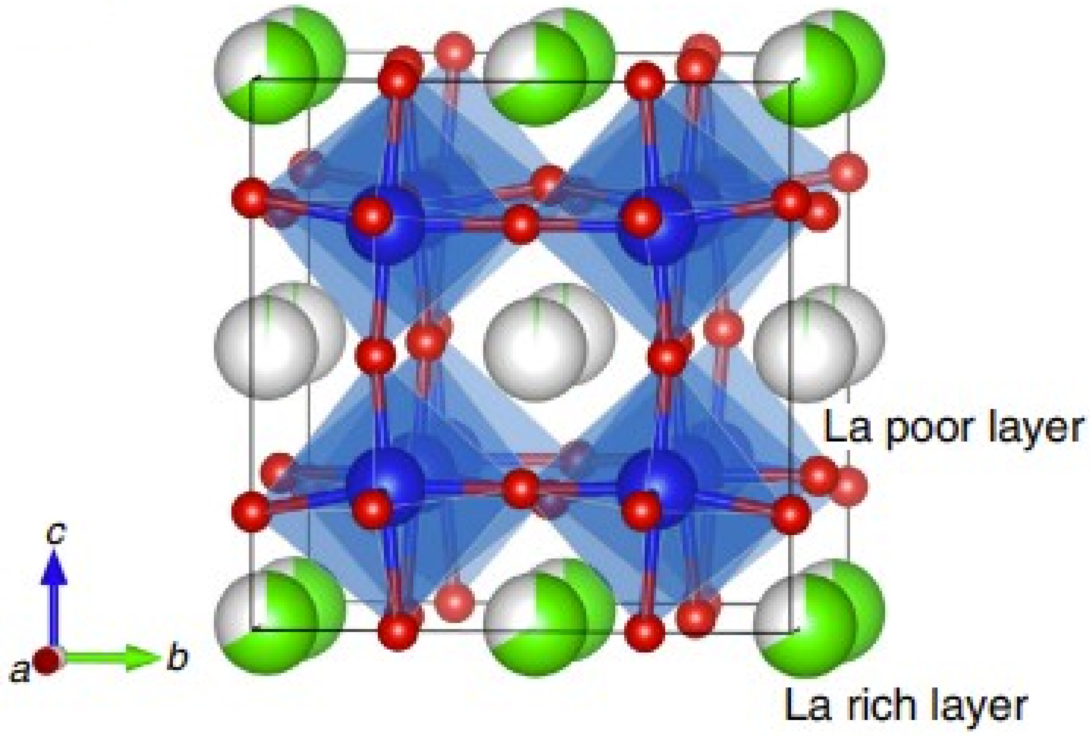

Figure 3.18: The Orthorhombic Cmmm symmetry of $La_{1/3}NbO_3$, with alternating 2/3 La^{3+} occupied and vacant (001) planes, and antiphase $a^-b^0c^0$ octahedral tilting. Reformatted from [156]

via tilt suppressions as opposed to cationic mobility (since the latter was considered energetically unlikely at these comparatively lower temperatures).

The tilt system of $La_{1/3}NbO_3$ involves antiphase $[NbO_6]$ rotations about an axes perpendicular to [001] and the direction of cation ordering, through an angle ~4.4 ° [159], comparable to the ~ 4.7 ° that within the comparatively less A-site deficient $La_{2/3}TiO_3$ [160]. These tilt angles are much lower than those of isostructural $Nd_{1/3}NbO_3$ and $Pr_{1/3}NbO_3$ at room temperature, with an $a^-b^0c^0$ tilt angle ~ 8.5 and 8 °, respectively [161], driving the higher orthorhombic-tetragonal phase transition temperatures in these latter compositions. The antiphase octahedral tilt about the a axes has been directly observed by STEM analyses, along with slight La occupancy of the Z=1/2 layer, shown in figure 3.18 and figure 3.19, previously considered nominally entirely La^{3+} vacant [156,163].

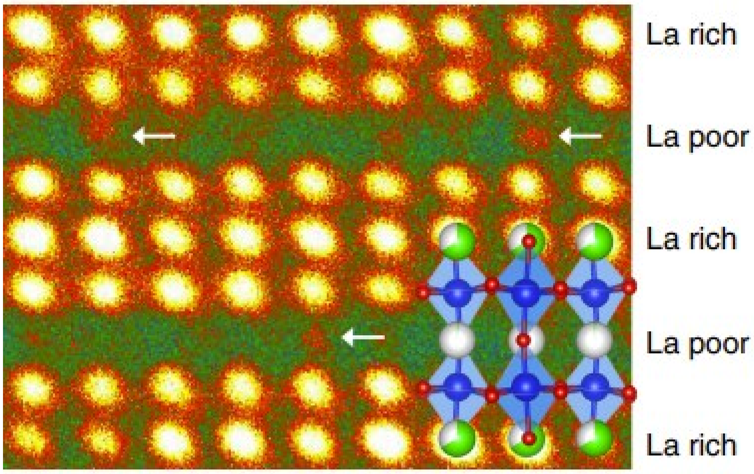

Figure 3.19: High angle annular dark field (HAADF) imaging of $La_{1/3}NbO_3$ along the [1-10] zone axis. This shows slight occupation of the Z=1/2 plane by La^{3+}. Reformatted form [156].

The result of this $a^-b^0c^0$ antiphase tilting is cell doubling along the a and b axes, which in combination with the cationic ordering along [001], results in the orthorhombic structure exhibiting a 2 x 2 x 2 unit cell multiplicity with respect to the aristotype pseudo-cubic perovskite cell. Intraoctahedral Nb displacements are also commonly derived from XRD structure refinements, with Nb (a cation already known to displace in octahedral environments consequent of second order Jahn-Teller effects) displacing away from the A site vacant layers forming alternating long (~ 2.072 Å) and short (1.901 Å) axial Nb-O bonds, where a bond length ~ 1.975 Å is typical of Nb(V) [159]. Thus, the structure shown in figure 3.18 becomes a complex function of Nb displacements, La^{3+}/V_{La}''' cationic ordering and antiphase $[NbO_6]$ octahedral tilting. More recent DFT-Monte Carlo analyses conducted on larger supercells have suggested an additional superstructure is associated to the modulation of vacancies and La^{3+} within the A site occupied layers. Based on the evidence of superstructures within the La rich layers from diffuse SAED satellite spots [164], Yang et al [165,166] suggested two energetically minimal La^{3+}/V_{La}''' modulations are possible at room temperature. One such configuration is termed a 'closed' arrangement, shown in figure 3.20, and involves a $4a_p \times 6a_p$ repeat unit consisting of a square of 4 A site vacancies enclosed by La^{3+} cations. The other is a 'striped' arrangement of La^{3+} density, proposed to coexist with the closed arrangement, where stripes of La columns run along the [110] direction. This represents an incommensurate structure with longer range ordering compared to the closed system. Striped clustering of these cations/vacancies appears to have been observed directly via STEM [163,164], with such modulated structures in combination with the c axis ordering favourable for thermoelectric properties – with good n-type stable thermoelectric properties reported [164].

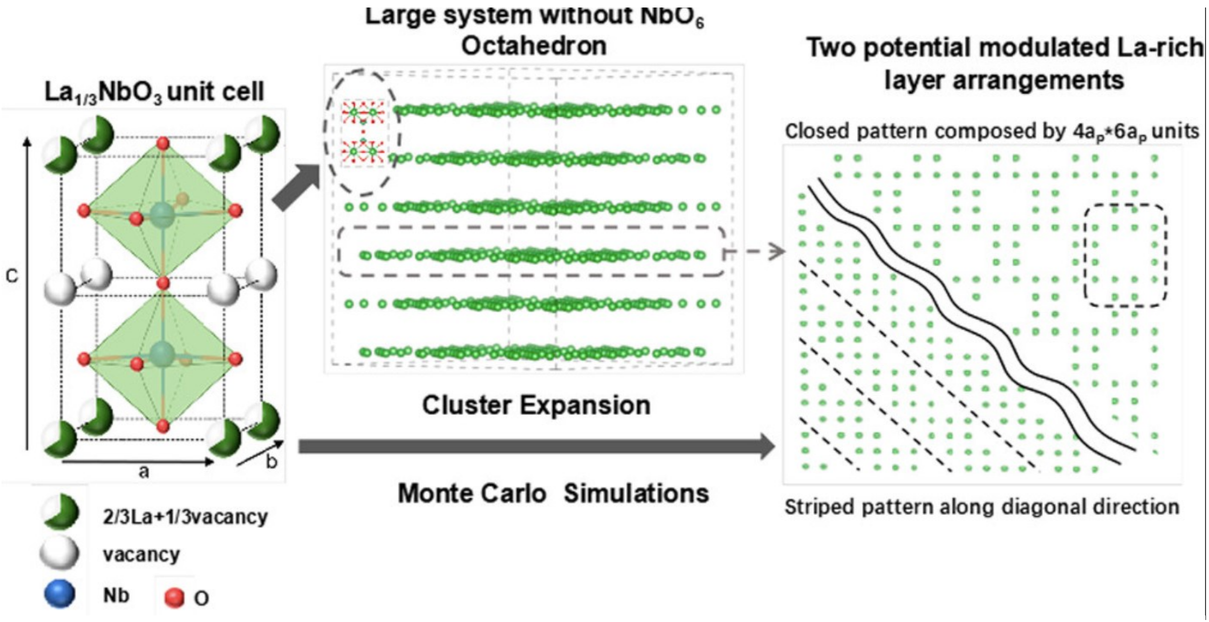

Figure 3.20: 'Closed' and 'striped' modulations of La proposed for room temperature $La_{1/3}NbO_3$, as derived from DFT-MC calculations. Reformatted from [165].

The dielectric response of $La_{1/3}NbO_3$ is shown in figure 3.21, specifically in the sub ambient regime [167]. A frequency dependent diffuse peak with a relative permittivity of ~ 140 at ~ 80 K is observed, analogous to the diffusivity observed within relaxor-ferroelectrics such as the aforementioned NNBT. At the same temperatures, no symmetry reduction is observed in diffraction patterns[167]. It was postulated that this diffuse peak is the result of uncorrelated antiparallel displacements of Nb as temperatures are reduced, such that no reflections are observed in diffraction responses. This is because the permittivity magnitude is too large for a simple polar dielectric model but too small with respect to a typical relaxor PNR response, whilst the lack of correlation and short range ordering induces the frequency dependence and diffuse nature of the permittivity peak observed[167]. This low temperature dispersion has been characterised elsewhere with a similar origin from cationic displacement, since it occurs at relatively low frequency ranges[168]. Although no TCC assessment can be made with respect to the entire X7R or X8R operating range, clearly the + 15 % boundary isn't exceeded until far below the -55 °C low temperature boundary. Nevertheless, the permittivity is relatively low with respect to class II MLCC integration, and rare earths like Lanthanum are expensive and unreliable based on the potential sourcing issues imparted by unpredictable geopolitical landscapes.

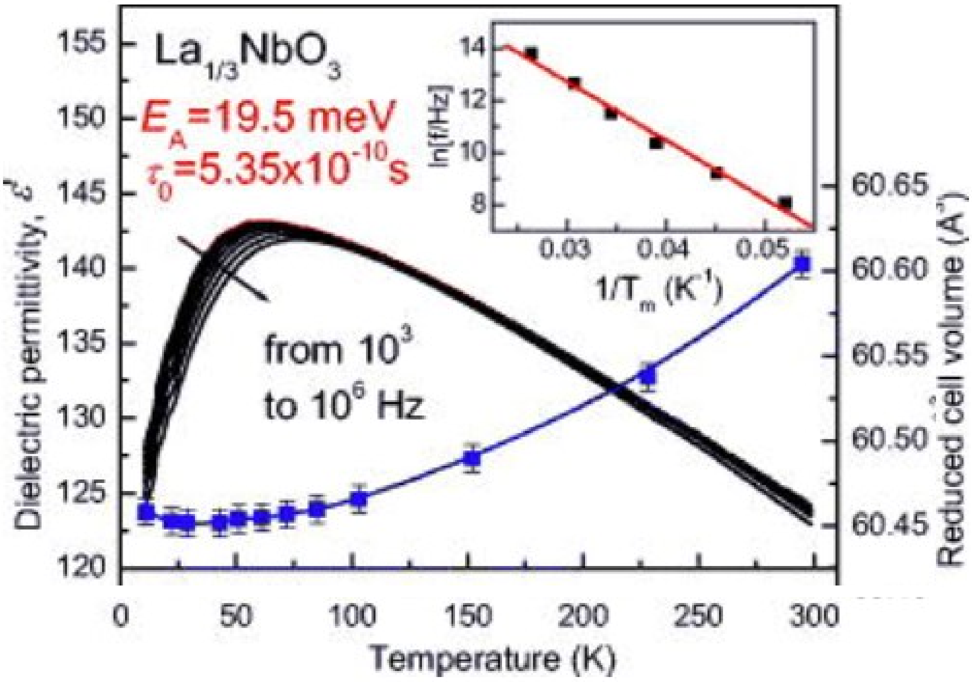

Figure 3.21: Sub ambient dielectric response of $La_{1/3}NbO_3$, with a clear frequency dependent diffuse peak occurring ~80 K. No macroscopic structural distortions are associated, based on powder diffraction studies. Reformatted from [167]

George and Vikar [169] analysed the electrical properties of $La_{1/3}NbO_3$, describing it as a mixed ionic-electronic conductor. A low activation energy, ~ 0.19 eV, was attributed to the conduction of La^{3+} through a liquid-like sublattice (given the number of vacancies present), whilst towards higher temperatures, above 800 K (where ionic transport numbers dropped), the reduction of $La_{1/3}NbO_3$ occurred inducing n-type conductivity, with a higher activation energy ~ 1.58 eV. Both conductivity domains are clear on figure 3.22. This electronic contribution was inferred from the loss of mass measured during a thermogravimetric analysis, whilst La^{3+} migration was inferred from the comparison of La^{3+} EDX intensities from the electrodes of an electrolysed sample, finding an intensity of La^{3+} five times greater at the cathode with respect to the anode. It must be noted, however, that electrolysis was conducted at ~1000 K, and no analysis of any electrode segregation phase was made[170]. No attempts were made to discredit O^{2-} or H^+ conduction, and so the ionic species that is mobile cannot be defined with certainty. Trivalent cation conduction through an A site deficient lanthanide perovskite, specifically $Y_x(Ta_{3x}W_{1-3x})O_3$[171], has been reported elsewhere; however, this also suffers from the same limitation of insufficient evidence to discredit O^{2-}/H^+ diffusion[170]. The thermoelectric analysis of $La_{1/3}NbO_3$ by Kepaptsoglou et al [164]did, however, reveal comparable n-type electrical conductivity whose magnitude increased and stabilised above 800 K.

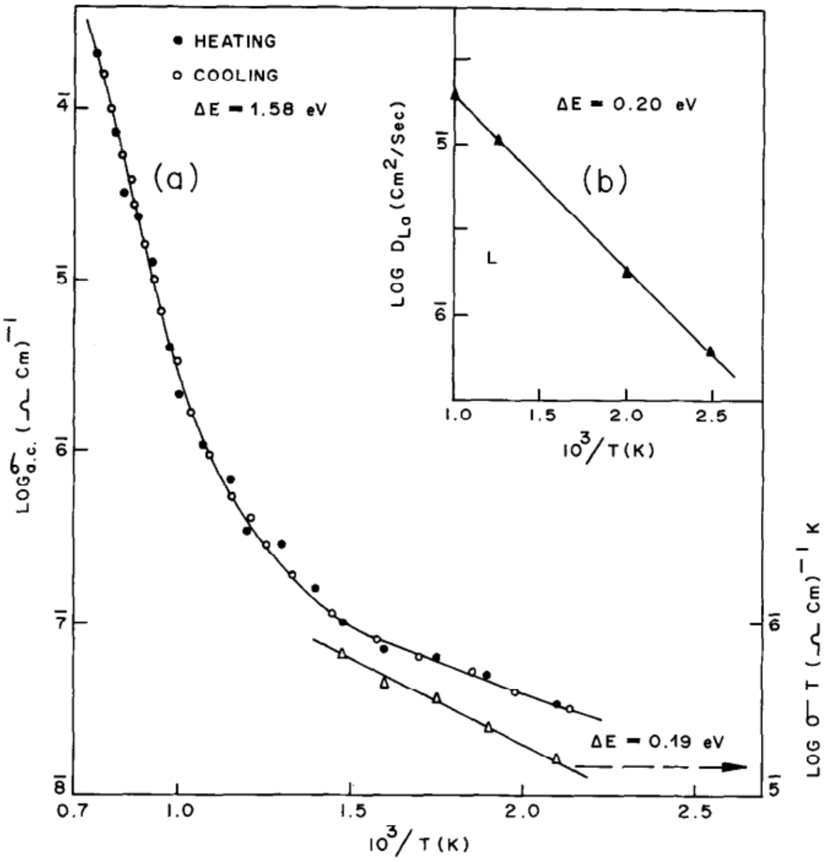

Figure 3.22: The variation in conductivity with temperature for $La_{1/3}NbO_3$, with two distinct conduction regimes: A low temperature ionic contribution and a high temperature n-type electronic contribution. Reformatted from [169].

3.5 $LiNbO_3$ – $La_{1/3}NbO_3$

Based on the highly A site deficient nature of $La_{1/3}NbO_3$, reports often regard the doping of Li into the A-site for the purpose of imparting Li^+ conductivity, given the extensive network of vacant sites present for such small, monovalent Li^+ ions to migrate between. Li^+ ionic conductivity is then particularly useful for integration within solid state lithium-ion batteries, as electrolytes or electrodes depending upon the transport number associated to the Li^+ conductivity. This had been reported experimentally for an analogously A site deficient Li^+ doped $La_{2/3}TiO_3$ (LLTO) perovskite with a room temperature Li^+ conductivity of ~ 10^{-3} Scm^{-1} for a composition ~ $La_{0.51}Li_{0.31}TiO_{2.94}$, the highest solid state Li^+ ion conductivity reported for an inorganic crystalline compound to date[172–174]. LLTO is inherently unstable in contact with elemental Li, with intercalation inducing the reduction of Ti^{4+} to Ti^{3+} and electronic conductivity, making LLTO unsuitable as an electrolyte [175]. Since the niobate equivalent offers a greater number of intrinsic A-site vacancies, it was considered that comparable or even superior Li^+ conductivities could be attained for these materials. This, however, was not realised and shall be discussed later.

Structurally, Li^+ doping was characterised to reduce the orthorhombicity of the $La_{1/3}NbO_3$ parent material, inducing a tetragonal and subsequent pseudo-cubic symmetry increase based on XRD diffraction patterns and the refined lattice parameters[176]. A perovskite solid solution limit was agreed by numerous authors, with ilmenite type $LiNbO_3$ precipitating[176–178], however the solid solution limit for perovskite stoichiometry was debated. Garcia Martin et al [177]suggested $LiNbO_3$ formation beyond $La_{(1-x)/3}Li_xNbO_3$ x=0.18, whilst Kawakami et al [176] showed no evidence of secondary phase formation until x=0.25. IS data was consistent in revealing ionic (Li^+) DC conductivity with an associated activation energy ~ 0.35 eV, with a maximum conductivity at room temperature of ~ 10^{-5} Scm^{-1} for compositions ~ x=0.08-0.1[176,177]. In single crystal LLNO, a more recent study has revealed a conductivity an order of magnitude higher, ~ 1.9 x 10^{-4} Scm^{-1} at an equivalent composition[179]. These are all lower than that reported for the LLTO analogue, despite a greater number of A-site vacancies.

Kawakami et al [176] reported that Sr doping for La^{3+}, $(Li_{0.25}La_{0.25})_{1-x}Sr_{0.5x}NbO_3$, increased the ionic conductivity by half an order of magnitude at x=0.125, primarily attributed to the expansion of the unit cell and migration bottlenecks between O4 oxygen anions at the octahedral vertices separating adjacent A site interstices, shown in figure 3.23. This expansion of the bottleneck

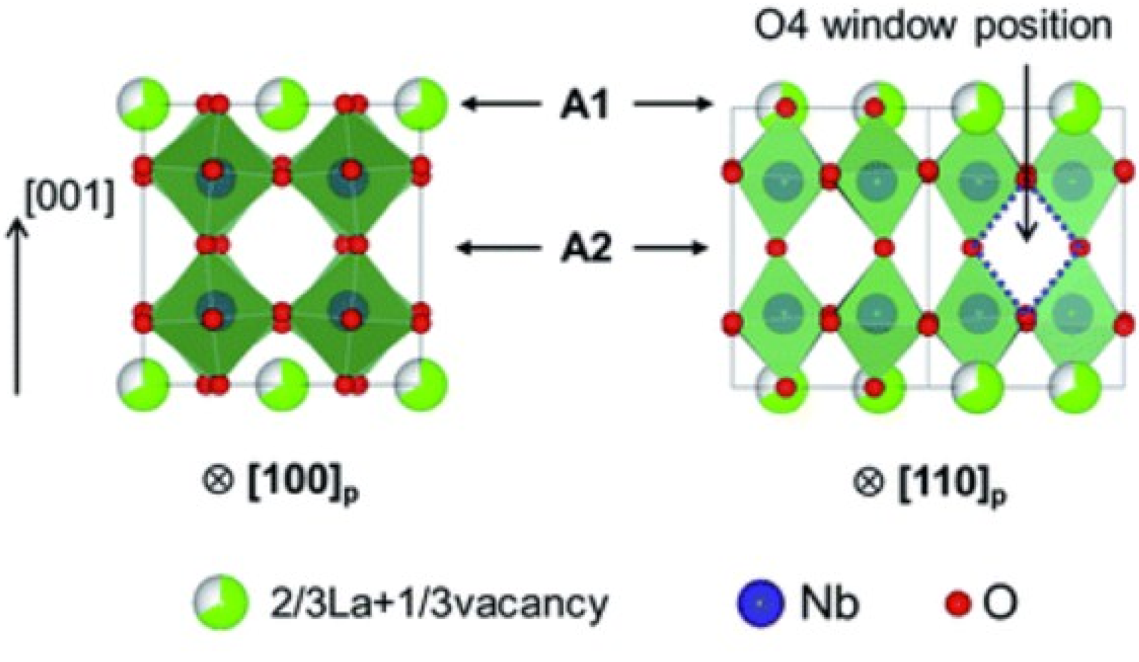

Figure 3.23: The average structure of orthorhombic Cmmm symmetry used to describe the $Li_xLa_{(1-x)/3}NbO_3$ perovskite with alternating (001) plane occupancies of A site cations, forming distinct A1 and A2 layers. The O4 bottleneck is shown for which Li^+ cations must migrate through (shown for the A2 layer). Reformatted from [163].

occurred on account of the larger Sr_{XII}^{2+} (1.44 Å) substitution for La_{XII}^{3+} (1.36 Å) [86]. The optimal conductivity in this Sr doped system was observed in the tetragonal region of the perovskite solid solution, and compositions greater than x=0.125 yielded lesser conductivities on account of the fewer vacancies imparted due to the lower oxidation state of Sr with respect to La. Ca doping for La instead of Sr yielded lower conductivities at the same composition, attributed to a lower unit cell volume with respect to the parent $La_{1/3}NbO_3$ material [180]. A similar observation in A site cation size and ionic conductivity was observed for $Li_xLn_{2/3}Nb_xTi_{1-x}O_3$ [181], with a larger conductivity associated with the increase in lanthanide ionic radii, from Nd to La. The same effect was reported for LLTO, where conductivity decreased monotonically with Lanthanide radius from La to Sm [182], concurrent with an increase in the associated activation energy [183]. Again, these cell expansions were considered to increase the diameter of the bottleneck area between adjacent A sites constructed from the O4 vertices of neighbouring $[BO_6]$ octahedra. However, local structure of these A site deficient perovskites is predicted to be highly influential to the diffusion coefficients of these Li^+ ions as they migrate through the structure[166], in combination to the bottleneck sizes.

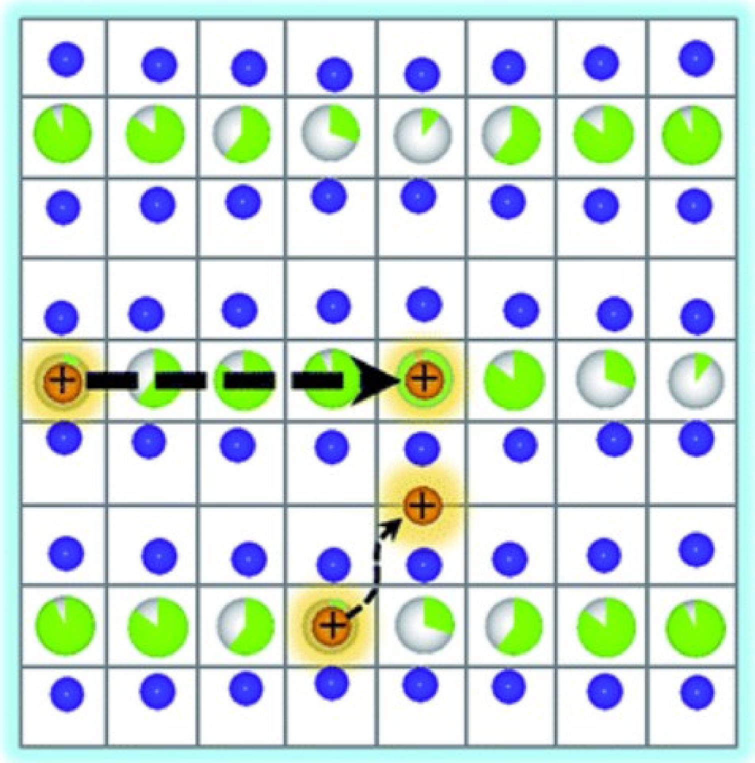

Figure 3.24: The La/Li long range ordering into alternating (001) planes, and microscale modulation of differing La/Li densities along these occupied planes. This is indicated by the differing portion of green shading representing columnar occupation. The Li^+ migration in LNNO is primarily along these Z=0 occupied planes, with some secondary migration between these planes. Reformatted from [163].

Local structure has been investigated in these materials via microscopy and diffraction techniques, with modulated structures confined to the micro- or nano-sale, depending on the literature and differing interpretations, and combinatorial to a long range ordering of Li/La into alternating (001) planes[163]. Select area electron diffraction (SAED) by Garcia Martin and Alario-Franco[184] revealed modulated arrangements of A site species along the (110) planes, such as the striped modulations of La and vacancies in the undoped parent material[165]. Similar findings were observed via HRTEM and ABF-STEM imaging by Gao et al[163], revealing comparable directionality to cation ordering in the La rich layers. Incommensurate modulations of columnar A site ordering were suggested, with periodicities varying between 3.5 and 3.7 unit cells wide, depending upon the Li content[163]. Li content was noted by both authors to influence the formation and scale of microdomains. The ordering of A site occupation density through the Z=0 planes was proposed to couple to the Nb displacements, producing a sinusoidal displacement distribution. Garcia-Martin et al [184] also defined a twinning of incommensurately modulated tilt sequences. The periodicity and size of the modulated structures within these microdomains is Li dependent, with high Li contents inducing an additional superstructure associated with the changing of the doubled c axes between the three principle crystallographic orthogonal axes.[184].

Gao et al revealed through the complimentary HAADF and ABF-STEM imaging that Li (and La) occupancies are constrained to the La rich layer as previously suggested from refinement of Nb-O bond lengths on increasing Li^+ content [178]. This is unlike in LLTO where Li occupies both the Z=0 and Z=1/2 layers, observed directly using STEM [185] and from ^{7}Li NMR where the Z=1/2 layer was proposed to exhibit a higher quantity of Li compared with greater associated mobility with respect to the Z=0 plane[175,181,186]. Consequently, Li^+ is considered to migrate two-dimensionally primarily through the A site occupied Z=0 layers in the niobate, rather than the vacant Z=1/2 layers as in LLTO (where there relatively close energy barriers for migration between Z=0 and ½ layers, and a combination of both likely occurs [187]). In this Z=0 layer of LLNO, the contraction of the cell and bottleneck due to smaller Li doping for La, combined with the extensive structural modulations induced by the greater number of A site vacancies generated compared to LLTO, impede Li^+ migration and reduce the conductivity by the order of magnitude described before between LLTO and LLNO[163].

3.6 $NaNbO_3$-$La_{1/3}NbO_3$ (XLNN) solid solution

Since $NaNbO_3$ and $La_{1/3}NbO_3$ exist as stable perovskite phases across a broad temperature range, each accommodating bond strain via cationic and octahedral tilts, it is not unreasonable to expect a solid solution to form between these two compositions, with A site vacancy formation mediating the conservation of electroneutrality. Given the diffuse and thermally invariant relative permittivity response associated with the La$_{1/3}$NbO$_3$ material, whose T_m and maximum observed relative permittivity can be increased with changing the transition metal to Ti [167], iterating the A-site vacancy concentration can clearly act as a T_m and TCC moderator.

Comparatively less work has been conducted on La$_{1/3}$NbO$_3$ with respect to NaNbO$_3$, and so it is perhaps unsurprising that very few publications regard the binary system between them. It wasn't until the turn of the millennium that the first reports on this solid solution were published by Pivovarova et al [188,189]. The latter report is more informative than the first with respect to both structural and electrical/dielectric responses across the system. In both reports, dielectric data is only reported for above-ambient temperatures, missing any dielectric relaxations below room temperature which are likely for compositions close to the La$_{1/3}$NbO$_3$ end member, considering its 80 K permittivity peak [167]. A site vacancies introduced upon La^{3+} doping as charge compensating defects could disrupt local ordering of cation displacements and induce a relaxor type response. This means that even compositions closer to the NaNbO$_3$ end member may exhibit a low temperature T_m, not observable on the dielectric studies by Pivovarova et al [189]. These studies were also conducted at 1 kHz, and a progressively rising permittivity towards higher temperatures is likely a product of DC conductivity effects. For these reasons and the little information inferable, this relative permittivity data has not been included within this review.

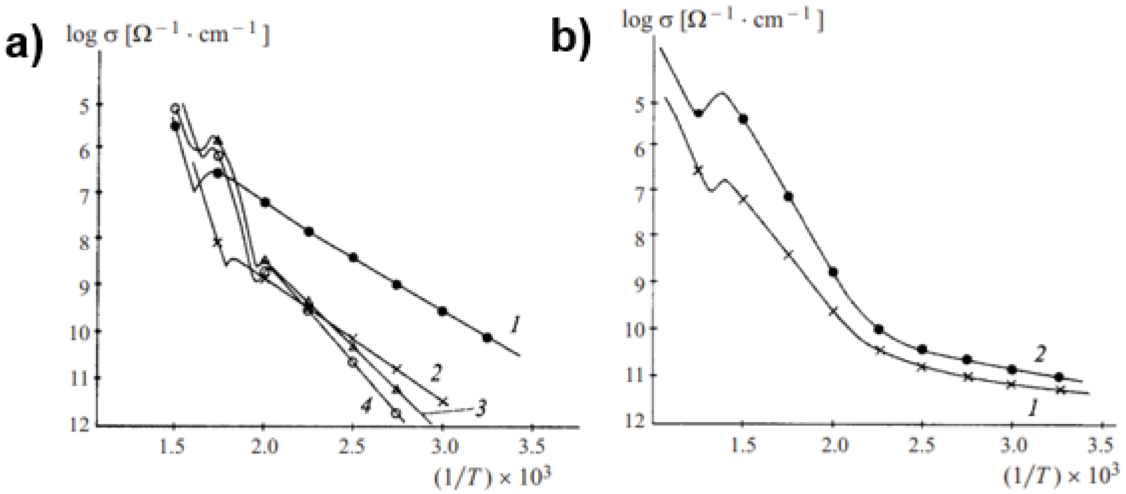

Figure 3.25: The DC conductivity of compositions in the LNN series. a) NaNbO$_3$ (1), 2 (2), 4 (3) & 6 (4) mol % La$_{1/3}$NbO$_3$ addition. b) 15 (1) & 20 (2) mol % addition of La$_{1/3}$NbO$_3$ addition. Reformatted from [189].

The temperature dependence of DC conductivity for compositions synthesised by Pivovarova et al [189] are shown in figure 3.25. For low compositions, ≤ 6 mol% La$_{1/3}$NbO$_3$ doping into NaNbO$_3$ shown in figure 3.25 a), a single activation energy appears. Comparatively, figure 3.25 b) shows a transition between two activation energy states with increasing temperature for 15 and 20 mol% La$_{1/3}$NbO$_3$ doping. The low temperature DC conductivity has a low activation energy ~ 0.2 eV, whilst higher temperatures have a higher activation energy ~ 1.4 eV. Collectively, figure 3.25

shows a transition from samples exhibiting a single conduction mechanism at low $La_{1/3}NbO_3$ contents to a conductivity regime that transitions between two mechanisms at higher $La_{1/3}NbO_3$ concentrations. This same temperature dependence of conductivity has been characterised in 25LNN by Kong et al [190], with the low temperature low activation energy associated to Na^+ conductivity, and the high temperature activation energy associated to an intrinsic electronic mechanism, postulated to be n-type by Pivovarova et al [189]. This could potentially be the result of reduction at elevated temperatures, with the partial removal under-bonded oxygen (based on the A site vacancies within the structure). There was, however, no evidence for Na^+ being the migrating ionic species in the report by Kong et al [190].

Structurally, Pivovarova et al [188,189] suggested compositionally driven room temperature polymorphism, from a 'rhombic' $NaNbO_3$ symmetry, possibly referring to the AFE P room temperature polymorph, to the 'intermediate (330-430 °C)' $NaNbO_3$ polymorph, possibly the orthorhombic R phase, at a composition of ~ 8 mol% La. At a composition between 10-15 mol% La^{3+}, an orthorhombic-tetragonal phase transition was suggested. A more detailed structural analysis by Mishchuk et al [191] showing diffraction patterns for the LNN series, shown in figure 3.26, suggests an entirely orthorhombic solid solution is achieved between the two $NaNbO_3$ and $La_{1/3}NbO_3$ end members. This study is complementary to that of Pivovarova et al in suggesting the P room temperature Pbcm symmetry is retained for low La^{3+} concentrations, below 8LNN,

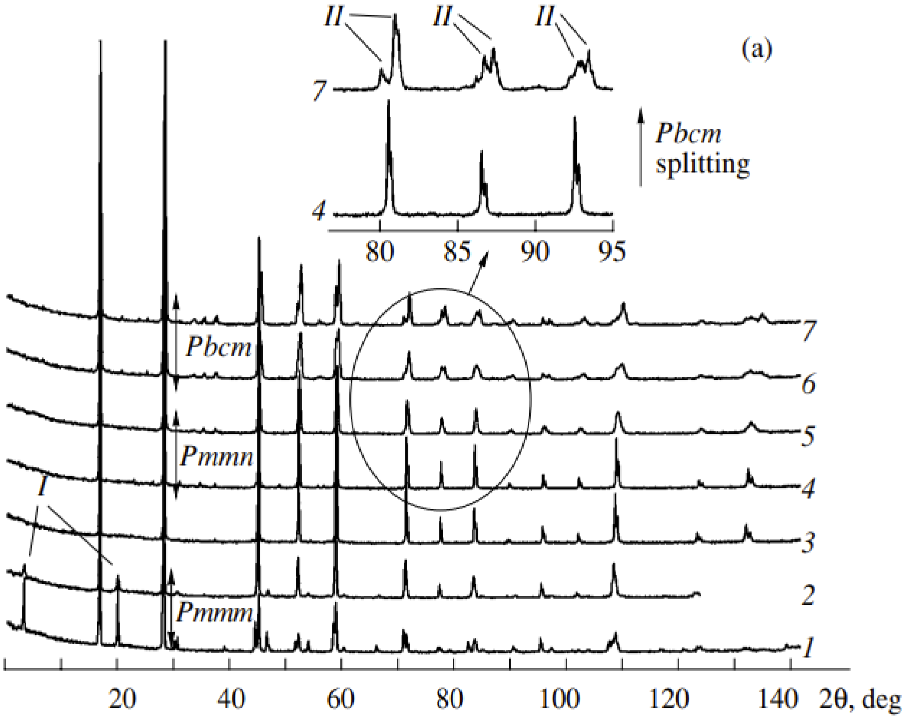

Figure 3.26: The compositionally driven room temperature polymorphism from $NaNbO_3$ (7) to $La_{1/3}NbO_3$ (1), accommodated through a series of symmetry changes. Reformatted from [191].

clear from the peak splitting highlighted in figure 3.26. There is a lack of detectable intensity ~ 40 ° (Cu-Kα) for these low La^{3+} doped compositions, a peak which would be indicative of doubling of the pseudo-cubic perovskite cell for the ferroelectric Q $NaNbO_3$ room temperature polymorph, hence inferring P phase stabilisation in LNN. Despite claims of phase purity, there do appear to be some low intensity peaks below 8LNN in the 17 - 30° 2θ range that are not characterised on a P phase Pbcm symmetry.

This structural report [191] then suggests a transition to Pmmn orthorhombic symmetry above 8LNN, a similar transition point to Pivovarova et al [189], and another symmetry proposed for the R polymorph of $NaNbO_3$ [192]. This is suggested to be retained until ~ 25 LNN, after which a transition to orthorhombic Pmmm symmetry is suggested. The composition marked with a '3' on figure 3.26 does, however, appear cubic in symmetry, with the progressive splitting of peaks towards higher 2θ characterised as $K\alpha_2$ reflections, and the small peak that is retained ~ 36 ° associated to the cubic (111) peak. The Pmmm symmetry shown towards the $La_{1/3}NbO_3$ end member marked with a '1' in figure 3.26 is now better characterised as Cmmm [156,159], whilst there is a drastically different peak splitting occurring between the peaks of '2' (25LNN) and '1' ($La_{1/3}NbO_3$) which could imply a tetragonal symmetry for the former, not ascribed within this report [191].

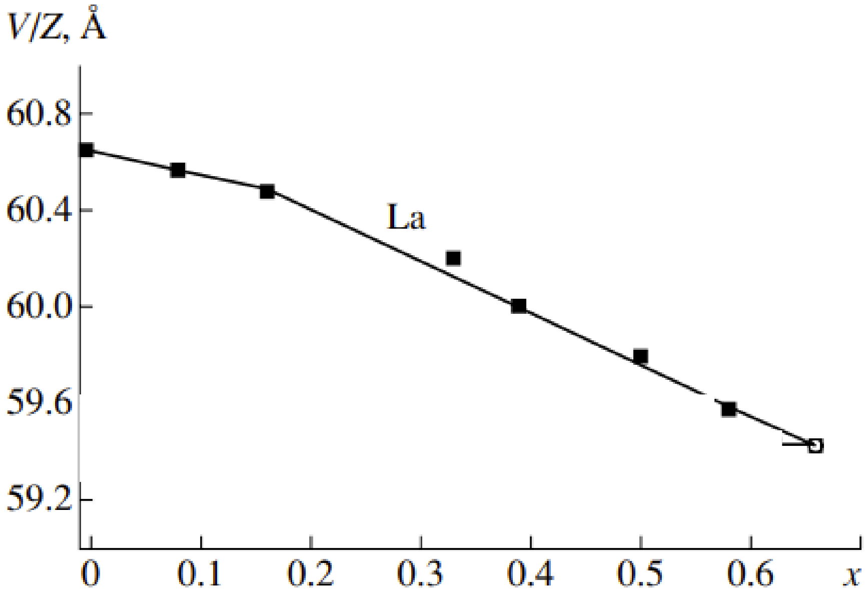

Figure 3.27: Unit cell expansion with increasing La content in $NaNbO_3$ (x=0.66) to $La_{1/3}NbO_3$ (x=0). Expansion rates drop as the solid solution nears its $La_{1/3}NbO_3$ end member, possibly influenced by progressive ordering of La/Na and A-site vacancies into alternating (002) planes. Reformatted from [191].

Figure 3.27 reveals an expansion of the unit cell with increasing La^{3+} content, despite the substitution of smaller La^{3+} (1.36 Å) for the larger Na^{+} (1.39 Å) [86]. This expansion subsequently levels off towards the $La_{1/3}NbO_3$ end member. The ordering peaks noted with an 'I' in figure 3.26 refer to the ordering of La^{3+} and A-site vacancies into alternating (001) planes, doubling the unit cell along the c axis. Since this reduction in cell expansion rate occurs for 25LNN onwards in figure 3.27, is it sensible to associate this reduced rate to the sudden ordering effect of A site vacancies. Bian and Li [193] have since conducted a structural analysis on a portion of this LNN solid solution, from 20LNN to $La_{1/3}NbO_3$, shown in figure 3.28. The results are consistent with previous suggestions that a tetragonal symmetry is observed at 25LNN, as opposed to the cubic symmetry defined previously[191]. This pseudo-cubic symmetry is achieved with higher Na^+ contents, ~20LNN, forming an orthorhombic Cmmm → tetragonal P4/mmm → cubic Pm3m phase transition sequence. The relevant peak splitting is clear in figure 3.28, whilst the asterisk is revealing of (001) ordering reflections, again indicating the doubling of the c axis and tetragonal symmetry for the 25LNN sample. This increase in symmetry with increasing Na^+ content is a product of increasing macroscopic disordering of A site species[193]. Increasing disorder is manifested in the increasing quantity of La^{3+} that was refined to occupy the Z=1/2 layer (assumed completely vacant in the $La_{1/3}NbO_3$ end member, with the exception of more recent HRTEM studies that suggest some Z=1/2 layer La^{3+} occupation [163]) with increasing Na^+ content (decreasing vacancy content)[193]. Although temperature dependence of relative permittivity was not presented, an increase in room temperature permittivity with Na^+ content was observed[193].

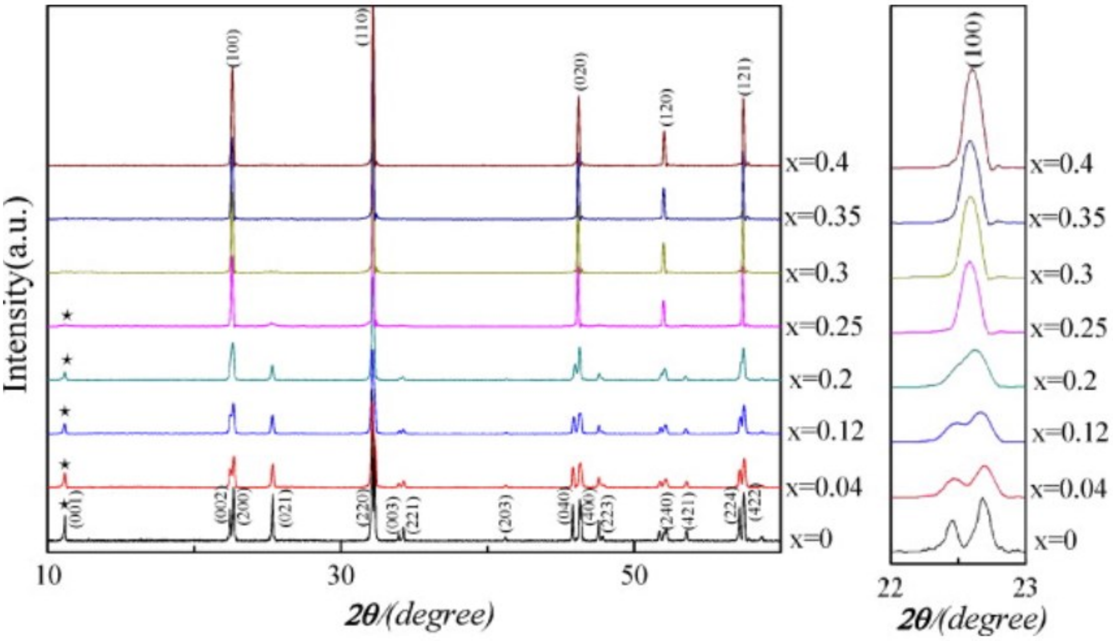

Figure 3.28: The diffraction patterns of components of the LNN solid solution, $La_{(1-x)/3}Na_xNbO_3$. The x=0 composition corresponds to $La_{1/3}NbO_3$ with orthorhombic Cmmm symmetry, whilst the x=0.2 corresponds to the cubic Pm3m 20LNN. Reformatted from [193]

Overall, little work regarding the structural evolution of the entire LNN solid solution appears to have been completed, whilst the investigations by Mishchuk et al [191] towards $NaNbO_3$ require amendments based on the conflicting and more recent understanding of symmetry towards the

A site deficient $La_{1/3}NbO_3$ end member. The temperature dependent dielectric response of the series is not well characterised, nor are its energy density characteristics and DC conductivity behaviour.

3.7 Alternate aliovalent A-site deficient $NaNbO_3$ perovskites

Bismuth doped $NaNbO_3$, $Bi_xNa_{1-3x}NbO_3$ (XBNN), has been studied by numerous authors [194–196]. A-site vacancies are assumed to form as the charge compensating defects based on the lack of secondary phase formation characterised via XRD, up to a concentration of ~ 20 mol%. Hereafter, perovskite stability is lost and $BiNbO_4$ phase formation occurs. This is unsurprising since the $Bi_{1/3}NbO_3$ end member is only metastable, with crystals formed from incongruent melting of Bi-excess stoichiometries [197]. This metastability of $Bi_{1/3}NbO_3$ is likely a function of the significantly different vacancy ordering and octahedral tilting present between this end member and the other rare-earth niobate systems. Bi^{3+}/vacancies only partially order between alternating (001) planes at Z=0 and ½ with 28 and 42 % planar occupancy respectively, unlike in $(La/Nd)_{1/3}NbO_3$ for example where 66.6 and 0 % occupancy is observed. There is no evidence of long range cooperative tilting of the NbO_6 octahedra [197], and so it exists with a macroscopic

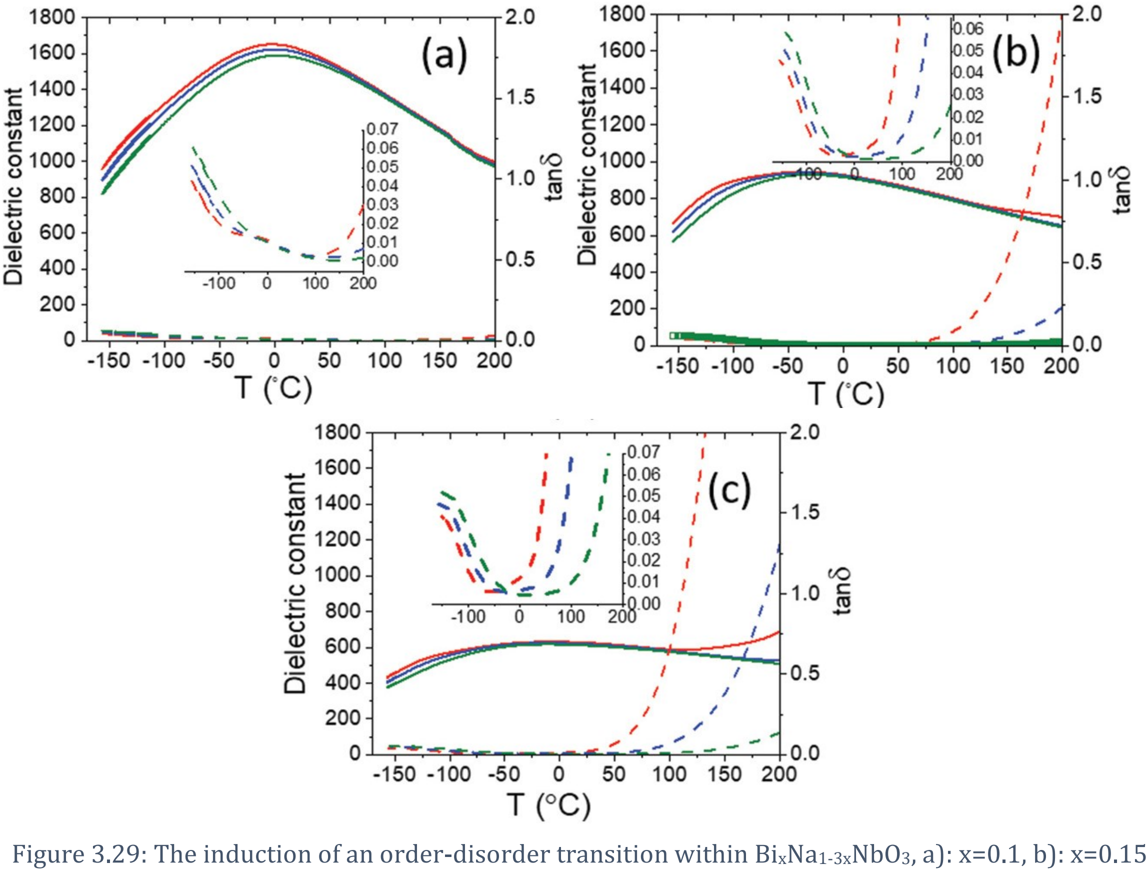

Figure 3.29: The induction of an order-disorder transition within $Bi_xNa_{1-3x}NbO_3$, a): x=0.1, b): x=0.15, c): x=0.2) with an associated frequency dependent relaxor dielectric response resulting with a reduction in TCC relative to the $NaNbO_3$ end member. Reformatted from [194].

P4/mmm tetragonal symmetry as opposed to an orthorhombic Cmmm symmetry. The stereochemical influence of the $6s^2$ lone pair of electrons on the Bi^{3+} cation results in it displacing away from high symmetry 4/mmm special sites by ~ 0.4 Å in the <111> directions , moving into 8 split atomic general positions[197]. This disorder in Bi positioning presumably limits the lack of correlation of local tilts that act to control the A-site interstice volume.

At a composition > 10BNN, diffuse frequency dependent dielectric responses are observed within the perovskite domain of the BNN solid solution, especially compared to that of $NaNbO_3$ [194,195]. This is shown in figure 3.29, alongside tan δ which shows a large frequency dependent space charge response. A tan δ < 0.05 is observed for the entire frequency range plotted (100 kHz – 1MHz) across the X7R or X8R temperature range for 10LNN only, figure 3.29 a). Levin et al [194] attributed this diffusivity in the relative permittivity response to an order-disorder transition of Bi and Nb displacements as out-of-phase octahedral tilts present in the P phase of $NaNbO_3$ are supressed. These cationic displacements couple to nanoscale vacancy/cation clustering, with modulations occurring as the structure relaxes to reduce the effects of under bonded oxygen with increasing vacancy content. The product of the disordered and locally modulated cation displacements are proposed to yield a short range polar ordering effect and the diffuse dielectric response observed[194]. A comparable effect is presented by Zhang et al[195], with equivalent order-disorder type dielectric transitions occurring at 10BNN, and in other Bi doped alkali niobates, such as $Bi_xAg_{1-3x}NbO_3$[198] that also yields diffuse responses at comparable Bi concentrations.

The average and local structure for BNN have been probed by x-ray diffraction, electron diffraction, total scattering, X-ray fine structure analysis and Raman [194,195]. The average and local structures are expectedly conflicting given the disorder associated to aforementioned A site deficient perovskite systems. The $NaNbO_3$ P phase Pbcm symmetry is lost as the Bi concentration increases. Levin et al [194]initially proposed 10BNN induced a Pbnm symmetry (suggested for the high temperature R and S phases of $NaNbO_3$ [199]) based on refinement results and the loss of antiphase tilting superlattice reflections. However, electron diffraction lacked the necessary glide symmetry conditions associated to such a symmetry, and that actually Q phase symmetry (or lower) was achieved. Further doping of Bi^{3+} induced a 'cubic' macroscopic symmetry via XRD refinements, but SAED suggested diffuse rods associated to the continued existence of in-phase tilting was now limited to short range local correlations [194]. Zhang et al [195] argue that the P phase symmetry is retained for low Bi^{3+} additions, <10BNN, which subsequently changes to the T2 $NaNbO_3$ phase with P4/mbm symmetry [200] at 10BNN (consistent with a lack of N glide symmetry stated by Levin et al [194]) and (pseudo)cubic Pm3m at 20BNN.

Sr-doped $NaNbO_3$, $Sr_xNa_{1-2x}NbO_3$ (XSNN), is another A site deficient $NaNbO_3$ system investigated within literature, although it differs from the Bi system discussed before since it generates only one A site vacancy per mol% Sr doping as opposed to two from Bi/Ln doping. SNN exhibits a perovskite solid solution limit between 20 and 25 mol% doping [201,202], much like the Bi^{3+} system, and induces a diffuse relaxor-ferroelectric type response at compositions between 10 and 15 SNN [201,203], as shown in figure 3.30. TCC is reduced with increasing Sr^{2+} content, whilst the dielectric losses remain low for a larger temperature range compared with Bi^{3+} compositions of the same doping content. There is, however, half the amount of A-site vacancies introduced with Sr^{2+} doping, and above 20SNN there is an observed increase in loss behaviour as shown in the BNN system previously [194].

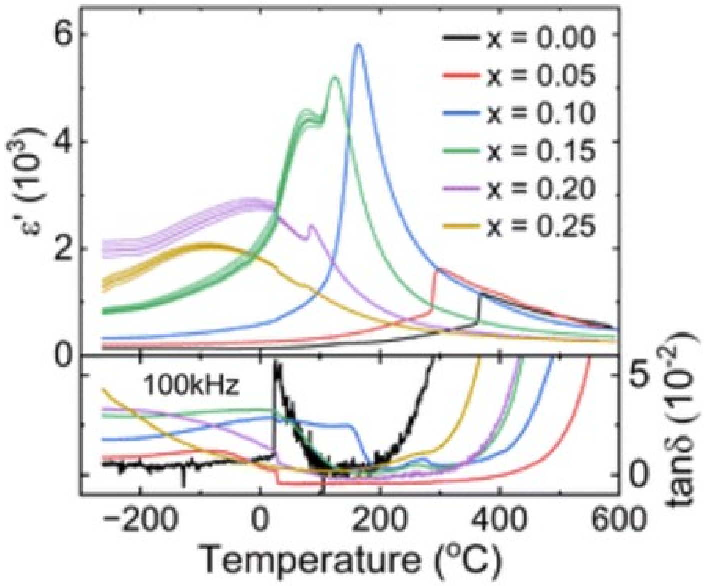

Figure 3.30: The dielectric response of Sr^{2+} doped $NaNbO_3$, showing an increase in the diffusivity of relative permittivity with increasing Sr^{2+} content. Higher Sr^{2+} contents also appear to involve an additional structural relaxation closer to room temperature. Reformatted from [201].

Structural refinements via XRD and SAED reveal the preferential stabilisation of the ferroelectric Q room temperature polymorph of $NaNbO_3$ with progressive Sr doping, based on superlattice reflections associated to the octahedral tilting and a pseudo-cubic cell multiplicity of 2 along the [001] axes consistent with the $NaNbO_3$ Q phase [201,204]. High resolution transmission electron microscopy (HRTEM) has directly observed domains with lattice periodicities changing from a four multiple (~ 166 nm, based on the ideal pseudo-cubic perovskite cell having a lattice length ~ 3.9 Å) to 2 fold (~ 80 nm) as the Sr content increases [204]. Ca-doped $NaNbO_3$ (XCNN) shows, again, comparable suppression of the relative permittivity when Ca concentrations exceed ~ 10 mol% [205]. Here, the antiferroelectric P phase is stabilised with increasing Ca doping. K^+ doping of $NaNbO_3$ is well characterised to 'induce ferroelectricity' and thus the Q polymorph of $NaNbO_3$ [106,206–208], alongside Li^+ doping [209]. The combined effect is a stabilisation of the ferroelectric Q phase when the Goldschmidt tolerance factor (ignoring the relative radii of A site vacancies) increases. Guo et al [210] suggested this with $CaZrO_3$ doping of $NaNbO_3$, where P phase stabilisation occurred on account of tolerance factor reduction with no A site vacancies formed in this self-compensating system.

Thus, not only is $NaNbO_3$ clearly supportive of A-site vacancies upon aliovalent A site doping as charge compensating defects, the structural mediation through disruption to the octahedral tilt network induces an order-disorder transition, influencing local Nb displacements and reducing long range correlations, producing a universal stabilisation of TCC at vacancy concentrations ~ 20 mol %. This is reflected in Bi^{3+}, Sr^{2+}, Ca^{2+} and K^+ A site doped $NaNbO_3$ systems, respectively.

3.8 Dielectric composite macrostructures for enhanced properties

For many of the materials discussed, such as $BaTiO_3$ and $NaNbO_3$, the dielectric properties are useful but not appropriate for temperature stable dielectrics in class II capacitors, on account of the highly temperature dependent relative permittivity they exhibit. Numerous reports have investigated the ability to utilise some of the desirable electrical behaviours of certain ceramics in appropriate macrostructural configurations to yield an overall system that meets certain output criteria. These multiphasic composite systems range from multilayered systems, where ceramics are laminated with other materials, often in the form of sandwich structures, or in more traditional composite systems where secondary phases/fillers are embedded within a matrix phase with associated multidimensional interconnectivities. For a biphasic composite, the dimensionality of each phase's intergranular connectivity can be described with an a-b notation, where a and b can vary between 0 and 3 depending on the dimensionality of connectivity between grains of each phase [140]. A connectivity of 3-0 means the grains of the matrix phase are connected in three dimensions whilst the secondary phase grains are isolated, distributed with no interconnectivity. 3-1 may refer to nanowire embedment within the matrix where the secondary phase grains are 1 dimensionally connected, 3-2 may be associated with planes of secondary phase grains with associated 2 dimensional connectivity that are embedded within the three dimensionally connected matrix phase. 2-2 connectivity may indicate a multilayered lamination of phases and 3-3 may be a percolated network of secondary phase grains throughout a matrix phase. Examples of biphasic composites with differing connectivities are shown in figure 3.31 [211] (specifically for piezo-active composites).

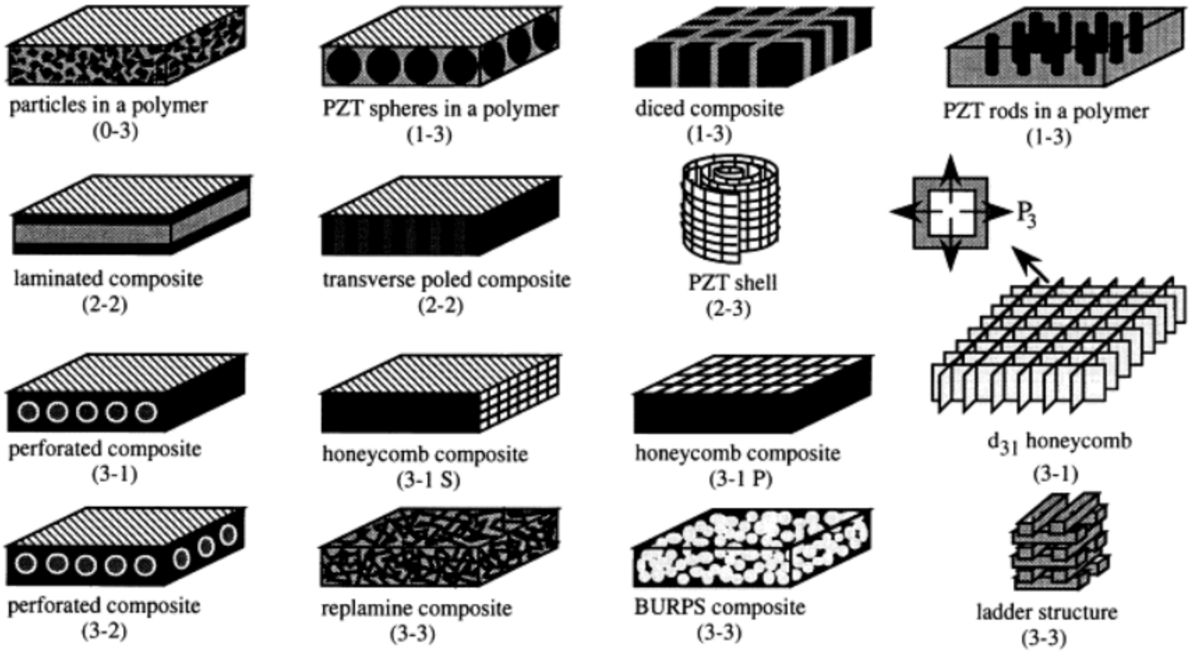

Figure 3.31: An example of the intraphasic connectivity's and associated assemblages of piezo-ceramic polymer composites. Reformatted from [211].

Polymer-ceramic composites are of frequent investigation within literature, particularly with the perspective of high energy density dielectric integration. Polymers exhibit inherently higher electric field induced breakdown resistance with respect to bulk ceramics (retained when the ceramic filler content is relatively low within the composite [212]), and so, when combined with a ceramic with good polarisability or linear polarisation-electric field dependence, can yield high recoverable energy densities, with high associated energy storage efficiencies. High breakdown strengths, ~ 489 kVcm^{-1}, and high associated efficiencies, ~ 90.3 %, were achieved for a 3-3 epoxy-$BaTiO_3$ composite [212], where the 3 dimensional connectivity of $BaTiO_3$ nanoparticles was achieved via the templating of 3D nanocluster wires of $BaTiO_3$ using organic substrates during a milling and freeze drying process. Using doped $BaTiO_3$, such as $Ba_{1-x}Sr_xTiO_3$ which exhibits a more linear relaxor type polarisation dependence with reduced polarisation saturation effects compared to parent material, would offer higher recoverable energy densities [213]. Use of $Ba_{0.8}Sr_{0.2}TiO_3$ nanowires embedded within a poly(vinylidene fluoride) (PVDF) matrix have achieved a high recoverable energy density ~ 14.86 Jcm^{-3} at 450 kVcm^{-1} [213]. This represents a large increase in recoverable energy density compared to commercially available polymer capacitors used for energy density applications, including biaxially oriented polypropylene capacitors (BOPP), which exhibit smaller recoverable energy densities ~ 1.2 Jcm^{-3} at higher electric fields of 640 kVcm^{-1} [214,215]. Not only this, but an improved volumetric efficiency is afforded to these nanocomposites compared to the commercially available polymeric systems such as BOPP, which are manufactured as physically large windings often inches in diameter

[214]. Other PVDF polymer-ceramic composites have also been investigated, such as PZT [216]or PZT based systems (Pb,La)(Zr,Sn,Ti)O_3 [217], with PVDF an attractive matrix since it exists as a semicrystalline polymer with good chain flexibility and a β-phase that exhibits spontaneous polarisation with pyro and piezoelectric properties [218].

The flexibility afforded to a polymer-piezoelectric composite give interesting prospects as kinematic energy harvesting devices, where the kinetic energy of a moving body is directly transferred to electrical energy via this composite electromechanical transducer [219]. This is convenient for small power applications where batteries are not convenient, such as pacemakers which harvest the motion of the heart [220], or for tire pressure sensors placed on the walls of tyres [219,221]. The intraphasic dimensional connectivity shown in figure 3.31 has a significant influence on the properties of these electroactive composites. For example, finite element modelling suggests piezoelectric charge coefficients and coupling constants are greatest for 3D networked 3–3 and long-fibre (1–3) $BaTiO_3$ reinforced PVDF composites, respectively, while acoustic impedance is minimised in 0–3 composites [222]. Increasing the piezoelectric sensitivity (such as d_{33}) is often associated with increasing the dimensionality of the connectivity between grains of the piezo-active element, such as moving from a 3-1 to a 3-3 assemblage [223]. Hydrophones, for example, often utilise piezoelectric composites with such a 3-3 dimensionality configuration [224].

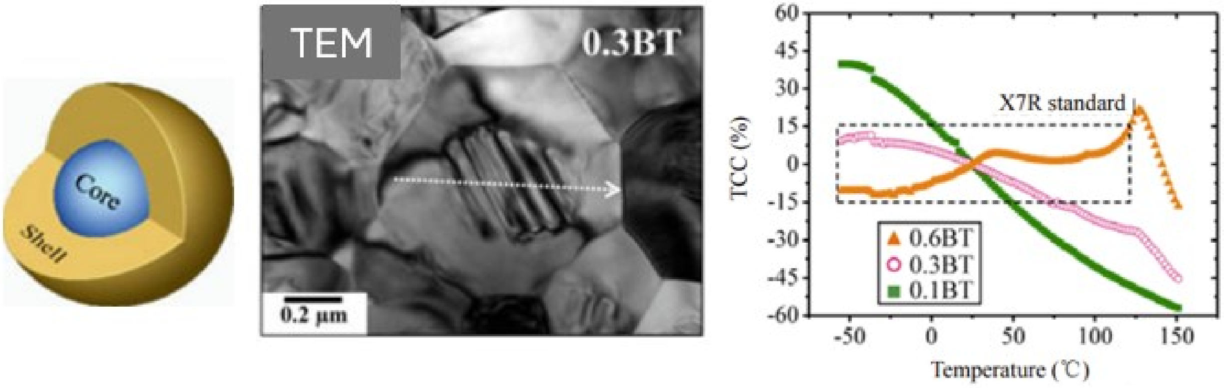

Figure 3.32: A schematic and a TEM micrograph of a Y,Mg doped shell and undoped $BaTiO_3$ grain core, where the core constitutes 30 % of the grain volume. The image to the right shows the effect of core shell grain structures on stabilising TCC. A thicker core: shell ratio for this Y,Mg doped system was better for X7R TCC. Reformatted from [80].

Regarding TCC stabilisation for dielectrics, one of the most common 'composite' architectures is a core shell structure, with a 3-0 type connectivity existing for the shell and encapsulated grain core, respectively. This is shown in figure 3.32, alongside its associated influence on relative permittivity stabilisation. This type of compositional heterogeneity induced by the limited diffusion of elements throughout the grain structure has long been characterised [76–78,80,225], with use in $BaTiO_3$ based systems for the stabilisation of TCC caused by the serial polarisation of these two separate polarising components. $BaTiO_3$ based core shell structures have also more recently been utilised for the enhancement of breakdown in PVDF-ceramic composites for energy storage applications, with SiO_2 shells offering a higher breakdown resistance compared to $BaTiO_3$ cores [226].

3.8.1 Composite mixing rules

Numerous models have been theorised to predict the influence secondary phase materials have upon the observed electric and dielectric properties of the matrix phase, depending upon volume fraction, interconnectivity, size and morphology, inherent electrical/dielectric properties and their associated directionalities/anisotropy. These are summarised well by Dang et al [227], with the simplest of these being series and parallel connectivity laws, which can apply to 2-2 composites where the lamination of heterophases is parallel and perpendicular to the direction of field/perturbing signal, respectively [227]. These are equated in equations 3.3 and 3.4 for the series and parallel 2-2 composites shown in figure 3.33 a) and b), respectively [227].

$$\epsilon_T = \frac{\varepsilon_M \varepsilon_S}{\epsilon_M \theta_S + \varepsilon_S \theta_M} \tag{3.3}$$

$$\epsilon_T = \varepsilon_M \theta_M + \varepsilon_S \theta_S \tag{3.4}$$

where $(\varepsilon_M, \theta_M, \varepsilon_S, \theta_S)$ are the permittivity (ε) and phase fractions (θ) of the matrix (M) and secondary phase (S). A mixed composite composed of spheroids distributed homogeneously within an isotropic matrix will exhibit a permittivity between these series and parallel distributions, shown in figure 3.33 c).

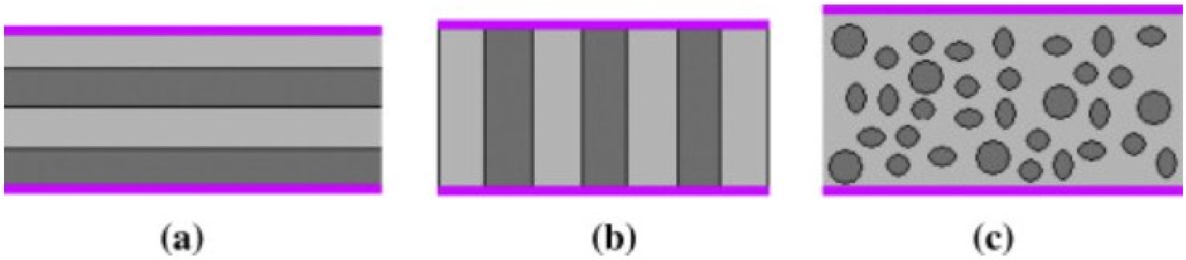

Figure 3.33: A serial (a) and parallel (b) connectivity of matrix and secondary phases in a 2-2 physically connected composite. c) is a 3-0 composite representing a mixed system, for which the discussed mixing laws attempt to predict based on phase properties. Reformatted from [227].

Lichtenecker's theory [227,228] is a direct observation of this, where an exponent , α, describes the variability of the mixing system between these two limiting mixing conditions. If α is -1, the mixing rule reduces to a series system, and if equal to 1, describes a parallel connectivity. Thus, α is a fitting factor that describes the topology and interactions of the secondary phase with the matrix [229]. This is shown in equation 3.5.

$$(\varepsilon_T)^\alpha = (\varepsilon_M)^\alpha \theta_M + (\varepsilon_S)^\alpha \theta_S \tag{3.5}$$

A Maxwell Garnett equation can predict the overall permittivity output according to equation 3.6. To account for non-sphericity, a depolarisation factor 'A' can be included to account for non-ideal secondary phase morphology. This is often derived empirically or obtained from literature, and is equal to 1/3 for an ideal sphere-shaped secondary phase particle [227]. This can characterise mixing for small quantities of secondary phase, accounting for less than 10 % of the volume fraction:

$$\epsilon_T = \varepsilon_M \left(1 + \frac{\theta_S(\varepsilon_S - \varepsilon_M)}{A(1-\theta_S)(\varepsilon_S - \varepsilon_M) + \varepsilon_M}\right) \tag{3.6}$$

A Bruggeman mixing rule, equation 3.7, was proposed for composites with higher filler contents, often above 10 % of the volume, and is considered effective for non-homogeneously distributed secondary phase systems, where these particles may be in close proximity [227]. This is given by equation 3.7, and holds for higher secondary phase contents up to 50 % of the volume fraction provided no percolative path is formed between these secondary phases[227]:

$$\frac{\varepsilon_S - \epsilon_T}{\varepsilon_T^{1/3}} = \left(\frac{(1-\theta_S)(\varepsilon_S - \varepsilon_M)}{\varepsilon_M^{1/3}}\right) \tag{3.7}$$

A more complicated mixing rule by Jaysundere and Smith [230] was proposed to account for the secondary phase interactions that may be induced by their volume fraction and close proximity. These include dipolar interactions and local field effects in the matrix. This equation is limited to secondary phase volume fractions up to 30 % [229]. The equation has not been presented here for its complicated nature. There are numerous mixing rules which are frequently modified with further assumptions regarding distribution, morphology and interactions between composite phases. Although some limitations on secondary phase fractions direct mixing choice, often composite properties are fitted empirically to mixing laws, with prediction based on a single mixing rule difficult without data on comparable systems.

3.8.2 NNBT Multi-layer architectures

The NNBT solid solution introduced in section 3.3 offer attractive properties with respect to prospective use as dielectrics. The centre of the solid solution offers diffuse relative permittivity maxima with high magnitudes, in excess of ~2000, whilst retaining low dielectric losses. Towards the BT end member of the solid solution, low $NaNbO_3$ additions induced a core shell compositional heterogeneity that incurs an even more stable TCC response than these relaxor components at the centre of the solid solution [136]. The diffusivity of these permittivity maxima are, however, insufficient for X7R or X8R rated dielectrics. Foeller et al [136,231] proposed a 2-2 composite macrostructure composed of a core shell 2.5NNBT composition and $BaTiO_3$ with a serial electrical connectivity, separated by an Au interdiffusion barrier, to satisfy X7R rated TCC criteria. A schematic for this bilayer system shown in figure 3.34.

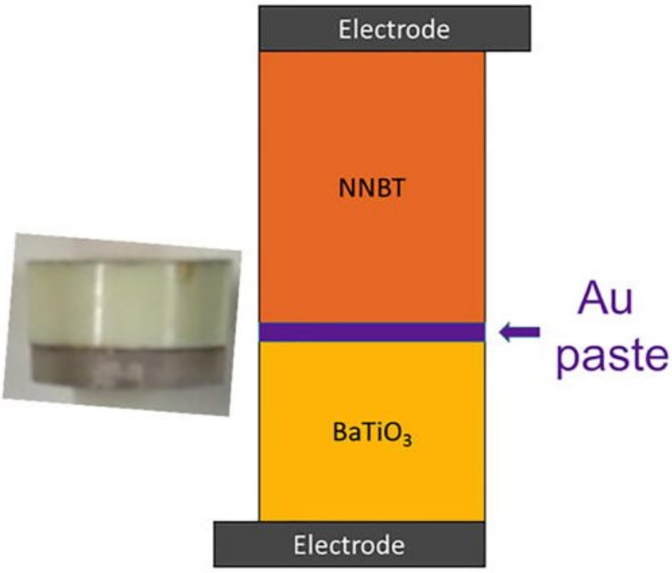

Figure 3.34: The NNBT based bilayer system proposed by Foeller et al [231] utilising an Au barrier layer to impede inter-diffusion between components.

The enhancement of TCC of the bilayer with respect to its 2.5NNBT and $BaTiO_3$ components originates from the series capacitance law, equation 3.8:

$$\frac{1}{C_T(T)} = \frac{1}{C_{NNBT}(T)} + \frac{1}{C_{BT}(T)} \tag{3.8}$$

Thus, components of the bilayer must provide relative permittivity response at complimentary temperatures and magnitudes in order to stabilise the overall device permittivity. For the system investigated, $BaTiO_3$ provides the high temperature permittivity response lacking in the 2.5NNBT composition that is inherently temperature invariant across the ambient and sub ambient temperature ranges, consequent of its thermodynamically stable core shell configuration [136]. Since nominal $BaTiO_3$ exhibits a permittivity often five times greater than that of NNBT, the volume fraction ratio of NNBT:$BaTiO_3$ must be weighted towards the NNBT to attain comparable permittivity magnitudes and a stable TCC response. Foeller et al [231] utilised a 66.6:33.3 thickness fraction ratio between these constituent phases, yielding the temperature stable dielectric response of figure 3.35.

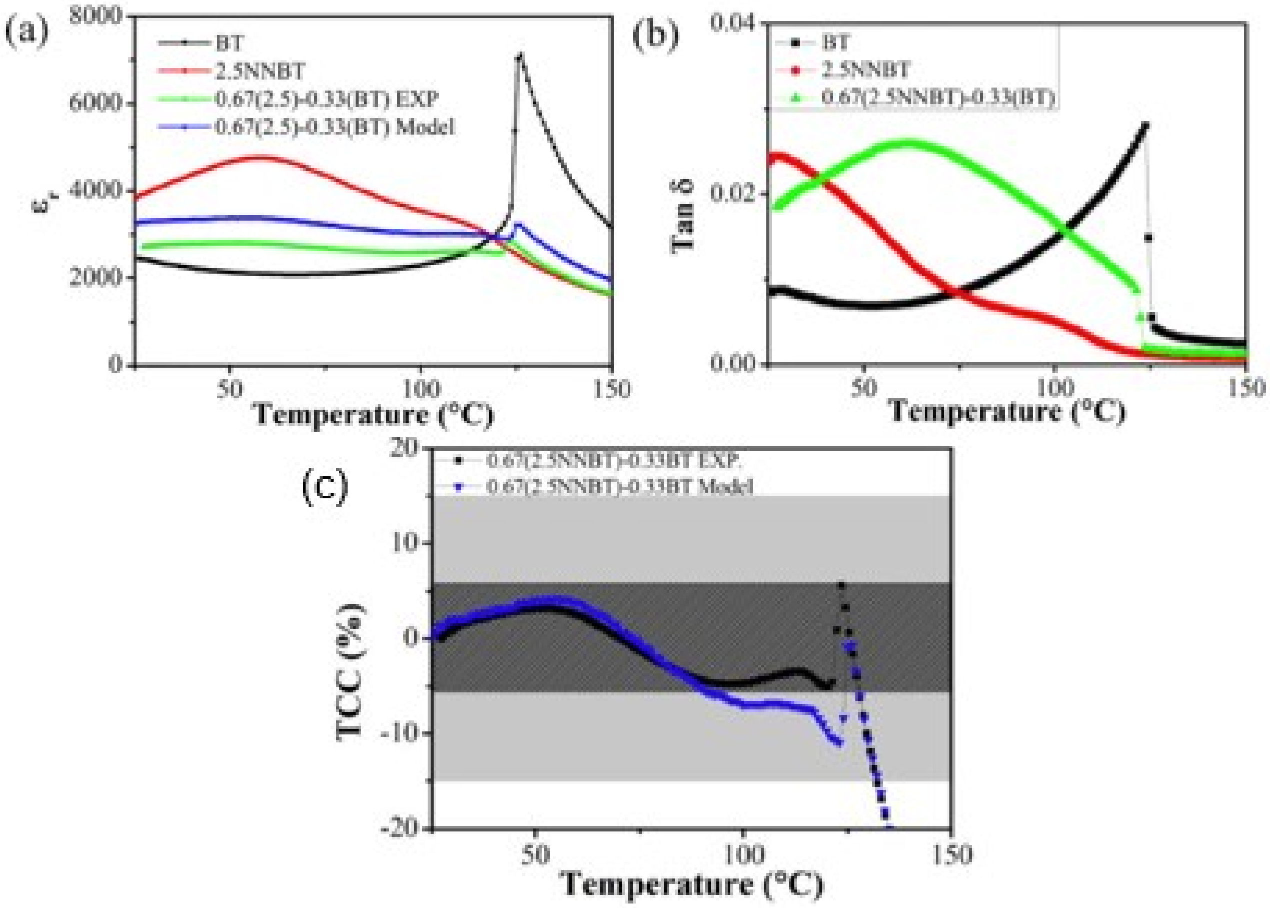

Figure 3.35: The X7R achieving 2.5NNBT:$BaTiO_3$ bilayer with a 66.6:33.3 thickness fraction ratio. The modelled serial response using equation 3.8 is compared to the experimental response, alongside the dielectric responses of its component materials. (a) Shows the relative permittivity, (b) shows the tan δ response and (c) shows the TCC profiles. Reformatted from [231].

The inherent benefit of using a simple serial configuration, in conjunction with an interdiffusion barrier, is the ability to experimentally replicate the modelled response based on equation 3.8. This is shown in the similarity in relative permittivity and TCC magnitudes in figure 3.35 a) and c), respectively.

Kerridge et al [232] extended the industrial attractiveness of such a system by developing a code that utilised user inputs for TCC rating and permittivity minima alongside available materials (with associated permittivity inputs), that produced an output of optimal bilayer and trilayer multilayer systems (materials and associated fractions) that attain such specified TCC criteria. The optimal systems were those with the highest possible relative permittivity magnitude and/or the widest TCC stability range. The same author then, using this optimisation code, presented an X7R achieving NNBT bilayer that utilised non-core shell NNBT components, with co-sintering in the absence of an Au interdiffusion barrier as shown in figure 3.34 [149]. Interdiffusion barriers would increase manufacturing complexity and cost, whilst also imparting interfacial porosity or local delamination that results in the lower permittivity magnitude of the experimental bilayer relative to the modelled bilayer, seen in figure 3.34 a). A 70:87.5 NNBT bilayer with associated thickness fractions ~ 25:75 was modelled to achieve X7R TCC rating [149], yet when sintered, its high temperature 87.5NNBT related permittivity peak is asymmetrically broader towards lower temperatures than expected, as shown in figure 3.36. This results in the +15 % TCC boundary being exceeded below 125 °C, figure 3.36 (b). The inference is that a serially connected interdiffusion-driven ternary component is developed at the interface, intermediary in composition between the 70 and 87.5NNBT, yielding a slightly lower T_m with respect to 87.5 NNBT. The permittivity contribution of this ternary phase then induces the lower temperature asymmetrical broadening of the high temperature permittivity peak, losing the multilayers X7R TCC rating. Kerridge [149] suggested this ternary layer accounted for ~ 10 % of the total thickness of the bilayer, ~ 100 µm thick, hence why the permittivity variation was so pronounced. No interdiffusion rates were characterised between differing components of the NNBT solid

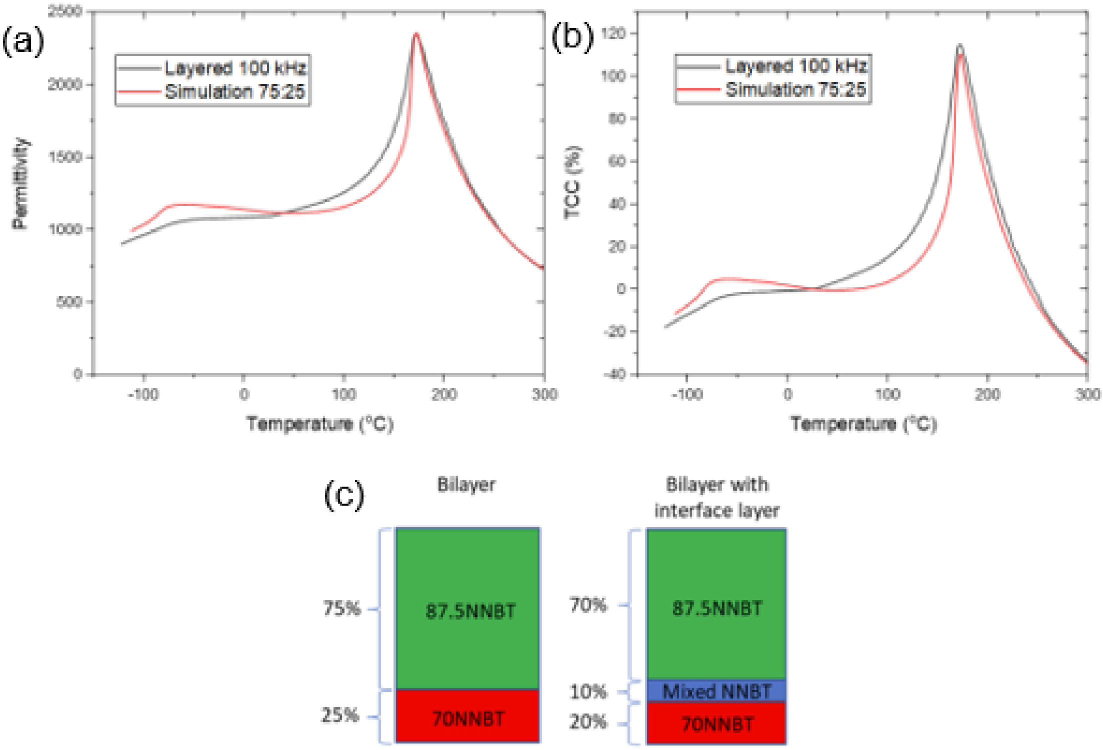

Figure 3.36: The variation in permittivity (a) and TCC (b) between modelled and experimental 70/87.5NNBT bilayers when co-sintered without an Au barrier layer. The proposed mechanism was the formation of an intermediary, serially connected NNBT composition at the interface (c). Reformatted from [149].

solution. This would be essential for identifying components of the NNBT solid solution that can be sintered without an interdiffusion barrier without compromising intended TCC temperature dependence. Alternatively, if NNBT diffusion rates can be characterised, the modelling of ternary compositions at the interface and their associated thicknesses and permittivity contributions could be predicted and integrated to the optimisation code of Kerridge et al [232], with output thickness fractions modified to account for this interfacial interdiffusion.

Despite multilayer systems being able to attain X7R rated TCC, with good coherence between predicted and experimental results, there are concerns relating to the commercial feasibility of these systems. Laminating and co-sintering tapes to manufacture multilayer architectures presents a disruptive technology to current monolithic tape cast procedures. The need to cast and laminate multiple tapes adds time to the capacitor build. The thermal compatibility of paired materials would need to be high to inhibit interlayer straining and delamination during sintering. Interdiffusion barriers are expensive and add undesirable manufacturing complexity, whilst the Na contained within the NNBT components is thermodynamically incompatible with Nickel electrodes during MLCC firing. Copper electrodes could be possible, but not at the sintering conditions of 1250 °C utilised for multilayer sintering [149,231,232].

3.9 Research Questions

NNBT has proven to show dielectric behaviour across its solid solution, with high permittivities retained despite transitioning to relaxor responses with reduced polar ordering as the solid solution moves away from either of its end members. An accompanying flattening of the permittivity occurs with this reduction in polar order, figures 3.14 - 3.16, producing materials far more temperature invariant compared to its BT or NN end member materials, figure 3.1 and 3.9 respectively. Foeller and Kerridge et al [136,149,231,232] had proven such dielectric properties of the NNBT solid solution could be exploited for X7R dielectrics using a serial lamnination of select NNBT compositions, but only whilst using a physical interdiffusion barrier between its constituent layers, figure 3.34. Sintering in the absence of these layers results in interdiffusion that is deleterious to this X7R TCC rating, figure 3.36, and so it is of interest to investigate if diffusion rates between its NNBT components vary, and can be lowered to mediate co-sintering of a bilayer without an expensive and industrially unfavourable diffusion inhibiting layer. Additionally, could an alternative composite assemblage to this 2-2 bilayer system produce temperature stable dielectric response and represent a less commercially destructive system compared to these bilayer systems? This is considering the fact that multilayers impart additional manufacturing stages and impose increased risks of physical defects, such as delamination during sintering.

In the search for temperature stable dielectrics, Perovskite A-site vacancy generation appears to reduce the temperature dependence of dielectric response in $NaNbO_3$, using varied aliovalent A-site dopants, figures 3.29 and 3.30. The $La_{1/3}NbO_3$-$NaNbO_3$ solution is compartiviely less understood than others reported, both structurally and with respect to its dielectric and electric behaviours. There are interesting and variable reported responses from the system, including dielectric, Na^+ and even La^{3+} conducting response. It is of interest to investigate if doping $NaNbO_3$ with La^{3+} can produce a complete solid solution, suggestable (but unknown) from the highly A site deficient nature of its $La_{1/3}NbO_3$ end member and the previous structural studies partially covering the solution. Additionally, does a flattening of dielectric response occur with increasing La^{3+} (and V_{Na}') concentration that is appropriate for X7R or X8R rated dielectrics? Such could represent a universal mechanism for TCC stabilisation in $NaNbO_3$, in line with the results obtained for alternate aliovalent A site dopants reffered to within this report. If a solid solution forms, where does a dielectric response limit exist along the solid solution? Clarification on its reported structural polymorphism and ionic conductivity behaviour should follow, potentially reporting a solid solution that finds itself with a variety of functional properties useful for different applications outside of the dielectric scope this thesis regards.

4 Experimental Methodology

4.1 Solid State Synthesis

Solid state methods were used for all lab-synthesised compositions in this thesis. This includes the NNBT compositions utilised in the ceramic composites of results chapters 1 – 3, and all of the LNN compositions synthesised and reported on within results chapter 4.

Solid-state synthesis utilises high temperatures to stimulate the solid state diffusion of ions, preferably homogeneously mixed and in the necessary stoichiometries to synthesise an energetically favourable phase [7,13]. Elements are introduced as reagents, the oxides and carbonates tabulated in table 4.1. These reagents were dried (180 °C for carbonates, 900 °C for TiO_2 and 1000 °C for Nb_2O_5 and La_2O_3) to remove any adsorbed/absorbed water. These dried reagents are then weighed according to the molar mass of each element necessary to satisfy the compositional stoichiometries shown in table 4.1.

These reagents were then wet-ball milled using isopropanol as the solvent and 10 mm diameter/20 mm long cylindrical Yttria-stabilised Zirconia milling media. Ball milling serves two main purposes: firstly, reducing reagent particle size and maximising surface area for solid-state diffusion, and secondly, providing a viscous flow of reagents to encourage homogeneous mixing prior to annealing. The slurries are milled for ~ 16 hours at 200 rpm. This maximises particle size reduction without incurring unnecessary contamination from the milling media.

Table 4.1: The compositions synthesised via solid state synthesis routes and the reagents used.

$La_xNa_{1-3x}NbO_3$ (LNN)	
Compositions Made (x)	0.01, 0.05, 0.075, 0.1, 0.15, 0.2, 0.25, 0.27, 0.29, 0.31, 0.33
$Na_xBa_{1-x}Nb_xTi_{1-x}O_3$ (NNBT)	
Compositions Made (x)	0.6, 0.7, 0.8, 0.875
Reagents Used	
Na_2CO_3 (99.9%), La_2O_3 (99.9 %), Nb_2O_5 (99.99 %), $BaCO_3$ (99.9 %), TiO_2 (99.9 %)	

The milled slurries are dried, sieved and annealed at 900 °C for 6 hours in a 'calcination' step, where phase formation of NNBT and LNN is achieved via solid state diffusion. A higher condition of 1000 °C for 6 hours was used for the $La_{1/3}NbO_3$ end member of the LNN solid solution for its lack of Na, which is relatively volatile. For NNBT and LNN, this calcination process was repeated after an intermittent re-milling. The solid-state synthesis route for the LNN solid solution is shown in figure 4.1.

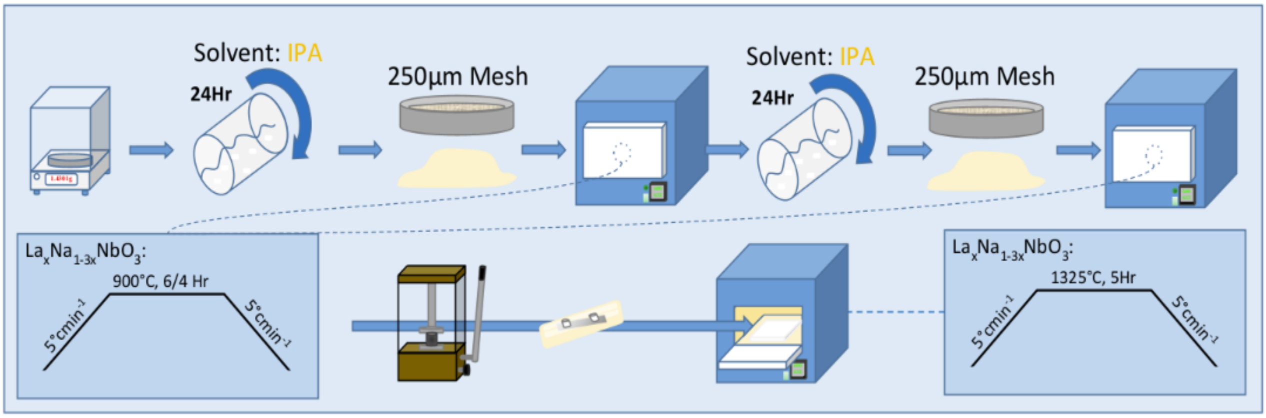

Figure 4.1: The solid-state synthesis route used to synthesise LNN compositions. The same route was used for the NNBT compositions but with a lower sintering temperature of 1250 °C.

For material characterisation purposes, a dense polycrystalline pellet of each composition was formed using the calcined powders. A 10 mm diameter green body pellet of calcined powder was formed using the uniaxial pressing of ~ 0.4 g of powder at ~ 25 MPa for 1 minute. The green body-density of this pellet is then improved through a subsequent cold isostatic pressing step, at a higher pressure of ~ 32 kpsi for 5 minutes. This has the beneficial effect of removing internal pressure distributions within the green body pellet introduced through the uniaxial pressing stage as well as maximising the green body density. The green body pellet is then densified through another annealing stage, termed 'sintering', at much higher temperatures compared to the previous calcination stages. Typically, sintering temperatures are in excess of $0.8T_{melting}$, where higher energies facilitate quicker diffusion of elements for grain coarsening and densification stages. The resulting dense pellet, often aimed for ~ 95 % of the theoretical compositional densities (based on unit cell volume and mass), is coated with a gold frit paste, fired at 850 °C for 2 hours to melt the frit and distribute and adhere the gold across the pellet surface, ready for electrical analysis. For microscopy analysis, a face of the pellet is polished instead.

4.2 X-ray Diffraction

4.2.1 Principle

X-ray diffraction (XRD) is a technique from which the space group of a crystalline material can be interpreted, based on the constructive interference between X-rays scattered (diffracted) by the electron density associated to atoms situated in select lattice planes [5,6]. Thus, XRD is based on the principle of wave-particle duality. Our ability to observe such constructive interference events is reliant upon reorientation of the sample to observe diffracting planes, such as powder diffraction using randomly orientated crystallites or an appropriate rotation of the diffracting single crystal relative to the incident beam (Bragg diffraction). Alternatively, this same effect can be induced by using a wide band of incident wavelength radiation (Laue diffraction)[10]. This is provided the wavelength of the incident radiation is of a similar order of magnitude to the interplanar atomic spacings. The study of interference events, including systematic absences, provides information on the Bravais lattice and symmetry elements present, allowing the three dimensional crystal structure to be defined.

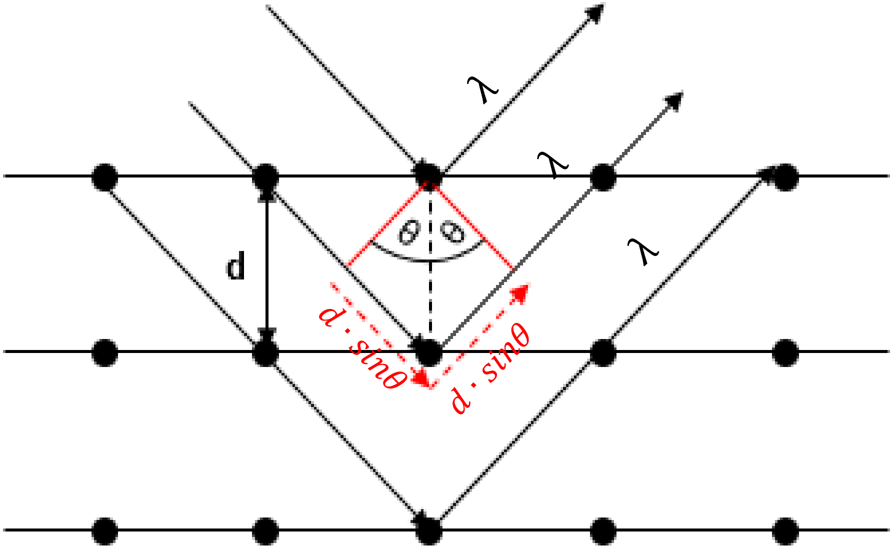

Figure 4.2: A schematic for the Bragg condition of constructive interference between scattered X-rays

For an incident beam to interfere constructively, the parallel scattered beams must be in-phase. That is, the difference between the distance one beam may have travelled relative to the other is an integer multiple (n) of the wavelength (λ) of the two waves, nλ. If this is drawn out schematically, figure 4.2, trigonometrically it is clear that the total additional path length travelled by the next scattered, parallel beam penetrating the surface is equal to $2dsin\theta$. This results in the Bragg condition for diffraction and constructive interference:

$$n\lambda \ = \ 2dsin\theta \tag{4.1}$$

where d is equal to the interplanar spacing between a set of parallel adjacent diffracting planes and θ is the angle subtended between the incident beam and the diffracting plane. Since different planes of the lattice will have inherently different lattice spacings, the crystal will need to be reorientated relative to the incident x-ray beam for all diffracting planes to be able to diffract with constructive interference conditions satisfied. Powder diffraction is an alternative to single crystal diffraction that inhibits the need for crystal rotation for all diffracting planes to be observed. In powder diffraction, the finite mass of powder is irradiated which is constituent of smaller crystallites, typically microns in size, randomly oriented relative to themselves and importantly orientated randomly relative to the incident x-ray beam. Consequently, there is a statistically large number of lattice planes orientated relative to the incident x-ray beam such that the Bragg condition for diffraction is satisfied [5,6]. Since each of these planes have differing d-spacings, and the crystallites are orientated azimuthally not just axially relative to the incident x-ray beam, a series of concentric diffraction cones are created by the irradiated powder [233].

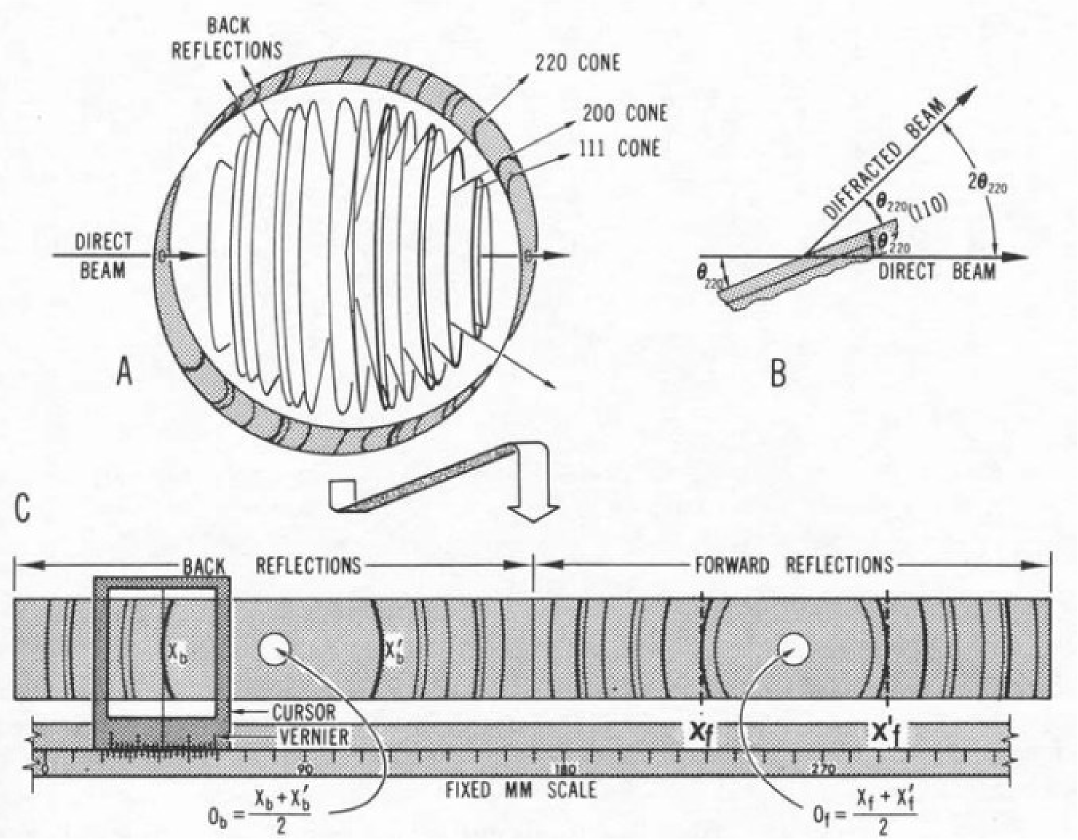

Figure 4.3: The effect of Debye Scherrer diffraction cones and the resultant rings they create on the photosensitive film placed inside a Debye-Scherrer camera. Reformatted from [233].

These cones project through three dimensions as shown in figure 4.3, and appear as rings – Debye Scherrer rings – should photosensitive film be exposed.

A Debye-Scherrer camera was one of the earliest forms of measuring the intensity and angular dependence of lattice diffraction, with a circular film intersecting these cones and producing a visually annular diffractogram. Figure 4.3 shows the formation of these rings on a film from the intersection of these three-dimensional cones. A more modern Debye-Scherrer geometry involves the movement of a photosensitive detector to intercept these rings in an analogous way to the film. A Debye-Scherrer geometry is also often referred to as a transmission geometry, as the beam transmits through the volume of the sample, and has many inherent advantages with respect to other reflection-based geometries. The effects of preferred orientation of the crystallites are minimised, inhibiting artificially enhanced diffraction peak intensities, and small sample amounts can be analysed. Reflection geometry is more frequent within laboratories, commonly known as a Bragg-Brentano geometry, and involves the 'reflection' of incident beams from the surface of a flattened powder specimen, which are subsequently detected by a moving detector [234]. In many cases, the X-ray source also moves relative to the specimen. A typical Bragg-Brentano geometry is also shown in figure 4.4.

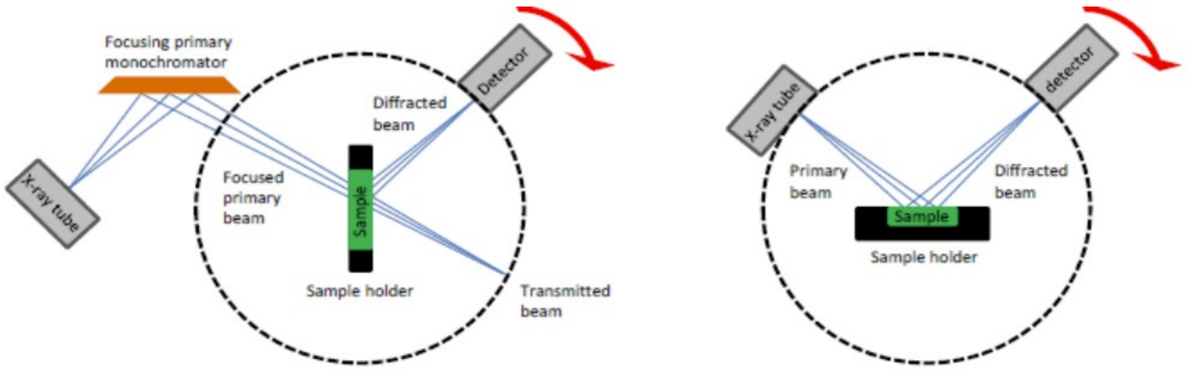

Figure 4.4: Two common lab diffractometer geometries: left) a Debye-Scherrer/Transmission geometry and right) a Bragg-Brentano reflection geometry. Reformatted from [234].

As the detector moves through space, a diffractogram of intensity relating to diffracting lattice planes against angle (2θ) is established, such as the one shown for cubic LaB_6 in figure 4.5. Each of these peaks can be related to a diffracting plane, with the degree of peak splitting indicating the appropriate crystal system of the material. For LaB_6, cubic at room temperature, all unit cell lengths (a, b and c of figure 2.1) are equal. The resulting effect is that the (100), (010) and (001) planes all share equivalent interplanar spacings, diffracting at the same angle. The (100) diffraction peak has a multiplicity of 6. For a tetragonal system, a and b are equal but the c unit cell length is larger. The resulting effect means that the (100) and (010) planes share equivalent interplanar spacings that are smaller than that of parallel (001) planes. The resulting effect is that the peak formerly associated to the <100> family of planes is now split, with a lower intensity peak occurring at a slightly higher 2θ corresponding to the elongation of the c unit cell length with respect to its a and b cell lengths. Peak splitting indicates a lowering of the symmetry from a high symmetry cubic analogue, and can indicate the crystal system present.

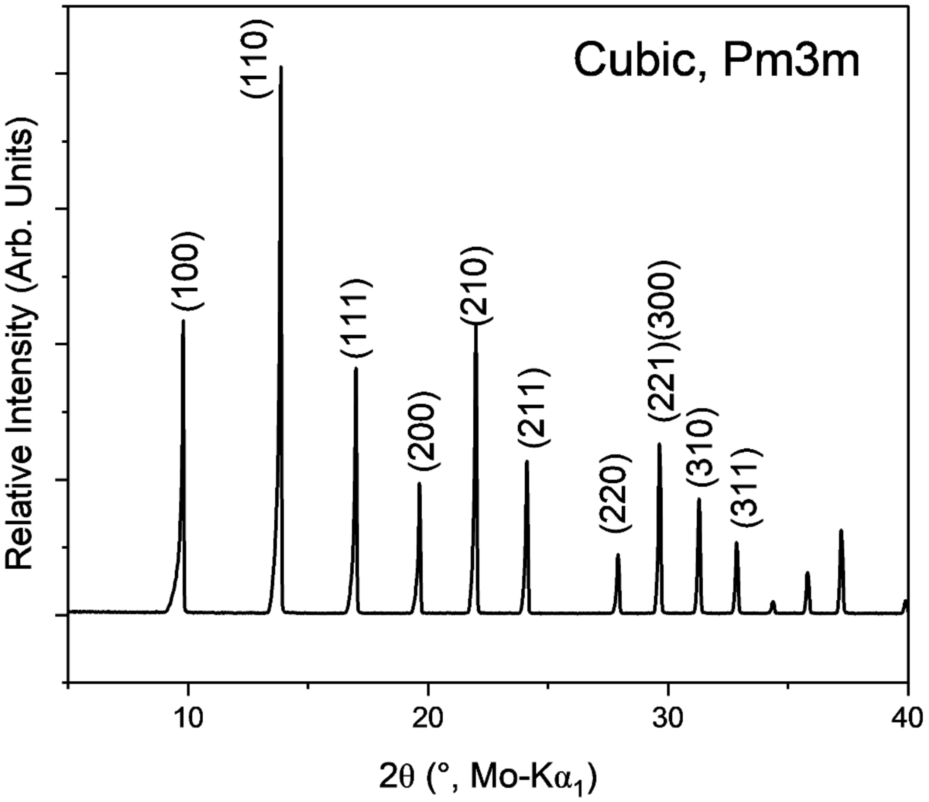

Figure 4.5: The diffraction pattern for cubic LaB_6, with indexed peaks according to the diffracting plane(s) responsible.

Although diffraction peaks are assigned to the responsible scattering planes, analysis of systematic absences gives indication of Bravais lattice types and other symmetry elements present in the unit cell, showing point symmetry can be reflected in the diffraction patterns [5]. Table 4.2 indicates a list of body centring types and the systematic absences imposed upon the diffraction pattern. Additional symmetry elements can induce similar absences, such as glide planes, which generate a h0l absence condition when l isn't even [235].

Since X-ray scattering is due to interactions between incident radiation and the electron cloud of an atom, the intensity of diffraction peaks are directly related to the mass of the atoms within the diffracting plane. Lighter elements, including oxygen, have a smaller effect on the intensity of the diffracting peaks. Alternative techniques, including neutron diffraction, are necessary to interpret the local structural displacements of oxygen ions and other light elements.

Table 4.2: The systematic absences observed in diffraction patterns for lattices with different body types.

Lattice Centering	Symbol	Absence Conditions
Primitive	P	N/A
Body Centred	I	h+k+l=odd
Face Centred	F	All unless h,k,l all odd or all Even
C-Centred	C	h+k=odd

Rietveld refinements are then conducted on diffraction data as a means of calculating structural intricacies, such as unit cell lengths and angles, atomic displacement, site fractions and isothermal parameters, as well as powder properties such as crystallite size and associated strains. An input file of similar symmetry to that manifested in the observed diffraction pattern simulates a 'calculated' pattern, according to a set of defined starting parameters. Each parameter is then sequentially set to refine using a least squares fitting method to minimise the difference between the calculated pattern and the observed pattern. Lattice parameter refinement is able to control peak positions whilst site fractions, coordinates and isothermal properties can influence the intensity associated to the calculated pattern's peaks. Crystallite size and strain will influence peak width, combined with the diffractometer optics (which are compensated for using an up-to-date instrument parameter file). When the difference between the observed and calculated pattern is minimised, the refined parameters can give a good indication of the structural properties of the irradiated samples.

4.2.2 X-ray Generation

The X-rays incident upon a material during XRD are generated via the electron bombardment of a metallic target and subsequent inelastic electron-electron collisions, all contained within an X-ray tube such as the one shown in figure 4.6 [236]. Electrons are emitted at the cathode via thermionic emission and are subsequently accelerated to high energies, typically up to 60 kV [237]. This electron beam bombards the core-shell electrons of the target atoms, Cu or Mo in this thesis, and the consequent inelastic electron-electron collision results in excitation of the core-shell electrons. After some period of time, these excited electrons relax back into the ground state, emitting the excess in energy between the excited and ground state as a characteristic X-ray. The energy and wavelength of the radiation can be termed K, L or M dependent on the electron transition occurring. For example, Kα radiation refers to electron decay from the L to K shell, whereas the Kβ radiation indicates the energy transition between the M and K shell. Within the L shell there are three quantum states from which the decay can occur, however selection rules limit the energy transition from the L to K orbitals, leaving two specific states – $K\alpha_1$ & $K\alpha_2$ wavelength radiation. This forms a Kα doublet where the intensity of $K\alpha_1$ is approximately twice that of $K\alpha_2$. These transitions are visualised in figure 4.7, whilst their energies and associated wavelengths are tabulated in table 4.3 [238].

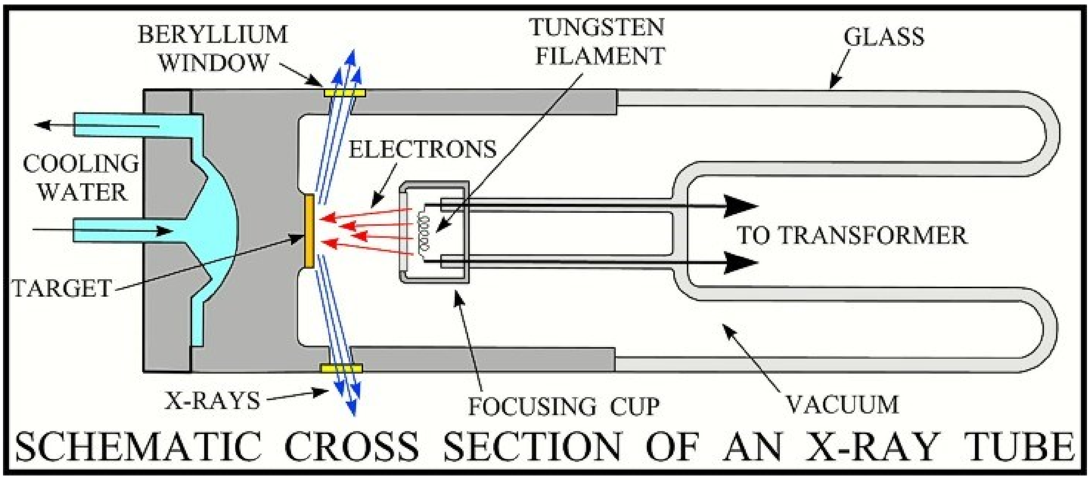

Figure 4.6: A schematic cross section of a typical X-ray tube. Reformatted from [236].

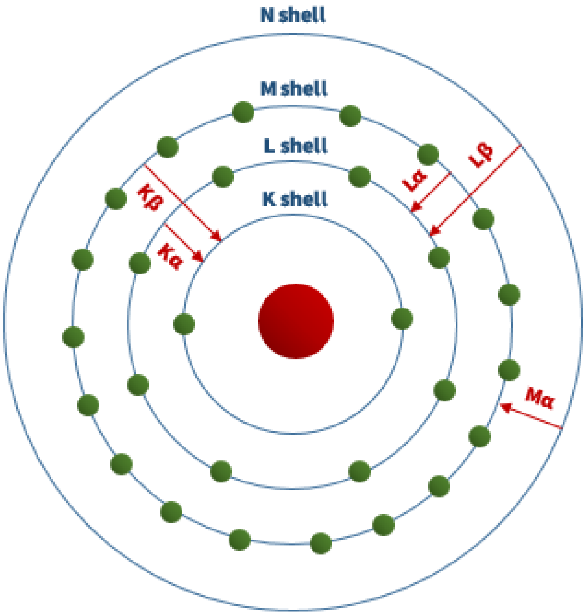

Figure 4.7: The energy level transitions associated with discrete wavelength characteristic X-ray emissions.

Table 4.3: Common radiation source orbital transitions, energies and associated wavelengths. [238]

Radiation	orbital Transition	Energy (KeV)	Wavelength (Å)
Cu-Kα_1	$2p_{3/2} \rightarrow 1s$	8.048	1.5405
Cu-Kα_2	$2p_{1/2} \rightarrow 1s$	8.028	1.5443
Cu-Kβ_1	$3p \rightarrow 1s$	8.905	1.3922
Mo-Kα_1	$2p_{3/2} \rightarrow 1s$	17.480	0.7093
Mo-Kα_2	$2p_{1/2} \rightarrow 1s$	17.375	0.7136
Mo-Kβ_1	$3p \rightarrow 1s$	19.608	0.6323

The wavelength of the X-rays that samples are irradiated with vary between diffractometers, with the variation in wavelength being useful for different applications. Larger wavelength radiation, such as Cu, will reduce the measurable d-space range but increase the observable separation between split peaks in diffractograms. This is particularly useful if unit cell lengths are similar in dimension. Conversely, smaller wavelength radiation, such as molybdenum or silver sources, offer a bigger measurable d space domain. This is useful for some compounds as high d-spacing peaks may reveal additional structural intricacies, where the scattering factor of some elements may become increasingly significant at higher d-space values. The selection of x-ray source should also conform to the elements present, accounting for the potential fluorescence or absorption effects some elements may induce within the sample.

The extent of energy transfer in such inelastic scattering events is wide ranging and results in the formation of a continuous wavelength (energy) emission spectrum. This, combined with the orbital transition energies, results in a photoemission spectrum resembling that in figure 4.8, which is specific to the photoemission spectrum of copper [239]. A spectrum of wavelengths is unnecessary since all of the structural information can be obtained from the diffraction of one incident wavelength. Additional wavelengths add unnecessary complexities to the diffraction pattern. Kβ radiation can typically be removed from incident radiation sources (or realistically, its intensity can be heavily attenuated) via the use of an appropriate material with an absorption edge between the Kα and Kβ wavelengths – for copper sources, a Nickel foil filter is typically used as its K-absorption edge (1.488 Å) lies between that of Kβ (λ_{mean}= 1.392 Å) and Kα (λ_{mean}= 1.542 Å). Its effect on attenuating this wavelength is shown in figure 4.8. Kα_2 cannot be removed from the Kα₁ in this manner. For truly monochromatic x-ray radiation, single crystals are often used. The preferentially cut crystals diffract the selected wavelength of radiation to be incident upon the sample. An example of a typical crystal used is Ge(111), cut along this plane as reflections with odd h values do not diffract (due to crystal symmetry (in Germanium, cubic Fd-3m) the unwanted wavelength λ/2 [9].

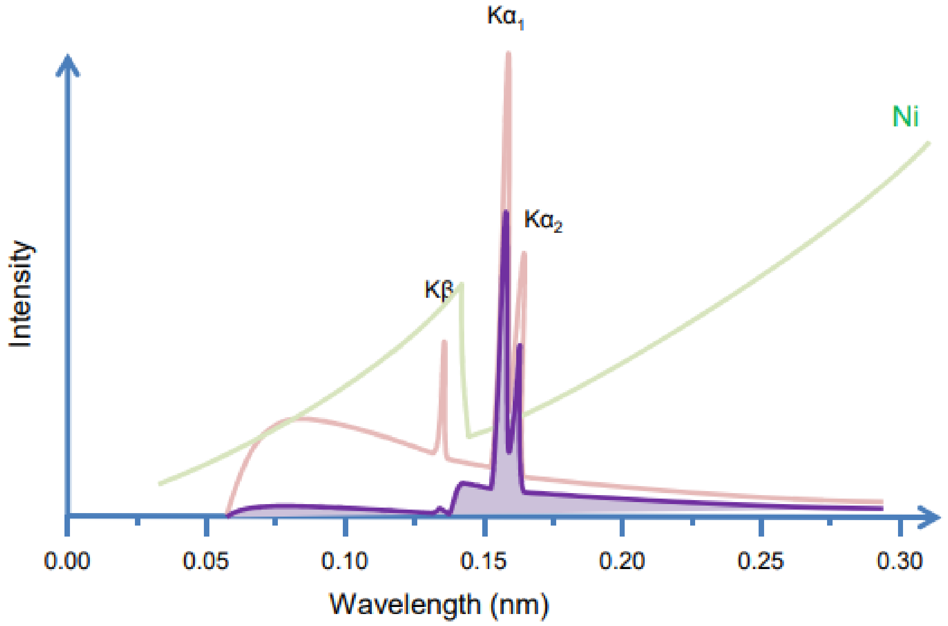

Figure 4.8: Emitted X-ray spectrum from a Copper tube before and after attenuation via a Nickel foil filter. b) The typical effect of Nickel filters on a diffraction peak using a copper source. Reformatted from [239].

4.3 Scanning Electron Microscopy

4.3.1 Electron-Matter Interactions

As a beam of electrons is incident upon the surface of a material, electron-atom interactions occur that result in momentum changes and associated energy variation of these incident electrons. These interactions are considered to be scattering events that are either elastic or inelastic in nature, depending on if energy is imparted into the irradiated material or not. A three-dimensional volume termed 'the interaction volume' is established beneath the surface of the irradiated material, shown in figure 4.9 [240], where different electron collisions result in the generation of energetically unique signals [241,242].

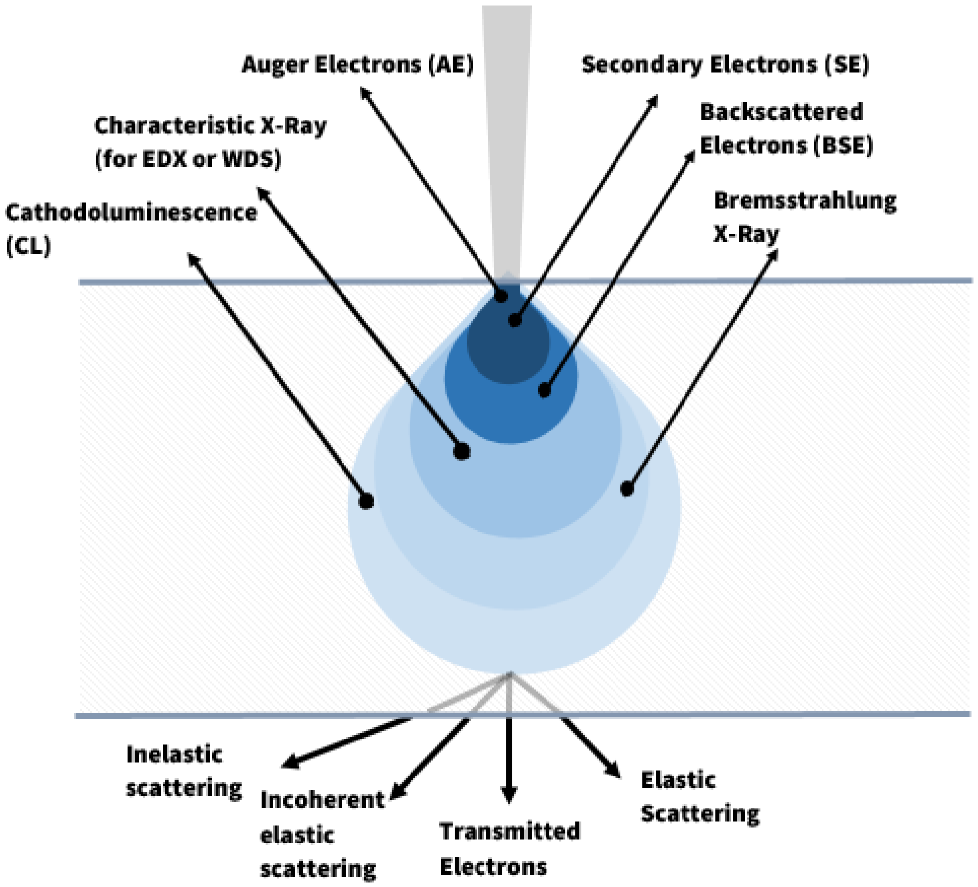

Figure 4.9: A generalised schematic illustrating a typical interaction volume for electron-matter interactions for an irradiated sample, showing the varied information depths of the different signals generated. Reformatted from [240].

Elastic scattering events describe electron-atom interactions that result in minimal (virtually no) energy exchange between the incident electrons and the sample. These interactions instead involve directional variation in the electron trajectory, a result of coulombic interactions between the incident electrons and the partially screened nuclei of the atoms [241,242]. This type of scattering is known as Rutherford scattering. It is unsurprising that the density of such scattering events (the elastic scattering cross section) is dependent upon the atomic number (Z) of the irradiated specimen. The majority of these directional changes are small, typically $< 5°$ [242], and whilst larger deflections of the primary beam can occur, those re-emergent from the surface as backscattered electrons are more commonly a function of multiple scattering events. Conversely, inelastic interactions involve significant energy transfer from the incident electrons with smaller angular deflections occurring, $< 0.1\ °$ [242]. The energy exchange between primary beam electrons and atoms produces a series of phenomena, ranging from phonon and plasmon wave excitation to secondary electron emission, Bremsstrahlung (or continuous wavelength) X-ray emission, Auger electron emission and characteristic X-ray emission [241,242].

It is important to recognize that both elastic and inelastic scattering events occur concurrently, and thus the interaction volume shown in figure 4.9 is a network of these varied interaction types. It is the diverse nature of the signals attainable from the interaction volume that gives the inherent versatility to electron microscopy techniques. Two types of signal used in SEM are secondary electron and backscattered electron signals, which will be discussed in more detail below.

Secondary electron (SE) emission is traditionally considered to consist of multiple steps: energy exchange between electrons as a result of an interaction event with an energy transfer sufficient for electron delocalisation, causing ionisation of electron shells. This is followed by the diffusion of these generated SEs to the surface and the subsequent exchange at the surface/vacuum interface. SEs are thereby formed from inelastic scattering events [241,242]. Numerous models propose the mechanism by which such SEs propagate through the material. These range from a single inelastic collision between the primary beam and a bound electron, or, via a cascading effect involving multiple SEs generated from an initial diffusing electron or a backscattered electron [241–243]. Regardless of the mechanism by which these electrons are generated, it is important to recognise that a significant amount of energy associated with the primary beam electron is expended in ionising the atom, and consequently the SEs emitted are inherently low energy electrons. 90 % of SEs are emitted with an energy < 10 eV [241]. The interaction depth for SEs is shallow for this reason [244], since a significant proportion of the SEs generated are of insufficient kinetic energy to reach the surface or escape the interface. Detectable signals are confined to a few nanometres beneath the surface of the material, however this varies according to the conductivity of the sample and are larger for insulating materials compared to metals, for example [244]. The yield of secondary electrons is dependent upon the angle of incidence between the primary beam and the irradiated sample and their intensity is much greater at the surface and edges of a sample. SEs can therefore be detected by appropriate semiconducting detectors, with the quantification of local SE intensities capable of producing a topographical image.

Backscattered electrons (BSE) result from large angle elastic scattering events involving the primary beam electrons, and thus have an inherently higher associated energy when compared to SEs. These result from a single columbic interaction with the charged nucleus of the atom, i.e. Rutherford scattering, or from the cumulative effect of sequential small angle scattering events of the incident primary beam electron [241,242,245]. As a result, the interaction depth of such scattering events protrudes further into the material. The columbic interactions with the nucleus gives BSEs an inherent sensitivity to atomic number, shown in figure 4.10 [241], suggesting this signal (its backscattered coefficient) can reveal local differences in atomic number and phase distributions within a sample. The interaction between scattered electrons of varied intensity and waveform will ultimately produce an interference pattern, producing contrasts in the overall image according to these local atomic numbers. Figure 4.10 indicates that there are limits to this elemental contrast however, with differences in backscattering coefficients smaller for elements of higher atomic number when compared to the differences between those of lower atomic numbers[241].

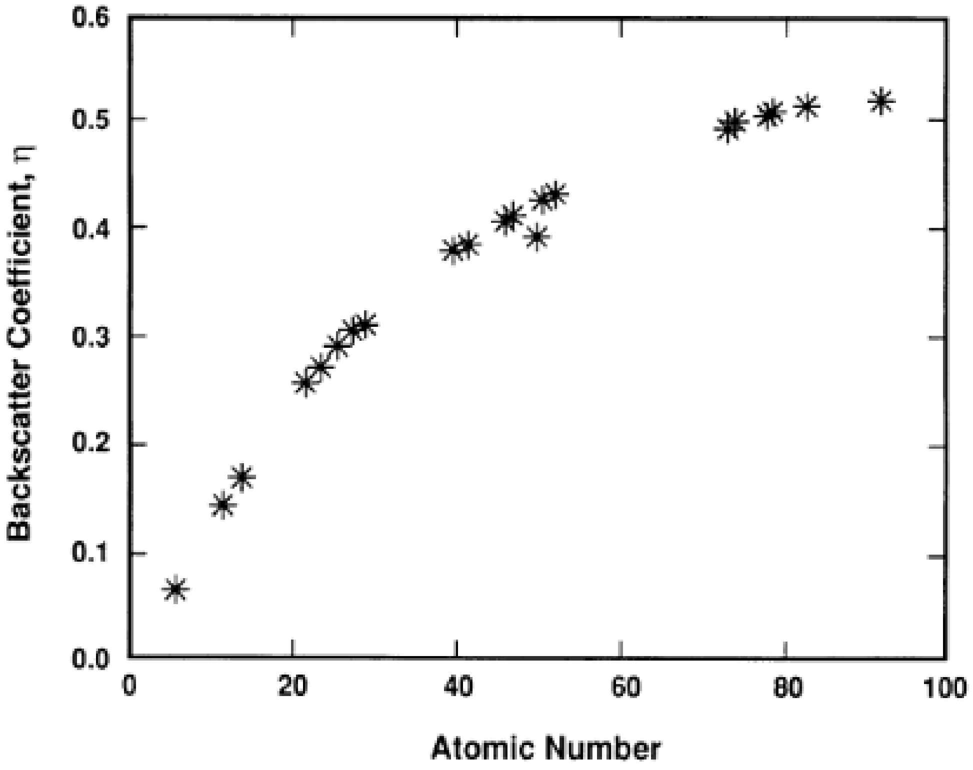

Figure 4.10: The dependence of backscattered coefficient on the atomic number of the scattering element. Reformatted from [241].

As alluded to, inelastic collisions can result in the emission of X-rays characteristic to the elements present in the sample. This radiation is emitted when a core shell becomes ionised, with electrons excited as a direct consequence of the primary beam energy transfer process. An electron-hole recombination process follows to stabilise the energy arrangement of the atom, with the difference in energy between the excited state and the ground state electrons emitted as a photon, of X-ray wavelength unique to the specific energy level transition. K,L,M transition lines were illustrated in figure 4.7. These characteristic X-rays can be used to qualitatively and quantitively analyse the elements present in the sample. Either the energy of the emitted photon or its associated wavelength can be used to identify elemental presence, with its relative concentration established via comparison between the intensity of the x-rays radiated from the sample and those of a known standard. This is, of course, a rather simplistic description of the process and makes multiple assumptions, such as a known efficiency for the photoemission process in the compositional/crystallographic environment occupied. It also assumes minimal primary electron interactions before photon emission and limited photon interactions after emission. In reality, it is necessary that ZAF corrections are made [241,242,246] - these are individual atomic number (Z), absorption (A) and Fluorescence (F) corrections - to accurately determine quantitative elemental distributions.

4.3.2 Energy Dispersive X-Ray Spectrometry

The utilisation of characteristic x-ray energies to identify the spatial distribution of elements within an electron irradiated area is referred to as energy dispersive x-ray spectroscopy (EDX or EDS). A semiconductor, traditionally Si-based, is used to detect the energy of incident photons emitted by the irradiated sample. The energy spectrum produced appears as that shown in figure 4.11 [247], and can subsequently be deconvoluted into a series of peaks corresponding to the elemental K, L or M type energy transitions for a specific element based on peak energy, as shown previously in figure 4.7. The intensity of the energy relative to a standard with known elemental composition and energy spectrum can yield a quantitative analysis of the amount of element present in the local irradiated area. The noticeable asymmetry associated with the energy transition peaks, sometimes appearing gaussian, is due to the insufficient resolution of the detector (typically between 120-140 eV) to resolve the sub-orbital transitions from each other – such as separating Kα1 and Kα2 from one another [242,248].

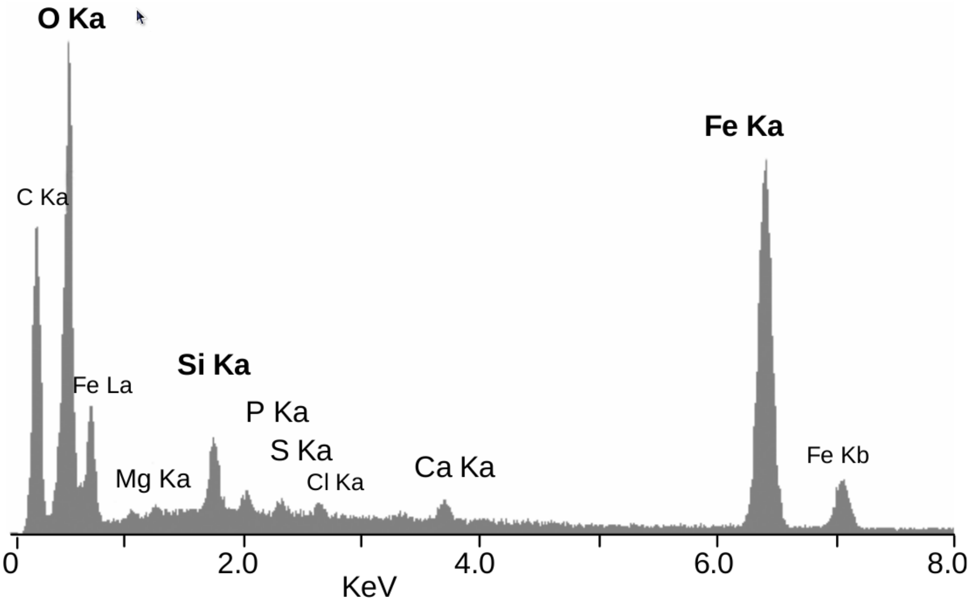

Figure 4.11: A typical energy spectrum for EDX, with peaks indicating the electron transitions within the elements composing the sample surface [247].

Since it is based on the inelastic collisions of electrons, EDX is inherently a surface analysis technique. Defining elemental distributions throughout the volume of the sample is not possible. It is also worth noting that given elemental identification occurs based on incident photon energy (as opposed to its associated wavelength, such as in wavelength dispersive spectroscopy WDS), erroneous results can occur based on the overlap of similar x-ray energies from the orbital transitions of different elements present. Furthermore, elements with low atomic numbers (Z<10), such as lithium, are difficult to detect based on the absorption of the emitted photons by the Beryllium detector window, or 'heavier' elements within the sample [241]. The contribution of the continuous wavelength radiation emitted from the electron-matter interaction adds a background energy to the EDX spectrum, producing low signal to noise ratios and resulting in relatively poor elemental detection limits of around 1000 ppm (~0.1 wt.%) [248] – although this can be reduced with increasing counting time, which is often of the order of minutes.

4.3.3 Electron Probe Micro Analysis & Wavelength Dispersive Spectrometry

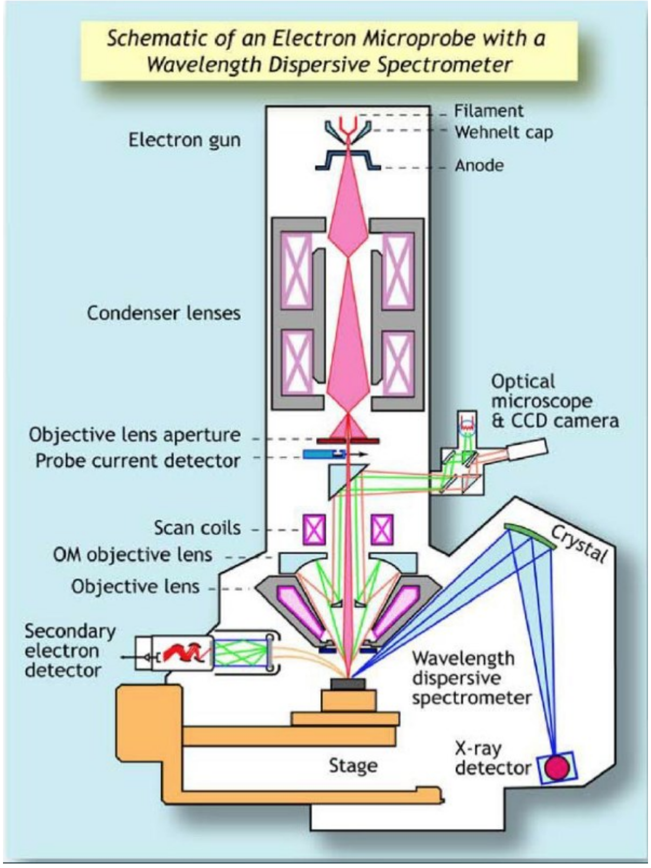

Figure 4.12: A schematic showing the significant components of an EPMA utilising WDS. Reformatted from [249].

Another method of quantitatively analysing elemental distributions within a sample is via wavelength dispersive spectroscopy (WDS). Similar to EDX in utilising the photo-emitted characteristic X-rays, it instead uses appropriately orientated crystals to selectively diffract the characteristic photons of interest, based on the expected associated wavelength. WDS is used within Electron Probe Micro Analysers (EPMA), with the principle of WDS shown schematically in figure 4.12 [249].

Devices often contain up to 5 crystals, each with varied d-spacings providing a diffraction range broad enough to selectively diffract a wide range of possible wavelengths associated with most elemental energy transitions. Having a finite number of crystals limits the number of elements that can be quantified simultaneously, unlike EDX which can quickly quantify all of the elements present in the surface composition (with the exception of the low atomic number elements as referenced previously), with a reasonable degree of accuracy. The isolation of photons via diffraction avoids the issues of overlapping energy often present in EDX spectra and inherently exhibits a significantly greater spectral resolution when compared to EDX. Not only this, but WDS offers greater signal to noise ratios and lower detection limits compared to EDX, with low atomic number elements readily analysed. Hence, utilising WDS within an EPMA is typically for a more accurate quantification of elemental distributions when the composition and phase structure is qualitatively understood. EDX and WDS techniques are complimentary with EDX being able to provide this prerequisite understanding of the composition of a specimen and WDS being able to accurately determine quantitative distributions.

4.4 Impedance Spectroscopy

4.4.1 Introduction

Impedance Spectroscopy (IS) is a technique in which the electrically-active regions of a physical microstructure can be probed. It relies on the variation of phase and associated magnitude between an applied voltage and a measured current across a broad frequency range, producing a complex impedance, a result of a material exhibiting polarisable, non-ideal resistor behaviours. This observed complex impedance response can be deconvoluted into a network of ideal resistors (R), capacitors (C) and inductors (L), whose connectivity is representative of physical charge dissipation and displacement processes that occur as the material is perturbed by the applied ac voltage. This electrical circuit that forms is representative of the electrically active physical components of the sample, and is called the equivalent circuit for this reason. Should a material exhibit an electrically heterogeneous microstructure, provided components of the circuit exhibit sufficiently disparate relaxation times [250], they can become distinguishable and independently identifiable as the complex impedance is plotted and mathematically weighted towards different R and C magnitudes. This relaxation time is governed by a time constant (τ), which is a product of the resistance (R) and capacitance (C) representing an equivalent circuit element, equation 4.2:

$$\tau = RC \tag{4.2}$$

Equivalent circuit analysis in IS is complimentary to physical microstructural observation techniques, such as SEM and EDX, and can facilitate the assignment of physical elements to a material's electrical response. The ability to perform IS measurements under varied conditions allows for the evolution of the material's equivalent circuit and its physical dependencies to be understood. IS measurements taken across broad temperature ranges allows for the temperature dependence of conductivities to be quantified. Variation of time constants with oxygen partial pressure, pO_2, is a technique capable of isolating the charge carrier type conducted through the sample, should conduction be electronic. For example, n-type conductivity may be deduced from an increase in conductivity (decrease in time constant) of an electrically active region in a reducing, low pO_2 atmosphere. Use of appropriate blocking electrodes provide the capability of identifying ionic conduction within a sample, a result of the capacitive elements they introduce within an equivalent circuit.

Since this work is focused primarily on dielectrics (with the potential for ionic conduction within the A site deficient perovskites of results chapter 4), inductive effects are not likely to contribute to the overall impedance response and so will not be discussed within this section. In order to derive the overall impedance associated with equivalent circuits, derived from [251,252], it is first necessary to derive the impedance response of the ideal capacitors and resistors that will construct it.

4.4.2 Derivation of ideal component impedances:

Ideal Resistor, R

For an ideal resistor, the voltage across and current through the resistor are in phase. The phase difference between the two sinusoidal current and voltage waves, φ, is 0 °. The time dependent voltage $V(t)$ is given in equation 4.3, based upon its maximum amplitude (V_0) at zero time, signal frequency (ω) and time (t)

$$V(t) = V_0 Sin(\omega t) \tag{4.3}$$

The time dependent current, $I(t)$, through an ideal resistor of resistance R is given by equation 4.4 relating to its maximum current amplitude I_0

$$\mathrm{I}(t) = I_0 Sin(\omega t) = \frac{V_0 \mathrm{Sin}(\omega \mathrm{t})}{\mathrm{R}} \tag{4.4}$$

The impedance, Z*, for an ideal resistor follows Ohm's law, and is given in equation 4.5. This impedance is real with no imaginary component:

$$\mathrm{Z}^* = \frac{\mathrm{V(t)}}{\mathrm{I}(t)} = \mathrm{R} \tag{4.5}$$

Ideal Capacitor, C

An ideal capacitor with an I-V response consistent with that shown in blue for figure 4.13 is considered. The time dependent charge, q(t), on the capacitor plates is given by equation 4.6, and is a function of the materials capacitance, C, and the time dependent voltage applied across its plates:

$$q(t) = CV(t) = CV_0 sin(\omega t) \tag{4.6}$$

The time dependent current can then be derived according to equation 4.7:

$$I(t) = \frac{dq}{dt} = \omega C V_0 cos(\omega t) = \omega C V_0 sin\left(\omega t\ + \frac{\pi}{2}\right) \tag{4.7}$$

$$Since\ cos(x) = sin(90° + x)$$

Thus, for an ideal capacitor, the current leads the voltage by a phase difference of φ = 90 °. Physically, current is required to flow to/from the electrodes of the capacitor for a potential difference to be established across the device. Considering Euler's relation, equation 4.8, equations 4.6 and 4.7 can be represented alternatively and the impedance of an ideal capacitor can be defined as purely imaginary, equation 4.10. Specifically, the imaginary impedance is referred to as an ac reactance, X_c. Based on equation 4.10 it is clear that an ideal capacitor is completely blocking to dc signals, as its reactance is infinitely large as the frequency of the applied signal tends to 0 rads^{-1}.

$$e^{jt} = \underbrace{cos(t)}_{Re} + j\,\underbrace{sin(t)}_{Im} \tag{4.8}$$

$$q(t) = CV_0 Im\left(e^{j\omega t}\right) \therefore I(t) = \frac{d\left(CV_0 Im\left(e^{j\omega t}\right)\right)}{dt} = CV_0 Im\left(j\omega e^{j\omega t}\right) \tag{4.9}$$

$$Z^* = \frac{V(t)}{I(t)} = \frac{V_0 Im\left(e^{j\omega t}\right)}{CV_0 Im\left(j\omega e^{j\omega t}\right)} = \frac{1}{j\omega C} = -\frac{j}{\omega C} \tag{4.10}$$

The phase differences between voltage and current for ideal resistors (red) and ideal capacitors (blue) are shown in figure 4.13 a). The frequency dependence of impedance for these same components is shown in figure 4.13 b).

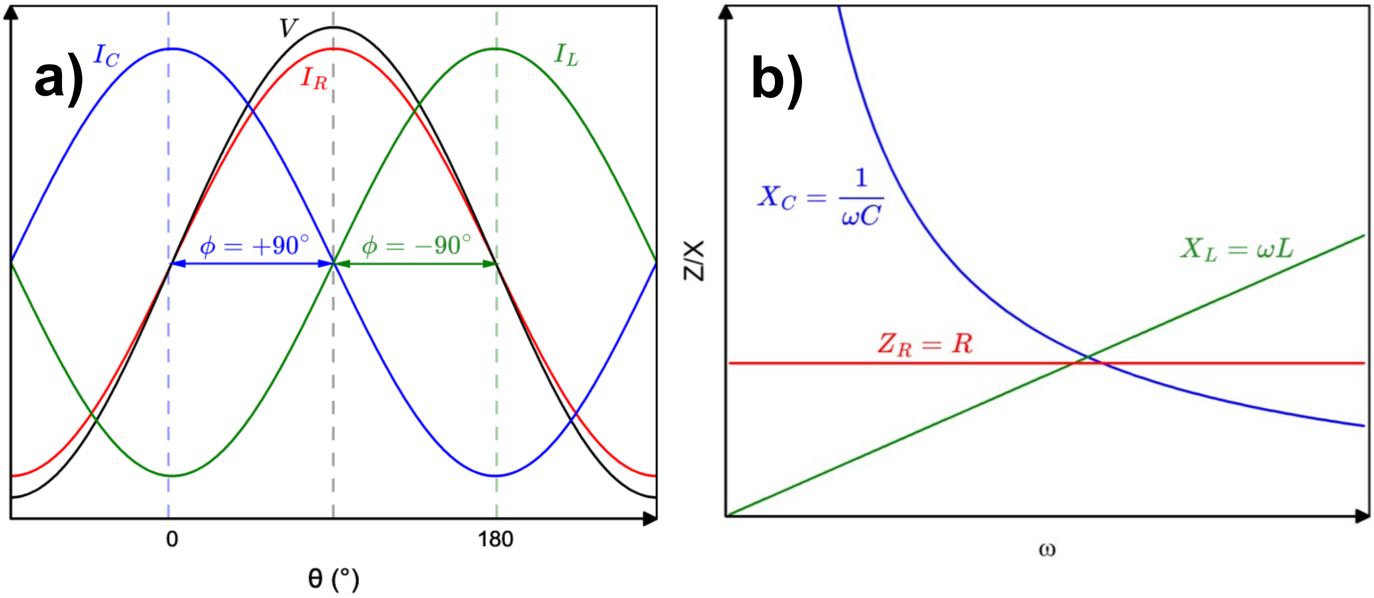

Figure 4.13: a) The typical phase differences between current and voltage (black) associated with an ideal resistor (red), capacitor (blue) and inductor (green). b) the impedance (or reactance) variation of these ideal components with frequency.

4.4.3 Impedance Formalisms & Equivalent Circuit Analysis

In reality, materials are not considered ideal resistors nor ideal capacitors but a network of the two, as the phase difference between current and voltage is not ± 90 ° nor is it frequency independent. The ability to fit appropriate equivalent circuits to a material's complex impedance response permits for the potential deconvolution of this response into components that constitute the 'electrical microstructure', and represent different electro-active regions of the physical microstructure. This is based on the condition that these different electro-active regions exhibit sufficiently different relaxation times , becoming distinguishable from one another. It is also important to emphasise that not all regions of a physical microstructure are electro-active in the temperature and frequency domain probed. The electrical microstructure is unique to a material and the conditions used.

As described previously, these equivalent circuits can be derived from a materials spectroscopic impedance response as a network of series or parallel arrangements of ideal resistors, capacitors and/or inductors. The ability to do so lies in the frequency dependent behaviour of such components which when connected appropriately can match the impedance response observed. Physically, a resistor may be considered to represent an energy dissipative response as current flows through the material, such as the energy dissipated in the re-orientation of dipoles, an 'inelastic' energy transfer process. The reactance of a capacitor is elastic in nature as energy is stored rather than dissipated, and may represent a polarisation mechanism instead (a charge separation).

It is worth noting that provided there are more than two elements in the equivalent circuit, it is possible to re-arrange the order of such elements and change their respective values and still fit the experimentally observed data [252]. It is often possible to fit the impedance response with multiple equivalent circuits. Hence, IS is often considered a secondary technique and pre-requisite knowledge of the microstructure, elemental and phase distributions via SEM and EDX analysis is complimentary. In accordance with an observed microstructure and the material investigated, the component values assigned should then be realistic. A useful effect inherent of the nature and size of an electrically-active component is the magnitude of its capacitance. Given capacitance is inversely proportional to the thickness of the material (equation 2.8), thinner components of the electrical microstructure, such as space charge or depletion layers, will have an inherently higher capacitance. This capacitance will be orders of magnitude greater than the capacitance associated with a bulk (grain) response. Table 4.4 is an example of the magnitudes of capacitance consistent with common electrically-active components often contributory to the electrical microstructure:

Table 4.4: The typical capacitance magnitudes associated with typical electrically-active regions of an 'electrical microstructure'. Reformatted from [250]

electrically-active Region	Typical Capacitance Magnitude (Fcm^{-1})
Bulk Ceramic	10^{-12}
Secondary Phase	10^{-11}
Grain Boundary	10^{-11} - 10^{-8}
Surface Layer	10^{-9} - 10^{-7}
Sample-electrode interface	10^{-7} - 10^{-5}
Electrochemical Reaction	10^{-4}

It is these magnitudes of the derived capacitances for the equivalent circuit elements which can then be used as an indicator to the physical component this element represents.

Impedance can be converted to other 'immittance' formalisms via the conversions shown in table 4.5. Although it is the same data being represented slightly differently, it is useful to do so for the weightings characteristic to each formalism. For example, Impedance is dominated by an element with the greatest impedance whereas the electric modulus may be dominated by the element with the smallest capacitance. This means that in an equivalent circuit containing multiple elements, such as two parallel RC elements in series (each with different R and C values), when overlaid these Z'',M'' spectroscopic plots can reveal two distinct time constants based on the differencing frequencies corresponding to peak maxima, f_{max}. The Z'' peak is dominated by the highest resistance resistor and the M'' peak is dominated by the smallest capacitor. Z* and M* are considered to be complementary to each other in the weightings that they offer to capacitance and impedance and are usually analysed on an overlapping spectroscopic plot involving these aforementioned imaginary components.

Table 4.5: The relationship between the immittance formalisms used to analyse the spectroscopic data. Reformatted from [252]

Formalism Name	Relation
Impedance, Z*	Z^*
Admittance, Y*	$[Z^*]^{-1}$
Electric Modulus, M*	$j\omega C_0 Z^*$
Permittivity, ε*	$[M^*]^{-1} = [j\omega C_0]^{-1} Y^*$

The complex impedances for common equivalent circuit components are discussed below, alongside expected frequency responses for the formalisms discussed in table 4.5.

Series RC

An ideal dielectric (one with no leakage current, perfectly insulating) can be considered as a series combination of a resistor and a capacitor, as represented in figure 4.14:

Figure 4.14: A series resistor-capacitor combination, often used to represent an ideal dielectric.

This would indicate a charge displacement mechanism, where the resistor can be interpreted as a local ac conductivity that is induced by the orientation of charge and local dipole formation. The capacitance is then equivalent to the polarisation induced by the dipole moment formed. Since an ideal dielectric exhibits no leakage current the resistor is not parallel with the capacitor. As the components are in series, the total impedance of the circuit can be derived by addition of the *impedance* of each individual component, remembering the complex nature of such – the impedance of a resistor is real whilst that of the capacitor is imaginary. The complex impedance of a series RC component is given in equation 4.11.

$$Z^{*} = R - j \cdot \frac{1}{\omega C} \tag{4.11}$$

Where its real and imaginary components are given as:

$$Z' = R, \quad Z'' = \frac{1}{\omega C} \tag{4.12}$$

It is clear that the real component of impedance is not frequency dependent and remains constant, equal to the resistance of the resistor. The reactance is inversely proportional to frequency, and so the resulting complex Z* plot is a vertical line, as shown in figure 4.15. The electric modulus of the circuit can be defined according to the relationship shown in table 4.5. This means that its real and imaginary components are given in equations 4.13 and 4.14, respectively.

$$M' = \omega C_0 Z'' = \frac{\mathrm{C_0}}{\mathrm{C}} \tag{4.13}$$

$$M'' = \omega C_0 Z' = \omega R C_0 \tag{4.14}$$

where C_0 is equal to the capacitance of the empty cell. The proportionality between the real component of Z* and the imaginary component of M* arises due to the multiplication by the imaginary number, j. The admittance of the series RC circuit is derived according to equation 4.15:

$$Y^* = [Z^*]^{-1} = \left[\mathrm{R} - \frac{\mathrm{j}}{\omega\mathrm{C}}\right]^{-1} \tag{4.15}$$

$$= \left[\frac{\omega RC - j}{\omega C}\right]^{-1} = \frac{\omega C}{\omega RC - j} \cdot \left[\frac{\omega RC + j}{\omega RC + j}\right] = \frac{\omega C[\omega RC + j]}{1 + [\omega RC]^2}$$

$$Y^* = \frac{1}{R} \cdot \left[\frac{[\omega RC]^2}{1 + [\omega RC]^2}\right] + \frac{j}{R} \cdot \left[\frac{[\omega RC]}{1 + [\omega RC]^2}\right]$$

Again, from the relationships between formalisms given in table 4.5, the complex permittivity is then derived as according to equation 4.16:

$$\varepsilon^* = [j\omega C_0]^{-1} \cdot Y^* \tag{4.16}$$

with its real component calculated according to equation 4.17:

$$\varepsilon' = \frac{1}{\omega C_0} \cdot \frac{\omega RC}{1 + [\omega RC]^2} = \frac{C}{C_0} \cdot \left[\frac{1}{1 + [\omega RC]^2}\right] \tag{4.17}$$

which tend to the following limits with frequency:

$$\omega \to 0 \Rightarrow \varepsilon' \to \frac{C}{C_0}, \omega \to \infty \Rightarrow \varepsilon' \to 0$$

likewise, the imaginary component can be described according to equation 4.18:

$$\varepsilon'' = \frac{1}{\omega C_0} \cdot \frac{1}{R} \cdot \left[\frac{[\omega RC]^2}{1 + [\omega RC]^2}\right] = \frac{C}{C_0} \cdot \left[\frac{[\omega RC]}{1 + [\omega RC]^2}\right] \tag{4.18}$$

$$\varepsilon''_{max}\ when\ \omega RC = 1\ \therefore \varepsilon''_{max} = \frac{C}{2C_0}$$

The immittance formalisms and their spectroscopic and complex frequency dependencies are shown in figure 4.15. A clear Debye peak can be seen for the imaginary components of admittance and permittivity when they are plotted spectroscopically. Of course, Debye peaks are of significance in ac responses as such a response is frequently used to describe the relaxing out of dipole reorientations or domain switching as frequency increases (although it must be considered that the ‘real’ mechanisms in real crystallographic environments are often more complicated than this idealistic response). For an ideal series RC circuit, the full width half maximum (FWHM) of these peaks would be equal to 1.144 decades of frequency. In reality, most Debye peaks are wider and asymmetric, and although this may indicate the presence of heterogeneity and a more complicated equivalent circuit, such variations in peak shape more likely characterise a universal departure of IS responses from ideality.

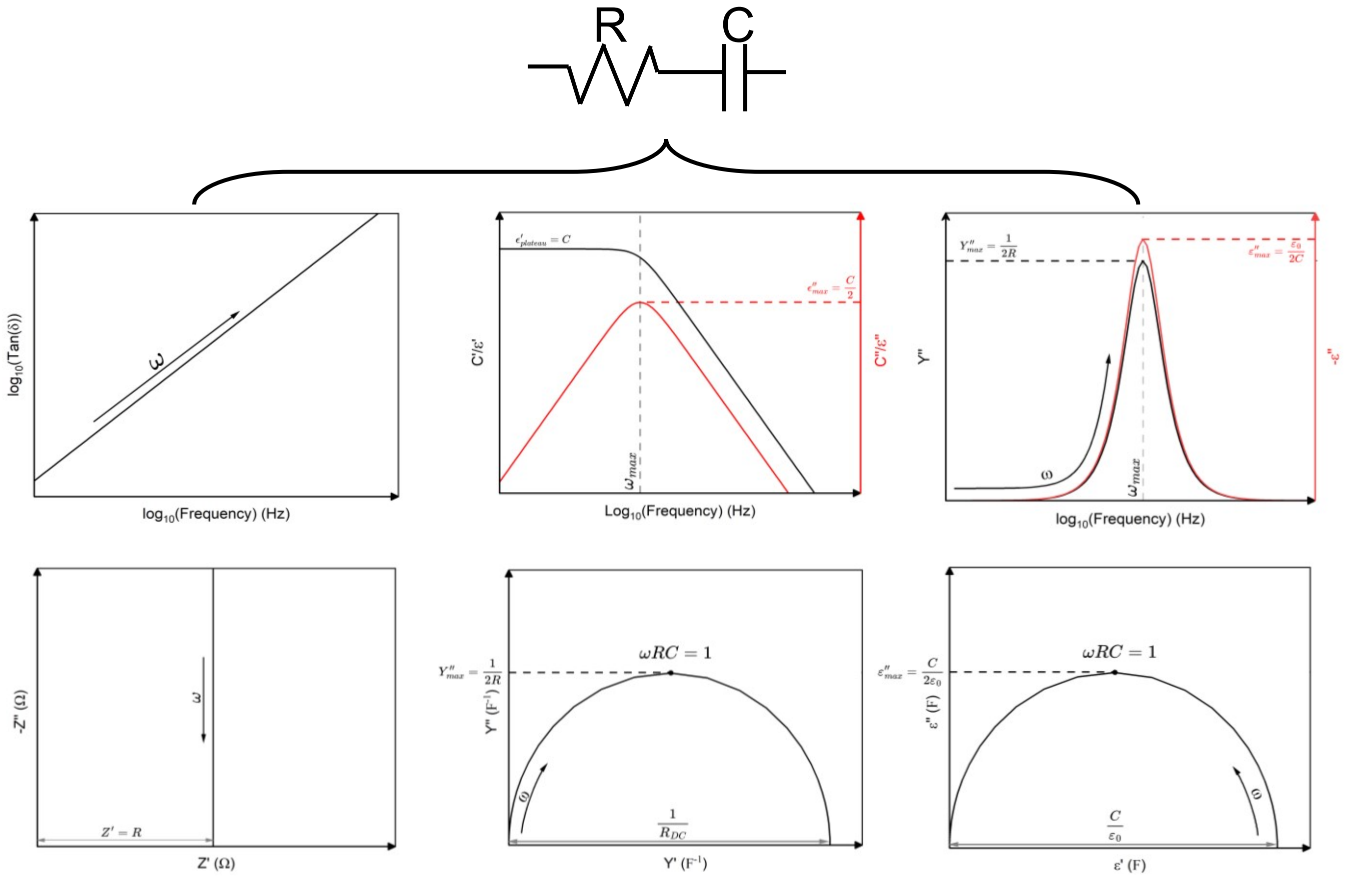

Figure 4.15: Some immittance formalisms for a series RC circuit and their observed frequency responses, plotted spectroscopically and in the complex plane.

Parallel RC Circuit

A parallel RC circuit, as shown in figure 4.16, is more frequently used to represent an electrically-active region, such as a grain bulk, and accounts for the realistic leakage current that occurs within semiconducting materials.

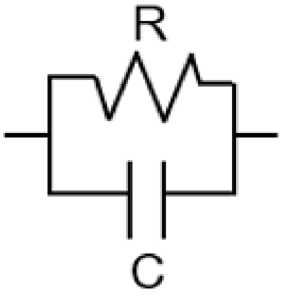

Figure 4.16: A parallel resistor-capacitor combination, commonly used in equivalent circuits to represent real components where some form of loss, such as leakage current, occurs simultaneously with polarisation responses.

It is the repeat unit in the equivalent circuit of the brick work layer model often used to represent the electrical microstructure of ceramics with multiple electrically active features, figure 4.18. As the resistor and capacitor are in a parallel configuration, calculating the total impedance of the system begins with the addition of the admittances of each component. Since the impedance of the resistor and capacitor are as follows:

$$Z_R = R, Z_C = \frac{1}{j\omega C} \tag{4.19}$$

then the total admittance of the parallel RC configuration can be given as equation 4.20:

$$Y^* = \frac{1}{R} + j\omega C \;\therefore Y' = \frac{1}{R}, Y'' = \omega C \tag{4.20}$$

Using the immittance relations in table 4.5, the complex impedance of the parallel RC element can then be calculated according to equation 4.21:

$$Z^* = [Y^*]^{-1} = \frac{R}{1 + j\omega RC} \tag{4.21}$$

$$Z^* = \frac{R}{1 + j\omega RC} \cdot \frac{[1 - j\omega RC]}{[1 - j\omega RC]} = \frac{R}{1 + [\omega RC]^2} - j \cdot \frac{\omega R^2 C}{1 + [\omega RC]^2}$$

$$Z' = \frac{R}{1 + [\omega RC]^2}, Z'' = R \cdot \frac{\omega RC}{1 + [\omega RC]^2}$$

A Debye type response can clearly be associated with the imaginary component of total impedance, as shown on the associated spectroscopic plot in figure 4.17. The electric modulus, along with its real and imaginary terms, can then be derived with the associated limits:

$$M^* = j\omega C_0 Z^* = j\omega \mathrm{C}_0 \left[\frac{R}{1 + [\omega RC]^2} - j \cdot \frac{\omega R^2 C}{1 + [\omega RC]^2}\right] \tag{4.22}$$

with the real component expressed as:

$$M' = \omega C_0 Z'' = \omega C_0 R \cdot \frac{\omega RC}{1 + [\omega RC]^2} \tag{4.23}$$

$$\omega \to 0 \Rightarrow M' \to 0$$

$$\omega \to \infty \Rightarrow M' \to \frac{\omega^2 C_0 R^2 C}{\omega^2 R^2 C^2} = \frac{C_0}{C}$$

likewise, the imaginary term can be derived:

$$M'' = \omega C_0 Z' = \frac{\omega C_0 R}{1 + [\omega RC]^2} = \frac{C_0}{C}\left[\frac{\omega RC}{1 + [\omega RC]^2}\right] \tag{4.24}$$

$$M''_{max} \Rightarrow \omega RC = 1 \therefore M''_{max} = \frac{C_0}{2C}$$

Some of the immittance formalisms and their associated spectroscopic and complex plane plots are shown in figure 4.17. It is noticeable that similar responses are observed in a parallel RC configuration as with a series RC circuit, but for a different set of formalisms. Both configurations feature semi-circle arcs in complex planes. For a series RC circuit this occurs for Y*, ε* whereas for a parallel RC circuit it occurs in for Z*, M*. The Debye peak seen in Y", ε" for a series configuration is now seen in Z", M" for a parallel one. It is noticeable that such peaks occur at a consistent frequency, associated with the time constant τ of the element, equal to the product of R and C, given back in equation 4.2.

For many elements in an equivalent circuit, the time constant of the electrically-active component may not be within the measurable frequency domain. It is common with IS measurements to vary temperature incrementally to change the resistivity of the component, thereby moving any Debye peaks or semicircles into the measurable frequency domain. Heating the sample (non-metallic) will reduce its resistivity and associated time constant, shifting any Debye peaks to the right (f_{max} moves to higher frequencies). This is necessary for the relatively resistive components of the equivalent circuit. Conversely, cooling the sample allows for the observation of more conductive equivalent circuit components with an increase in time constant.

The DC resistance of this parallel RC element can be calculated in multiple ways – the simplest of which is from the diameter of the semi-circular Z* arc in its complex plane. Alternatively, it can be calculated directly or indirectly from the peaks of either the Z" or the M" spectroscopic plots, respectively. The latter is often used and involves calculating the effective capacitance of the circuit element and using the relation that holds at M''_{max}:

$$\omega RC = 1 \tag{4.25}$$

The DC conductivity is then calculated from the inverse of the resistivity, having corrected the resistance for the geometry of the sample. This highlights how IS can be used to identify the temperature dependence of DC conductivity, through analysis of the equivalent circuits evolution (arc diameter, peak heights and positions) with temperature, be it an Arrhenius-type temperature dependence or otherwise.

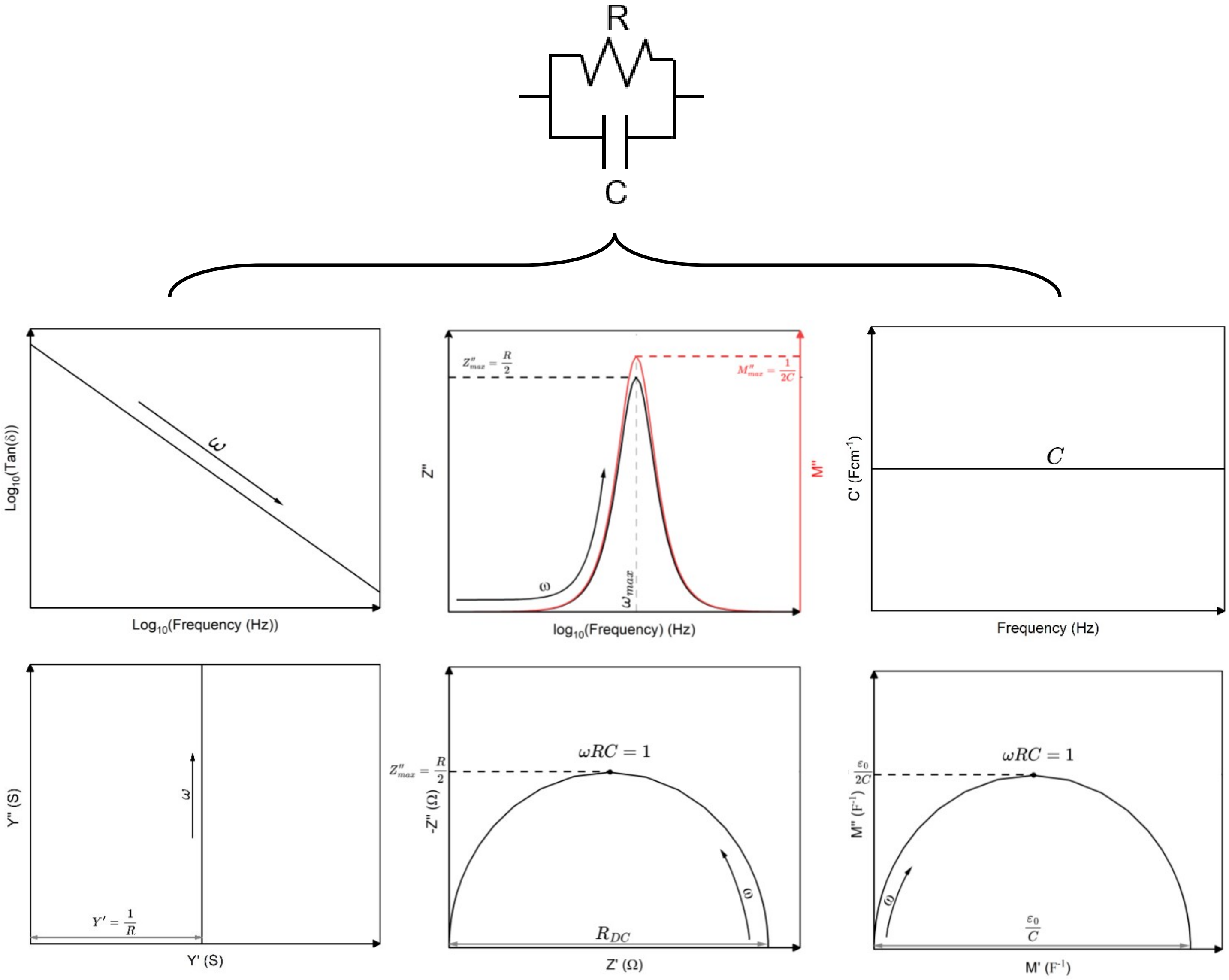

Figure 4.17: Immittance formalisms for a parallel RC circuit and their observed frequency responses, plotted spectroscopically and in the complex plane.

2 Parallel RC elements in Series

As stated previously, 2 parallel RC elements connected in series is an equivalent circuit often associated with the conventional brick work layer model used to represent a typical ceramic microstructure. This is one consisting of electrically-active grains and grain boundaries of differing resistivities, figure 4.18. The two parallel RC elements are connected in series since the current must sequentially flow through each of these electrically active features. This series connection of parallel RC elements is not reserved for a grain-grain boundary electrical microstructure, but anywhere where two electrically-active regions are probed sequentially across the frequency range investigated and exhibit distinct, varied time constants. Compositional heterogeneity, such core-shell grain structures with an associated distribution in resistivities, could equally be modelled by this equivalent circuit type, as could the formation of Schottky barriers at grain boundaries or at electrode interfaces – where drastically different capacitance magnitudes would exist between each parallel RC component.

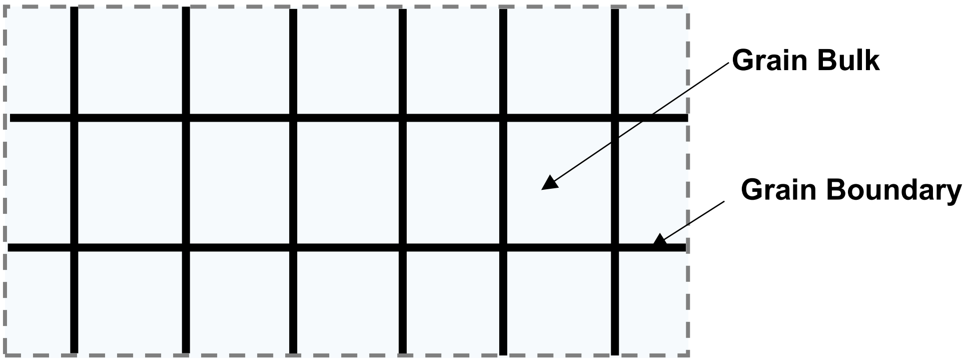

Figure 4.18: A brick work layer model typical of grain-grain boundary electrical microstructures.

Since in series, the total impedance of *each* parallel RC element is added together to give the total impedance of the equivalent circuit:

$$Z^* = Z^*_{RC1} + Z^*_{RC2} \tag{4.26}$$

The real part of the complex impedance and its limits derived as:

$$Z' = \frac{R_1}{1 + [\omega R_1 C_1]^2} + \frac{R_2}{1 + [\omega R_2 C_2]^2} \tag{4.27}$$

$$\omega \to 0 \Rightarrow Z' \to \mathrm{R}_1 + \mathrm{R}_2, \omega \to \infty \Rightarrow Z' \to 0$$

Whereas the imaginary component of the impedance can be derived as:

$$Z'' = R_1 \cdot \frac{\omega R_1 C_1}{1 + [\omega R_1 C_1]^2} + R_2 \cdot \frac{\omega R_2 C_2}{1 + [\omega R_2 C_2]^2} \tag{4.28}$$

The equations for the electric modulus and other formalisms become relatively large and are not derived here.

When considering an equivalent circuit where $R_1<R_2$ and $C_1<C_2$, two distinct semi-circle arcs occur in Z*, each corresponding to one of the parallel RC elements – with the largest diameter arc corresponding to the RC element with the largest resistance (R_2), figure 4.19. There are also two clear plateaus in the C' response – each associated with the respective capacitance for the RC element it represents. The higher C' plateau represents C_2 in this case, with C_1 corresponding to the lower plateau. Two more arcs occur in M*, with the largest capacitance (C_2) associated with the largest diameter arc in this case.

It is then noticeable that two distinct peaks are visible in the overlaid Z'', M'' spectroscopic plot, with the distinct time constants of each parallel RC element manifested in the separate f_{max} of these peaks. The inherent weightings of Z'' and M'' to resistance and capacitance, respectively, means that the R_1C_1 element that would otherwise have been overlooked in Z'' can be identified in the separate M'' peak. This highlights the complimentary nature of these formalisms when plotted together. From figure 4.19, only one peak can be seen for M'' whereas two peaks are visible for Z''. This is due to the difference in the magnitude of capacitances for C_1 vs C_2 being much greater than that of the difference in resistances, R_1 vs R_2.

Should a material have two (or more) RC elements with similar time constants (RC combinations), the effect would be of a single f_{max}, with one or more of these Z'' or M'' Debye peaks potentially being asymmetric or having a broad FWHM (depending on the respective R and C values of each element). Thus, identifying sample heterogeneity and associating electrical properties to each region is highly dependent on the respective time constants of each element – it is not always possible to separate the contributory features of an electrical microstructure as a result.

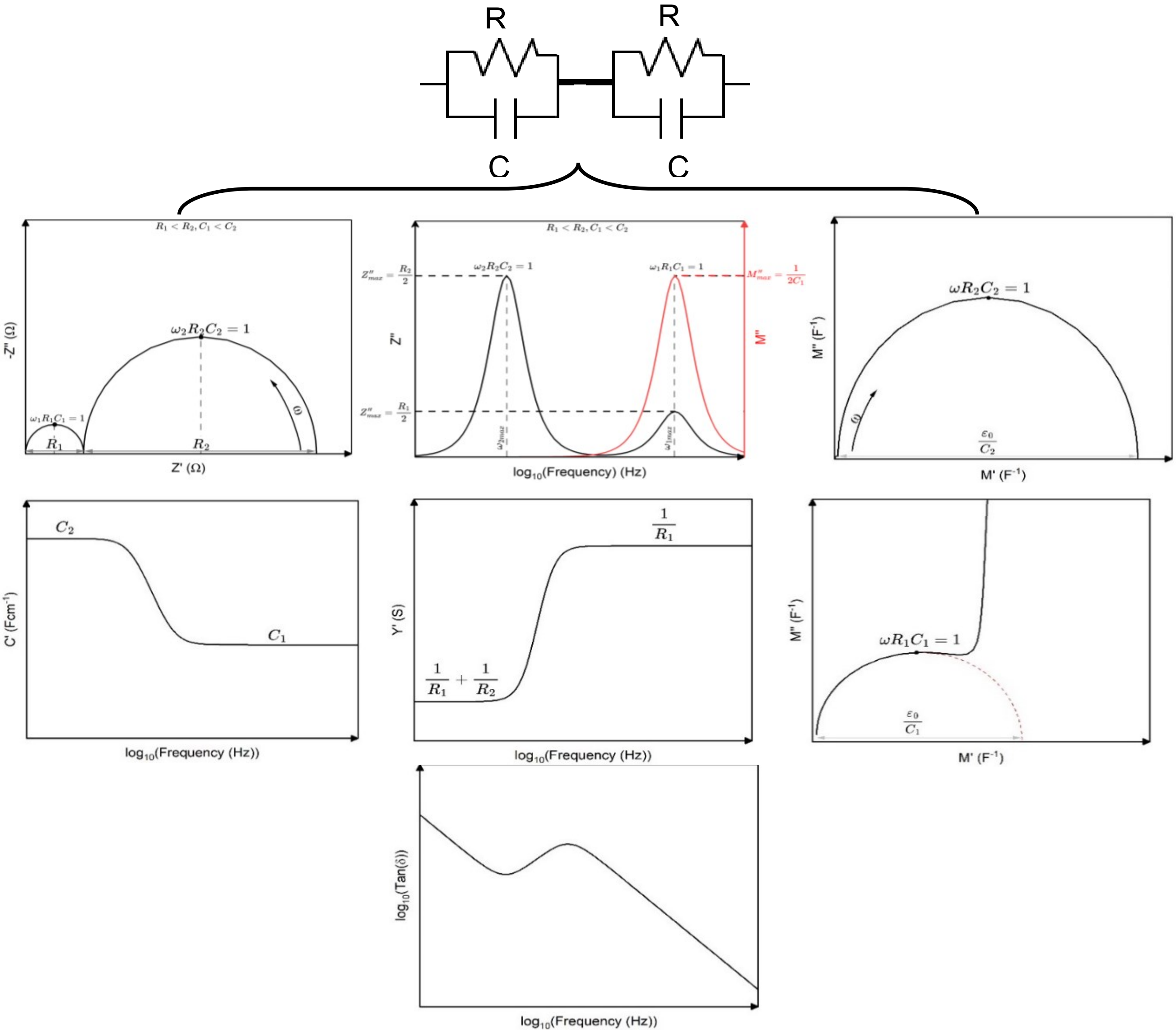

Figure 4.19: Immittance formalisms associated with two parallel RC elements connected in series.

4.4.4 Constant phase element (CPE)

The previous derivations for equivalent circuit impedance (and other immittance formalisms) assume frequency independence for the R and C components. In reality, this is not the case and the resulting effect is that the equivalent circuit elements discussed above (e.g. parallel or series RC elements) are insufficient to characterise the spectroscopic impedance responses of the real materials measured. For a parallel RC element representative of the bulk ceramic response, for example, the observation is often that the semi-circle Z* arc typical of this circuit element type is often elongated with respect to the simulated response. This non-ideality is also manifested in a high frequency dispersion in Y' where the ideal parallel RC element defines a purely frequency independent plateau. This is described as a ‘universal dielectric response’, with this frequency domain defined by Jonscher’s power law [253,254] which describes the degree of dispersion observed towards higher frequencies, characterised with a gradient ‘n’. The physical responses inducing this diffusivity are argued within literature, varying from a distribution of relaxation times of the real dielectric, a hindrance of dipolar reorientation, differing dipolar shapes or an effective dielectric viscosity [255]. All are consistent with the non-ideality being a product of many body interactions from the relaxing dipole moments. Within the power law region, it is also considered the effects of charge carrier hopping are influential [256], and that the gradient associated to the dispersive region can indicate the dimensionality or scale of carrier migration.

To fit the observed IS response whilst accounting for this non-ideality, constant phase elements (CPEs) are typically added in parallel to an RC element or replacing an R or C component of the element, such as that shown in figure 4.20, with an associated impedance according to equation 4.29. The power coefficient ‘n’ corresponds to the dispersion gradient from the high frequency domain of Y’, whereas A is related to the log(Y’) axial intercept.

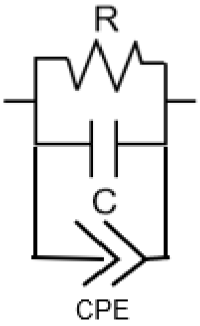

Figure 4.20: Parallel RC element with a CPE in parallel.

$$Z^{*}_{CPE} = [A(j\omega)^{n}]^{-1} \tag{4.29}$$

‘n’ can vary between 0 and 1, and from equation 4.29 it becomes clear that the impedance of a CPE will reduce to that of an ideal capacitor for n=1 and to that of an ideal resistor for n=0.

4.5 Dielectric Spectroscopy

Dielectric Spectroscopy (DS) differs from impedance spectroscopy in that DS is usually conducted at a single frequency across a temperature range, with parallel capacitance (C_p) and dielectric loss (tan δ) directly measured. This is opposed to a broad frequency range at a single temperature, as with IS [252].

The real component of permittivity (ε') can then be calculated using from the parallel capacitance measured using equation 4.30, where ε_r and ε_0 are the relative permittivity of the dielectric and permittivity of free space (8.85×10^{-14} $\mathrm{Fcm^{-1}}$), respectively, whilst A is the cross sectional overlap area of the internal dielectric layers with associated thickness d. Rearranging this equation gives the relative permittivity.

$$C_P = \frac{\epsilon_r \epsilon_0 A}{d} \tag{4.30}$$

It is typical to plot relative permittivity and tan δ against temperature, with 'anomalies' such as peaks often revealing structural relaxations such as phase transitions. Repeating the temperature measurements for multiple frequencies can be useful to reveal the frequency dependence of such relaxations. Ferroelectric phase transitions are typically frequency independent and are characterised by a sharp peak in relative permittivity. Relaxor-type transitions involving the relaxing out of local, nano-scale regions of polarity (polar-nano regions, PNRs) offer frequency dependent behaviour as a direct function of the dynamism of PNRs and the variation in the correlation lengths of polarisation. This relaxation is thus characterised by a frequency dispersion in both relative permittivity and tan δ peaks.

tan δ is defined as a ratio of the imaginary component of complex permittivity against its real part – a factor quantifying the degree of energy loss/attenuation within a sample when undergoing polarisation:

$$\tan \delta = \frac{\epsilon''}{\epsilon'} \tag{4.31}$$

Typically for dielectrics, a tan δ < 5 % (0.05) indicates good dielectric behaviour. Small losses are associated with low levels of thermally activated intrinsic conduction or local ac conductivity such as dipole reorientations. Peaks in tan δ can, as previously stated, be associated with structural relaxations such as a ferroelectric-paraelectric transition. It is then necessary to complement this data with other structural characterisation techniques, such as variable temperature XRD, to confirm this as the source of the peak in losses. Otherwise, higher tan δ can be indicative of larger, often longer range (DC) transport mechanisms within the samples. These contributions may include ionic conduction or thermally activated intrinsic DC conductivity, and can typically be seen at higher temperatures where carrier concentrations increase. Space charge effects will show a relaxation with frequency reflected in the tan δ, as described in section 2.2.4.

As tan δ is a ratio, it may not reveal loss associated with relaxation events should the real and imaginary components of permittivity increase in proportion. It is often beneficial to plot the imaginary component of permittivity by itself with temperature, by multiplying the tan δ by the relative permittivity calculated from equation 4.30, to reveal the intrinsic loss behaviour of a material.

From equation 4.30, miniaturising an MLCC whilst satisfying a requisite capacitance output necessitates a dielectric with as high a permittivity as possible, with internal dielectric layers as thin as possible. The influence of the latter is an inherently higher electric field across the layers, in accordance with equation 4.32.

$$E = \frac{V}{d} \tag{4.32}$$

This higher field will increase the potential for dielectric breakdown as described in section 3.1, depending upon the dielectric's electric field induced dielectric breakdown strength, $E_{\mathrm{breakdown}}$. Equation 4.30 can be redefined according to the capacitance per volume of the dielectric, $v_{dielectric}$ [257,258]:

$$\frac{C}{v_{dielectric}} = \frac{\varepsilon_0 \varepsilon_r}{d^2} \tag{4.33}$$

And for a given working voltage, V, the minimum thickness is limited by the electric field breakdown strength such that equation 4.33 can be given as [257,258]:

$$\frac{C}{v_{dielectric}} = \varepsilon_0 \varepsilon_r \cdot \left[\frac{E_{dielectric}}{V}\right]^2 \tag{4.34}$$

Where the capacitance observed per unit volume can be defined as being proportional to a 'merit index', $\varepsilon_r \cdot (E_{dielectric})^2$. This merit index compares a dielectric's ability to resist breakdown and simulatanously offer a high permittivity, both of which are evidently essential to MLCC integration. This figure of merit can therefore be used to quantitatively compare varied dielectric materials with prospective MLCC integration.

4.6 P-E Analysis

The electric field dependence of polarisation is typically measured using a modified Sawyer-Tower circuit [259], such as the one shown in figure 4.21 below [260]:

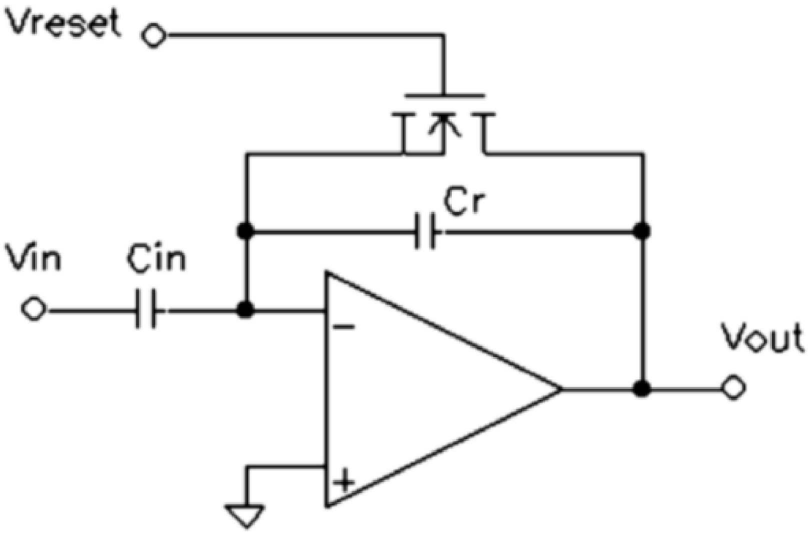

Figure 4.21: A modified Sawyer-Tower circuit, used to calculate the electric field dependence of polarisation in a sample. Reformatted from [260]

An ac voltage, V_{in}, is applied predominantly across a sample (C_{in}) due to its capacitance being typically much smaller than that of the reference capacitor (C_r) in the circuit. Consequently, an electric field according to equation 4.35 is applied across the sample material, where d is equal to the sample thickness [261].

$$E = \frac{Vin}{d} \tag{4.35}$$

The capacitance across the reference capacitor shares the same charge as that across the sample material's plates, and so, based on equation 4.36, the polarisation across the sample can be calculated [261]:

$$P = \frac{q}{A} = \frac{CrVout}{A} \tag{4.36}$$

where A is the surface area of the electrodes on the reference parallel plate capacitor.

4.7 Experimental Setup of Analysis Techniques

Bulk, sintered polycrystalline samples are used in the form of ~ 8 mm diameter pellets for all of the aforementioned techniques with the exception of XRD, which utilises powder formed from the crushing of sintered pellets. These pellets are formed via the solid-state synthesis route described in section 4.1.

4.7.1 SEM/EPMA

It is important that high density (~ 95 % of the theoretical density) bulk samples are measured as porosity increases the uncertainty/error associated with EDS/WDS quantitative analyses. This is based on the potential for additional scattering interactions ejected electrons and photons can have as a direct consequence of pore geometries. Similarly, the surface of the sample investigated must also be as flat as possible with respect to reducing this associated error. To achieve a flat surface, the bulk pellet is ground and polished with a series of abrasive silicon carbide sheets, starting with a highly abrasive P800 grade paper and working to a finer P2500 grade paper. The surface is then polished further using 6, 3 and then 1 μm diamond suspensions with an appropriate polishing mat. A colloidal silica suspension is then used with a vibratory polisher to finish the polishing procedure, producing a strain free surface. An additional thermal etching step was used for SEM to reveal the grain structure of the surface. This involved annealing the sample post-polishing to a temperature ~150 °C below the sintering temperature for ~ 15 minutes, although this is material dependent and it is possible to under-etch or over-etch the samples.

The polished samples are mounted on an aluminium stub using a conductive silver paste and carbon coated, with this carbon layer deposited on the specimen surface typically 5-10 nm in thickness. This conductive coating in combination with the silver paste provides a conductive pathway to facilitate charge dissipation, thereby preventing charging artifacts from degrading the quality of the images. The coating is thin enough to prevent impairment of the observable morphological effects of the specimen surface, and will not contribute to the X-ray energy spectrum (unlike Au coatings that are often used for SEM imagery).

SEM was conducted on an Inspect F50 (Philips, FEI) with a 15 kV accelerating voltage and a working distance ~ 10 mm. For EPMA, a JEOL JXA 8530F Plus with an accelerating voltage of 15 kV and a probe current of 80 Na was used. The standards used to quantify Ba, Na, Nb, Ca and Ti concentrations within the composite ceramics investigated in results chapter 2 are tabulated in table 4.6.

Table 4.6: The standards used for the quantification of cations.

Standards used for WDS analysis in EPMA	
Element	Standard
Ba	Barite, $BaSO_4$
Ca	Wollastonite, $CaSiO_3$
Na	Jadeite, $NaAlSi_2O_6$
Nb	Nb_2O_5
Ti	Rutile, TiO_2

4.7.2 Dielectric Spectroscopy and Impedance Spectroscopy

The polycrystalline sample pellets are ground rather than polished for DS and IS measurements. P800 and P1200 silicon carbide abrasive papers are used for mass removal to flatten the surface. Gold electrodes are applied to the adjacent surfaces using a gold conductive paste, establishing a parallel plate capacitor. This paste is a gold frit and requires an annealing step, 850°C for 2 hours, to melt the frit and create a coherent gold coating on the pellet.

This electroded pellet is then located into the centre of a cylindrical alumina compression jig with spring loaded platinum contacts providing electrical contact between the pellet and the impedance analyser (via BNC cables). An Agilent E4980A (Agilent, USA) LCR meter is used to measure the parallel capacitance and tan δ for DS measurements, at 5 select frequencies: 1, 10, 100, 250 and 10^3 kHz. These measurements are taken every 1 °C. For IS measurements 48 different frequencies are used along a logarithmic scale between 20 Hz – 1 MHz.

The jig containing the sample is loaded into a tube furnace to heat the sample as necessary. For DS measurements, the sample is heated to 500 °C, whereas for IS measurements, the heating regime is varied and is dependent upon the time constant of the equivalent circuit element being measured (bulk response or otherwise). Given that this thesis concerns dielectric materials, the DC conductivity is low at room temperature and the need for heating to decrease the time constant of relaxation into the measurable frequency domain is normally required. When the sample is heated such that the frequency of relaxation is observable, measurements are taken incrementally every 25 °C so the temperature dependence of the DC conductivity can be calculated. As the sample is incrementally heated, ~30 minutes is reserved between sequential measurements to ensure satisfactory thermal equilibration of the sample has occurred.

Should the time constant of the electrically-active component be too low at room temperature, close to or outside of the 1 MHz maximum frequency, the sample can be cryogenically cooled. This involves locating the pellet between two gold electrodes within a Helium cooled cryocooler (Oxford Instruments, UK), capable of reaching temperatures as low as 4 K. For DS measurements, the sample is always cryogenically cooled to $\sim$ 100 K (although this may differ according to the sample), to measure sub ambient permittivity responses.

For IS measurements in varied oxygen partial pressures, the sample is loaded into a thermally resistant sealed glass jig, with platinum contacts connecting the pellet to the LCR meter. A selected gas can then be passed over the sample for a period of 24 hours prior to measurements taking place, to ensure sufficient diffusion/exchange between the atmosphere and the sample. For atmospheric impedance, a Solartron SI 1260 (Solartron Metrology, USA) is used, with the sample principle as stated in the conventional air-based measurements.

For IS measurements, in order to calculate the most accurate sample R and C values for the representative equivalent circuit, the contribution of the intrinsic capacitances and inductances associated with the jigs must be removed from the measurements. This is achieved by running room temperature ‘open circuit’ IS measurements, called so as the platinum sample contacts in the compression jigs are separated only by air (as opposed to a sample). This open circuit measurement subtracts the parallel capacitance associated with the jig from the equivalent circuit, something that becomes of particular importance should the electroactive region have a capacitive component within the pico- to nano-Farad range that is typical of the jig contribution [252]. To remove the inductive contributions of the jigs, a ‘closed-circuit’ room temperature IS measurement is taken, where the platinum contacts are in direct contact. This measurement becomes significant for higher conductivity samples that are more susceptible to inductive interference from the jigs - from the contacts, BNC cables or even the LCR meter itself.

4.7.3 Polarisation-Electric Field Measurements

Polarisation-Electric field measurements were taken using a TF Analyser 2000E (aixACCT systems, Germany) with an FE-Module, and analysed in the aixPlorer software. P-E loops were measured at 25 °C using a bipolar field application. The bulk sintered pellets were measured using gold electrodes fired on as described previously. Each of the bulk samples was ground to 0.5 mm to ensure consistent sample thickness for all measurements. The electrodes fired on were of a radius 0.5 mm less than that of the pellet on both the upper and lower surfaces. This was sufficient to prevent arcing between the two electrode surfaces under high applied voltages. The sample was immersed in silicon oil for the same reason. The electric field applied was incrementally increased from 0 $kVcm^{-1}$ in 10 $kVcm^{-1}$ increments, with the bipolar polarisation response measured until dielectric breakdown of the samples was observed. This was utilised to quantify a dielectric breakdown strength of the compositions. However, this is type of breakdown quantification does not define any statistical dependencies of electric field induced dielectric breakdown. A set of 'identical' ceramic samples will inherently exhibit a range of dielectric breakdown strengths, not characterised in this way. A Weibull statistical distribution of breakdown strengths is one mechanism of describing a distribution of failure in these 'real' ceramic materials, where the cumulative dielectric breakdown probability P can be fitted against applied electric field E (relative to its nominal breakdown field E_0 corresponding to the 63.2 % cumulative breakdown probability) for a larger sample size. β represents a fitting/shape parameter in a two parameter Weibull distribution [262].

$$P(E) = 1 - \exp\left[\frac{-E}{E_0}\right]^{\beta} \tag{4.37}$$

Consequently, average breakdown strengths can be defined, alongside confidence margins on failure and the overall range of breakdown strengths. Cumulative failure probability can be estimated for a known operational electric field. This offers insight into the reproducibility of the ceramics and their field resistance, and would be more appropriate for commercial scale application of the ceramic compositions investigated. This type of analysis neccesitates a larger sample size (compared to the single ceramic analysis described initially) that is not available from the lab-scale synthesis of dielectric compositions at this stage. The assumption of breakdown strength from single ceramic samples as opposed to a large batch is sufficient for comparison of dielectric properties within this thesis.

4.7.4 X-ray Diffraction

Powder X-ray diffraction was conducted on all sintered samples. These samples were sintered as bulk pellets, described in section 4.1, and subsequently crushed and ground using a pestle and mortar into a powder of crystallites typically microns in size. These powders were then annealed at 600 °C for an hour with a slow cooling rate of 0.8 $°Cmin^{-1}$ to alleviate the effects the strain imparted by the new surface formation might have on diffraction peak width. The powders were measured using two different machines. The Panalytical X'Pert^3 (Malvern Panalytical, Netherlands) was used for general phase analysis, with a reflection type Bragg-Brentano θ-2θ geometry. An accelerating voltage of 45 kV and a beam current of 30 mA was used, with Cu-K$\alpha_{1,2}$ (1.54 Å) radiation irradiating the samples. 99 % of Cu-Kβ radiation was filtered out using a Ni insert. The powder sample was backfilled into a sample holder 20 mm in diameter, whilst a scan step of 0.01° was used alongside a 2θ range of 10 – 100 °.

For Rietveld refinements, diffraction patterns were measured using a STOE STADI P (STOE, Germany) diffractometer in Debye-Scherrer/transmission θ-2θ geometry. A monochromatic Mo-Kα_1 (0.7090 Å) wavelength was used, with a scan range of 2 – 50 ° and a step size of 0.01 °.

Phase identification was identified using the ICDD SIeve+ software, comparing peak positions to PDF cards of known phases in the ICDD database. Rietveld refinements were conducted using GSAS II [263] software, refining background coefficients, instrument parameter Cagliotti functions (for peak shape), lattice parameters, crystallite size and micro strain, atomic coordinates, site fractions and isothermal parameters.

5 Results Chapter 1: Composite arrangement of $Na_xBa_{1-x}Nb_xTi_{1-x}O_3$ (NNBT) – $BaTiO_3$ (BT) as an alternative to multilayer systems for reduced TCC dielectrics.

5.1 Introduction

As described in chapter 3, $BaTiO_3$ (BT) is a prototypical ferroelectric material that undergoes a series of phase transitions upon cooling, with the paraelectric-ferroelectric displacive type cubic-to-tetragonal transition characterised by a sharp, large permittivity peak manifesting the associated change in order parameter. $NaNbO_3$ (NN) differs from BT in being characterised as an antiferroelectric material at room temperature consequent of the antiparallel arrangement of Nb^{5+} cation displacements that occur, forming the 'P' phase. The maximum permittivity observed for NN at the paraelectric-antiferroelectric phase transition is considerably smaller than that of BT but is observed at a much higher temperature, ~360 °C, and with a considerable permittivity variation with temperature. Both BT, and in particular NN, share the inherent compositional flexibility capable of hosting a variety of species within its component A and B site sublattices afforded to it by their perovskite structures, through cation displacements, independent and/or cooperative octahedral $[BO_6]$ tilting sequences or a combination of both.

Dopants with a range of radii and valence, or vacancies, have been well characterised to stabilise in the perovskite structure at the expense of symmetry reductions. In fact, chapter 3.3 characterised the capability of solid solution formation between NN and BT, forming the self-compensating $Na_xBa_{1-x}Nb_xTi_{1-x}O_3$ (NNBT) series, with relaxor-ferroelectric dielectric properties obtained when the solid solution transitions towards equimolar NNBT compositions. Unfortunately, the TCC variability remains unsuitable for X7R or X8R class II dielectrics despite the high permittivities and low dielectric losses they exhibit. Chapter 3.8 revealed the capability of using these NNBT compositions in bilayer laminations with serial electrical connectivities to make use of the good dielectric properties they exhibit, utilising the compositionally driven distribution in T_m afforded to the solid solution.

This results chapter will focus on work not conducted by Foeller et al [231] or Kerridge et al [149,232] regarding the compatibility of these bilayer structures for X7R rating when sintered without the use of Au interdiffusion barriers, characterising interdiffusion rates between NNBT compositions. Interdiffusion has already been reported to occur at the interface of 70/87.5 NNBT bilayers, inducing a ternary NNBT components ~ 100 µm thick, and inducing a loss of X7R rated

TCC [149]. Compositional homogenisation studies between NNBT components considered for bilayer use will assess the rates of diffusion between components of the NNBT solid solution to understand if there are preferential areas along the binary solution that compositions could be selected from to inhibit the requirement for expensive diffusion berries during sintering in a bilayer configuration. Diffusion rates will be analysed through the sintering of NNBT ceramic composites and analysis of the permittivity responses to identify the retention of electrically distinguishable heterogeneity post sintering, with respect to the permittivity responses expected of the NNBT composite components. In the process, the retention of compositional heterogeneity in a NNBT based biphasic ceramic composite post sintering will reveal TCC stabilisation and an alternative NNBT macrostructure for X7R rated class II dielectrics in MLCCs that could compete with bilayer systems proposed previously for dielectric commercialisation.

5.2 Chapter Overview

This results chapter will begin with an overview of the dielectric and structural characteristics of the NN-rich half of the NNBT solid solution, considered for NNBT bilayers in work by Foeller et al [136,231] and now considered for ceramic composite structures for X7R class II dielectrics. Kerridge et al [149] observed the deleterious effect of losing X7R rated TCC when the 70/87.5NNBT bilayer was co-sintered in the absence of the Au diffusion barrier used by Foeller et al [231]. However, work published had no comparison of how fast the interdiffusion rates were between NNBT materials. Thus, this chapter will progress with a series of diffusion studies regarding the permittivity responses of sintered composites of NNBT and BT under short dwells. This will involve identifying if phase related permittivity responses (BT or NNBT related anomalies based on associated T_m and diffusivities) are distinguishable post sintering, comparing their intensities and inferring retained volume fractions.

Following the observation that compositional heterogeneity retained due to lower diffusion rates between certain components of the NNBT solid solution offer a more thermally invariant permittivity response, the remainder of the chapter focuses on optimising the permittivity responses of these now composite structured NNBT systems as an alternative to multilayer architectures for X7R rated dielectrics. This focuses on quantifying the dielectric response and physical microstructures of the composites, and determining the reproducibility of such configurations. Reproducibility is an essential parameter to sustain any hope of industrialisation and challenge to the NNBT multilayer systems proposed.

5.3 Experimental Conditions

All samples were synthesised using the conventional solid-state route. NNBT samples were calcined once at 1000 °C and sintered at 1250 °C for 5 hours. The 70/87.5NNBT bilayer was sintered using the same conditions by Kerridge [149].

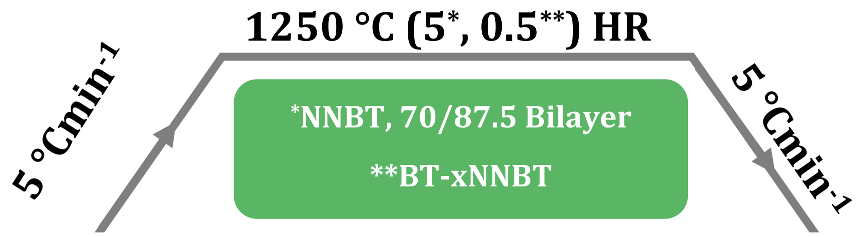

Figure 5.1: The sintering conditions used in Results Chapter 1. * Indicates the dwell time used for NNBT and 70/87.5NNBT bilayer sintering. ** The dwell time used for samples hand mixed in homogenisation studies and for the BT-60NNBT composites investigated.

To investigate homogenisation rates between hand-mixed components of the NNBT solid solution upon sintering, the same sintering temperature was used albeit at a shorter dwell period of 0.5 hours with the intention of preserving electrically measurable compositional heterogeneity. The composite systems consequent of this homogenisation study, formed of hand mixed BT-60NNBT, initially in a 50:50 wt.% ratio but later with optimised weight percent ratios retained these same sintering conditions.

Sample density (ρ) measurements were calculated using the geometrical method:

$$\rho = \frac{m}{V} \tag{5.1}$$

The average thickness and diameter of the pellets was measured using digital callipers with an associated uncertainty of ±0.005 mm, from which the sample volume (V) could be calculated. Mass (m) of the sample was measured on an electronic balance with an associated uncertainty of ±0.05 mg. The theoretical density of NNBT samples was obtained from Rietveld refinement of the X-ray diffraction patterns based on the total mass in the unit cell (from refined site occupancies) with respect to its volume (from refined lattice parameters). Relative density was then quantified as the ratio of sample density to the theoretical density:

$$\rho_{rel} = \frac{\rho_{sample}}{\rho_{Theoretical}} \times 100 \tag{5.2}$$

For the 70/87.5NNBT bilayer and composite BT-NNBT architectures, the theoretical density was calculated using:

$$\frac{1}{\rho_{Total}} = \frac{x_1}{\rho_1} + \frac{x_2}{\rho_2} \tag{5.3}$$

where (x_1, ρ_1), (x_2, ρ_2) are the volume fraction and theoretical density of phase 1 and 2, respectively, in a binary phase multilayer system or composite.

5.4 $Na_xBa_{1-x}NbxTi_{1-x}O_3$ (NNBT) compositions utilised

5.4.1 Overview

Four NNBT compositions were investigated, having previously been considered for use within the NNBT based multilayer arrangements for reduced TCC dielectrics:

Table 5.1: The NNBT compositions synthesised and characterised.

Composition	Acronym
$Na_{0.6}Ba_{0.4}Nb_{0.6}Ti_{0.4}O_3$	60NNBT
$Na_{0.7}Ba_{0.3}Nb_{0.7}Ti_{0.3}O_3$	70NNBT
$Na_{0.8}Ba_{0.2}Nb_{0.8}Ti_{0.2}O_3$	80NNBT
$Na_{0.875}Ba_{0.125}Nb_{0.875}Ti_{0.125}O_3$	87.5NNBT

This corresponds to a range beginning close to the centre of the solid solution, 60NNBT, and ending towards the NN-rich end, i.e. 87.5NNBT.

5.4.2 XRD of NNBT

All NNBT samples synthesised are refined with a phase pure average structure post sintering, with all peaks observed in the diffraction patterns being indexed, figure 5.2. The associated refinements are listed in Appendix 1, figures A1-A4. Samples do not appear phase pure after calcination at 1000 °C for 6 hours, appendix 1 figure A5; however, the secondary phases in the calcined powders do not appear to have affected phase formation during the elevated temperatures of sintering. Additional higher temperature calcinations (prior to sintering) were not utilised due to the volatility of Na at such temperatures, and the potential non-stoichiometry additional calcinations could induce.

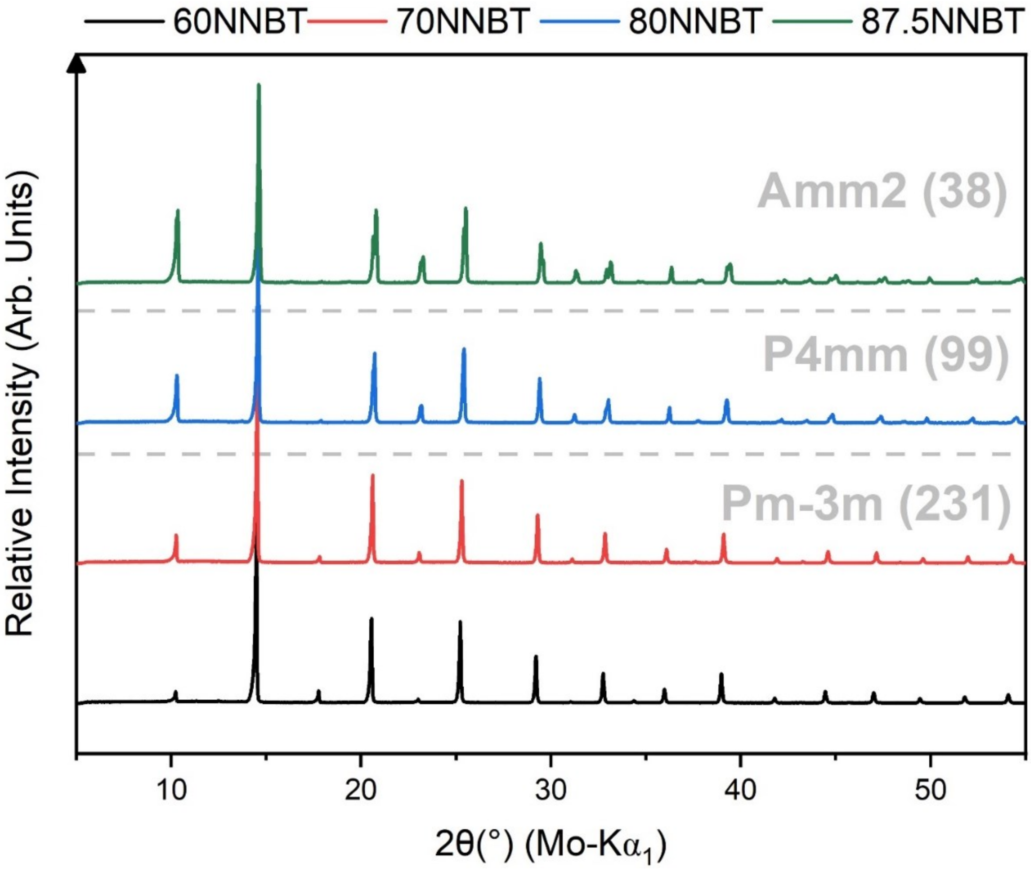

Figure 5.2: XRD diffraction patterns for the sintered NNBT compositions at room temperature, transitioning from orthorhombic Amm2 to tetragonal P4mm and cubic Pm3m with increasing BT content.

87.5NNBT exhibits an orthorhombic Amm2 symmetry, with in-phase and anti-phase tilting of its [NbO_6] octahedra producing the S1 and S2 superlattice reflections evident in figure 5.3, at (2θ~16.3 °, 19.3 °). As the NN content decreases, a suppression of the in-phase and anti-phase octahedral tilts present within the orthorhombic observed from figure 5.3 with a loss of the S1 and S2 superlattice reflections. This induces a ferro-distortive transition to a tetragonal P4mm symmetry in 80NNBT. Splitting of the Bragg peaks assigned to the pseudo-cubic sub-cell, such as the (002)/(200) shown in figure 5.3, reveal this tetragonal distortion. This is subsequently lost upon further BT substitution into the respective A and B sublattices, with a cubic Pm3m symmetry describing a compositionally disordered average 70NNBT and 60NNBT structure.

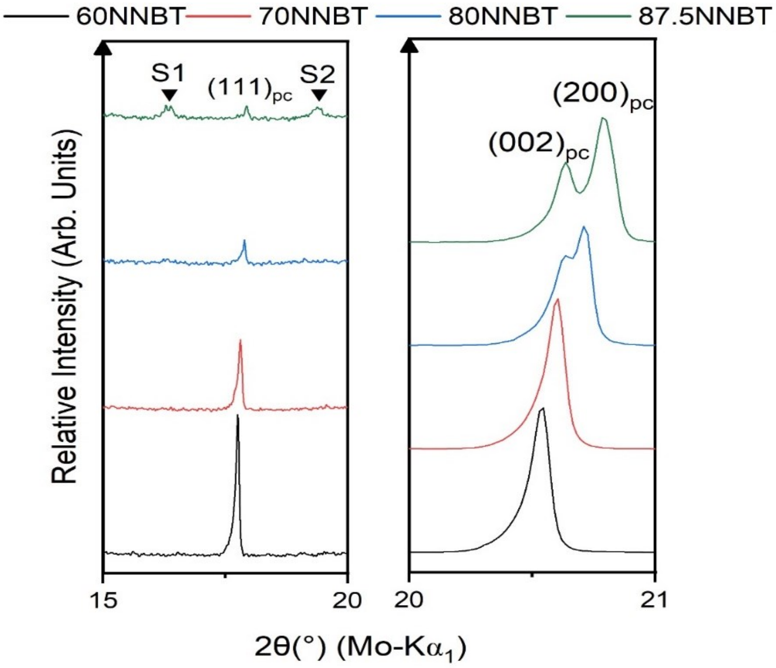

Figure 5.3. Loss of super lattice reflections (S1 and S2), associated with in-phase and out-of-phase tilting as the BT content increases. The right-hand side reveals a loss of peak splitting associated with an increase in symmetry as the solid solution transitions through its orthorhombic, tetragonal and cubic symmetries.

The refined site fractions are close to the nominal stoichiometry for all compositions, appendix 1 tables A1-A4. Relatively linear expansion of the pseudo-cubic sub-cell is observed as the solid solution progresses from 87.5NNBT to 60NNBT on account of the substitution of Na (1.36 Å) by the larger Ba (1.61 Å)[86]. The theoretical densities of the synthesised NNBTs, calculated from the refined site occupancies and lattice parameters, are tabulated in table 5.2. The theoretical densities decrease with increasing NN content despite the decreasing unit cell volume shown in figure 5.4. The relative densities for the sintered NNBT samples are also tabulated in table 5.2. All NNBT samples have ρ_{rel} >95%, with density increasing in proportion to NN content with the exception of 80NNBT with 97.2%.

Table 5.2: The theoretical and sample densities of the NNBT compositions synthesised.

Composition (NNBT)	Theoretical Density (gcm^{-3})	Sample Density (gcm^{-3})	Relative Density (%)
60	5.049	4.853 ± 0.062	96.1± 1.23
70	4.924	4.850 ± 0.038	98.5± 0.77
80	4.770	4.636 ± 0.22	97.2± 4.61
87.5	4.681	4.626 ± 0.054	98.8± 1.15

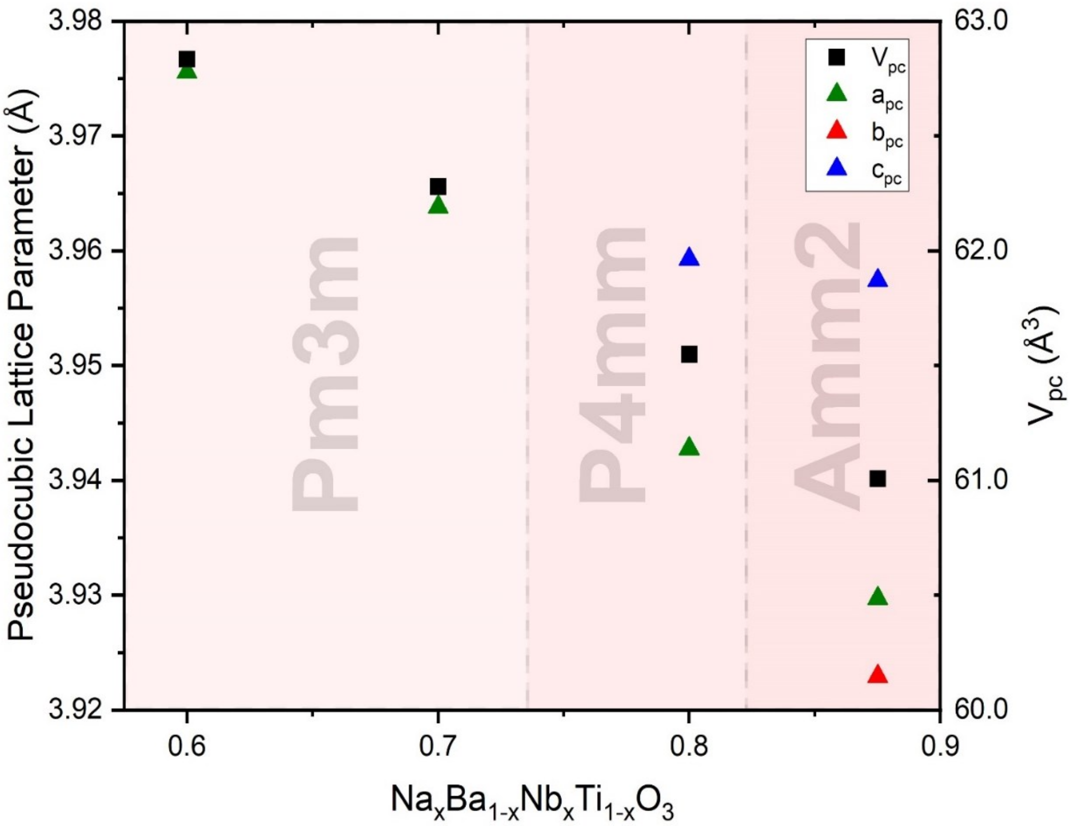

Figure 5.4: Room temperature pseudo-cubic sub-cell lattice parameter and volume variations with NNBT composition. A linear increase in volume is observed for increasing BT inclusion, obeying Vegard's Law.

5.4.3 SEM of the synthesised NNBT compositions

Figure 5.5 shows the micrographs from the back scattered electron (BSE) signals obtained from regions of each NNBT composition synthesised. Grain size progressively decreases with increasing BT content, whilst dense but variable microstructures are evident across the range of the solid solution analysed. The relatively NN-rich compositions show a fairly conventional ceramic microstructure featuring a distribution of differing grain sizes, each with a truncated octahedral type morphology and dihedral angles at the interstices typical of dense ceramics. 60 and 70NNBT exhibit a range of morphologies within the microstructure, including smaller grains of this octahedral type but also much larger platelet formations and rounded areas dispersed amongst the microstructure. Aside from morphological variation, no significant contrast is evident within the bulk of the sample that would imply secondary phase formation.

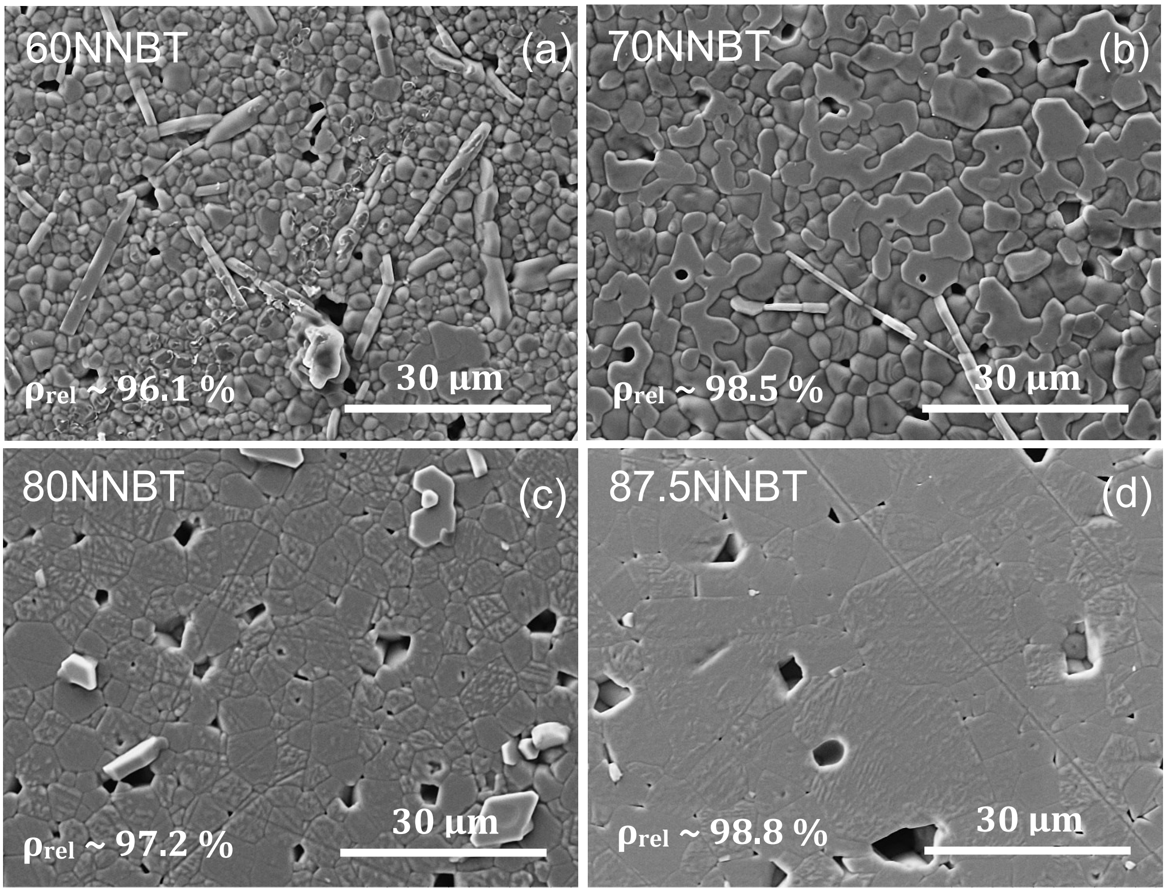

Figure 5.5: Back Scattered electron (BSE) micrographs of the NNBT compositions, all at 2000 magnification. Variable morphology is observed within the 60NNBT (and to some extent 70NNBT) samples with respect to the conventional ceramic microstructure observed in the 80 and 87.5NNBT compositions.

5.4.4 Electrical Characterisation

The permittivity responses for the NNBT compositions are shown in figure 5.6.

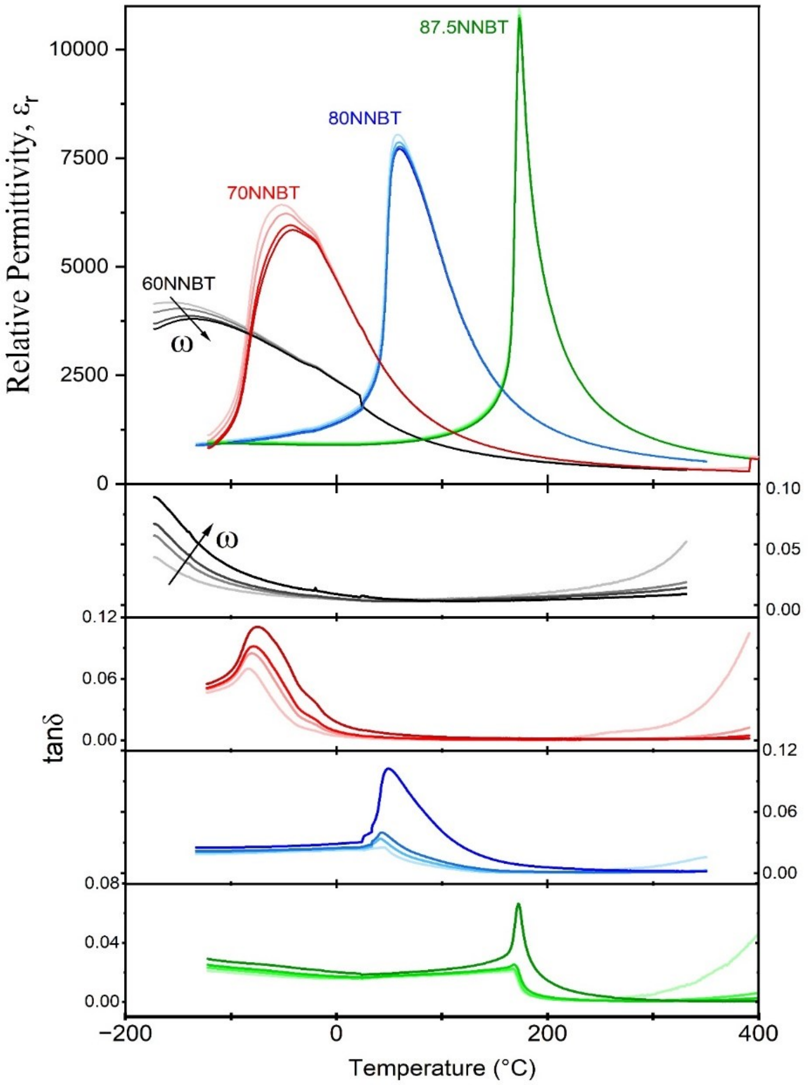

Figure 5.7: The (overlaid) relative permittivity and (independently plotted) dielectric loss responses for each NNBT composition.

There is a clear transition from 87.5NNBT exhibiting a sharp, frequency independent permittivity-temperature dependence, typical of ferroelectrics, to a diffuse, highly frequency dependent response associated with 60NNBT - a prototypical relaxor response. A clear shoulder is evident on the permittivity response of 70NNBT towards higher temperatures, a response not evident within the other synthesised samples. As expected for relaxor materials, frequency dependence is manifested in both permittivity and tan δ as the solid solution transitions towards 60NNBT. Higher frequencies exhibit a lower maximum permittivity at a higher corresponding temperature, T_m. Conversely, the tan δ is greatest for higher frequencies, clear from figure 5.6. The enhancement in relaxor response towards the centre of the NNBT solid solution and the corresponding shortening in polar correlation lengths results in a reduction in maximum permittivity and associated temperature. A decrease in permittivity from ~11000 at 173 °C in 87.5NNBT to ~4000 in 60NNBT at -135 °C is observed. The distribution in T_m afforded to the NNBT solid solution is shown in figure 5.7, constructed from dielectric data published and experimental data observed (all at 250 kHz), covering a total range of ~560 °C.

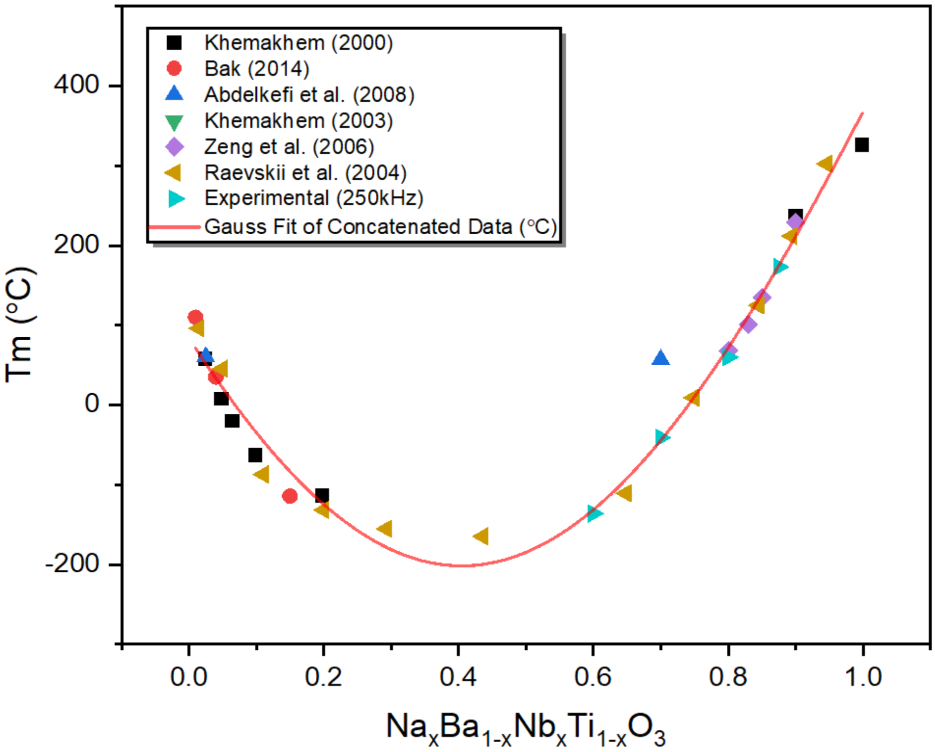

Figure 5.8: The distribution in the temperatures associated to the maximum permittivity response (T_m) of compositions across the NNBT solid solution, including responses from published data.

Attempts to quantify the extent to which the long-range ferroelectric order has been lost with increasing BT content are given in the modified Curie-Weiss Equation 5.4:

$$\frac{1}{\epsilon} - \frac{1}{\epsilon_m} = (T - T_m)^\gamma \ \ where\ 1 \le \gamma \le 2 \tag{5.4}$$

This can be plotted alternatively as $\ln((1/\varepsilon) - (1/\varepsilon_m))$ versus $\ln(T-T_m)$ according to Equation 5.5, as shown in figure 5.8.

$$\ln\left(\frac{1}{\epsilon} - \frac{1}{\epsilon_m}\right) = \gamma \ln(T - T_m) \tag{5.5}$$

The relaxor parameter γ is calculated as the gradient of the linear fit to the depolarisation response above T_m. This relaxor parameter γ attempts to quantify the extent of diffusivity in the permittivity and thus the length scale of ordering of the intrinsic polarisation. A γ value of 1 is indicative of prototypical ferroelectric response with long range ordering of dipole moments, for which the modified Curie Weiss equation will reduce to the conventional Curie Weiss law. A value closer to 2 suggests the traditional Curie Weiss exponential decay of the permittivity with temperature is not followed, but instead the local PNR clusters are able to interact and sustain local fields and polarities that would have otherwise been disrupted by the increasing thermal motion above a ferroelectric curie temperature, T_c.

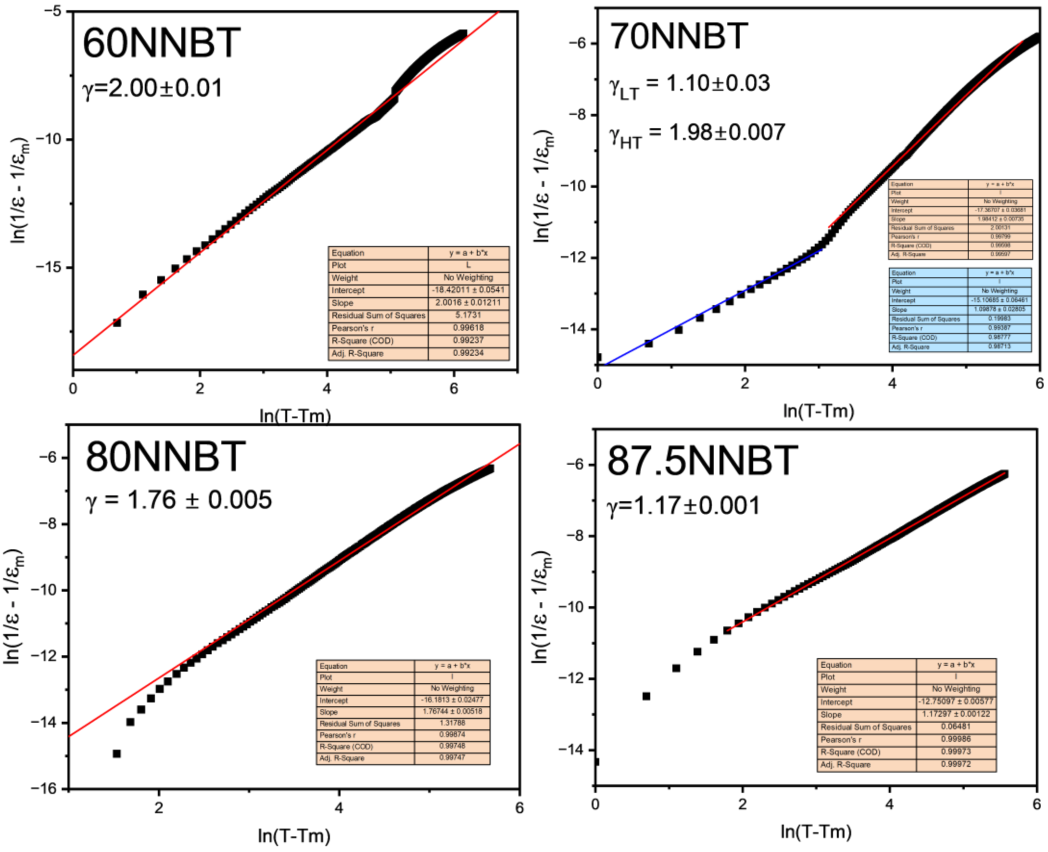

Figure 5.9: A plot of the natural logarithm of the modified Curie Weiss equation, equation 5.5, for each of the synthesized NNBT compositions. A larger depolarisation gradient equal to γ is shown for materials closer to 60NNBT.

Table 5.3 shows the γ coefficients calculated from the gradients of the linear fits of figure 5.8 for each of the NNBT compositions synthesised. The linear fit parameters are shown better in figure A6.

Table 5.3: Modified Curie-Weiss Parameters for the synthesised NNBT compositions.

Composition	γ Coefficient
60NNBT	2.00 ± 0.01
70NNBT	1.10± 0.03 / 1.98 ± 0.007
80NNBT	1.76 ± 0.005
87.5NNBT	1.17 ± 0.001

A transition from ferroelectric to relaxor behaviour from 87.5NNBT to 60NNBT is reflected in the increase in γ from 1.17 ± 0.001 to 2.00 ± 0.01, table 5.3. The former coefficient does imply that 87.5NNBT is not quite the prototypical ferroelectric material as suggested by its sharp, frequency independent permittivity response in figure 5.6.

The dielectric loss shown in figure 5.6 is low for all NNBT compositions, tan δ <0.05 up to 400 °C, suggesting dielectric behaviour is retained for all compositions. There appears to be some (but low) space charge contributions towards higher temperatures that are relaxed out as frequency increases.

The TCC response for each of the synthesised NNBT compositions at 250 kHz is shown in figure 5.9.

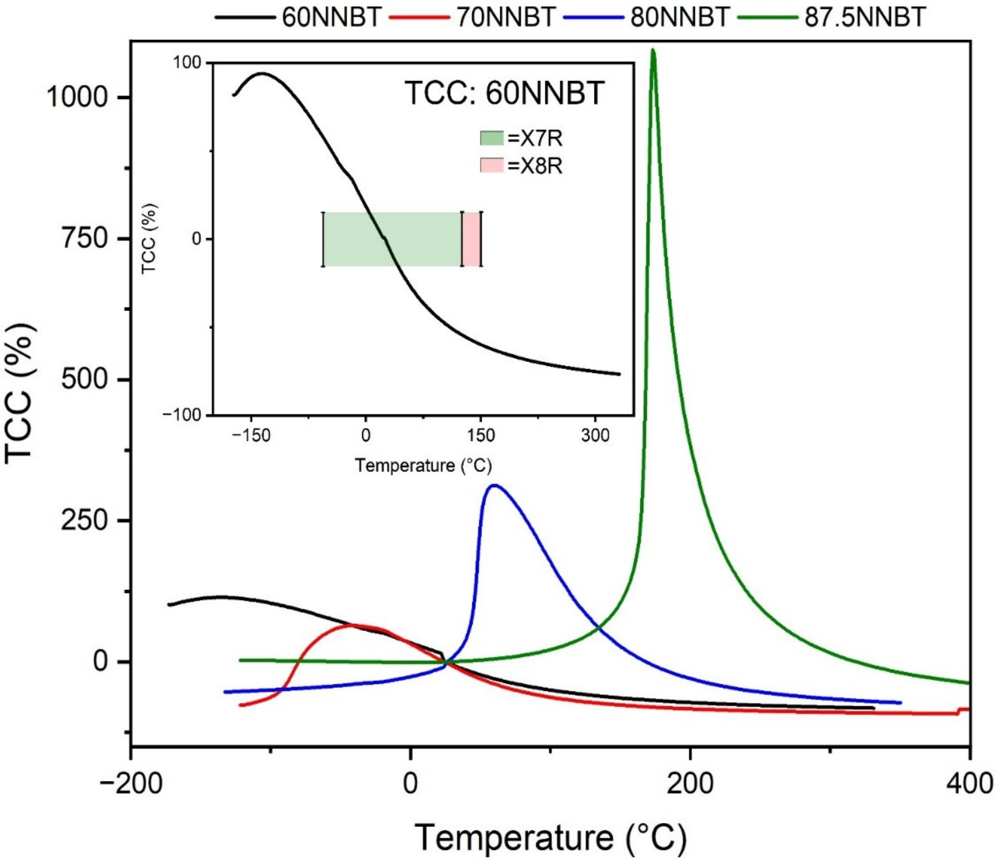

Figure 5.10: A comparison of the TCC profiles (for 250 kHz) for the various NNBTs, showing the suppression in temperature dependence of permittivity as the solid solution progresses towards its centre.

Of the compositions synthesised, 60NNBT exhibits the most diffuse thermally stable TCC response. The maximum and minimum TCC values are 93 and -76 %, respectively, whilst the X7R ±15 % TCC window is only attained between the range of 4 and 42 °C. This is much lower than the -55 to 125 °C boundaries specified for X7R rating. Thus, none of the NNBT compositions alone are appropriate for X7R (or X8R) rated dielectrics.

5.4.5 Impedance Spectroscopy of NNBT compositions

Overlaid M'' and Z'' spectroscopic plots for each of the NNBT compositions at 550 °C is shown in figure 5.10.

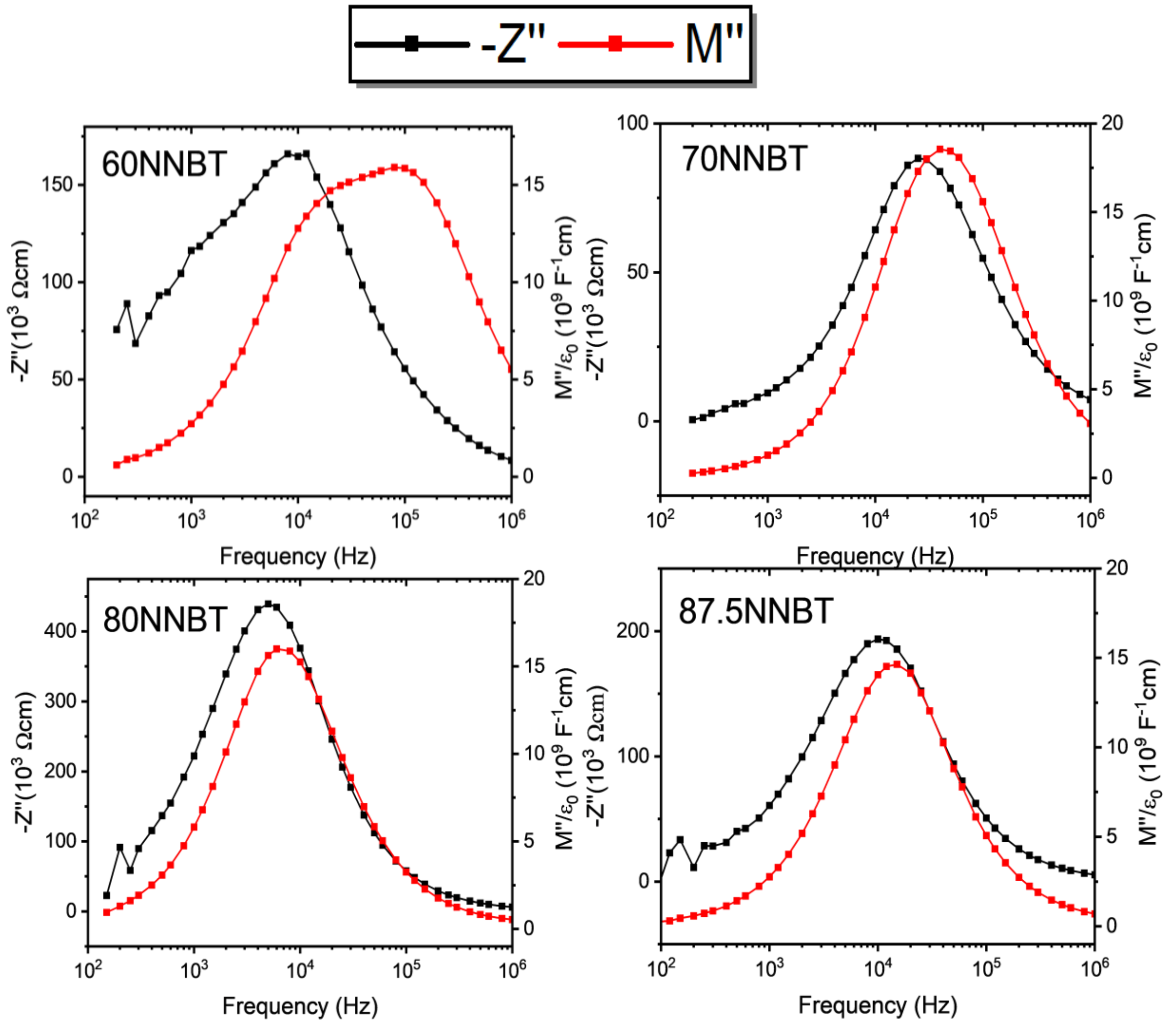

Figure 5.11: Overlaid Z'' & M'' spectroscopic plots for each NNBT composition at 550 °C. Except for 60NNBT, the electrical microstructure of each composition appears to be represented by a single, non-ideal parallel RC element.

With the exception of 60NNBT, the equivalent circuit representing the electrical microstructure of the samples can be represented by a single, albeit non-ideal, parallel RC element. This is inferred from the presence of a single Debye peak within each formalism with (relatively) equivalent time constants, thereby sharing the same frequency corresponding to -Z''/M'' maxima, fmax. In each sample, the frequency corresponding to the maximum -Z'' value, is slightly lower than the M'' equivalent. This disparity is not of a magnitude significant enough to suggest the presence of multiple parallel RC elements but instead represents the departure of the parallel RC element from ideality. This non-ideal response is also reflected in the broadening of the peaks above the full-width half-maximum (FWHM) ideal of 1.14 decades (on a log (frequency) scale), with each FWHM of the M'' peaks shown in table 5.4. There is a noticeable broadening of 60NNBT, based on a FWHM of 1.93, with respect to the other materials synthesised. This is consistent with the observation of a clear shoulder in the M'' peak towards higher frequencies in figure 5.10.

Table 5.*4*: The FWHM for the M'' Debye peaks in figure 5.10, at 550 °C, plotted on a log(f) scale.

FWHM of NNBT M'' Debye peaks at 550 °C Composition	FWHM (decades)
60NNBT	1.93
70NNBT	1.56
80NNBT	1.40
87.5NNBT	1.39

The C' plateaus for these NNBT compositions, at 550 °C, are represented in figure 5.11. Only one single high frequency plateau is evident for each of the materials, with the exception of 60NNBT which shows an inflection point marked by an asterisk.

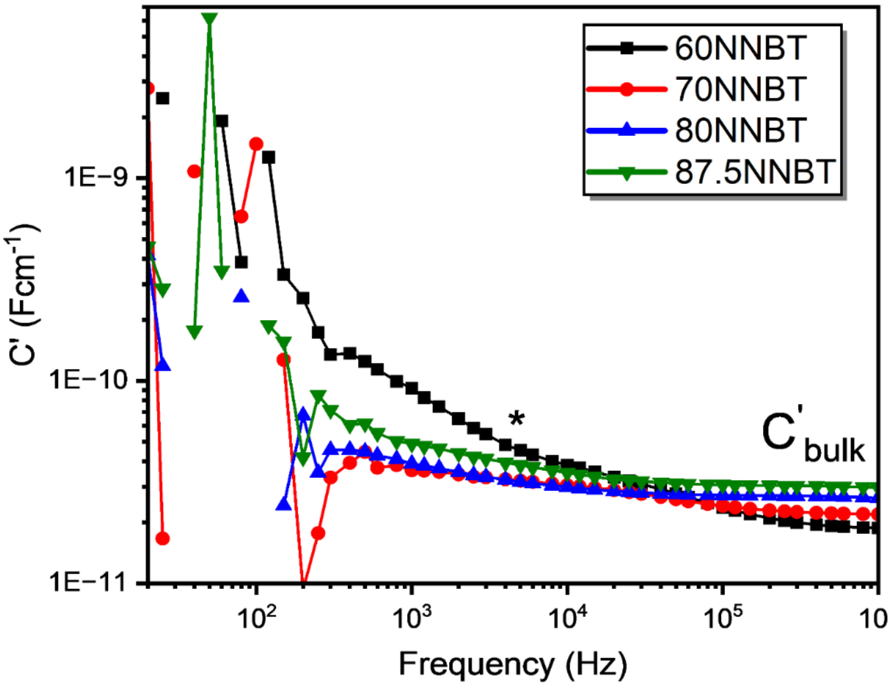

Figure 5.12: C' spectroscopic response of the NNBT compositions at 550 °C. The high frequency plateau (corresponding to the peak of the M''/Z'' Debye peaks) shows a capacitance magnitude consistent with a bulk response.

For these other NNBT compositions, these C' plateaus correspond to the frequency domain of the M''/-Z'' fmax, and are all in the 10^{-11} Fcm^{-1} range. This suggests that the electrical responses observed in figure 5.10 and 5.11 are that of the bulk material. The electrical microstructure of 60NNBT is clearly different from the other compositions synthesised. There appears to be two capacitance components of similar magnitude constituting the equivalent circuit of 60NNBT. This could be represented by two parallel RC elements connected in series. The more conductive component manifested by the shoulder in the M'' peak at higher f_{max} (since there is no corresponding –Z'' response overlaid in figure 5.10) appears to have a slightly smaller capacitance, but still of a bulk order of magnitude, and may represent the inflection point of figure 5.11.

The Z* plot for each of the materials is shown in figure 5.12 at 550 °C.

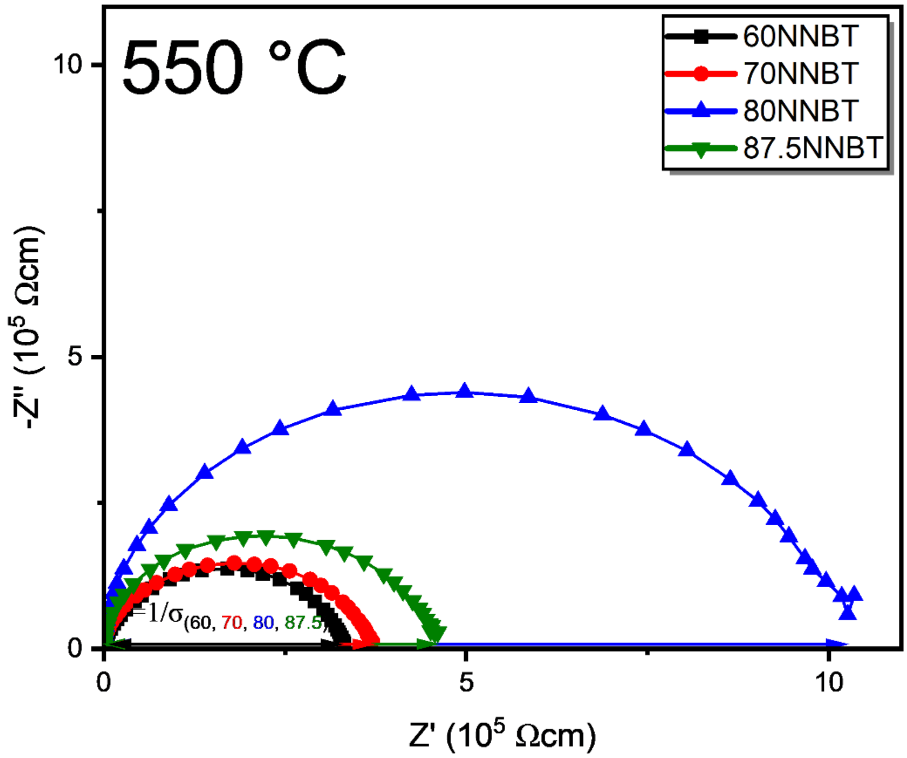

Figure 5.13: Comparison of the Z* plots for each of the synthesized NNBT compositions at 550 °C. The total DC conductivity for each of the compositions is calculated from the inverse of diameter of the single semi-circle.

The Z* plots are consistent with a single, albeit elongated, semi-circle corresponding to a non-ideal parallel RC element. No low frequency spike is observed, suggesting electronic conduction to be dominant. The total DC conductivities of the synthesised NNBT materials were calculated from the inverse of the Z' intercept of the Z* semi-circles for each of the NNBT materials. The temperature dependence of the total DC conductivity for each NNBT composition is compared in figure 5.13, and alongside components of the wider solid solution in figure 5.26.

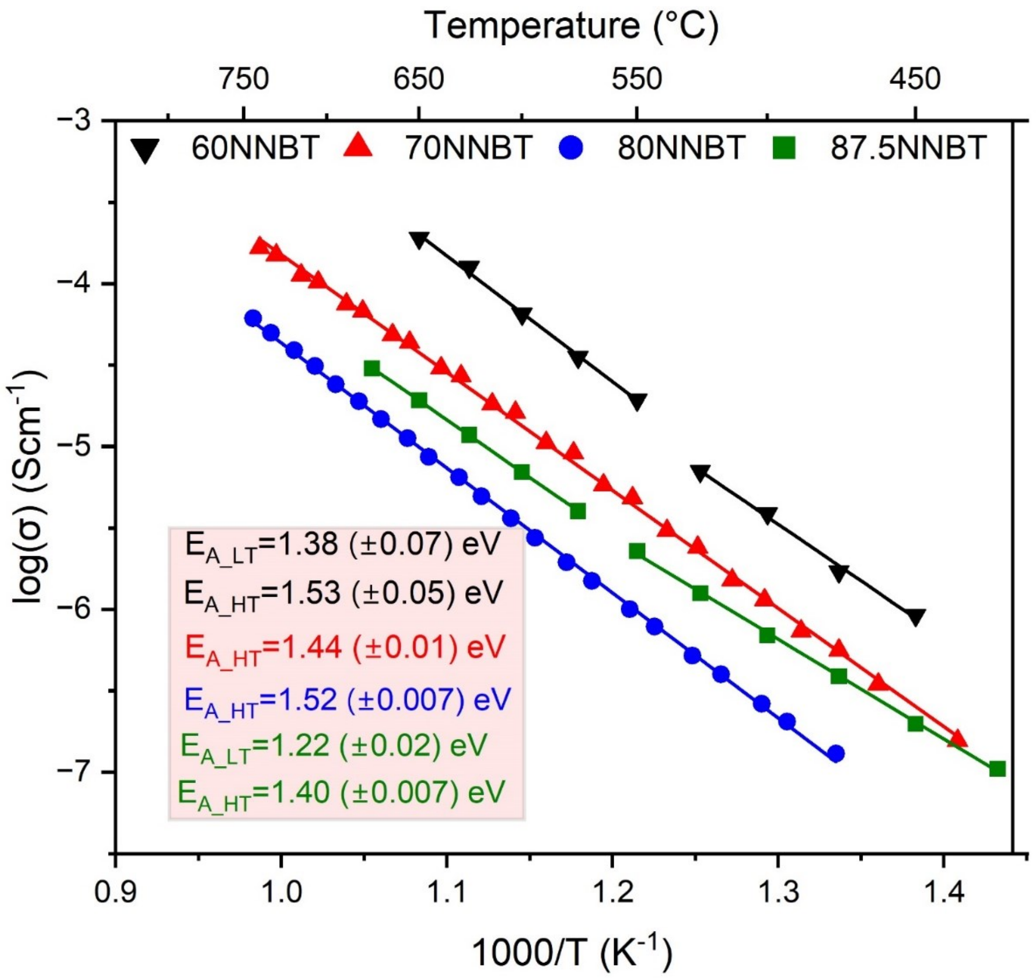

Figure 5.14: Arrhenius plot showing the temperature dependence of total DC conductivity for the NNBT compositions. With the exception of 87.5NNBT, conduction appears to be dominated by intrinsic electronic contribution.

Figure 5.13 reveals the lowest conductivity amongst the investigated NNBT compositions occurs at 80NNBT. As Ba and Ti substitute into NN it initially appears to decease the conductivity until 80NNBT, hereafter further substitution of BT increases the conductivity to its maximum in 60NNBT. This increase in conductivity is consistent with the significantly higher conductivity observed in BT-rich samples synthesised by Foeller et al [136], shown comparatively in figure 5.28. For 87.5NNBT, two distinct activation energies are observed, termed E_{A_LT} and E_{A_HT}, each relating to the low temperature and high temperature conductivity regimes respectively[1]. Consistent activation energies are observed for the high temperature conduction regime of 87.5NNBT and for the single activation energy evident for 70 and 80NNBT. This activation energy, ~1.50 eV, is approximately half the band gap of both NN (~3.4 eV) and BT (~3.2 eV) [264,265] parent materials, corresponding to an intrinsic electronic band gap contribution.

---

[1] *A similar effect is observed for 60NNBT, however, considering the unique electric modulus response observed for 60NNBT and the errors associated with these high and low temperature fit gradients of 60NNBT, it is difficult to associate this to variation in activation energy and conduction mechanisms with reasonable certainty.*

5.5 NNBT Overview

All NNBT compositions synthesised appear phase pure post sintering, based on both XRD and SEM analyses. Although some contrast appears on the platelet formations that are evident for 60NNBT from the BSE micrographs of figure 5.5, this may be a product of the sharp geometry and inclination angle relative to the incident electron beam such grain structures exhibit. The linear expansion of the ideal ABO_3 perovskite unit sub-cell with BT content in figure 5.4 is complimentary to the suggestion of complete perovskite solid solution formation for the compositions synthesised, in accordance with Vegard's law. Local straining due to the difference in radii between A and B site cations results in the loss of octahedral tilting which actively mediates local A site bonding requirements, and likely factors into an order-disorder transition between correlated Nb displacements which imparts the transition between the large and relatively sharp permittivity response of 87.5NNBT and the diffuse, lower permittivity response of 60NNBT, shown in figure 5.6. The polar correlation length in 60NNBT is consequently confined to the nanoscale, forming dynamic polar nano regions of a range of sizes and associated dynamism which imparts the diffuse and frequency dependent permittivity response observed. This is quantified with the relaxor parameter γ increasing towards 2 as the compositions transition from 87.5NNBT to 60NNBT. Figure 5.9 reveals the dramatic reduction of TCC associated with this relaxor transition, albeit not conforming to the desirable X7R commercial specification. However, low dielectric losses and high permittivities are observed across the solid solution, with a range of associated T_m's shown in figure 5.7.

This stimulated the use of NNBTs for temperature stable dielectrics as components of a bilayer macrostructure. This structure utilised the provision of permittivity across a large temperature range, a total range ~ 560 °C from figure 5.7, if the component materials were selected with complimentary diffusivities and T_m, X7R rated TCC could be achieved.

5.6 Interlayer diffusion within NNBT based multilayers

5.6.1 NNBT homogenisation study – formation of a temperature stable ceramic composite

A homogenous hand-mixture, a biphasic composite, of the 70NNBT and 87.5NNBT constituents of the optimised X7R bilayer system from Kerridge [149] was sintered under a short dwell, 1250 °C for 0.5 hours, to investigate homogenisation rates that induce the ternary phase reported to form at the interface. A short sintering dwell was used instead of a more conventional dwell period ~5 hours in an attempt to retain electrically observable compositional heterogeneity (identifiable in the permittivity response as multiple peaks of varied T_m). The relative permittivity response (at 250 kHz) of the composite post sintering is shown in figure 5.14 alongside the individual 70NNBT and 87.5NNBT permittivity responses.

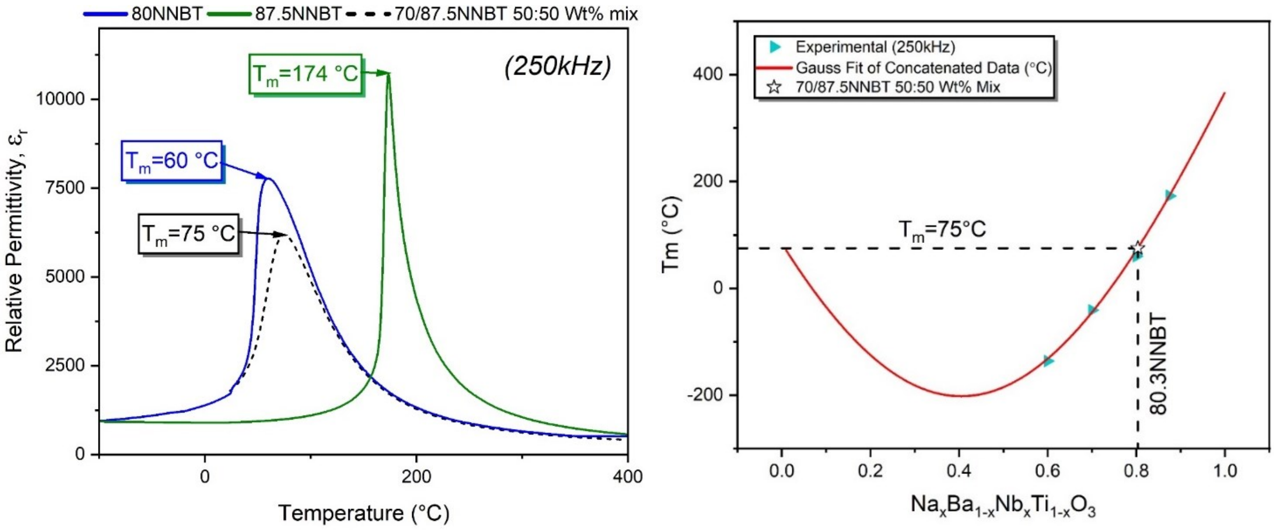

Figure 5.15: Homogenisation of the equimolar mix of 70 and 87.5NNBT, sintered at 1250C for 0.5 hours. T_m associated correlates to a composition of 80.3NNBT.

For the sintered mixture, a single permittivity peak is evident with a T_m ~75 °C. Using the gauss fit of the T_m distribution along the NNBT solid solution, figure 5.7, this peak temperature would correspond to a composition of ~80.3NNBT. This is consistent with the equimolar 79NNBT composition expected upon homogenisation. The permittivity peak maximum is lower than the 70NNBT or 87.5NNBT samples, a manifestation of the lower relative density obtained from the short 0.5-hour sintering dwell used for the mixed sample (76.5 ± 1.8 %) compared to the 5 hours used for the individually sintered samples (table 5.2).

5.6.2 Changing NNBT components to retain a ceramic composite structure post sintering

Although diffusion rates are sufficiently high enough between 70 and 87.5NNBT components to produce a single permittivity response indicative of compositional homogenisation under the 0.5 hour sintering dwell, this may not be the case for the whole NNBT solid solution. In an extension to the homogenisation study, all of the NNBT compositions synthesised were homogeneously hand-mixed with the BT solid solution end member to form an equimolar 50:50 wt.% binary composite and sintered under the same conditions of 1250 °C for 0.5 hours. This range in composition between mixed materials represents the largest compositional variance possible across the solid solution (for each NNBT composition). The resulting relative permittivity responses for each BT-NNBT mixture post sintering at a frequency of 250 kHz are shown in figure 5.15.

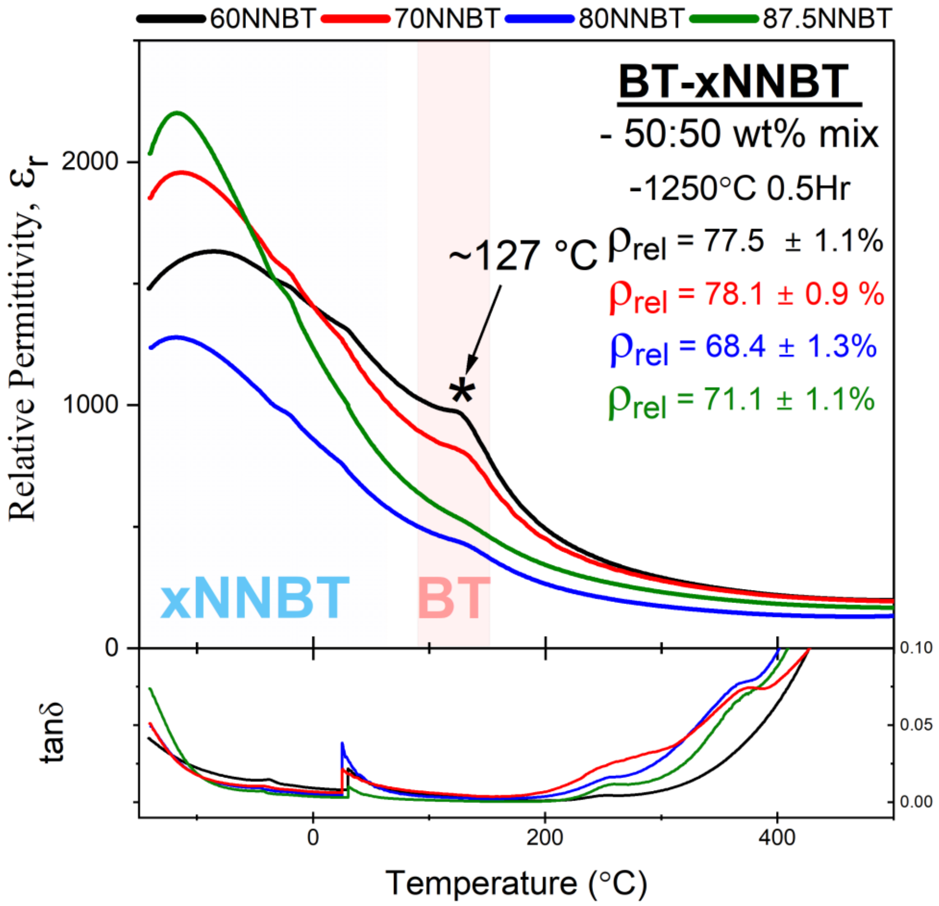

Figure 5.15: The relative permittivity and dielectric loss (at 250 kHz) for BT-xNNBT 50:50 weight percent mixes, sintered under a short 0.5 hour dwell at 1250 °C. Using 60 (black), 70 (red), 80 (blue) and 87.5NNBT (green). Variation in the intensity of a permittivity peak ~127 °C suggests a varied concentration of BT.

Multiple 'peaks' are visible in the permittivity responses as the materials are heated from the low temperature regime, suggesting the presence of electrically distinguishable compositional heterogeneity is retained post sintering for all composites. The most intense permittivity peak is at sub-ambient temperatures, which from figure 5.7 would associate this peak to a relaxor type NNBT composition. Significantly for all composites an additional permittivity anomaly is observed at ~127 °C. This temperature is consistent with the ferroelectric-paraelectric phase transition of BT, for which 50 wt.% of the starting composite was constituted. The presence of two peaks of considerably different T_m is indicative of retention of (at least) a 'binary' phase NNBT based composite post sintering. The magnitude of this high temperature permittivity peak grows as the NN content in the initial NNBT component of the mixture decreases, i.e. a more relaxor-type NNBT is used in the pre-sintered composite. There is a progressive decrease in the maximum permittivity observed at low temperatures as the NN content in the NNBT decreases, i.e. the NNBT mixed is more of a relaxor-ferroelectric than a prototypical ferroelectric. This is with the exception of 80NNBT, that is substantially lower in permittivity than all of the other mixes. This a product of the lower relative density, 68.4 % of this composite with respect to the other sintered composites.

Of all of the sintering mixtures investigated, BT-60NNBT offers the lowest dielectric losses, shown in figure 5.15. tan δ is <0.05 until 400 °C (above which the dielectric losses rise sharply), and therefore retains good dielectric behaviour. BT-60NNBT also exhibits the most temperature stable permittivity response relative to the other composites formed, an effect of these phase-related high and low temperature permittivity maxima of varied diffusivities being more comparable in magnitude relative to the other BT-NNBT mixtures. This suggests TCC stabilisation in the composite can be enhanced should the magnitude of these phase dependent permittivity maxima be closer. Through iteration of the starting volume fractions (much like the multilayer system), desirable TCC response could be attained, closer to an X7R specification. Since BT-60NNBT offered the most stable TCC response from this initial study and the lowest dielectric losses, iteration of BT and 60NNBT volume fractions in the corresponding composite system were investigated with the prospect of enhancing TCC to satisfy X7R rated specification.

5.6.3 Optimising the TCC of the BT-60NNBT through variation in the mixing ratios

Figure 5.16 shows the variation between the relative permittivity responses of BT-60NNBT for varied mixing ratios of BT and NNBT utilised in the pre-sintered composite (at 250 kHz). A higher starting fraction of BT results in an increasing intensity of the peak at ∼127 °C. As proposed, the combinatorial effect of this increase in permittivity associated to the high temperature peak and its consequential comparability in magnitude with the low temperature permittivity response results in a stabilisation of TCC. The TCC comparison of 60NNBT and two BT-60NNBT mixes (50:50 wt.% used in the initial homogenisation tests and the 80:20 wt.% optimised for TCC stabilisation) are shown in figure 5.17 to emphasise the stabilisation effect of achieving similarity in permittivity from its contributory phases, as well as a comparison of the TCC associated to the NNBT composite relative to the most thermally invariant NNBT composition synthesised. The 80:20 wt.% post sintered BT-60NNBT composite yields the most stable TCC response, meeting X7R TCC specifications. It does so with an associated permittivity magnitude ∼2000 across the -55 to 125 °C operating temperature range and a tan δ < 0.05 up to ∼400 °C. Figure 5.16 reveals that the variability in mixing ratios does influence dielectric loss, however all compositions retain

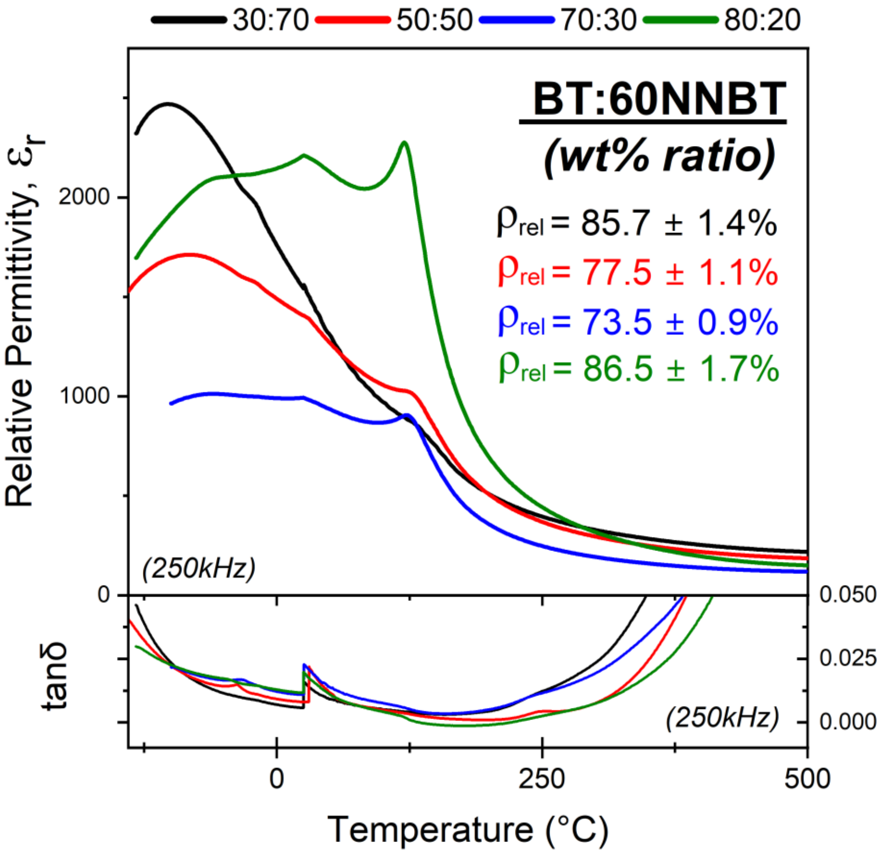

Figure 5.16: The relative permittivity and dielectric loss (at 250 kHz) for BT-60NNBT at 30:70 (black), 50:50 (red), 70:30 (blue) and 80:20 (green) weight percent mixes, sintered under a short 0.5 hour dwell at 1250 °C.

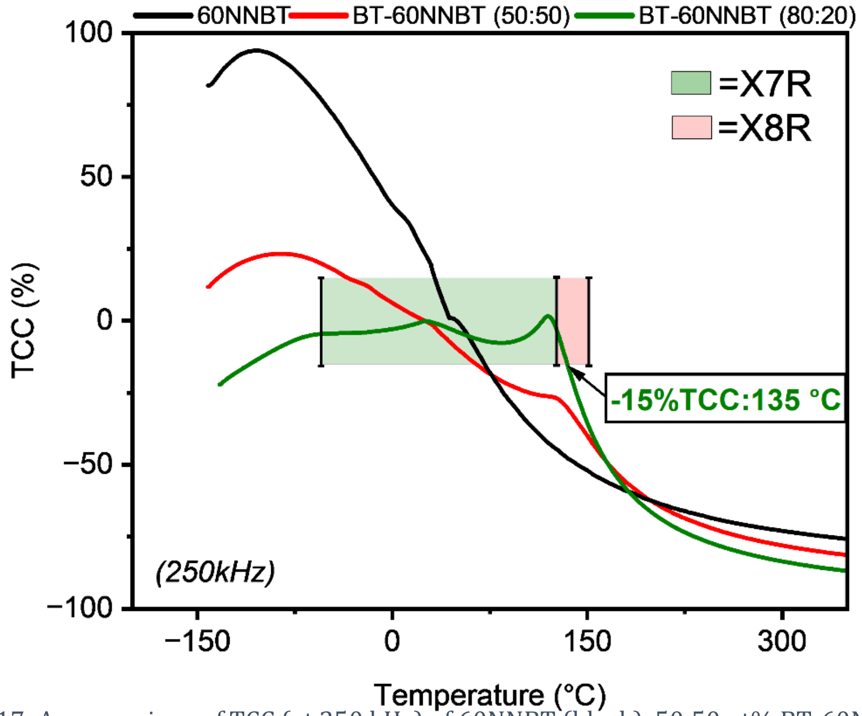

Figure 5.17: A comparison of TCC (at 250 kHz) of 60NNBT (black), 50:50wt% BT-60NNBT used for investigating homogenisation rates between the two components (red), and the optimised TCC BT-60NNBT (80:20wt%) composite that meets X7R rated TCC specification (green).

good dielectric behaviour for a range in excess of the X7R operating window. All composites appear to exhibit the onset of high thermally activated losses, likely a DC conduction contribution, however this onset is delayed according the starting ratio of composite components. The largest loss response is observed in the most NNBT rich starting ratio (30:70), whilst the 80:20 composite that yields X7R rated TCC offers the lowest loss response at low temperatures and delays the onset of the thermally activated contribution to higher temperatures relative to the other composites formed.

5.6.4 Reproducibility of the X7R rated BT-60NNBT Composite

Since the composite system is formed from a 0.5 hour hand mixture of its BT and NNBT components, considering the inherent uncontrollability of this mixing mechanism (relative to wet ball milling methods) it is important to assess the reproducibility of the X7R rated dielectric response observed for the 80:20 wt.% BT:60NNBT composite. Was the stable TCC response achieved as a fortunate result of the phase distribution and particle morphology post mixing? Considering the reliance of the composite response on diffusion rates between its component

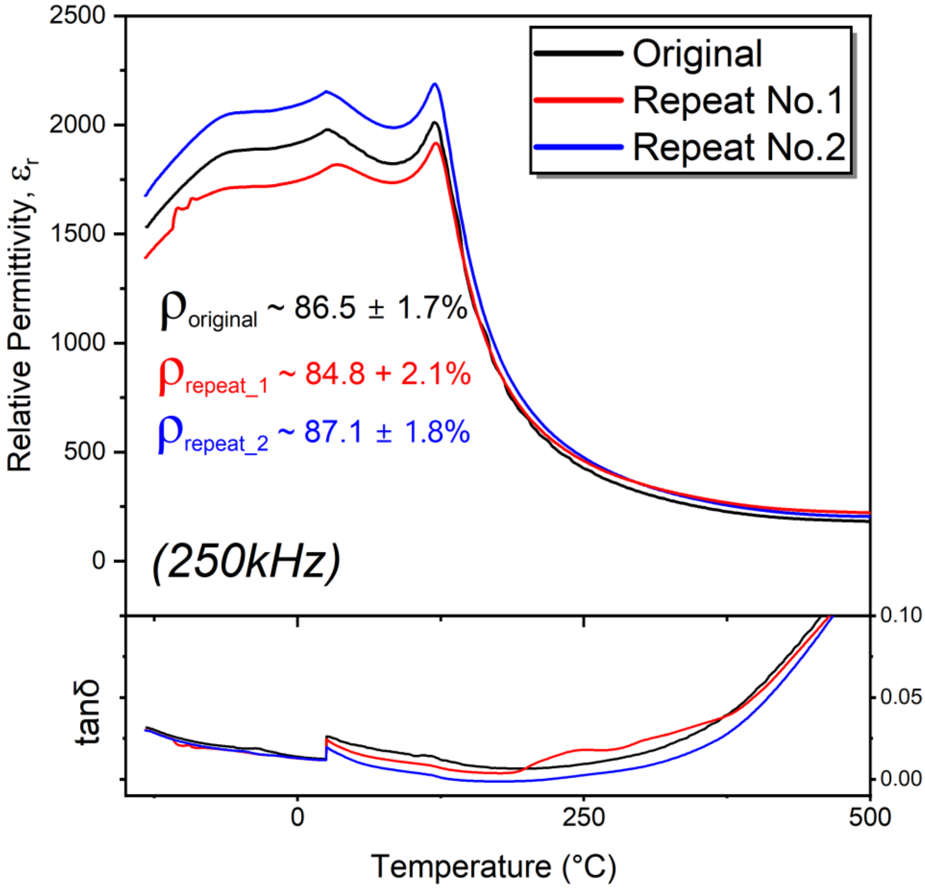

Figure 5.18: The relative permittivity and dielectric loss (250 kHz) for 3 hand mixed BT-60NNBT composites. Variation is observed between the permittivity and tan δ, although this is relatively small and is likely a product of density variations with limited consistency inherent of a pestle and mortar mixing of the composite components.

phases, it is important to understand how sensitive the dielectric response of the composite system is to pre-sintering processing. Three different 80:20 wt.% BT-60NNBT batches were synthesised via the same hand mixed approach, with DS measurements taken for each and shown in figure 5.18. Variable permittivity magnitudes and losses are evident for the three different batches, with the highest magnitude of ~2100 observed from the second repeat batch and the lowest magnitude of ~1750 observed for the first repeat batch. This is reflected in the density variation that exists between these repeated composites, between 84.8 ± 2.1 – 87.1 ± 1.8 % of the theoretical density, respectively. Comparison of the TCC variation for each batch is shown in figure 5.19.

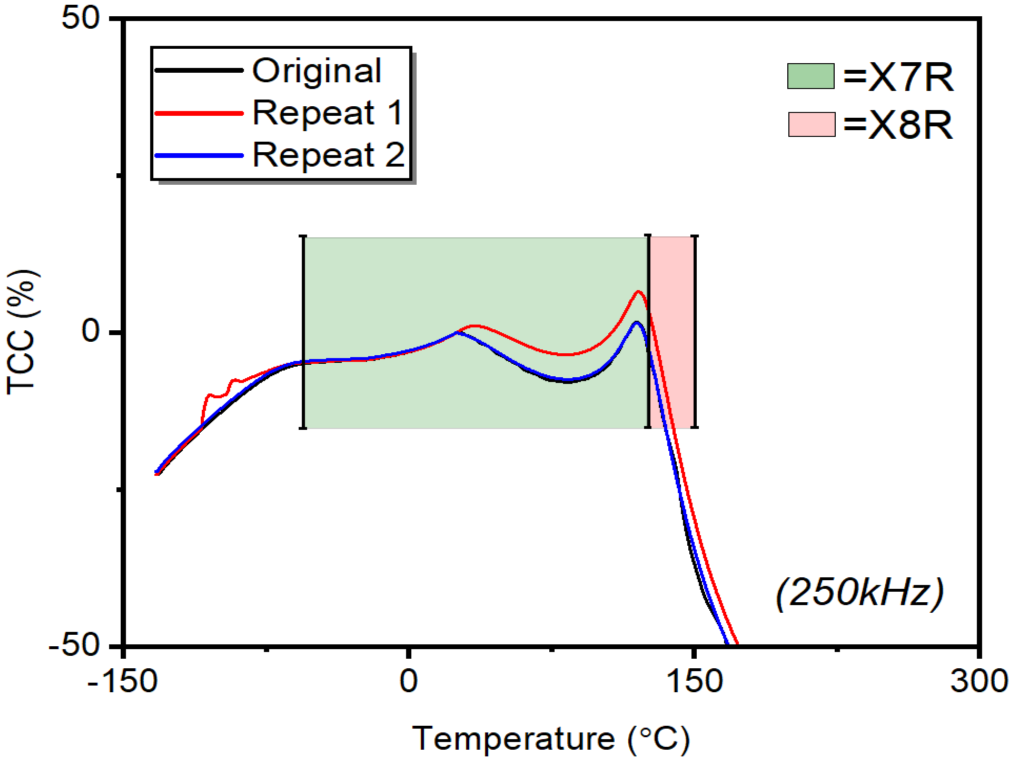

Figure 5.19: Reproducibility of the BT-60NNBT (80:20 wt.%) composite, validated as a result of the similarity in TCC response of three independent batches.

TCC removes the influence of density effects and instead shows the inherent temperature dependence of permittivity for each of the repeat composites via comparison of their associated shapes. The TCC profiles for the original batch and the second repeat are superimposable, with some variability observed within the first repeat regarding the intensity of the high temperature BT related permittivity peak relative to the low temperature NNBT related response. Nevertheless, all repeats show a 'biphasic' composite polarisation response constituent of high and low temperature polarisation contributions from its BT and NNBT component phases, respectively, and each with a magnitude comparable to the other. This behaviour is somewhat insensitive to the uncontrollability of hand mixing. This consistency in TCC response suggests microstructural variability is confined to density variations as opposed to major changes in phase fraction or composition. The resulting X7R TCC rating is achieved for all repeats, with a 1 °C variability in $T_{-15\%}$ (the temperature corresponding to the -15 % TCC threshold being met) between repeat 2 and the other two batches.

Dielectric losses, shown in figure 5.18, are almost identical at sub-ambient conditions but do vary between these repeated composites at elevated temperatures, with the original sample offering the highest losses, the second repeat batch the lowest and the first batch in between the two. An anomaly in the losses of the first repeat composite at ~250 °C breaks this trend for a brief period, something not reflected in the permittivity response. Within the X7R operating range, losses vary by a maximum of ~ 0.011 between the three samples, with the highest tan δ of ~0.026 recorded within this range for the original batch composite. This dielectric behaviour is only lost at ~400 °C for all repeated composites, with this dielectric response again appearing insensitive to any microstructural variation imparted by hand mixing of the component phases. Frequency dependence in both permittivity and dielectric losses is observed across both the low temperature and high temperature permittivity responses associated to both the NNBT and BT component phases, figure A7, A8 and A9 in appendix 1. At ~ -46 °C, a spike in the tan δ response can be seen which is subsequently relaxed out with increasing frequencies. A progressive decrease in the high temperature losses with frequency indicates a relaxation of space charge effects. Frequency dependence in permittivity is more significant at lower temperatures where the polarisation response is dominated by the 60NNBT relaxor component of the composite. Its effects on the BT related permittivity peak are minimal, with slight increases in permittivity maxima with frequency. Despite this, from 10 kHz to 1 MHz, the X7R TCC conditions are sustained whilst retaining good dielectric responses.

5.6.5 SEM of BT-60NNBT (80:20 wt.%) Composites

SEM reveals clear compositional heterogeneity is retained within these BT-60NNBT composites post sintering. Elemental mapping via EDX, particularly for Na and Nb in figure 5.20, show clear concentrations confined to regions a few microns in length, relative uniformly dispersed amongst the surrounding grain structure. The surrounding 'matrix' is comparatively dark suggesting little to no diffusion of the Na and Nb into this matrix. The converse effect can be seen within the Ba and Ti maps, with darker regions corresponding to low Ba and Ti concentrations (relative to the surrounding matrix) superimposable upon these Na and Nb rich regions. It is important to note that a detectable signal does still exist for Ba and Ti within these heterophase regions, and so the map suggests the smaller Na and Nb 'rich' regions correspond to NNBT phases that originate from the initial pre-calcined 60NNBT mixed with the BT.

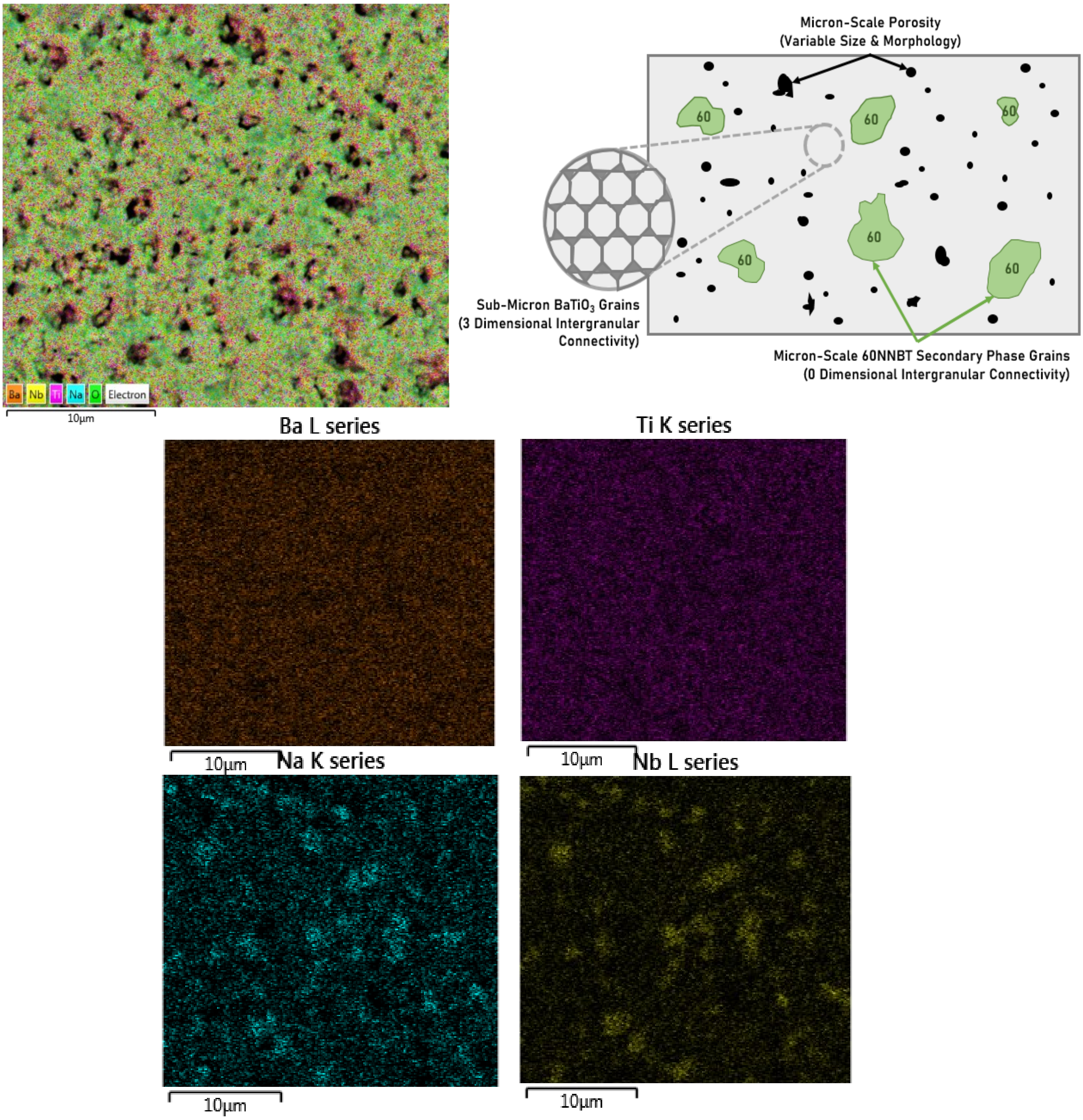

Figure 5.20: SEM/EDX elemental mapping of Ba, Ti, Na and Nb within the composite. Clear secondary phases relating to 60NNBT can be seen as evidence of the compositional heterogeneity inferred from the dielectric response.

The visual disparity in size between such Na and Nb rich regions relative to the surrounding Ba and Ti grain structure confirm these secondary regions to originate from the mixed 60NNBT, given the 80:20 wt.% pre-sintered ratio of BT:60NNBT. Intragranular concentration variation of Na and Nb within these NNBT secondary phases is inferred from variable pixel intensity in the corresponding elemental maps. This would suggest compositional heterogeneity within these secondary phase grains. However, consideration of the inherent resolution limitations of EDX, particularly so for the mapping of Na, suggests such concentration gradients within these NNBT regions observed should be considered with reasonable uncertainty. Na and Nb signals are detected amongst the BT based matrix (outside of the smaller NNBT regions) suggesting some diffusion of these species into the BT during sintering. Additional secondary phases, such as those evident in the 70NNBT of the bilayer sample, do not seem apparent in the composite structure – although EDX spot analyses of the secondary NNBT phases would be necessary to associate a perovskite stoichiometry and rule out any other structural formations. The overall microstructure composed of NNBT phase grains homogeneously distributed within a BT polycrsytal matrix phase is schematically visualised in figure 5.20, reflecting these EDX results.

5.6.6 Impedance Spectroscopy of (80:20) BT:60NNBT Composite

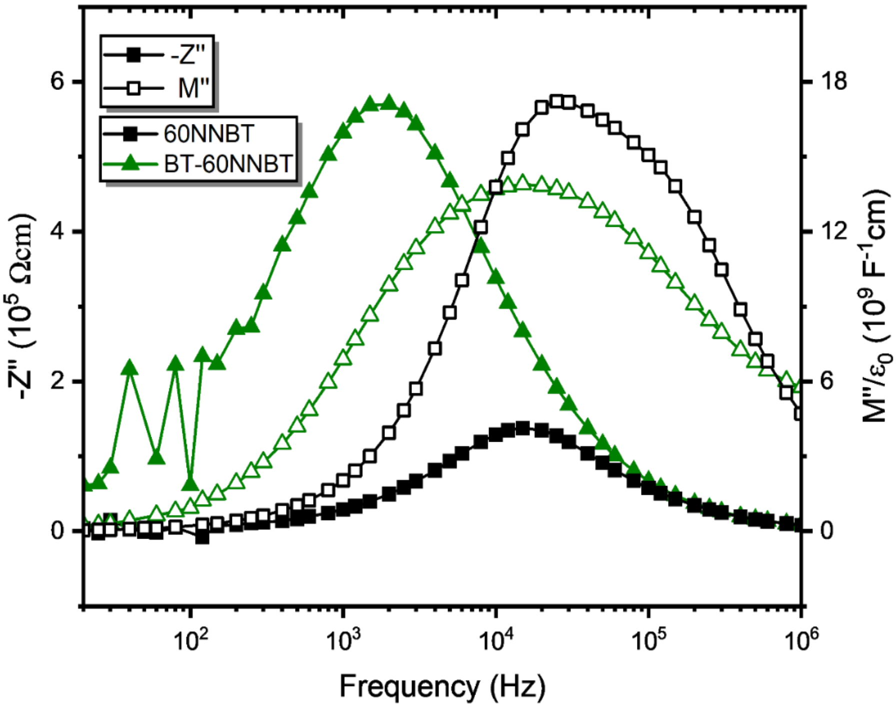

Figure 5.21: The M'' and Z'' spectroscopic plots for 60NNBT and the BT-60NNBT composite at 550 °C. Both responses are indicative of heterogeneous electrical microstructures based on the broadness of these Debye peaks and the variable fmax observed.

The IS responses of the BT-60NNBT sample is indicative of a heterogeneous response expected for a binary composite composed of materials with differing grain sizes and conductivities. The Debye peaks in the spectroscopic responses of M'' and Z'' for the BT-60NNBT composite are plotted in figure 5.21. These M''/Z'' peaks are far broader than the expected FWHM of 1.14 decades of an ideal parallel RC element, with the composite exhibiting an M'' FWHM ~2.7 decades. The f_{max} associated to the Z'' and M'' peak maxima are comparatively disparate and suggest the presence of a heterogeneous electrical microstructure consistent of components with variable time constants. 60NNBT, overlaid, shows a similar heterogeneity in its electrical microstructure with a secondary element of varied capacitance and lower resistivity clearly visible on the M'' peak in a high frequency shoulder. Despite this, the broadness and disparity in f_{max} in the composite is clearly more pronounced when compared to 60NNBT. This effect of electrical heterogeneity in the BT-60NNBT composite is also represented in the depression and elongation of the Z* arc, figure 5.22. This is potentially indicative of a serial distribution of parallel RC elements, each of varied time constants and corresponding to the different phases composing the physical microstructure. The composite, like its components, does not show any low frequency responses/dispersions indicative of ionic conductivity – suggesting the conduction within the composite is electronic in nature.

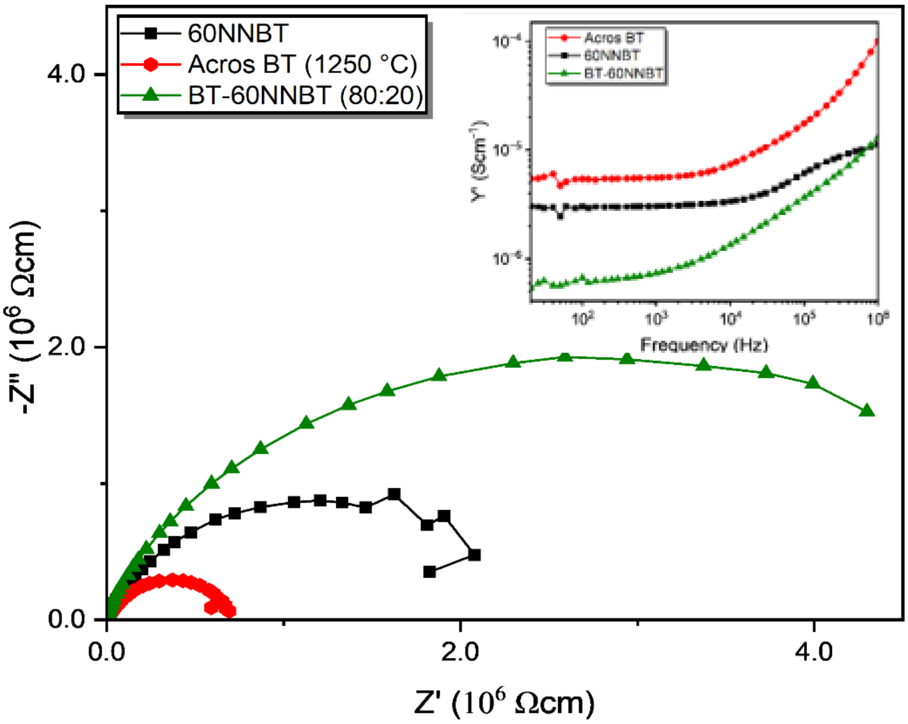

Figure 5.22: A comparison of the complex impedance response of the BT-60NNBT (80:20) composite relative to its constituents (independently sintered) for 550 °C. The Inset reveals the spectroscopic admittance (Y') response of these three materials. The overall effect is greater DC resistivity for the composite compared to the individual materials.

When the IS responses of the composite components are overlaid against the response of the composite itself, the capacitance (C') response, figure 5.23, appears very much dominated by the 60NNBT response, virtually overlaid upon the 60NNBT C' plot. The capacitance magnitude is shown in figure 5.23 to be ~10^{-11} Fcm^{-1}, suggesting the composite IS response is dominated by its bulk component, as opposed to any grain boundary components or surface contributions. Only one clear C' plateau is evident for the composite material. The suggestion of a serial connectivity between multiple parallel RC elements, each referencing a component phase of the physical microstructure, is impossible to deconvolute from this C' plot. The electrical microstructure is probably better modelled with a constant phase element (CPE) that will account for the non-ideal response observed in the low frequency C’ dispersion and the depression/elongation of the Z* arc.

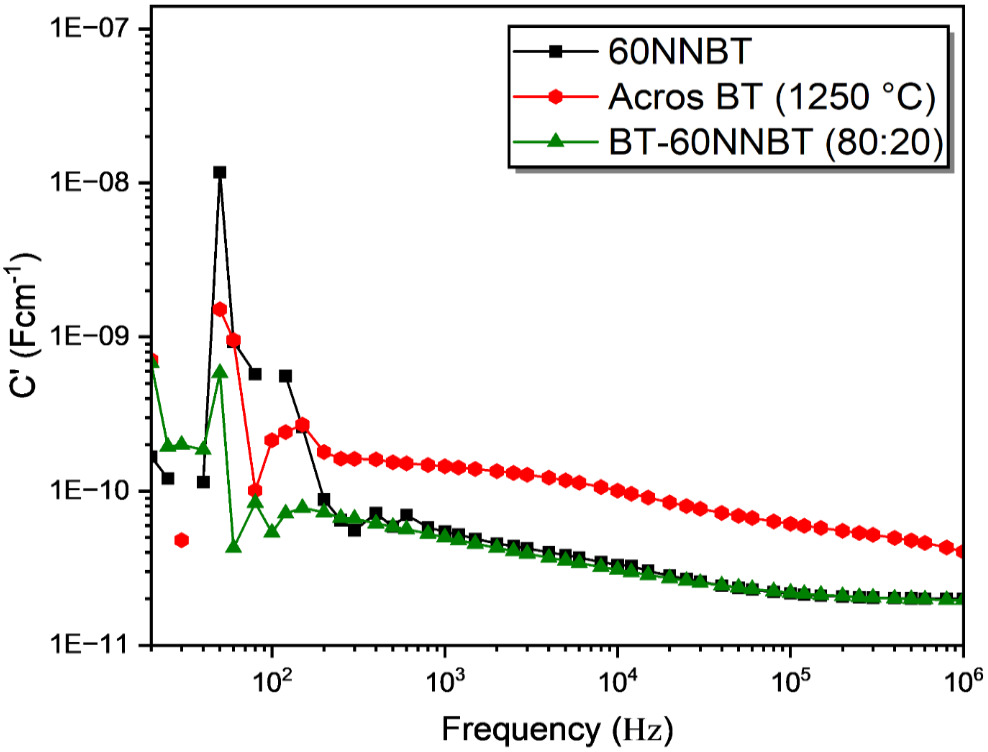

Figure 5.23: The C' spectroscopic response of BT and 60NNBT (the components of the composite) and the BT--60NNBT composite structure for 550 °C.

The total DC conductivity of the composite system is calculated from the inverse of the diameter of its associated Z* arc, and is plotted against temperature alongside independently sintered NNBT compositions in figure 5.24, including those measured by Foeller [136] towards the BT rich end of the NNBT solid solution. Based on the greater width of the composite Z* arc relative to its component materials, figure 5.22, the total DC resistivity is larger for the composite relative to its component materials. The low frequency Y’ spectroscopic data in figure 5.22 inset directly corresponds to the DC conductivity of the samples and is another representation of this resistivity/conductivity relationship. The total DC conductivity of the composite is lower with respect to all synthesised NNBT compositions and those NNBT compositions towards the BT boundary of the solid solution[136], shown in figure 5.24. The activation energy associated to the electronic conduction is consistent with that observed in 87.5NNBT, forming two discrete energies – a lower energy ~1.30 ± 0.02 eV at lower temperatures and increasing to ~ 1.51 ± 0.01 eV at higher temperatures.

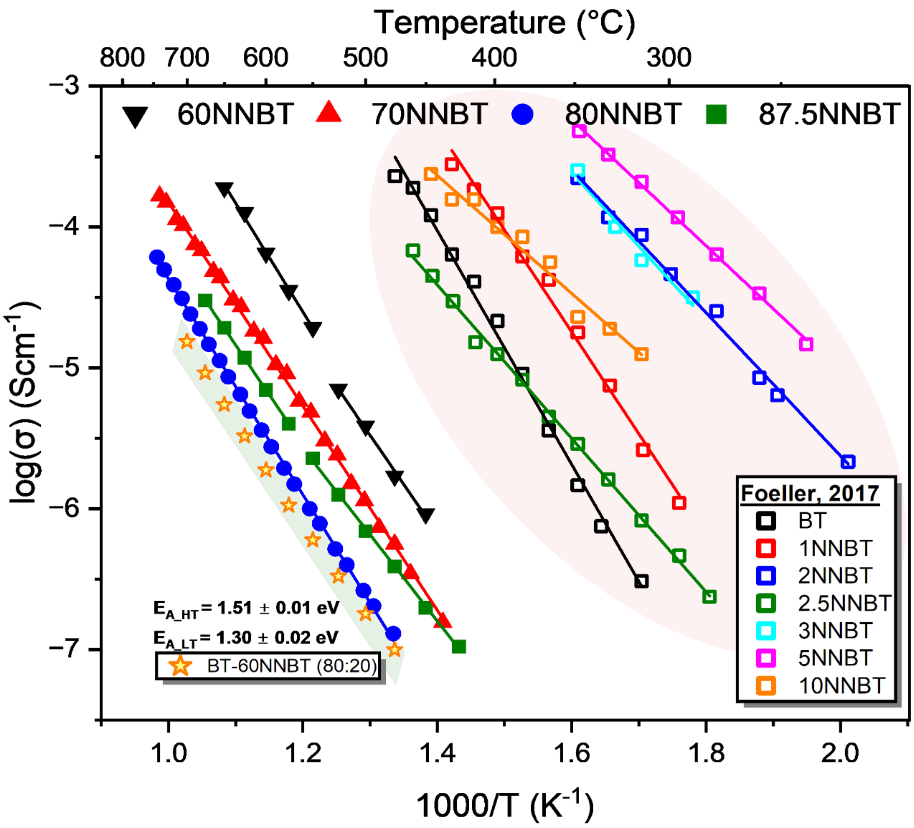

Figure 5.24: The total DC conductivity of the BT-60NNBT composite relative to the other synthesised NNBT materials.

5.7 Discussion

Investigations into the inter-diffusion rates between an equimolar mixture of 70 and 87.5NNBT compositions revealed that a short sintering dwell of 0.5 hours was sufficient for the 70/87.5NNBT equimolar composite to appear to homogenise, forming a single monolithic equilibrium 80.3NNBT. This was inferred from the single permittivity peak observed in figure 5.14. The dwell period was sufficient for interdiffusion to occur but not for complete grain coarsening and densification to occur, inducing a lower permittivity relative to independently sintered 70 and 87.5NNBT plotted on figure 5.14. No XRD or SEM characterised this sample, and so complete compositional homogenisation cannot be verified. Regardless, the significance of this analysis was to understand how quickly diffusion and associated permittivity variation would occur relative to its components, since compositional variation at the interface of a multilayer is only an issue when the permittivity profile and associated TCC begins to vary. High diffusion rates clearly exist between these two NNBT compositions, limiting the industrial practicality of this 70/87.5 NNBT bilayer when sintered without a diffusion barrier and inducing the 10 % thickness fraction the interdiffusion layer constitutes in the 70/87.5NNBT bilayer reported by Kerridge [149].

Expanding the diffusion study to equimolar mixes of NNBT with BT revealed the ability to preserve compositional heterogeneity post sintering provided the difference in NNBT composition was sufficiently large. Compositional heterogeneity was inferred from figure 5.15 from the appearance of two main dielectric anomalies, ~ -90 and 127 °C, respectively. The former exhibits an associated diffusivity, which combined with its sub ambient T_m and figure 5.7, likens such to a relaxor NNBT type material. Each of the composites exhibit a sub ambient permittivity peak with comparable T_m, suggesting the NNBT composition formed is comparable and originates from this relaxor centre of the NNBT solid solution. This is despite a range of NNBT materials being utilised in the pre sintered composites.

The peak at ~ 127 °C shares a T_m with that expected of the ferroelectric-paraelectric tetragonal-cubic phase transition of BT. Considering such was used within the pre-sintered composite at 50 wt.% starting fraction, this high temperature peak is considered predominantly to be the polarisation response of undoped BT retained within the sintered composite. The fact that this BT related permittivity peak increases in magnitude when the NNBT composition utilised within the pre-sintered composite originates from the relaxor centre of the solid solution, suggests higher volume fractions of BT are retained in the post sintered composite. Consequently, lower diffusion rates are associated.

An energetic well, analogous to the NNBT T_m map across the solid solution constructed and shown in figure 5.7, may exist towards the centre of the solid solution. This is inferred not only by this higher volume fraction of BT preserved within the composite post sintering, but that the NNBT composition formed within the composite post sintering appear to be comparable in originating from this relaxor centre, sharing comparable T_m i.e. this NNBT composition is thermodynamically stabilised. A bilayer system may have exhibited a smaller interdiffusion layer and a less pronounced variation in its associated permittivity response had one of its components originated from the relaxor centre of the solid solution. A longer dwell period of 5 hours for the composites would be necessary to validate this theory, however, matching the sintering conditions of the bilayer [149]. The requirement of such a relaxor NNBT component for industrial feasibility and removal of Au diffusion barriers may need to be integrated into the optimisation code generated by Kerridge et al [232] to deduce a new optimal 60NNBT-containig bilayer fraction to satisfy X7R criteria.

The notable effect of retaining such compositional heterogeneity in the form of a biphasic ceramic composite post sintering is an enhancement in the thermal stability of permittivity relative to the independent component materials, 60NNBT and BT, as proposed. 60NNBT and BT are complimentary in sustaining stable TCC consequent of the distribution in T_m amongst the two phases: 60NNBT contributing to the low temperature permittivity response and BT providing the high temperature permittivity response. It is apparent from figure 5.15 and 5.17 that under equimolar mixing conditions between 60NNBT and BT, X7R and X8R TCC specifications are still not met. $T_{-15\%}$ falls short of the high temperature 125/150 °C operating bound by ~ 30 °C. Increasing the volume fraction of BT retained post sintering should increase the associated permittivity peak ~127 °C and improve the high temperature TCC characteristics of the resulting composite. By varying the starting weight percent ratios of BT and 60NNBT mixed prior to sintering, specifically towards a higher BT content, given the lower diffusion kinetics found to exist between BT-60NNBT relative to other NNBT materials, the high temperature permittivity peak associated with the BT matrix could be controlled. With the aim of producing a BT permittivity peak of similar magnitude to the low temperature 60NNBT related permittivity response, the overall composite response could be 'levelled', ultimately producing a more thermally stable dielectric response.

The 80:20 wt.% BT:60NNBT composition was identified to optimise the TCC response, with $T_{-15\%}$ shifted to higher temperatures with increasing BT content retained post sintering, to an optimised 135 °C for this starting mixture thereby meeting X7R TCC requirements, shown in figure 5.17. A permittivity magnitude ~2000 was observed at room temperature with good dielectric behaviour with an associated tan $\delta < 0.05$ until 400 °C, clear from figure 5.16. This response was (relatively) repeatable for this hand-mixed composite system, with minimal variation in TCC indicating the inherent polarisation-temperature dependence could be repeated, but the magnitude in permittivity variation between repeat samples suggested that the level of porosity was comparatively less controllable. Not only did this composite system exhibit a TCC more stable than its constituent components, but a total DC conductivity lower than its component materials, clear from figure 5.24.

SEM and EDX analysis of this composite in figure 5.20 reveals a 3-0 intergranular connectivity [140] between the BT matrix phase and homogeneously distributed 60NNBT secondary phases. This is shown schematically in figure 5.20. Intragranular compositional gradients appear within the secondary NNBT phases, inducing a diffuse low temperature permittivity response in the composites that is broader than that expected of the independently sintered 60NNBT in figure 5.6. The assignment of the low and high temperature permittivity anomalies to these respective NNBT and BT phases, inferred initially from the equimolar composite of figure 5.15 and 5.16, appears correct based on these EDX results.

The magnitude of the BT associated permittivity peak, although ideal in its compatibility with the 60NNBT low temperature response, was far lower than perhaps expected given its 80 wt.% fraction in the composite, composing the matrix phase of the composite clear from the SEM/EDX of figure 5.20. It was certainly considerably lower than the permittivity associated to a nominally, independently sintered BT sample. The strain imposed by its local environment constituent of pores, comparatively larger, irregularly shaped 60NNBT grains and the compositional gradient associated to the secondary phase, may have supressed the polar modes associated to the typically large ferroelectric-paraelectric peak in BT. Simultaneously, the small BT grain sizes and high grain boundary density, evident in the composite from SEM, may also limit the formation of long range ferroelectric domains that sustain the high permittivity response. The extensive porosity network evident in SEM and from density measurements could also significantly lower the average field BT grains were exposed to, also contributory to the observable lower permittivity magnitude associated to the BT when used as the composite matrix.

This porosity, a product of the low sintering dwells utilised to achieve the necessary compositional heterogeneity for TCC stabilisation, is a significant drawback to the current composite system. The reliance of the composite to the retention of compositional heterogeneity limits the ability to sinter for extended periods or at higher temperatures that would typically attain higher densities. The mass transport necessary to remove porosity would be deleterious to the compositional heterogeneity and stable X7R TCC. Electric field strength (something not tested here) is likely to be a weakness of the current system based on the extensive porosity and air that is sustained within the sample post sintering. Use of sintering aids such as glass or oxides that are capable of forming a liquid phase during sintering could aid in the densification of the composite at such short sintering dwells. Nevertheless, this 3-0 NNBT based composite system does provide an alternative macrostructure to the bilayer systems discussed previously where the useful dielectric properties of NNBT components can be utilised to attain a high permittivity, low loss dielectric that meets X7R TCC rating. There are no concerns relating to delamination, nor is there a necessity for expensive Au diffusion barriers. The formation of the composite, after a short mixing period of 0.5 hours, represents a potentially less industrially disruptive system with respect to the bilayer structures for a single slurry could theoretically be cast.

5.8 Conclusions

Diffusion rates between 70 and 87.5NNBT are sufficiently high enough to induce complete dielectric homogenisation in an equimolar composite formed of these two materials. This explains the formation of a ternary interdiffusion layer in 70/87.5NNBT bilayer system by Kerridge [149] in the absence of a physical interdiffusion barrier, with a thickness that accounts for 10 % of the total bilayer and is deleterious to X7R TCC rating. Interdiffusion and compositional homogenisation can be limited when one component originates from the relaxor centre of the NNBT solid solution. This is suggested to be the product of enhanced thermodynamic stability for compositions towards the NNBT solution centre, limiting the driving force for compositional diffusion between components when a BT-relaxor composite is sintered compared to one utilising NNBT materials closer to the end members. Consequently, a composite mixture of relaxor NNBT and BT could be retained post sintering with a heterogenous dielectric response composed of a high temperature BT related permittivity peak and a low temperature relaxor NNBT response. This is analogous to a core shell microstructure where a BT permittivity peak is coupled with a low temperature 'paraelectric' shell response. Since multilayers were reliant on a similar effect of high and low temperature permittivity contributions to provide an overall thermally stable dielectric response, these composite architectures provided an alternative microstructure to attain TCC stabilisation.

A ceramic composite architecture composed of a BT matrix and homogeneously distributed 60NNBT secondary phase, with a 3-0 physical connectivity, is able to achieve a reproducible X7R rated permittivity response when its constituent phases are hand mixed in a 80:20 wt.% fraction and sintered with a short dwell period (0.5 hours). Electronically insulating behaviour extended far beyond the X7R operating temperature range, with $\tan \delta < 0.05$ up to ~400 °C, whilst the magnitude of permittivity achieved, ~2000, is sufficiently large to afford flexibility in MLCC chip design without thinner or additional layers necessary to achieve a specified device capacitance (relative to a lower permittivity material). The composite is hindered by extensive porosity consequent of the short dwell periods used to retain the necessary compositional heterogeneity that sustains the stable TCC response. The largest relative density achieved for the composite system was ~87.1 ± 1.8 % of the theoretical value. This would, although not tested, limit the electric field induced breakdown strength of the material. This would be deleterious to its inclusion within a MLCC based on the somewhat high electric fields sustained across the dielectric layers consequent of their low thickness, negating the aforementioned qualities as a dielectric.

The next stage in the development of these NNBT based ceramic composites as temperature stable dielectrics will be to push $T_{-15\%}$ from ~ 135 °C to 150 °C or above, thereby extending the TCC stability from X7R to X8R rating. Results chapter 2 will focus on the utilisation of A site doped BT with increased T_C (relative to undoped BT) as the matrix phase of the composite to push the high temperature permittivity peak in these composites, associated to the matrix phase, to higher temperatures and achieve X8R rated TCC.

5.9 Appendix A

5.9.1 NNBT Refinements

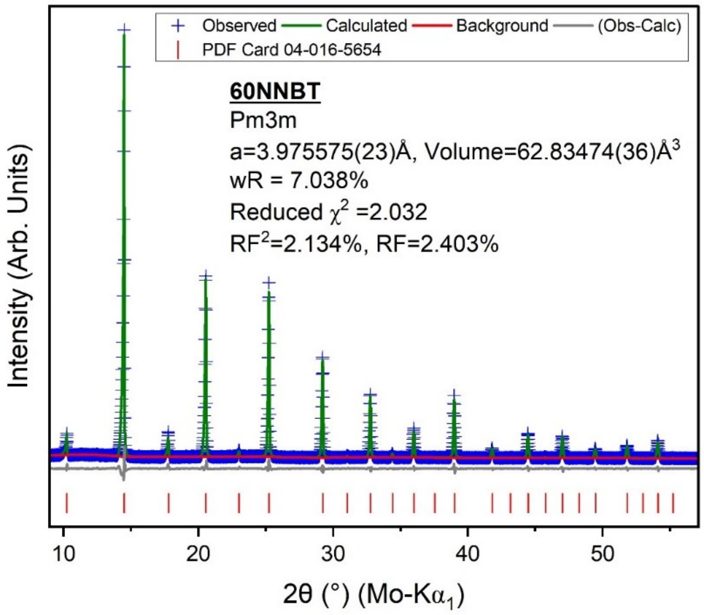

Figure A1: Rietveld refinement of the 60NNBT XRD diffraction pattern, fit to a Pm3m cubic symmetry with starting parameters sourced from the named PDF file.

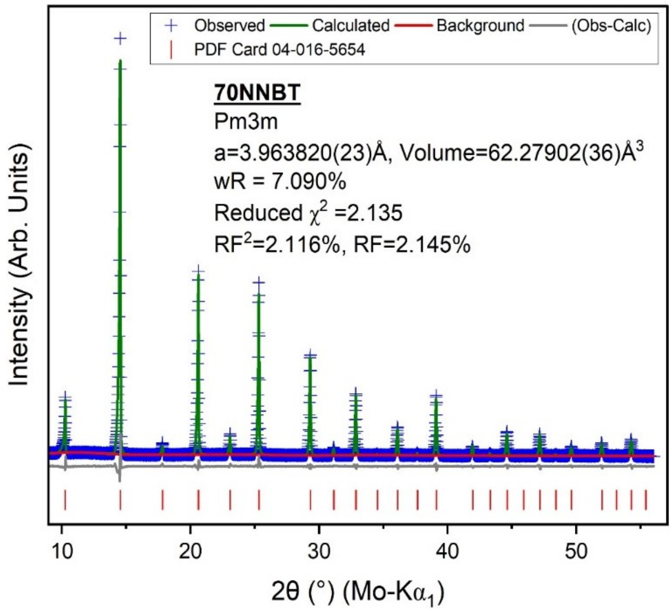

Figure A2: Rietveld refinement of the 70NNBT XRD diffraction pattern, fit to a Pm3m cubic symmetry with starting parameters sourced from the named PDF file.

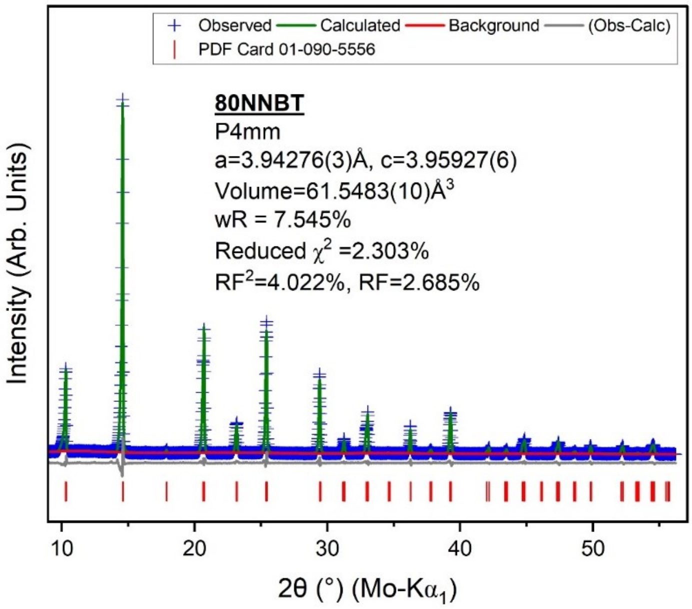

Figure A3: Rietveld refinement of the 80NNBT XRD diffraction pattern, fit to a P4mm tetragonal symmetry with starting parameters sourced from the named PDF file.

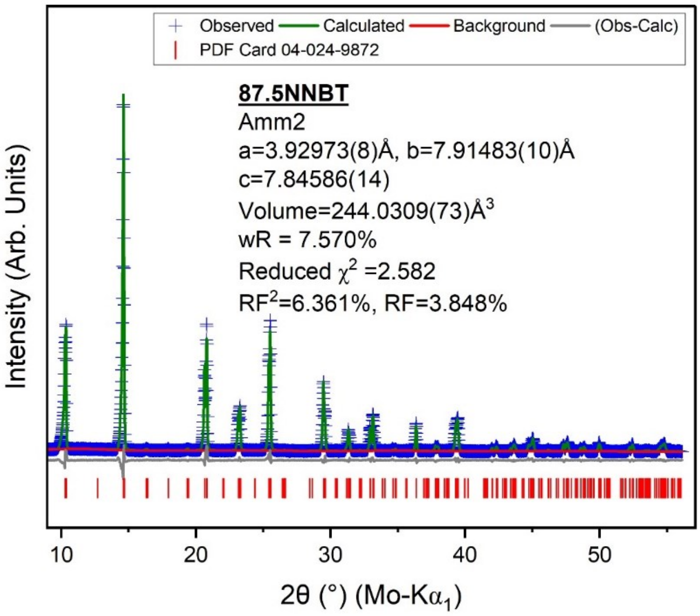

Figure A4: Rietveld refinement of the 87.5NNBT XRD diffraction pattern, fit to an Amm2 orthorhombic symmetry with starting parameters sourced from the named PDF file.

Table A1: The refined atomic site coordinates, fractions and Uiso parameters for synthesised 60NNBT

Atom	x	y	z	Site Fraction	Multiplicity	Uiso
Na	0	0	0	0.581(10)	1	0.0090(12)
Ba	0	0	0	0.382(2)	1	0.0087(3)
Nb	0.5	0.5	0.5	0.570(3)	1	0.0110(3)
Ti	0.5	0.5	0.5	0.398(6)	1	0.0070(8)
O	0	0.5	0.5	0.999(4)	3	0.0098(5)

Table A2: The refined atomic site coordinates, fractions and Uiso parameters for synthesised 70NNBT

Atom	x	y	z	Site Fraction	Multiplicity	Uiso
Na	0	0	0	0.706(4)	1	0.0147(8)
Ba	0	0	0	0.298(1)	1	0.0088(3)
Nb	0.5	0.5	0.5	0.694(1)	1	0.0102(2)
Ti	0.5	0.5	0.5	0.297(2)	1	0.0061(8)
O	0	0.5	0.5	1.018(4)	3	0.0110(5)

Table A3: The refined atomic site coordinates, fractions and Uiso parameters for synthesised 80NNBT

Atom	x	y	z	Site Fraction	Multiplicity	Uiso
Ba	0	0	0.002(11)	0.201(1)	1	0.0113(4)
Na	0	0	0.02(20)	0.781(4)	1	0.0107(7)
Ti	0.5	0.5	0.498(28)	0.201(2)	1	0.0059(11)
Nb	0.5	0.5	0.495(5)	0.793(1)	1	0.0097(2)
O(1)	0.5	0	0.444(4)	0.964(7)	2	0.0067(13)
O(2)	0.5	0.5	-0.033(3)	1.096(11)	1	0.022(3)

Table A4: The refined atomic site coordinates, fractions and Uiso parameters for synthesised 87.5NNBT

Atom	x	y	z	Site Fraction	Multiplicity	Uiso
Na	0	0.7585(8)	0.0011(18)	0.85(4)	4	0.0107(5)
Ba	0	0.7590(9)	-0.0038(27)	0.126(1)	4	0.0136(6)
Nb(1)	0.5	0	0.2455(4)	0.87(1)	2	0.00823(30)
Ti(1)	0.5	0	0.2576(46)	0.14(1)	2	0.0020(22)
Nb(2)	0.5	0.5	0.2438(13)	0.88(1)	2	0.0056(2)
Ti(2)	0.5	0.5	0.2678(29)	0.11(1)	2	0.0131(2)
O(1)	0	0	0.2875(17)	1.05(2)	2	0.0175(42)
O(2)	0	0.5	0.2302(25)	0.97(2)	2	0.0136(32)
O(3)	0.5	0.7355(26)	0.2698(14)	1.16(1)	4	0.0266(16)
O(4)	0.5	0	0.0068(64)	0.86(2)	2	0.0111(30)
O(5)	0.5	0.5	-0.0208(46)	0.84(2)	2	0.0230(40)

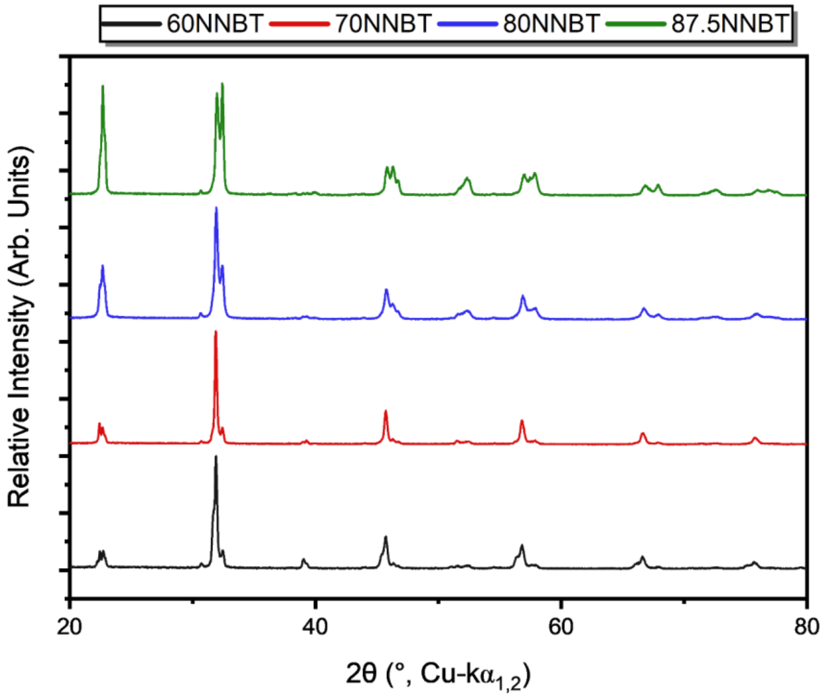

Figure A5: The XRD diffraction patterns for the NNBT compositions after calcination at 1000 °C for 6 hours. There is an observable lack of phase purity, particularly for the 60 and 70NNBT materials considering the cubic symmetry shown post sintering.

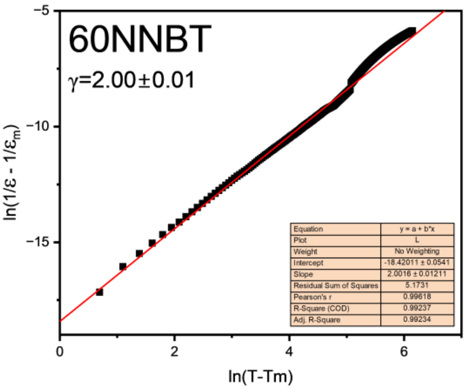

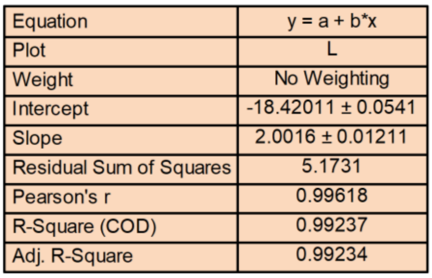

Equation	y = a + b*x
Plot	L
Weight	No Weighting
Intercept	-18.42011 ± 0.0541
Slope	2.0016 ± 0.01211
Residual Sum of Squares	5.1731
Pearson's r	0.99618
R-Square (COD)	0.99237
Adj. R-Square	0.99234

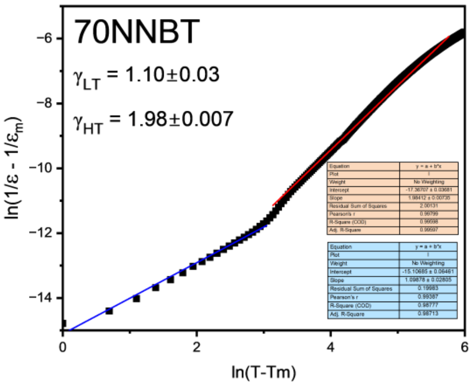

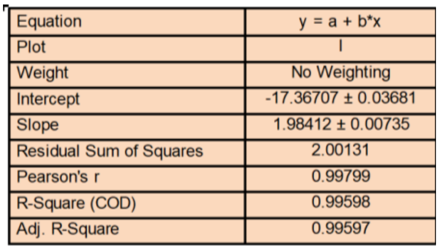

Equation	y = a + b*x
Plot	I
Weight	No Weighting
Intercept	-17.36707 ± 0.03681
Slope	1.98412 ± 0.00735
Residual Sum of Squares	2.00131
Pearson's r	0.99799
R-Square (COD)	0.99598
Adj. R-Square	0.99597

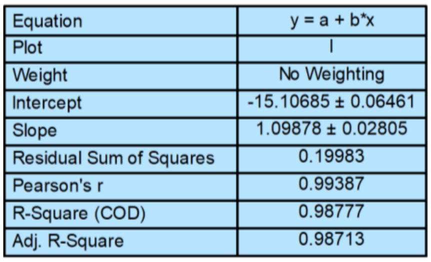

Equation	y = a + b*x
Plot	I
Weight	No Weighting
Intercept	-15.10685 ± 0.06461
Slope	1.09878 ± 0.02805
Residual Sum of Squares	0.19983
Pearson's r	0.99387
R-Square (COD)	0.98777
Adj. R-Square	0.98713

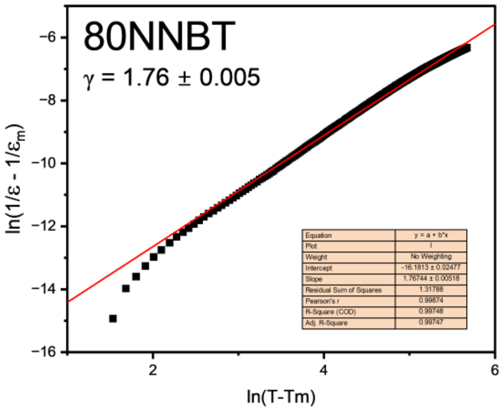

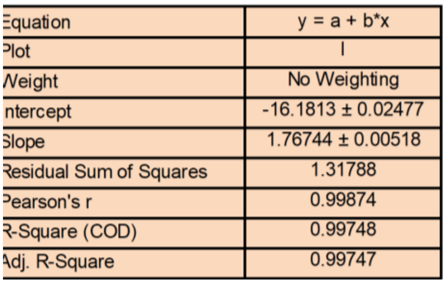

Equation	y = a + b*x
Plot	I
Weight	No Weighting
ntercept	-16.1813 ± 0.02477
Slope	1.76744 ± 0.00518
Residual Sum of Squares	1.31788
Pearson's r	0.99874
R-Square (COD)	0.99748
Adj. R-Square	0.99747

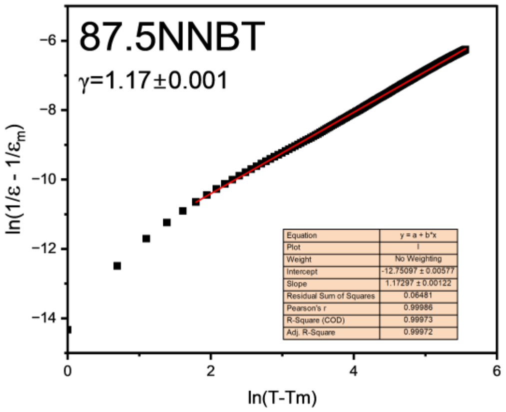

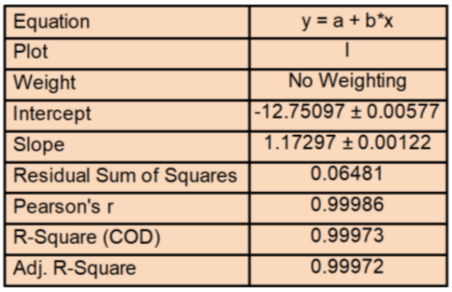

Equation	y = a + b*x
Plot	I
Weight	No Weighting
Intercept	-12.75097 ± 0.00577
Slope	1.17297 ± 0.00122
Residual Sum of Squares	0.06481
Pearson's r	0.99986
R-Square (COD)	0.99973
Adj. R-Square	0.99972

Figure A6: The calculation of the γ relaxor coefficient for each NNBT composition based on the logarithmic Curie-Weiss equation 5.5. The linear fit parameters for each plot are shown on the right.

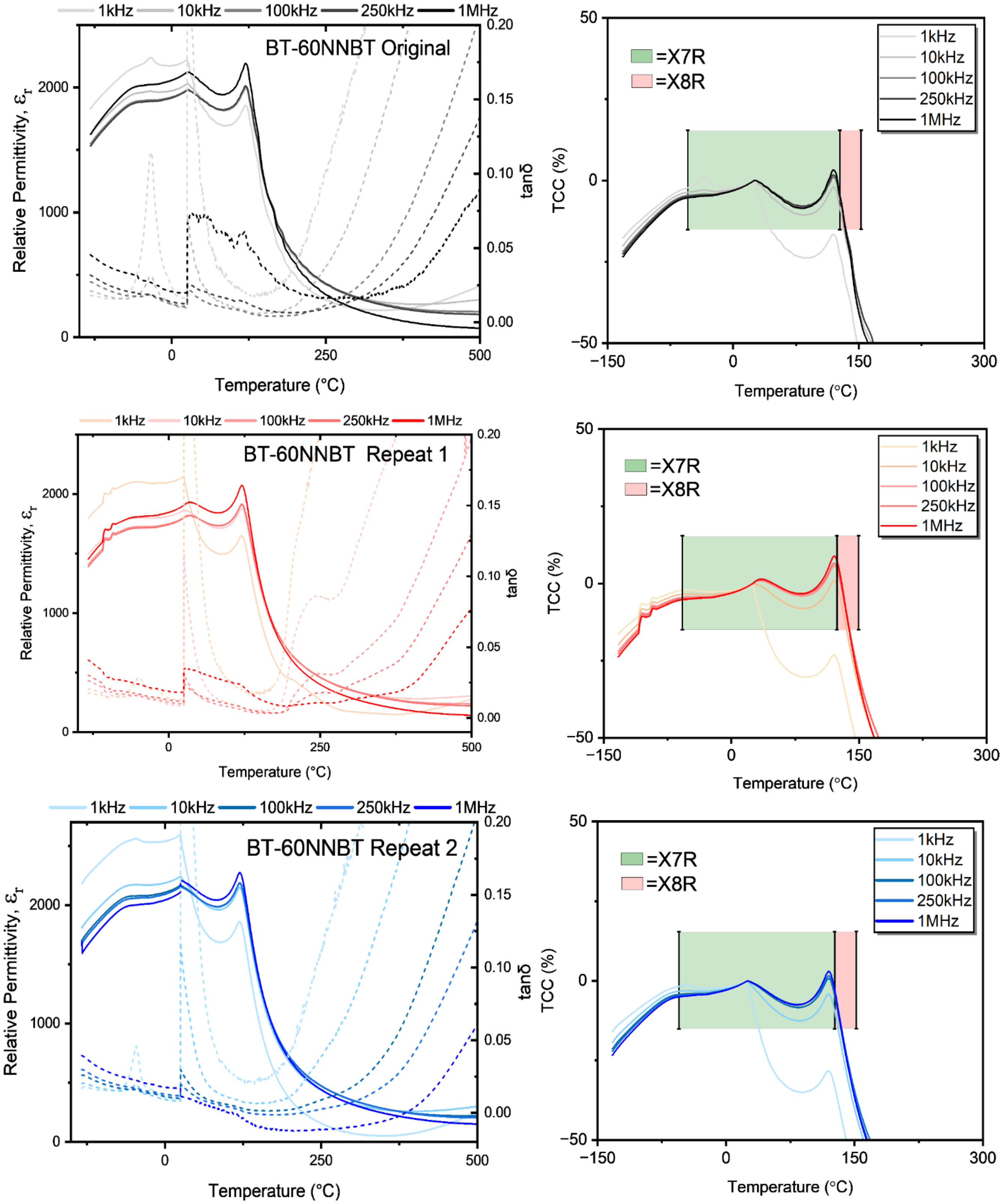

Figure A7-A9: The frequency dependent dielectric response (left) and TCC (right) of the BT-60NNBT (80:20 wt.%) composites. A8) Original A9) Repeat 1 A10) Repeat 2.

Permittivity magnitude and losses vary across the frequency range investigated, yet X7R rated TCC is observed for the composite under all measured frequencies except 1 kHz.

6 Results Chapter 2: Optimisation of the BT-60NNBT based composite towards X8R rated TCC specification using $Ba_{1-x}Ca_xTiO_3$ (BCT)

6.1 Introduction

The previous results chapter concluded with the ability to achieve X7R rated TCC specification for a hand-mixed composite arrangement of BT and 60NNBT in an 80:20 wt.% mixing ratio. Regarding X8R rated TCC, although the low temperature TCC characteristics retain temperature invariance far beyond the -55 °C lower limit for X8R specification, TCC exceeds the -15% limit ~15 °C below the 150 °C high temperature boundary. The rapid decay in permittivity consequent of the ferroelectric-paraelectric transition in the BT matrix phase is responsible for this. Should the T_c associated to this BT matrix be shifted to a higher temperature, $T_{-15\%}$ will consequently be shifted in proportion towards this 150 °C X8R boundary. Upon isovalent substitution of Ca for Ba in the BT matrix, the resulting strain imposed due to this disparity in A site ionic radii sustains dipole moments in the unit cell and the consequent polarisation to higher temperatures. $Ba_{1-x}Ca_xTiO_3$ (BCT) has been shown to increase T_c in proportion to calcium content, clear from figure 6.4, until a saturation concentration is achieved at ~ 8 at% [92,95], as described in chapter 3.2. BCT is readily available commercially with varied Ca concentrations and morphologies. Isovalent substitution of BT with BCT with a higher associated T_c may therefore represent an industrially feasible mechanism for extending the TCC response of the composites to meet X8R demands.

Ca substitution will come in the form of hand-mixing industrially sourced BCT nano-powders with 60NNBT in the same 80:20 wt.% ratio, replacing BT as the matrix phase of the composite. The BCT compositions used have 3, 5 and 7 mol% calcium substitutions onto the A-site of the perovskite (named BC3T, BC5T and BC7T, respectively). DS and IS are used to identify the polarisation response and the effect of BCT on shifting $T_{-15\%}$ to higher temperatures, whilst assessing if dielectric behaviour is retained. This is especially important considering the potential alternate B-site location of Ca in the perovskite phases utilised within the composite, an acceptor doping mechanism [94,99]. An additional extrinsic p-type contribution to the conductivity, through oxidation of oxygen vacancies formed upon acceptor doping, would be observable in the tan δ and/or DC conductivity of the composites. B-site substitution would decrease the associated

T_m of the BCT matrix and be deleterious to the attainment of X7R or X8R rated TCC. DS would reflect such behaviours with a shift in the high temperature permittivity peak associated to the matrix phase of the composite, whilst wavelength dispersive Spectroscopy (WDS) via Electron Probe Micro Analysis (EPMA) will be used to quantify the cationic distributions within the BCT-60NNBT composites and attempt to link observed dielectric behaviours to the compositional distribution of the composites. Structural characterisation via XRD will be complimentary to WDS in assessing the compositional distribution of cations within the composite, specifically to identify phase formations.

6.2 Experimental Conditions

The BCT used as the matrix phase in the composites was industrially sourced, with its nomenclature, Ca content and particle size tabulated in table 6.1.

Table 6.1: The industrially sourced BCT used in the targeted X8R ceramic composites

Commercial Materials used as Matrix Phase in Composite			
Commercial Name	Ca^{2+} Content (mol%)	Composition	Particle Size (nm)
KCM200	0	$BaTiO_3$	200
BC3T-200	3	$Ba_{0.97}Ca_{0.03}TiO_3$	200
BC5T-T2	5	$Ba_{0.95}Ca_{0.05}TiO_3$	200
BC7T-200	7	$Ba_{0.93}Ca_{0.07}TiO_3$	200

All BCT-60NNBT composites were synthesised using the same hand mixed 80:20 wt.% ratio optimised for X7R rated TCC in results chapter 1: sintering conditions of 1250 °C for 0.5 hours:

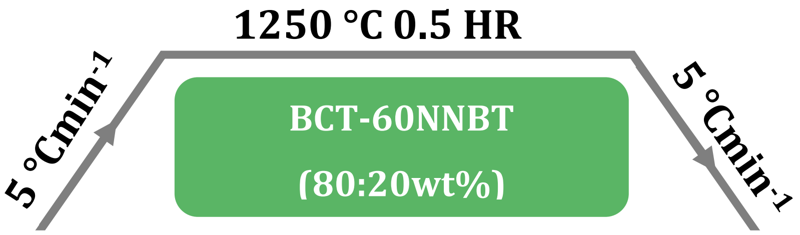

Figure 6.1: The sintering conditions used to synthesise the BCT-60NNBT ceramic composites.

6.3 Isovalent Ca A-site doping of the BT matrix within the composite to meet X8R rated TCC specification

6.3.1 XRD of commercially sourced BCT

The XRD diffraction patterns for each of the commercially sourced BCT powders at room temperature are overlaid and shown in figure 6.2. The diffraction peaks are consistent with a P4mm (#99) tetragonal space group, the room temperature ferroelectric polymorph of undoped BT. The a ≠ c condition is reflected in the splitting of relevant peaks, figure 6.2 inset. All diffraction peaks are characterised and associated to the reflection conditions of the space group, indicating phase purity (on the bulk scale at least) for each of the BCT materials. Lattice parameter variation with Ca content is shown in figure 6.3 and tabulated in table 6.2. Figure 6.3 shows a decrease in both a and c lattice parameters with increasing Ca content, with the rate of decrease of the a lattice parameter greater than that of the c parameter. This lattice parameter variability is evident in the shifting of the split (002)/(200) peak on figure 6.2 inset. The variability in lattice parameter decrease along these orthogonal axes results in the increasing tetragonality, c/a, that occurs with increasing Ca content, figure 6.3 and table 6.2. The c/a ratio does slightly decrease upon 3 mol% Ca addition into the BT A site sublattice prior to the subsequent increase. This is a product of the

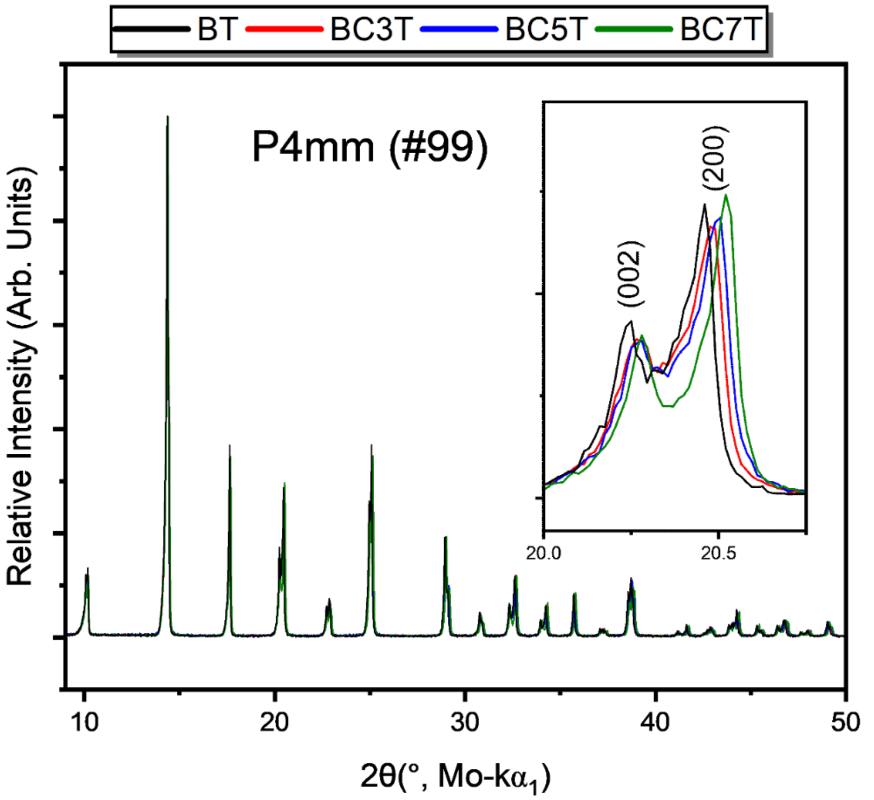

Figure 6.2: XRD patterns of the three BCT compositions used to form the ceramic composites. The inset reveals the tetragonal splitting forming the (200) and (002) diffraction peaks.

similarity between the decrease in a and c lattice parameters when moving from BT to BC3T, unlike the rest of the investigated solid solution range. The decrease in peak intensities with increasing Ca content can be associated to the lower atomic form factor of Ca relative to Ba, in conjunction with the relative displacements of Ti with the increasing c/a of the unit cell.

The volume of the unit cell (not shown) will decrease with Ca concentration as a result of this combined reduction of both a and c. This is a size effect attributed to the lower ionic radii of $Ca^{2+}_{(XII)}$ (1.34 Å) relative to $Ba^{2+}_{(XII)}$ (1.61 Å)[86].

Table 6.2: The lattice parameter and corresponding c/a ratio variation with Ca content.

Ca Content	a (Å)	c (Å)	c/a
0 (BT)	3.99286(74)	4.03244(10)	1.00991(31)
3 (BC3T)	3.98833(66)	4.02761(94)	1.00984(29)
5 (BC5T)	3.98504(73)	4.02679(103)	1.01047(32)
7 (BC7T)	3.98012(58)	4.02544(82)	1.01138(25)

6.3.2 The effect of Ca doping on Tc of BT

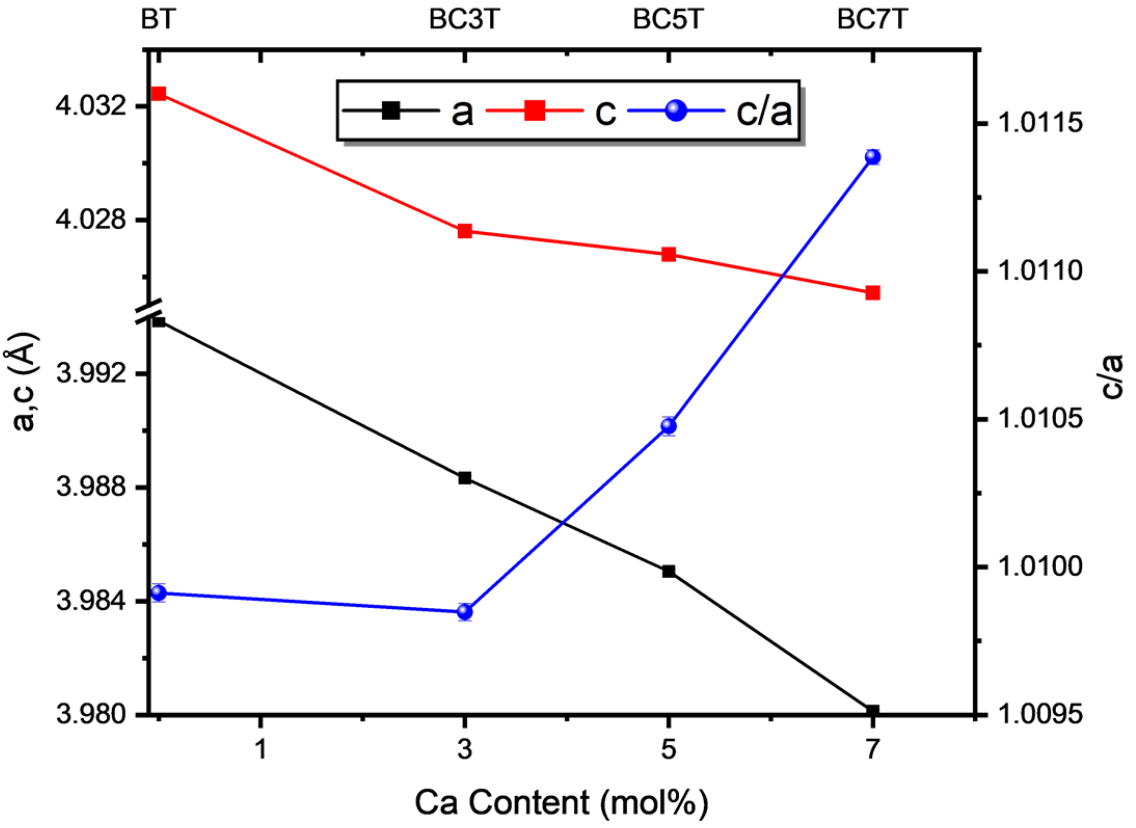

Figure 6.3: The variation in lattice parameters and c/a ratio for tetragonal BT and BCT compositions investigated. A clear increase in the c/a ratio is observed with increasing Ca content.

Figure 6.4 compares the dielectric response of BT, BC3T, BC5T and BC7T.

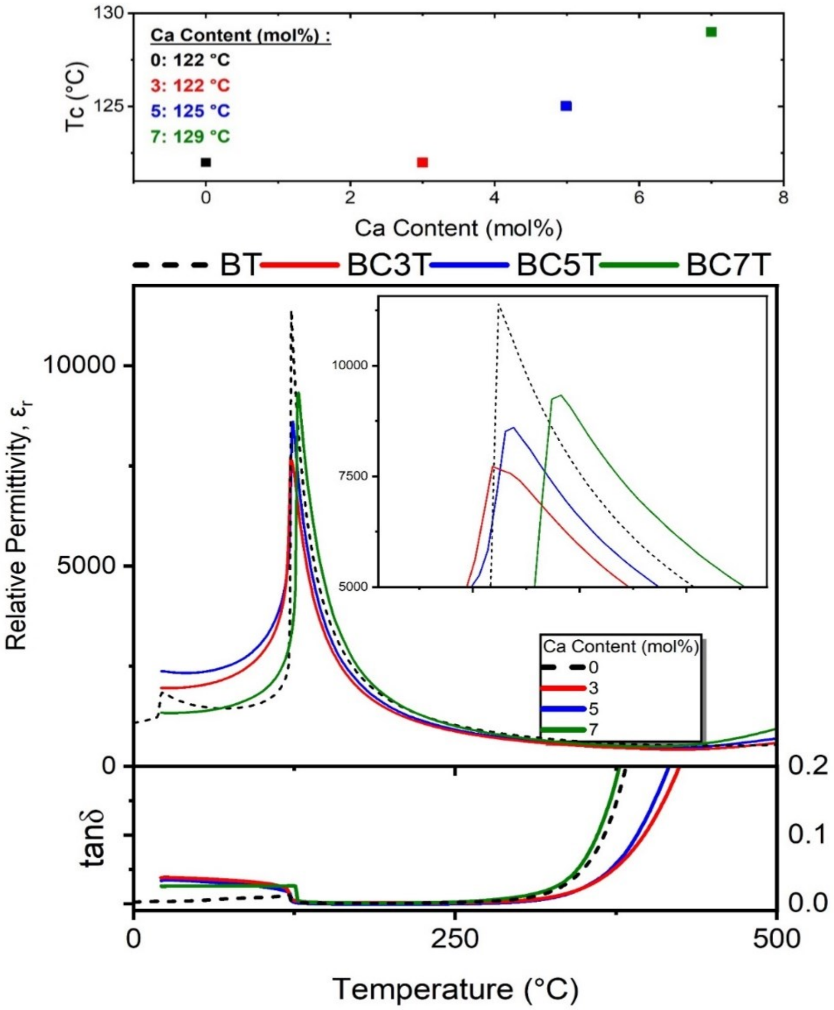

Figure 6.4: The effect of Ca doping on the dielectric response of $Ba_{1-x}Ca_xTiO_3$, including associated Tc shifting.

An increase in Tc accompanies Ca concentration, with Tc increasing from 122 °C in undoped BT to 129 °C in BC7T, representing a ΔTc of +7 °C. Of the compositions investigated, Tc only increases for 5 mol% onwards with respect to undoped BT; 3 mol% does not show a shift in Tc. Although the data shown are only for above-ambient conditions, the rise in permittivity at room temperature towards the tetragonal-orthorhombic phase transition clear in the undoped BT appears supressed for all BCT compositions. It is likely that the associated transition temperature has decreased with Ca substitution into the A-site sublattice.

The tan δ is < 0.05 until 400 °C for 3 and 5 mol% Ca. The thermally activated increase in losses present within all samples, a product of DC conductivity contributions surpassing the local ac polarisation losses, occurs at comparatively lower temperatures within the undoped BT and BC7T. These compositions retain low losses, tan δ is < 0.05, until ~ 350 °C. Thus, good dielectric behaviour is retained for all BCT compositions across a temperature range that far exceeds the X8R intended operating conditions. However, the thermally activated DC losses that are initially supressed from BT via small Ca substitutions into the A-site reappear for BC7T. At lower temperatures, the local ac losses are greatest in the BCT compositions relative to undoped BT. BC7T shows the lowest losses within this sub-Tc regime compared to BC3T and BC5T which are comparable in value.

6.4 Synthesis of BCT-60NNBT (80:20) composites for X8R rated TCC

6.4.1 XRD of BCT-60NNBT composite

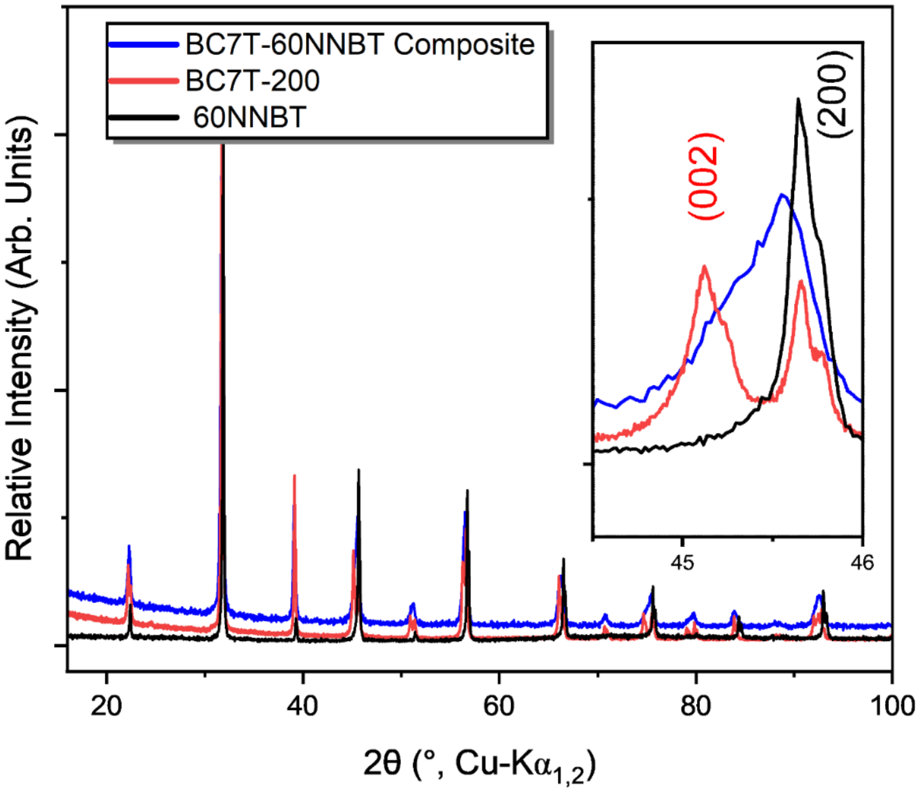

Figure 6.5: XRD diffraction patterns of the BC7T-60NNBT composite overlaid against the patterns of its BC7T and 60NNBT components.

The XRD pattern for the BC7T-60NNBT composite at room temperature is shown in figure 6.5, alongside the patterns of its constituent phases. The XRD pattern shown was measured using Cu-K$\alpha_{1,2}$ wavelength radiation (compared to lower wavelength Mo-Kα_1 radiation used for previous refinements) to maximise the observable disparity between the tetragonally split peaks of the BC7T matrix phase and thereby better distinguish the heterophases that constitute the composite. Each of the BCT-60NNBT composites are plotted against each other in figure 6.6, showing comparable peak shapes and positions. No peaks outside of those expected for the tetragonal BCT and pseudo-cubic 60NNBT are evident. Comparison of the (111) reflection for each composite reveals a shift to higher 2θ with increasing Ca content in the matrix phase used. This is consistent with the same observed shift in (111) for the BCT compositions sintered independently, figure 6.6 (right).

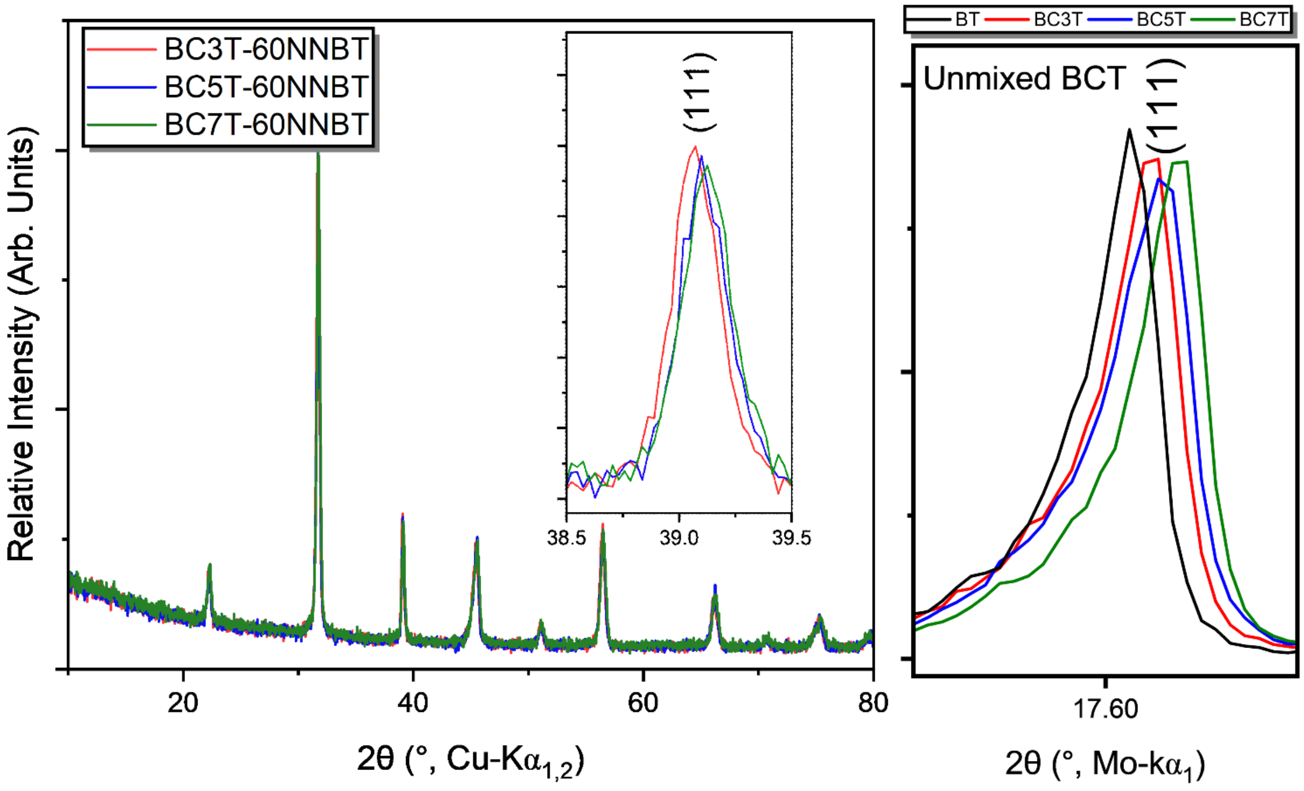

Figure 6.6: The XRD patterns for the BCT-60NNBT composites with different Ca concentrations in the starting BCT phase (BC3T, BC5T and BC7T). The shift in the (111) peak indicates variability in lattice parameters caused by this different Ca concentration. This is consistent with the observed peak shift in the same (111) reflection with increasing Ca content for independently sintered BCT (Right).

The pattern may first appear pseudo-cubic on the basis of a lack of clear peak splitting. On closer analysis, many peaks are relatively broad and asymmetric, indicated from the inset of figure 6.5, something more exaggerated for reflections of higher d-spacing's. For the inset of figure 6.5, this composite (200) related reflection (blue) exhibits a clear shoulder towards lower 2θ angles. This asymmetry is likely due to co-incidence of the constituent tetragonally split (200)/(002) peaks of the BC7T matrix and the (200) of the pseudo-cubic 60NNBT, with the shoulder specifically related towards the (002) peak of the BC7T matrix phase. The composite (200)-related peak maxima and shoulder are not perfectly coincident with the reflections of its component phases sintered independently. This suggests the interplanar spacing's and thus lattice parameters associated to the BC7T and 60NNBT phases vary when substituted in as components of the composite macrostructure compared to their independently sintered equivalents. The shoulder of the composite peak associated to (002) appears closer to (200) in the composite compared to BCT sintered independently. This could result in a change in c/a ratio for BC7T when it is integrated into the unique microstructure associated to the composite.

6.4.2 EPMA (WDS) of the BCT-60NNBT composites

WDS was used via EPMA to quantify and map the A and B site cationic distributions throughout the BCT based composites. Figure 6.7 maps these cationic distributions alongside the morphological attributes of the BC7T-60NNBT composite sintered at 1250 °C for 0.5 hours. Figure B1 in appendix B shows the cationic distributions for BC3T-60NNBT. The intention of this cationic mapping is twofold:

i) To map and qualitatively analyse the distributions of cations between the matrix and secondary phases within the composite, potentially identifying intraphasic compositional gradients

ii) To analyse Ca concentrations within the matrix phase to suggest A or B site substitution via comparison against superimposable Ba or Ti deficiencies. The areas of the lowest Ba and Ti concentration within the matrix will be mapped and compared to areas of the highest Ca concentration in the matrix, identifying if these regions are superimposable. This may imply Ca site preference in the perovskite.

A microstructure comparable to that obtained in figure 5.20 (results chapter 1) for the BT-60NNBT composite is observed. This is, on the macroscale, a biphasic composite constituent of larger, micron length NNBT secondary phases of variable size and irregular morphology distributed relatively homogeneously amongst a matrix phase composed of BCT related sub-micron grains more regular in shape, shown schematically in figure 5.20. Na and Nb concentrations are coincident with Ba and Ti deficiencies and superimposable upon these secondary phase regions, hence their assignment to the NNBT phase used in the pre-sintered composite mix. The proportion of the imaged surface area covered by these grains is much smaller, hence termed secondary phases, and is consistent with the smaller 20 wt.% mixing ratio of 60NNBT relative to the 80 wt.% of BCT. Likewise, the surrounding matrix phase is comparatively Ba, Ti and Ca rich, indicating a BCT type matrix. An extensive porosity network runs throughout this matrix phase, unsurprising for the low relative density calculated of 79.7 %.

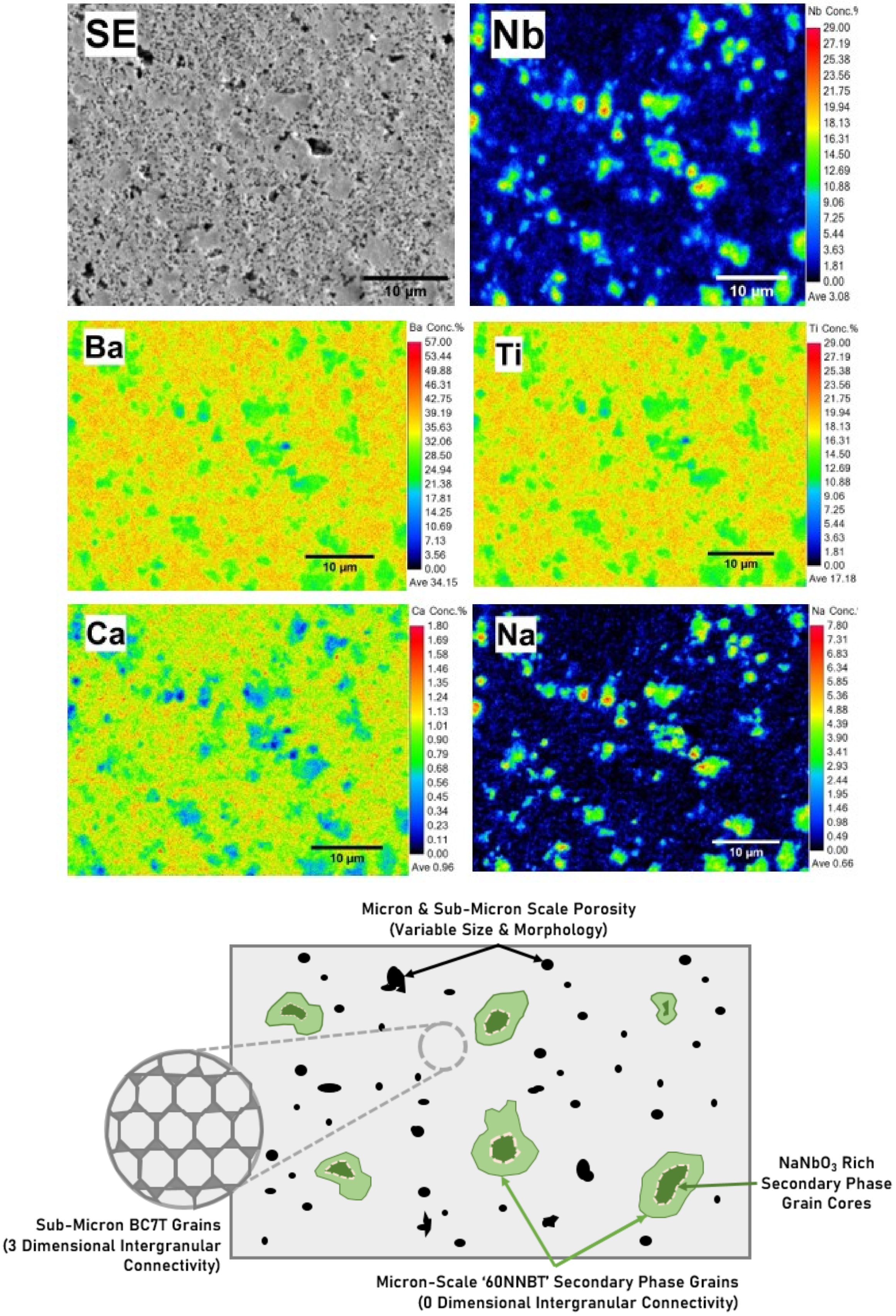

Figure 6.7: Elemental mapping of A and B site cation distributions throughout BC7T-60NNBT ceramic composite, from WDS via EPMA.

Intragranular compositional variance is clear amongst the secondary NNBT phases with core-shell type distributions existing along the cross section of many grains. For these compositionally variant secondary phases, $NaNbO_3$-rich concentrations exist towards the inner portion of the grains. These concentrations are generally not centralised (at least for the cross section of the visible grains). This microstructure and compositional heterogeneity is shown schematically in figure 6.7. Despite Ba and Ti concentrations appearing comparatively more uniformly distributed in the surrounding matrix phase, when the scaling is reduced, figure 6.8 a) and c), similar compositional variance is clear. This compositional variance is 'intra-phasic', extending across the matrix phase as opposed to being confined within each of the constituent sub-micron grains. Since figure 6.8 a –c) reveal heterogeneous cationic concentration is distributed throughout the matrix, it is worth understanding their relative coincidence. Should Ba or Ti deficient regions be superimposable upon Ca-rich areas, A or Ba site preference for the Ca substitution may be implied.

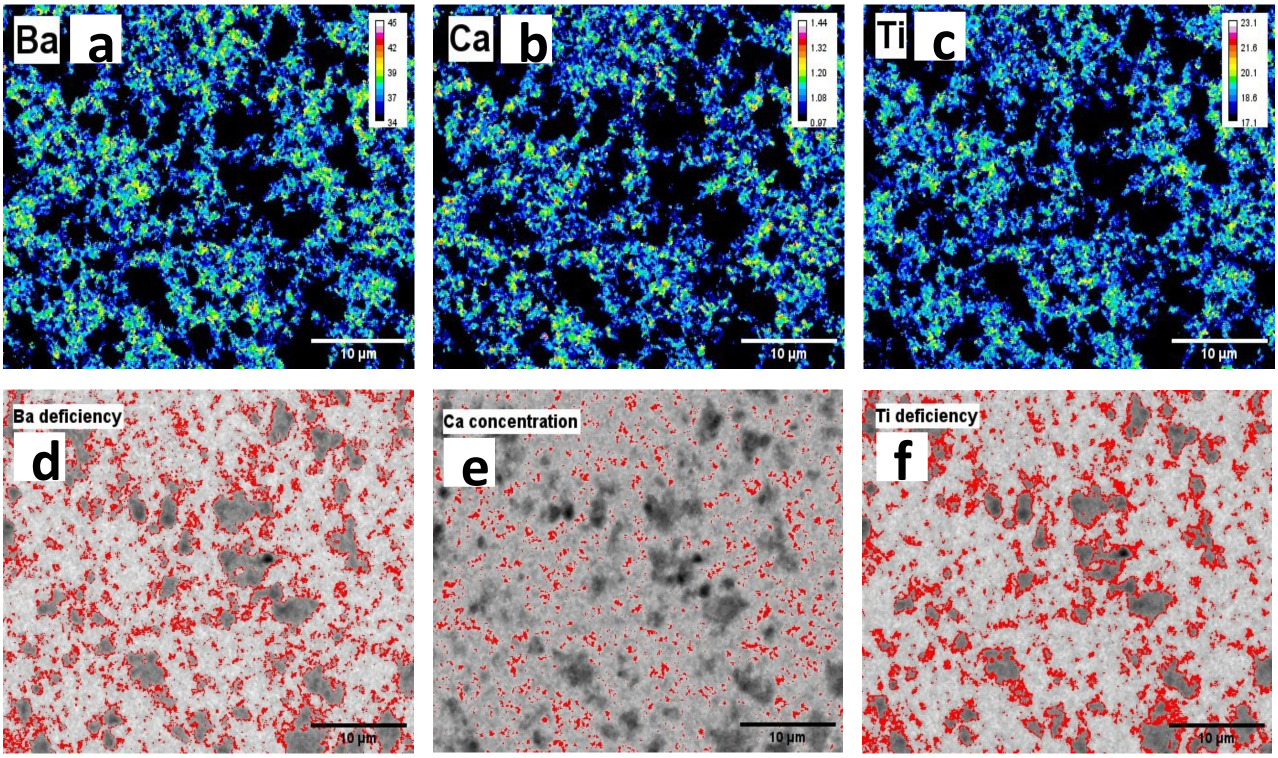

Figure 6.8: a -c) Ba, Ca and Ti elemental maps with a smaller scaling to reveal compositional heterogeneity within the matrix phase. d & f) Ba and Ti compositional deficiencies relative to the modal matrix composition. e) The top 5% Ca concentrations within the matrix phase.

Figure 6.8 d) and f) reveal the lowest 10% of Ba and Ti concentration within the matrix phase, with areas falling within this threshold marked in red. The upper 5 % of Ca concentration found within the BCT matrix phase is highlighted in red in figure 6.8 e). These data are presented simultaneously in an attempt to visually and qualitatively associate high Ca concentration within the matrix to corresponding Ba or Ti deficiencies, thereby inferring the preferential A or B site occupation. There is, however, no visually clear suggestion of preference towards either site. Deficiencies in the Ba and Ti (that are not related to the NNBT secondary phases) do not appear to be consistently superimposable upon the observed Ca concentrations. They instead appear predominantly around the circumference of the NNBT secondary phases.

6.4.3 DS of the Hand-mixed BCT-60NNBT composites

The effect of using BCT as opposed to BT as the matrix phase of the composite is reflected in its dielectric response, figure 6.9. All BCT composites show comparable bi-phasic permittivity responses constituent of a diffuse, low temperature frequency dependent permittivity peak related to the NNBT phase, and a high temperature comparatively frequency independent permittivity peak associated to the BCT matrix phase. This high temperature response can be shown in figure B5 (Appendix B) to increase in width with increasing Ca content, relative to the dip that occurs ~ 100°C. Relative permittivity decreases in magnitude in proportion to the Ca

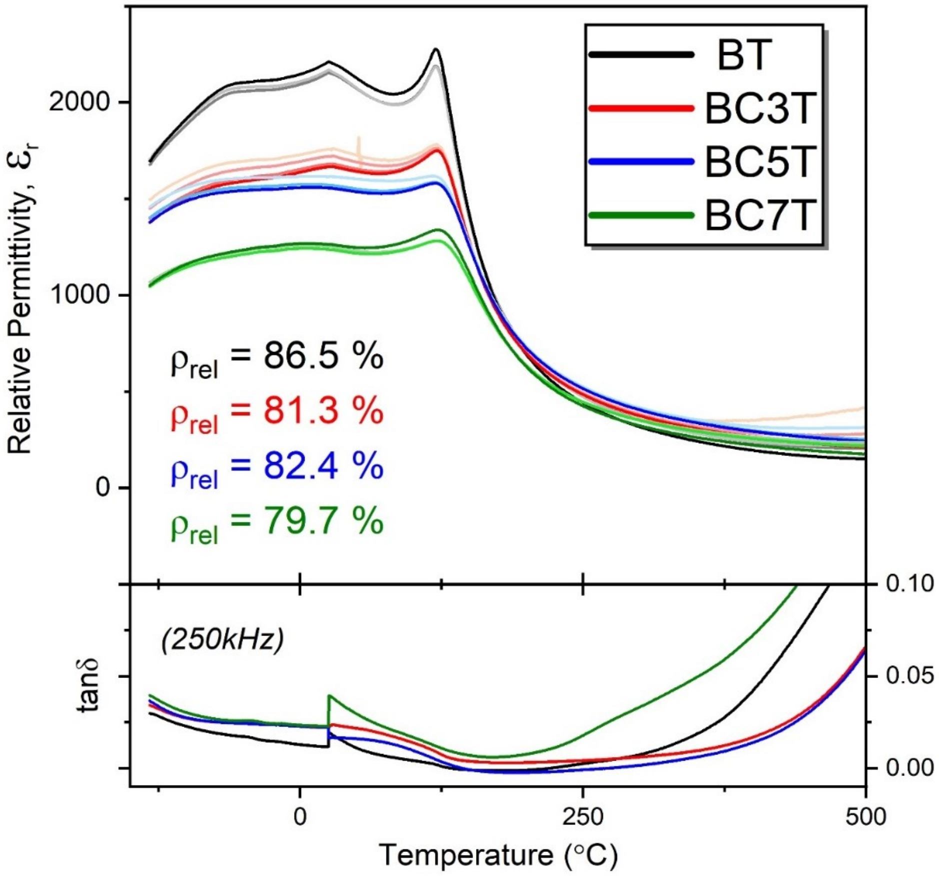

Figure 6.9: The effect of Ca substitution on the dielectric responses of the hand mixed ceramic composites.

content, compared to the BT-60NNBT parent composite. The BC3T and BC5T based composites are much closer in permittivity magnitude than BC5T and BC7T based composites. There is variation between the relative densities of each composite system investigated, varying from 79.7 % in the BC7T system to 86.5 % in the original BT-60NNBT composite, as all BCT composite systems exhibit a relative density lower than that quantified for the BT-60NNBT composite of results chapter 1.

The BCT-60NNBT composites retain good dielectric responses across the X8R operating temperature range, with the trend in local and DC/higher temperature losses reflecting that observed between the independently sintered BT and BCT in figure 6.4. That is, the BT and BC7T lose dielectric behaviour towards lower temperatures compared to BC3T and BC5T based composites. tan δ < 0.05 up to 475 °C for the BC3T and BC5T composites, whilst BT and BC7T show higher losses and exceed this arbitrary tan δ = 0.05 threshold at comparatively lower temperatures, 410 and 350 °C, respectively. Comparing figure 6.4 and 6.9, although the trends in dielectric loss are comparable between the independently sintered BCTs and the BCT based composites, the temperatures where tan δ > 0.05 are much higher for the composite systems than for the independently sintered BCT samples. This increase in dielectric losses towards higher temperatures is indicative of thermally activated DC conduction, and such long-range losses appear to have been supressed for the BCT when used as a matrix phase of this binary composite relative to its monolithic equivalent.

Below the T_m attributed to the BT/BCT related high temperature permittivity peak, the BCT composite systems exhibit higher dielectric losses with respect to the BT composite. Higher, local polarisation related losses are incurred within these BCT composites at these lower temperatures. At sub-ambient conditions these now AC/local losses are virtually superimposable amongst the BCT composites, but greater than that of the BT system. Variability is only observed towards the lower end of the measured temperature range, -133 < T (°C) -100. Within this range, tan δ is greatest for the BC7T composite and lowest for the BC5T composite. This compares to the permittivity response in the according temperature range, with a more gradual decline in permittivity observed in the BC7T composite and the sharpest decline observed in the BC5T sample. The incline in tan δ towards room temperature, met with a sudden drop, is a product of the differing experimental environments the sample is exposed to during sub- and above-ambient DS[2].

---

[2] Moisture adsorbed/absorbed onto/into the sample consequent of the atmospheric conditions in the post-ambient testing jig induce higher losses which eventually decrease as the sample is heated. In the cryostat used for sub-ambient DS, the low pressure necessary for cooling results in moisture vaporisation from the sample, producing low losses on account of a decrease in the charge carrier concentration. Merging of the data results in a step-type increase in losses observed at room temperature as the sample is heated.

Figure 6.10 compares the TCC associated with the various BCT-60NNBT composites and the X7R-rated BT-60NNBT from results chapter 1. It is clear that although all BCT-60NNBT composites sustain X7R rated TCC stability, only the BC7T based composite shifts the $T_{-15\%}$ to a temperature sufficiently high enough to meet X8R TCC requirements. BC7T addition shifts the $T_{-15\%}$ by 17 °C, whilst BC3T and BC5T only increase it by 8 and 9 °C, respectively.

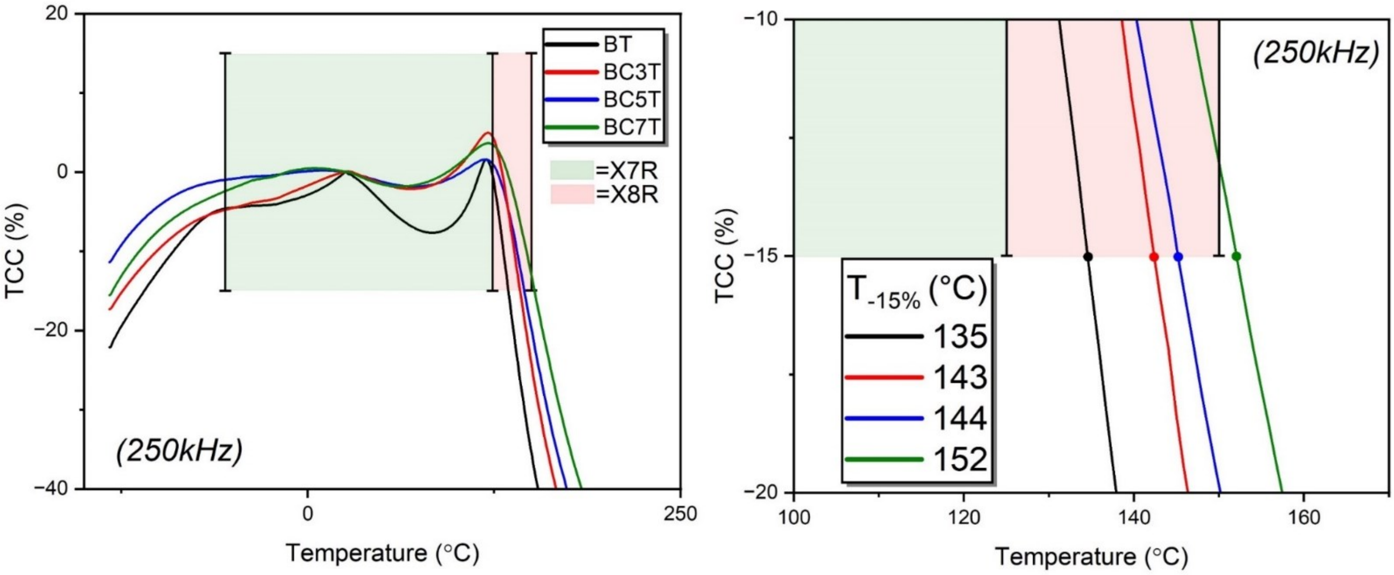

Figure.6.10: The effect of variable BCT as the matrix phase on the TCC of the ceramic composites. The image on the right reveals the shift in $T_{-15\%}$ with BCT, with X8R TCC specification met only by the BC7T based composite.

Table 6.3: T_m associated to the BT/BCT permittivity maxima in the composite responses of figure 6.9

Composition in composite	Associated T_m (°C)
BT	121
BC3T	121
BC5T	121
BC7T	122

Despite the observable difference in Tc between these BCT compositions when sintered independently, figure 6.4, there is no variation in T_m associated to the BT and BCT related permittivity peaks in the composite system, as shown in table 6.3. The Ca concentration does not appear to have shifted T_m as had been expected, yet $T_{-15\%}$ has still successfully shifted to elevated temperatures as intended.

Since an increasing diffusivity/width of the BCT-related permittivity peak had been quantified in figure B5, could this have been responsible for the shift in $T_{-15\%}$, effectively delaying the onset of

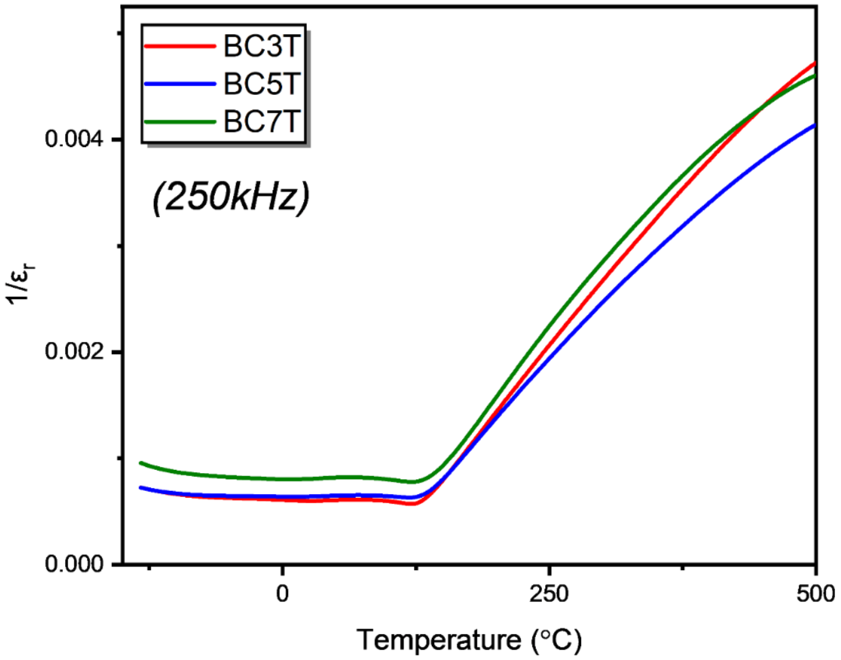

Figure 6.11: Curie-Weiss plots showing the reciprocal of relative permittivity (1/ε_r) with temperature at 250 kHz for each of the BCT composites synthesised.

the Curie-Weiss permittivity decay? Or could the different Ca concentrations instead be changing the relaxor parameter γ that describes the rate of polarisation decay beyond the ferroelectric-paraelectric transition? To try and understand the underlying contribution to this $T_{-15\%}$ shift, the Curie-Weiss plot, figure 6.11, and the modified logarithmic Curie-Weiss plot (results chapter 1, equation 5.5) which linearises the permittivity decay beyond T_m, was plotted, figure 6.12. Both the Curie-Weiss and modified Curie Weiss plots, figure 6.11 and 6.12 respectively, are complimentary in showing how the permittivity decay varies between each of the composites. This is clear from the different gradients observed for increasing 1/ε_r above T_m (~ 121 °C) in figure 6.12. The benefit of linearising the depolarisation response using equation 5.5 and plotting as figure 6.12 is the quantification of this diffusivity in permittivity decay, with γ. Figure 6.12 reveals not only variability in this depolarisation decay between BCT composites, based on the differing linear fits, but that two different decay regimes are apparent as two linear fits. This is also suggested from the bending of the Curie Weiss plot in figure 6.11.

These two depolarisation regimes are termed γ-Low temperature and γ-High temperature in figure 6.12. Since the $T_{-15\%}$ falls within the γ-Low temperature regime, it is this area that will concern our attention. There is a variable γ parameter between the composites within this region, varying from 1.92 in the BC7T composite to 2.16 in the BC5T composite (which exceeds the maximum coefficient value of 2 proposed in the modified Curie Weiss law). Importantly, there is no trend in this diffusivity parameter nor are they sufficiently disparate to attribute the significant shift in $T_{-15\%}$ between the composites to variable intrinsic depolarisation responses that yield γ.

When comparing the γ-Low temperature linear fit of the composites of figure 6.12, the major difference between these depolarisation responses is the temperature it takes for the response to converge to this linear temperature dependence with this associated γ. Figure 6.12 (right) shows markers, white stars, that highlight the temperature range taken to converge from T_m to the linear fit. Quantification of this convergence range, termed $\Delta\ln(T-T_m)$, shows that the temperature taken to converge to its intrinsic low temperature depolarisation response increases with Ca concentration, and is greatest for BC7T. This result is consistent with the peak widths

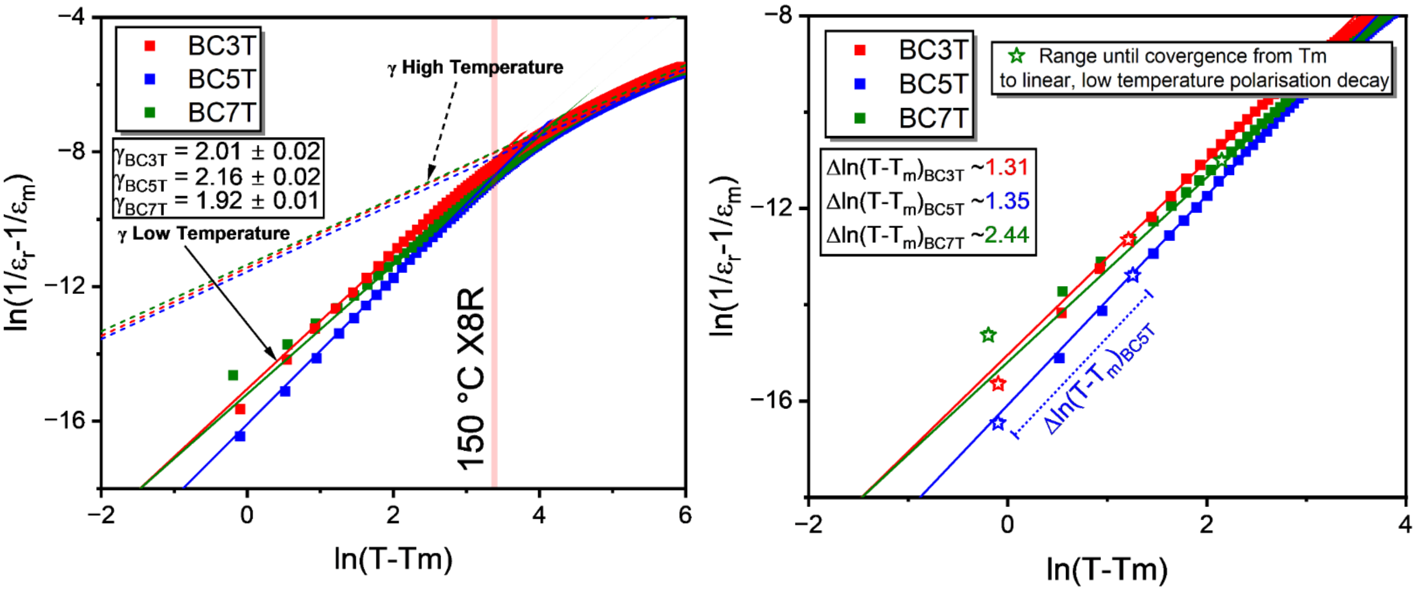

Figure 6.12: The natural logarithm of the polarisation decay in the BCT-composites. The intrinsic polarisation decay due to increasing thermal motion is interrupted, changing gradient at high temperatures due to DC losses adding a competing, thermally activated contribution to polarisation. The data converges to its linear, intrinsic polarisation decay in the low temperature regime slowly as a result of the diffuse BCT permittivity peak, with the convergence temperature range marked out and quantified in the bottom image with white markers.

associated to the BCT permittivity peak being greatest for the BC7T composite, figure B5, and thus this convergence temperature range is a product of the increasing peak widths of the BCT permittivity peak in the composite permittivity responses. This relationship between convergence range and Ca content is consistent with that for the $T_{-15\%}$ shift. The close proximity of $T_{-15\%}$ for BC3T and BC5T-based composites, separated by just +1 °C, is very much comparable to a close proximity of the $\Delta\ln(T-T_m)$, separated by just 0.04. This compares well with BC7T composites which show a much larger of $T_{-15\%}$, variation from BC3T composites of ~9 °C and a $\Delta\ln(T-T_m) \sim 1.13$.

6.4.4 IS of BC7T-60NNBT Composites

Z* plots and Z''/M'' spectroscopic plots for the X8R rated BC7T-60NNBT composite, at 500 °C, are shown in figure 6.13 and 6.14, respectively. The composite is overlaid with its components and the X7R achieving BT-60NNBT composite from chapter 1 (at the same temperature). The Z* plots for both composites are irregular elongated arcs, a potential representation of a heterogeneous electrical microstructure. This electrical microstructure could be composed of multiple parallel RC elements with varied R, C values, but hidden under the guise of this 'single' elongated arc. In

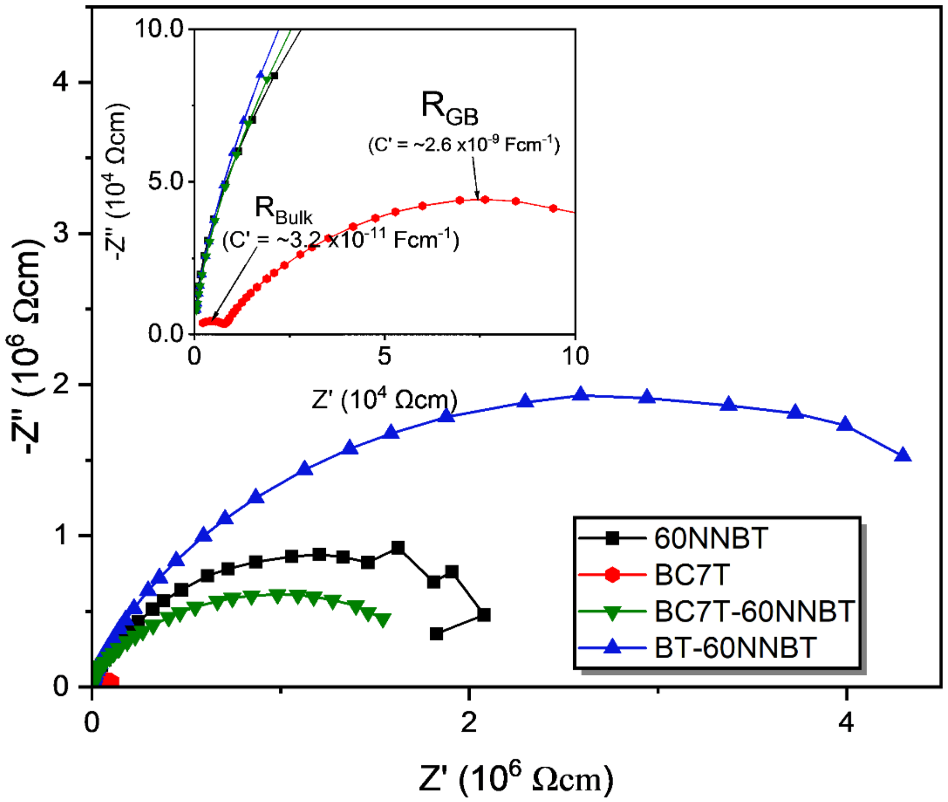

Figure 6.13: The Z* response of the BC7T-60NNBT composite, compared against its BC7T and 60NNBT samples (independently sintered) and the BT-60NNBT predecessor from Chapter 1.

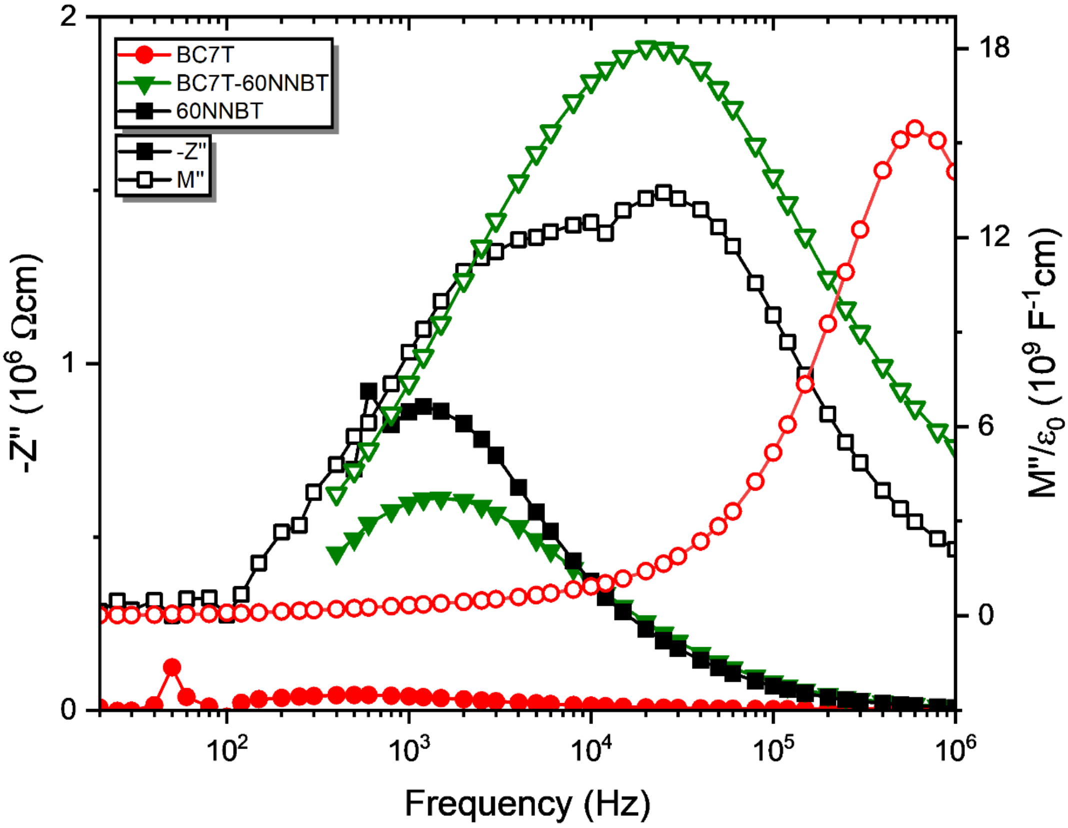

Figure 6.14: The Z''/M'' spectroscopic plots of BC7T-60NNBT at 500 °C, overlaid with its BC7T and 60NNBT components at the same temperature (sintered independently).

this case the element with the greatest DC resistivity dominates the Z* plot. The broad M'' (and Z'') peaks of the BC7T composite, figure 6.14, are comparable in suggesting this electrical heterogeneity. The disparity in f_{max} between the diffuse M'' and –Z'' peaks suggests that these separate RC elements vary in R and C and each dominate one of these two immittance formalisms. The more conductive element with the greatest f_{max} and lowest R value is not scaled on the Z'' peak but exhibits a smaller capacitance compared to the other more resistive element, based on its dominance of the M'' peak scaling. This is of course a primitive description of a serial connectivity between two parallel RC elements of differing conductivities and capacitances. The reality is likely a distribution of conductivities throughout the composite, with a more complicated connectivity. It does, however, serve well to describe the effects compositional heterogeneity induce on producing such a –Z''/M'' response. No low frequency spike is evident in the Z* plot (figure 6.13) or on the –Z'' spectroscopic response (figure 6.14).

The total DC conductivity of the BC7T-60NNBT composite is more consistent in magnitude with its most resistive component, 60NNBT, compared with the BT-60NNBT composite from results chapter 1, based on similarity of Z* diameters (Z' intercept values) in figure 6.13. The composite is slightly lower in DC resistivity based on its smaller intercept value (1.95 vs 2.39 MΩcm). The BC7T-60NNBT composite appears orders of magnitude more resistive than the total DC resistivity response of its matrix phase, BC7T, which dominates the volume fraction of the physical microstructure. BC7T-60NNBT also appears more conductive than its BT-60NNBT predecessor, based on the smaller diameter of this Z* arc (1.95 vs 5.61 MΩcm). These conductivity relationships are better visualised in figure 6.16, showing the Arrhenius-type temperature dependence of total DC conductivity for all of the composite systems as calculated from the Z' intercept value of the single elongated Z* arcs.

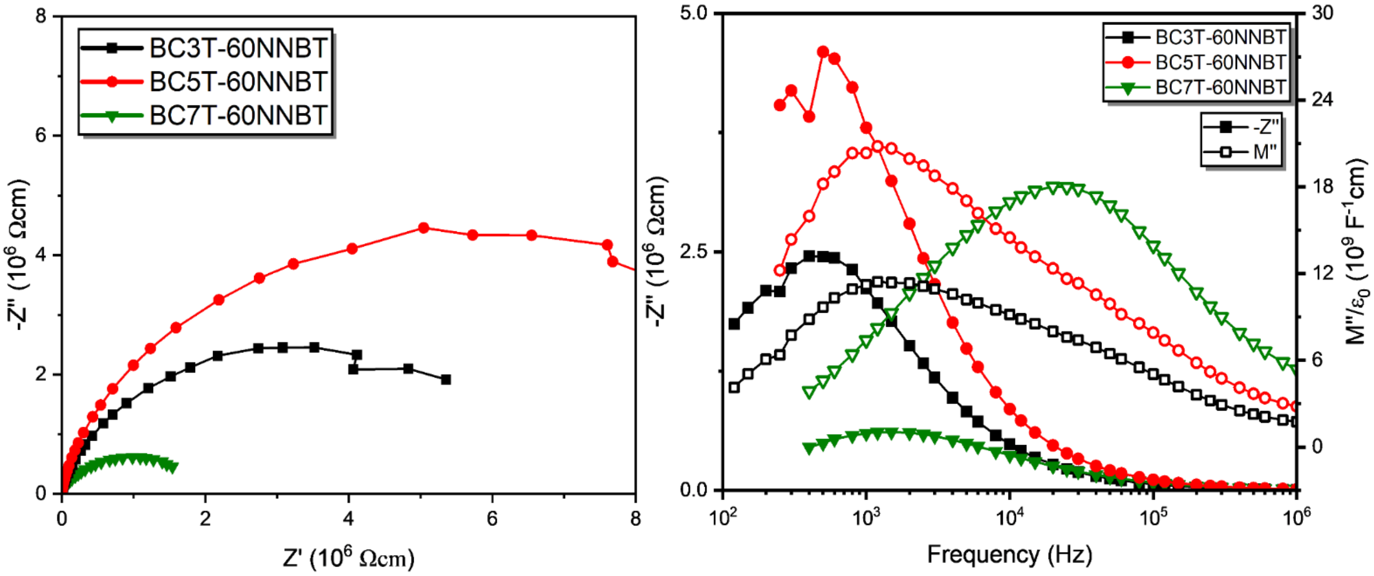

Figure 6.15: left): a comparison of the Z* plots at 500 °C for each of the BCT-60NNBT composites. right): Comparison of the M''/Z'' spectroscopic plots for each of the BCT-60NNBT composites at 500 °C.

Comparison between the M''/Z'' spectroscopic plots for each of the BCT-60NNBT composites, figure 6.15, reveal an electrically heterogeneous microstructure for all BCT composites. The Z* plots appear as single elongated arcs for all composites, particularly for BC3T and BC5T based composites. For these composites, the M'' peaks appear significantly more asymmetric, constituent of at least two relatively distinguishable peaks with differing f_{max}. For the BC7T based composite heterogeneity in the M'' peaks is less apparent, and is instead better distinguished from the disparity in f_{max} between its M'' and –Z'' peak maxima. In all cases, the impedance is dominated by the most resistive parallel RC element but the capacitance response is more convoluted, particularly so for the BC3T and BC5T composites as a result of the closer similarity in C magnitudes (with multiple peaks manifested in M'') compared to the BC7T composite.

An additional commonality is clear between the BC3T and BC5T based composites in that the more resistive RC element exhibits the smaller capacitance, whilst the more conductive element shares the biggest capacitance. For the BC7T based composite, the converse is true. The M'' asymmetry (the shape of the M'' peaks) is consistent within these two BC3T and BC5T based composites. For all of the composites, the difference between the f_{max} associated to each of the two regions of disparate conductivity (separate RC elements) are similar, i.e. each RC response is of similar frequencies for all of the composites. This suggests that the capacitance variation between the two RC elements/ contributory electroactive components of the composite is more extensive than the variability of each regions conductivity. The capacitance magnitudes for each of the electroactive regions that respond for each BCT composite are all in the ~10^{-11} Fcm^{-1} range. Thus, each response considered can be described as a bulk-type contribution to the electrical microstructure.

The variation in total DC conductivity calculated from the diameter of the Z* arcs for each of the BCT-60NNBT composites is plotted in figure 6.16. The total DC resistivity of the BC7T-60NNBT composite is smaller compared to these other two composite systems, clear from the smaller Z* arcs shown in figure 6.15 and the total conductivity distributions for the composites plotted in figure 6.16. This is also reflected in the higher dielectric loss observed, indicating a consistency between the local ac losses and longer-range DC conductivity. All composites, however, show a total DC conductivity that is lower than its component phases, and are all similar in magnitude. Towards higher temperatures, all of the BCT composites appear to converge to a consistent conductivity and share similar activation energies, tabulated in table 6.4. this ranges from 1.16 ±

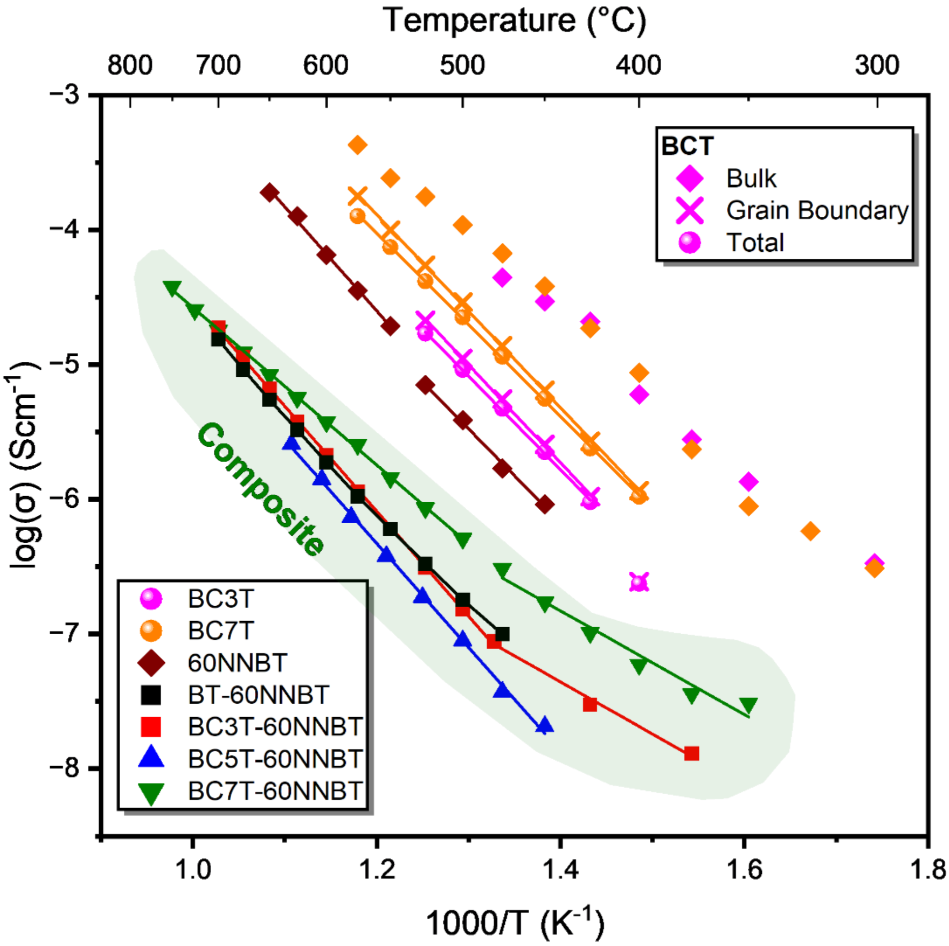

Figure 6.16: The temperature dependence of the total conductivity for each of the composites synthesised (BT and BCT based), as well as the component phases sintered independently. These conductivities were extracted from the Z' diameters of the Z* arcs.

0.01 eV in the BC7T based composite to 1.54 ± 0.01 eV in the BC3T composite. The low temperature regime for the two more conductive composites, BC3T and BC7T based composites, show an additional linear temperature dependence, with a lower and very comparable activation energy of 0.76-0.77 ± 0.07 eV. It is also quite probable that could the total conductivity of the BC5T based composite have been measured to lower temperatures, a similar activation energy of conduction could have been derived.

Table 6.4: The activation energy associated to the high and low temperature total DC conductivity regimes of the BT,BCT-60NNBT composites and their component phases sintered independently.

Activation energy associated to the total DC conductivity of BT,BCT-60NNBT composites

Sample	Low Temperature Ea (eV)	High Temperature Ea (eV)
BC3T	-	1.38 ± 0.02
BC7T	-	1.35 ± 0.02
60NNBT	1.38 ± 0.07	1.53 ± 0.05
BT-60NNBT	1.30 ± 0.02	1.51 ± 0.01
BC3T-60NNBT	0.77 ± 0.07	1.54 ± 0.01
BC5T-60NNBT	-	1.53 ± 0.03
BC7T-60NNBT	0.76 ± 0.07	1.16 ± 0.01

6.5 Discussion

Rietveld refinements of the XRD data of BT and BCT powders shown in figure 6.2 reveal a phase pure P4mm tetragonal symmetry, unsurprising as the maximum Ca concentration, 7 mol%, does not surpass the solid solution limit of ~ 25 mol% [90]. The volumetric contraction observed in figure 6.3 is consequent of the size effect induced by the comparatively smaller $Ca^{2+}_{(XII)}$ (1.34 Å) substituting for $Ba^{2+}_{(XII)}$ (1.61 Å) [86,87]. The rate of decrease of the a parameter is greater than for the c parameter inducing the progressive increase in the c/a ratio observed in figure 6.3. This tetragonality is induced by the effect of the small and consequently under-bonded Ca displacing away from the A-site centre in order to reduce its anion coordination [96,98]. This contributes a dipolar charge imbalance compared to the larger Ba which is capable of centralising in the large 12-fold coordination environment of the BT A-site. It is also proposed that the Ca displacements and the varied Ca-O bonding environment that occurs can change the ground state for the Ti-O interactions, with Ti interactions/energies (specifically orbital hybridisations) previously suggested to be influential in the Ti intraoctahedral off-centring [88,96]. In this way, Ca off-centring can directly interact and couple to the Ti displacements and stabilise this ferroelectric dipole moment to higher temperatures. The shift in Tc to higher temperatures with increasing c/a ratio, figure 6.4, suggests this A-site occupation and subsequent Ca off-centring is occurring. B-site occupation, either independently or simultaneous to A-site Ca occupation, has been reported to dramatically decrease Tc and thus from figure 6.4 we can suggest this has not occurred. B-site occupation would alleviate some of the Ca-O bond straining by changing the anion environment that coordinates such (introducing oxygen vacancies), reducing c/a, which has not occurred. The tan δ associated to the higher temperature DC losses in BC3T and BC5T are lower compared to BT and BC7T, and do not suggest any significant acceptor doping of Ca. Instead, Ca has been reported to increase the enthalpy of reduction when doped into the A-site of BT [101]. The lower concentration of oxygen vacancies formed in BC3T and BC5T with respect to BT as a result of this enthalpy change will result in a lower p type conductivity upon re-oxidation on account of fewer charge carriers. This suggests this rise in tan δ is caused by this intrinsic p-type conductivity contribution. In BC7T the tan δ is very similar to that of the undoped BT. Perhaps the enthalpy for reduction is no longer as high considering the more extensive under bonding between the Ca and O, and thus charge carrier density is able to increase to a similar extent seen within undoped BT.

When these BCT compositions are used with 60NNBT to form a composite structure equivalent to that of results chapter 1, under the same sintering conditions, SEM micrographs in figure 6.7 confirm a 3-0 composite macrostructure equivalent to the one seen within the BT-60NNBT is replicated, shown schematically in figure 6.7. Significant porosity is observed again, in agreement with the calculated relative density of ~ 79.7 %. WDS elemental mappings, figures 6.7 and 6.8, reveal clear compositional heterogeneity in both the BCT matrix and NNBT secondary phases of the composites, something not discernible from the insufficiently resolute EDX analyses of figure 5.20. The diffusivity of the low temperature NNBT related response was noted in the previous chapter as being far more diffuse than that expected of independently sintered, nominal 60NNBT, shown in figure 5.6. Here we have evidence that this low temperature diffusivity is the product of a serial connectivity of slightly different relaxor NNBT compositions, each with shifted T_m.

A perovskite stoichiometry appears to be retained based on the superimposable Ba:Ti and Na:Nb concentrations, such that A:B ratios would be conserved at ~ 1. No regions of irregular cation concentration not expected of BCT or NNBT type phases is evident within figure 6.7. This is complimentary to the XRD analysis of the composites in figure 6.5 and 6.6, where all reflections can be associated to interplanar spacings consistent with a perovskite symmetry. No additional reflections are characterised. It should be considered, however, that many of the peaks are quite diffuse as a result of the coincident tetragonally split BCT and pseudo-cubic locally variable 60NNBT. There is also likely a large strain component associated to the composite microstructure formed of different grains shapes and morphologies with a high interfacial surface area. Additional reflections could be hidden within these diffuse reflections. Comparatively NN rich cores are relatively centralised within these NNBT secondary phase grains. This could be a function of the NN related phase impurities that are present in the 60NNBT calcined powders, chapter 1 figure A5. These impurities could act as a nucleation site for the formation of these intragranular asymmetric concentration distributions within the NNBT grains of the composite upon sintering. It would be interesting to map the compositional variance within secondary phase grains in a composite system formed of 60NNBT that is phase pure post calcination to analyse the influence of phase impurities on these intragranular compositional gradients.

Ca deficiency (relative to the matrix phase) is superimposable upon the larger secondary NNBT phases (alongside Ba and Ti deficiency), however the outer edges of these phases do show Ca intensity suggesting some (but little) Ca diffusion and substitution into the NNBT phase has occurred. This Ca is then confined to the (comparatively) BT-rich NNBT outer circumference of these grains. This is likely influential on the decrease in NNBT related permittivity magnitude with increasing Ca content, from figure 6.9, as it is unlikely to be density induced since all BCT-60NNBT composite densities are of comparable magnitude. The relative densities decrease by 1.6 % between BC3T and BC7T composites, but permittivity decreases by ~ 35 %, which is excessively large to be associated to a density contribution. Ca is comparatively less polarisable than the Ba for which it dopes for in both the matrix and outer regions of the NNBT secondary phases. The preferential off centring of Ca in the cubo-octahedral A site coordination was previously described to couple to the B cation displacements in BT, influencing the observed increase in Tc. Here, in NNBT phases where the permittivity contribution is influenced by localised, nanoscale Nb cation displacements from second order Jahn Teller instabilities, the heterogeneous distribution of Ca which is likely to interact electronically with these Nb cations, influencing the cooperative dipolar correlations and the size/dynamism of the PNRs that resulted in the large permittivity observed in 60NNBT. Alternatively, there could be the formation of a low permittivity secondary phase, that exists at low quantities to avoid detection via XRD and has not been observed by WDS/SEM, which only probes a small select cross sectional surface of the composite.

The compositional heterogeneity of the BCT matrix phase clear from WDS elemental mappings of figure 6.7 and 6.8 results in a distribution of BCT components constituting the matrix, each with varied T_m and associated volume fractions. The modal concentration of BCT in each composite may be similar based on the comparable T_m associated to the high temperature permittivity peaks, ~ 121 °C from table 6.3, but the range of BCT compositions is inherently different within the composites, and greatest in the BC7T system. This is a consequence of its larger starting Ca concentration in the BC7T material. This larger range of BCT compositions induces the increasing width of the BCT related permittivity peak, figure B5, since each effective BCT composition will have an inherently different T_m. The broader high temperature permittivity response for the BC7T composite delays the onset of the intrinsic thermally induced Curie Weiss depolarisation. This is shown in figure 6.12 as the onset of linear Curie Weiss depolarisation is converged to at higher temperatures for BC7T composites compared to BC3T or BC5T equivalents. There are a greater number of higher Ca doped BCT compositions in the BC7T system that are capable of sustaining polarisation towards higher temperatures, producing this deviation from linearity. The result is a shifting of $T_{-15\%}$ to higher temperatures and attaining X8R rated TCC, clear from figure 6.10. The strain imposed by the compositional distribution within the matrix phase could also influence the stabilisation of tetragonal distortions within the matrix phase to higher temperatures, contributing to the diffusivity of the BCT related permittivity maxima in the BC7T composite.

Figure 6.8 was utilised to reveal any potential coincidence between the Ca rich areas and the Ba/Ti deficient areas. This could have revealed the A or B site location of Ca within the matrix phase, particularly important to see if A-site substitution had been retained when the BCT was integrated into the composite. However, Ba and Ti deficiencies within the matrix phase predominantly occur along the circumference of the secondary phase grains and are difficult to correlate to the sites of Ca concentration. It is difficult to associate a particular sub lattice environment for the Ca within the composite from such mappings. Attempts to quantify A:B ratios were hampered by experimental issues, and although not shown, gave unexpectedly low cationic wt.% distributions with ratios that offered little interpretation. This is likely a product of the high degree of porosity within the composite samples, which encourages multiple scattering events for photoemitted electrons, changing their associated energies and wavelengths. The tan δ data remains relatively low for all composites whilst T_m remains ~ 121 °C, clear from figure 6.9, which remain the best indication of A site Ca occupation with respect to this WDS analysis attempt.

All composites, BCT and BT based, offer a total DC conductivity lower than their component phases sintered independently. These are 'banded' together with the BT-60NNBT composite, clear within the green area of figure 6.16, showing somewhat comparable activation energies and conductivity magnitudes across the entire temperature range. At high temperatures, the linear temperature dependence of conductivity and associated activation energies are of similar magnitudes. These are 1.51, 1.54 and 1.53 ± 0.01 eV in the BT, BC3T and BC5T composites and a lower 1.16 ± 0.02 eV for the BC7T based composite. This is typical of a value expected for intrinsic band conduction, based on the reported band gaps of BT (~3.2 eV) [266] and NN (~3.4 eV) [267]. For the latter three composites, this activation energy is almost identical to that quantified for 60NNBT, 1.53 ± 0.05 eV (Chapter 1), and slightly larger than that expected for the independently sintered BC3T and BC7T, 1.38 and 1.35 ± 0.02 eV, respectively. This might suggest a dominance of the DC conductivity at these elevated temperatures by the 60NNBT secondary phase. For the former, the BC7T based composite, the activation energy is lower than what would be expected of intrinsic band conduction in either of its component phases.

For the composites with measurable Z* responses at lower temperatures (the more conductive composites BC7T and BC3T), a separate linear temperature dependence of conductivity is observed. This linear region has a comparatively lower gradient and thus activation energy compared to the high temperature conductivity dependence. This activation energy is ~0.76 ± 0.07 eV in the BC3T and BC7T based composites, typifying extrinsic defect dominated conduction. This low temperature regime is likely highly sensitive to the pre-sintering processing of the composite. Defects and inter-granular interfacial effects are likely to influence the energy barrier for conduction. The low temperature conductivity response would likely vary between different samples of with the same component phases, based on the unique microstructures they yield. Repeat measurements may also reveal dissimilar conductivity behaviours, particularly if defects and associated energies change upon the thermal history of the sample. For the BC7T based composite, the high temperature activation energy is lower than what would be expected of intrinsic band conduction in either of its component phases, but higher than that observed at lower temperatures. This could imply a potential crossover between extrinsic and intrinsic conduction states. Alternatively, this lower activation energy is closer to that quantified for BC7T (1.35 ± 0.02 eV, table 2.3) than 60NNBT and could suggest a transition between the dominant electroactive material. This might transition from 60NNBT dominant in the BC3T and BC5T composites to BC7T dominant in this BC7T composite. The BC7T composite had been described to offer a more compositionally broad BCT matrix that shifted $T_{-15\%}$ to a greater extent than the other two BCT composite systems, figure B5. Perhaps the interconnectivity of these compositionally variant BCT species is then yielding this variable activation energy compared to the independently sintered BC7T.

Such a difference between BC7T based composites and the other two BCT composite systems is unsurprising since the BC3T and BC5T have been comparable to each other and different to BC7T-composites in other electrical/dielectric analyses. They both share closer permittivity magnitudes and $T_{-15\%}$ values. Their M'' responses share similar profiles in terms of the more resistive electroactive region offering the smallest capacitance. This is the converse to that of the BC7T composite, figure 6.15. This could also be indicative of a switch between the dominant electroactive material in the electrical microstructure, since the larger 60NNBT grains would inherently offer a lower capacitance and potentially correlate to the more resistive element in the BC3T and BC5T based composites. For BC7T, the more resistive element offers the smaller capacitance and thus the total impedance could be dominated by the BC7T related phases.

This is, of course, assumes each of these electroactive regions separated from one another based on the irregularly shaped M'' and disparate fmax correspond to each of these phases. The equivalent circuit is also likely to be much more complicated than a serial connection of two parallel RC elements, making this analysis primitive and qualitative. The roles of interfacial capacitances and resistances in such an irregular and variable microstructure will most likely influence the total impedance response of the composites and make reliable interpretation difficult.

6.6 Conclusions

X8R rated TCC can be achieved for the BC7T-60NNBT composite system when utilising the same 80:20 wt.% pre-sintered mixing ratio optimised for X7R rated TCC in the BT-60NNBT (results chapter 1) and equivalent low dwell sintering conditions of 1250 °C for 0.5 hours. Ca concentrates locally throughout the matrix phase, producing a distribution of BCT components. The resulting effect of variable T_m associated to these volume fractions of locally variant BCT is a diffuse high temperature permittivity response. This diffuse permittivity response stabilises the polarisation to temperatures beyond the conventional Tc of independently sintered BCT materials, delaying the onset of thermally induced Curie Weiss type depolarisation to an extent that shifts $T_{-15\%}$ above the 150 °C X8R threshold. WDS has revealed intragranular compositional variance within both bulk components phases of the composite that sustain diffuse permittivity responses in the low and high temperature regimes, essential for the TCC stabilisation acquired.

Obtaining the X8R rated criteria by substituting BT for BC7T comes at the expense of significantly reduced room temperature permittivity, decreasing by nearly one half to ~1100, and greater dielectric losses. Porosity is still prevalent throughout the composite microstructure and based on the need for thinner layers of the BC7T-60NNBT dielectric to attain device capacitance consistent with the higher permittivity BT-60NNBT, porosity will likely be costly for the induction of premature electric field induced dielectric breakdown.

The next stage of the composite system for use as an MLCC dielectric is to assess commercial feasibility. Specifically, the subsequent results chapter will investigate if a comparable dielectric response can be replicated using synthesis conditions and materials more relevant to commercialisation, including ball milling and commercial nanopowders. The density will be improved without compromising compositional heterogeneity, and electric field strengths will be quantified.

6.7 Appendix B

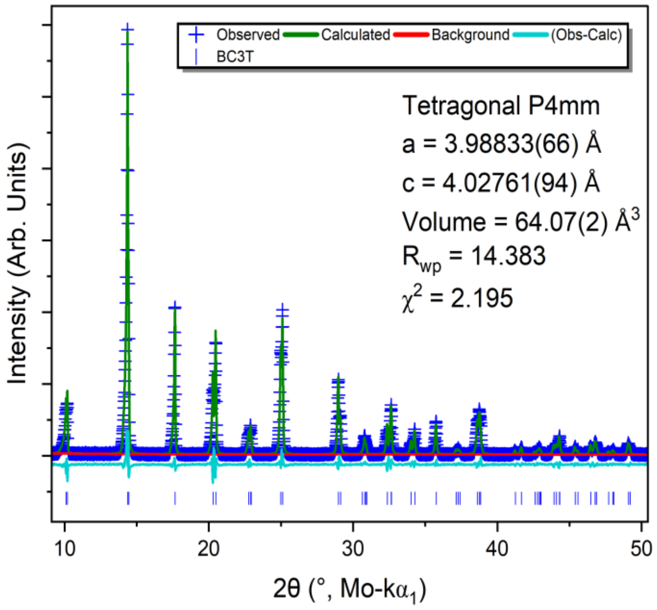

Figure B1: Rietveld Refinement of BC3T sintered at 1290 °C for 5 hours.

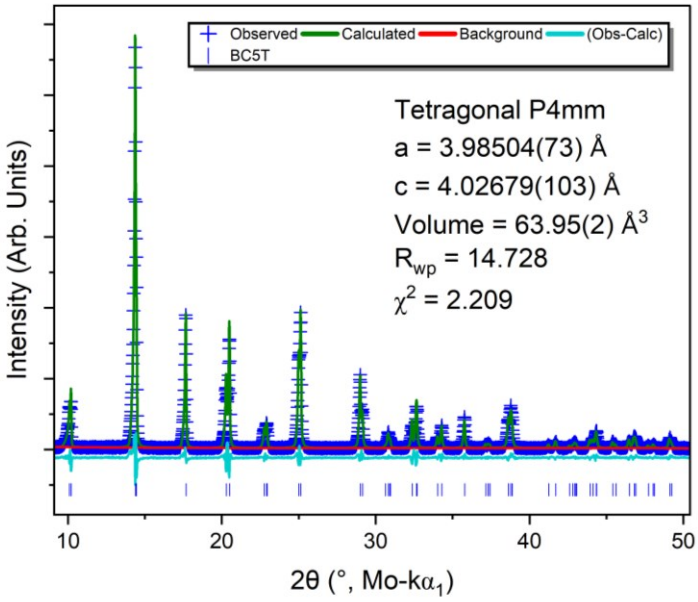

Figure B2: The Rietveld refinement of the BC5T sample sintered at 1290 °C for 5 hours

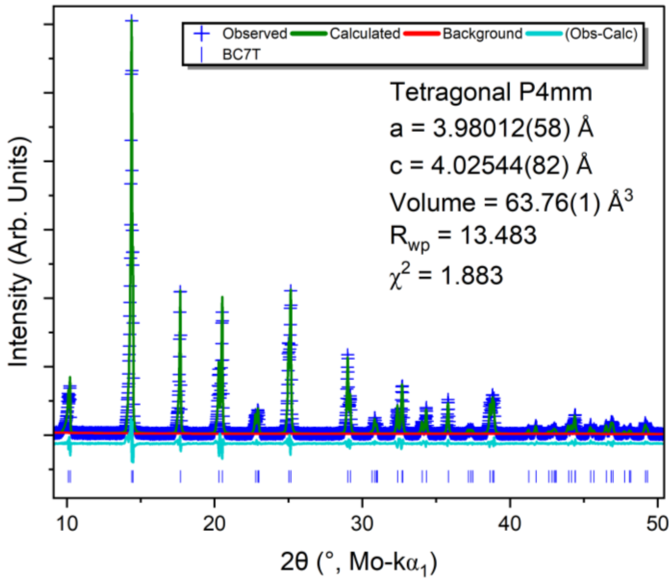

Figure B3: The Rietveld refinement of the BC7T sample sintered at 1290 °C for 5 hours

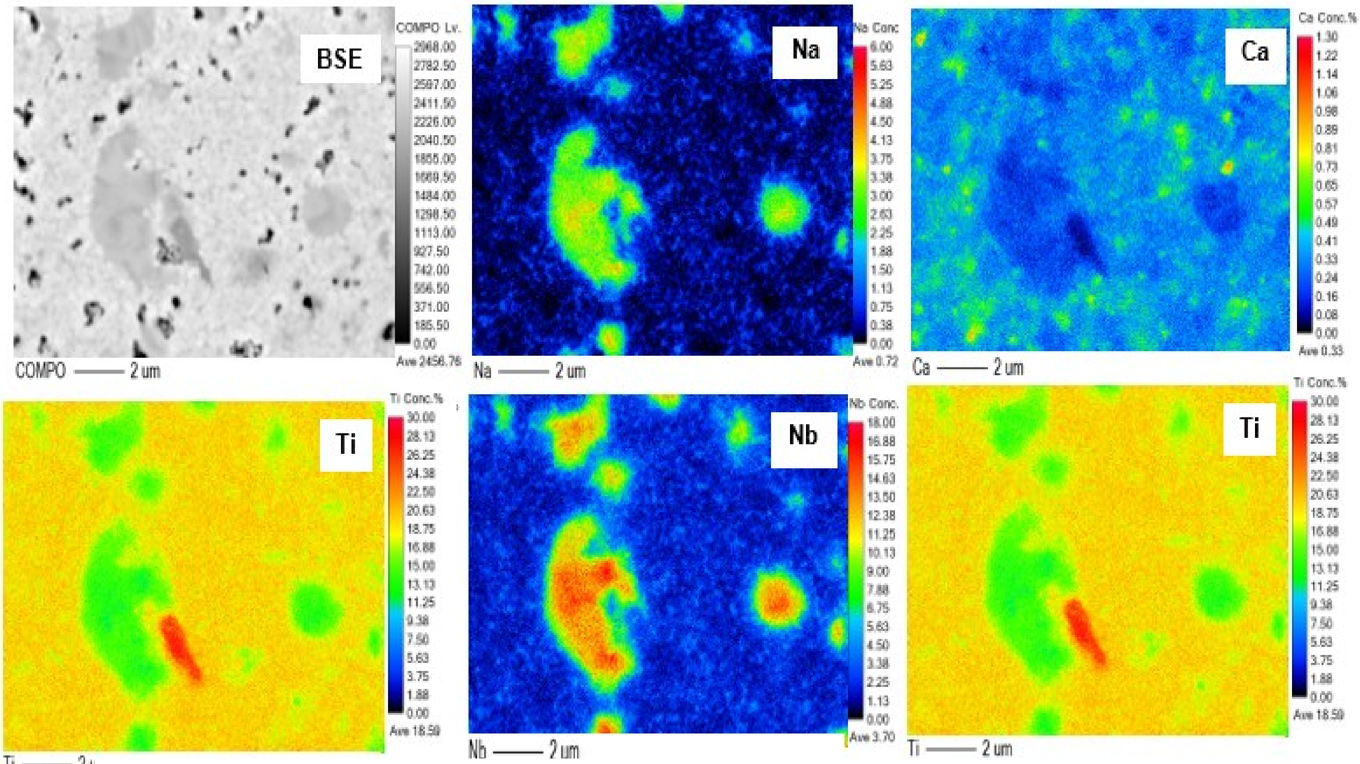

Figure B4: The distributions of A and B site cations composing the BC3T-60NNBT composite sintered at 1250 °C for 0.5 hours. Compositional heterogeneity is clear in the matrix and secondary phases.

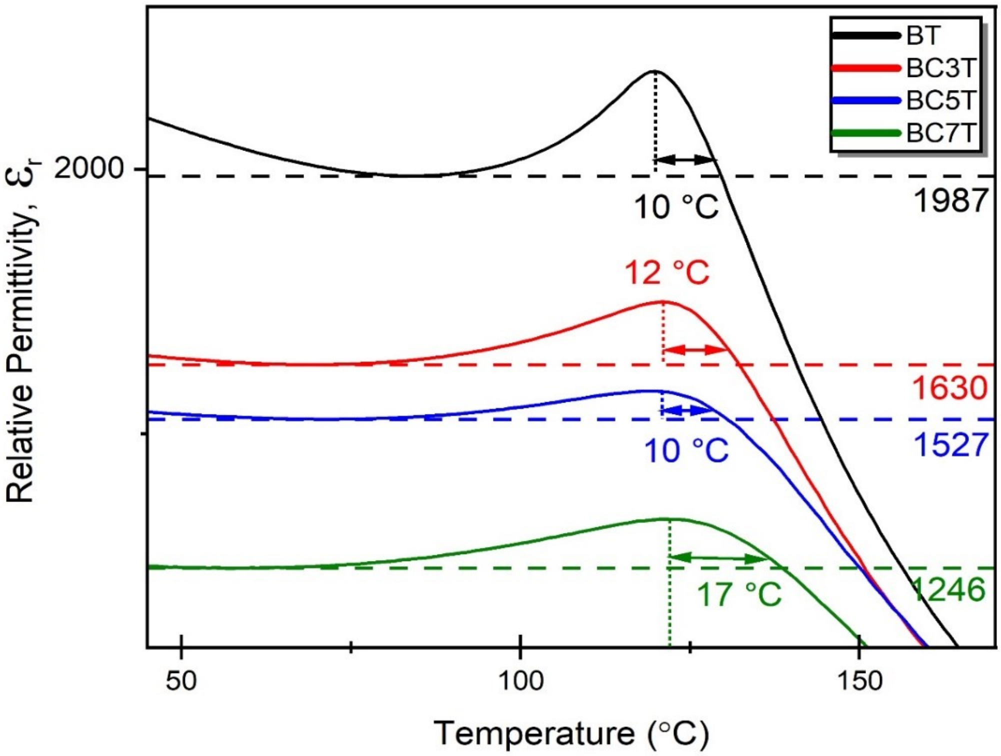

Figure B5: A comparison of the width of the BCT related permittivity peaks in the hand mixed BCT-60NNBT composites.

7 Results Chapter 3: Industrial scalability of the BCT-60NNBT composite system

7.1 Introduction

The previous results chapter concluded with the ability to achieve X8R-rated TCC specification for a hand-mixed composite arrangement of BC7T and 60NNBT in an 80:20 wt.% mixing ratio. Density calculations and SEM micrographs revealed an extensive degree of porosity exists within these composite systems investigated, ranging from 79.7 to 86.5 % in BC7T and BT based composites, respectively. This is inherent of the low sintering dwells afforded to the composites, used to retain the electrically distinguishable compositional heterogeneity that is essential for the provision of the TCC achieved. Low densities are deleterious to the magnitude of the permittivity, but potentially more significantly, offer comparatively lower electric field induced dielectric breakdown strengths with respect to fully dense ceramics. Specifically, pores act as nucleation site for dielectric breakdown on account of the large local electric fields that are geometrically induced around the circumference of the pore (depending on size, shape distribution and pore inter-connectivity of course) [268,269]. Prospective integration into MLCCs is hoped for these composite dielectric systems, but the higher electric fields these thin dielectric layers are typically exposed to, compared to the bulk ceramics analysed so far, will likely prove problematic on account of this significant porosity observed. Increasing the densification at current sintering conditions would be optimal to reduce porosity and retain the same extent of compositional heterogeneity that has yielded the good, repeatable, X8R rated dielectric responses.

Glass is often used industrially in low weight percentages as a sintering additive, to lower sintering temperatures, improve densification and limit grain growth [270]. This occurs typically through a liquid phase sintering mechanism [271], as the glass melts at lower temperatures with respect to the ceramic, wetting the grains, re-packing and densifying with high associated kinetics. Glass can therefore help improve breakdown through a reduction in porosity, but also in controlling grain sizes by inhibiting grain coarsening stages during sintering, with breakdown frequently improved in proportion to grain boundary density [272–274]. Large quantities of literature have been dedicated to the use of glasses for this control over microstructure and dielectric breakdown strengths, including in BT [275–277], where the lower sintering temperature afforded by glasses is also beneficial for BME electrode integration. In ceramics with prospective use as high energy density capacitors, such as $Ba_{0.4}Sr_{0.6}TiO_3$ (BST) [278–284], glass addition facilitates an enhancement of breakdown strength which allows linearly polarisable dielectrics to achieve higher maximum polarisation and increase the recoverable energy densities stored.

Additions of glass to the composite system would be useful in reducing porosity that has been extensively characterised, without the need of extending sintering temperatures or dwells that would be deleterious to the compositional heterogeneity that sustains the X8R rated TCC. Glass will be added in varied quantities with density, DS and electric field induced polarisation behaviour (P-E response) characterised, associating a field induced breakdown strength to the composites. SEM/EDX will characterise any changes in microstructure imposed by the glass sintering additive, with correlations made to the DS results. The composite systems will then be synthesised with a more commercially feasible synthesis route to assess industrial scalability. This includes the composite pre sintered components being milled via ball milling as opposed to hand mixing, which would afford larger batch sizes necessary for commercialisation. DS responses of ball milled and hand mixed composites will assess if reproducible X8R rated dielectric response can be sustained upon this milling transition. It would also be preferable to synthesise the 60NNBT secondary phases during sintering from interdiffusion between the commercial NN and BT in a stoichiometric ball milled mixture of BCT, NN and BT. This would alleviate an additional calcination step to form 60NNBT pre-milling, expediating composite synthesis and reducing costs. DS will analyse the effect a stoichiometric mix of these commercially available nano powders has on reproducing the X8R rated permittivity response.

7.2 Experimental Conditions

The B7CT and BC3T used in the composites was industrially sourced, with their nomenclature, Ca content and particle size tabulated in table 6.1. The industrially sourced glass mixed into the composites pre-sintering, via a 6 hour wet ball milling, has the composition tabulated in table 7.1.

Table 7.1: The compositional content of Asahi glass, used as a sintering aid for enhanced composite densification, sourced from Kyocera-AVX.

Asahi Glass Sintering Additive Data Sheet – As Received from Kyocera-AVX	
Composition (wt.%)	
SiO_2	40.1 ± 2.0 %
BaO	40.9 ± 2.0 %
CaO	14.5 ± 1.0 %
Li_2O	4.0 ± 0.5 %
SrO	0.8 % Max
Al_2O_3	0.15 % Max
Fe_2O_3	0.05 % Max
Particle Size Distribution (Diameter, μm)	
Post Milling D50	0.85
Post Milling D90	1.60
Thermal Properties (°C)	
Transition Point	555 ± 20
Softening Point	630 ± 20

All BCT-60NNBT composites were synthesised using the same 80:20 wt.% ratio optimised for X7R rated TCC in results chapter 1, with the same sintering conditions of 1250 °C for 0.5 hours:

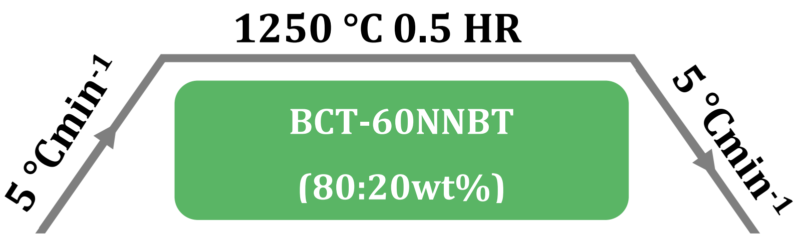

Figure 7.1: The sintering conditions used to prepare the BCT-60NNBT ceramic composites.

7.3 Hand-Mixed vs. Ball-Milled BC7T composites

7.3.1 XRD of Hand-Mixed and Ball-Milled BC7T Composites

The XRD patterns comparing the BC7T-60NNBT composites made from a pre sintering 0.5 hour hand mixing and a 6 hour ball-milling of the component phases are shown in figure 7.2. All reflections accounted for by the overlapping of the P4mm BC7T and Pm-3m pseudo-cubic 60NNBT reflections, and are coincident between the two composites regardless of their pre-sintering mixing mechanism. No additional phases are evident from the lack of additional reflections. Slight shifting in 2θ is apparent between the two composites, shown on the inset image of figure 7.2 for the (101)(110) reflections. There are slight changes in peak intensities between these two composites.

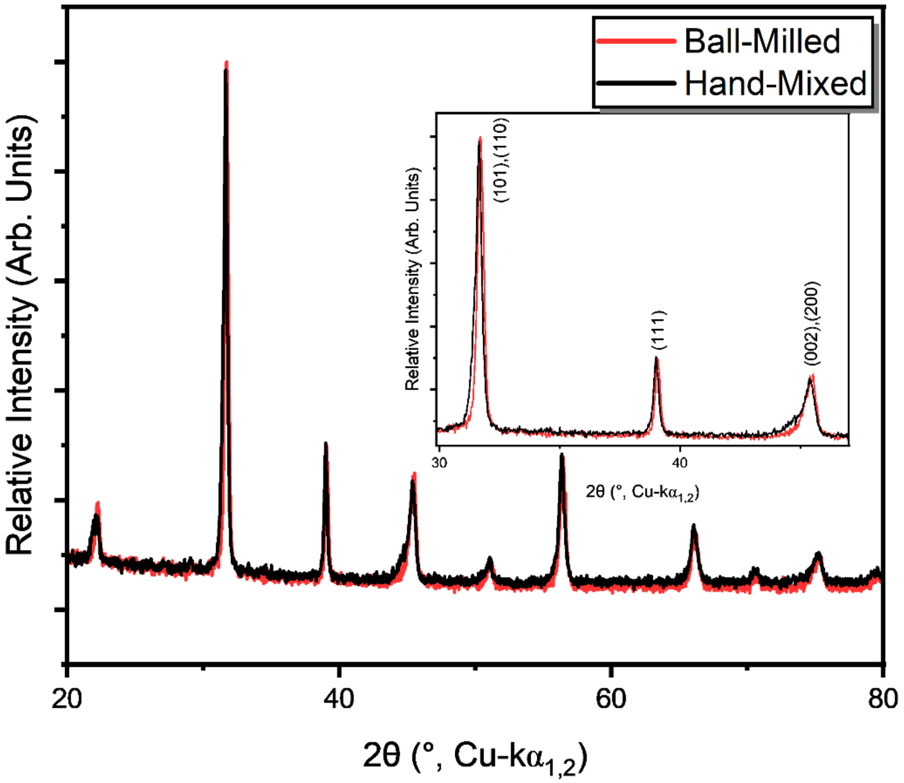

Figure 7.2: The XRD diffraction patterns for BC7T-60NNBT composites formed from hand mixing vs ball milling of its constituents.

7.3.2 DS Responses of Hand-Mixed vs Ball-Milled BC7T composites

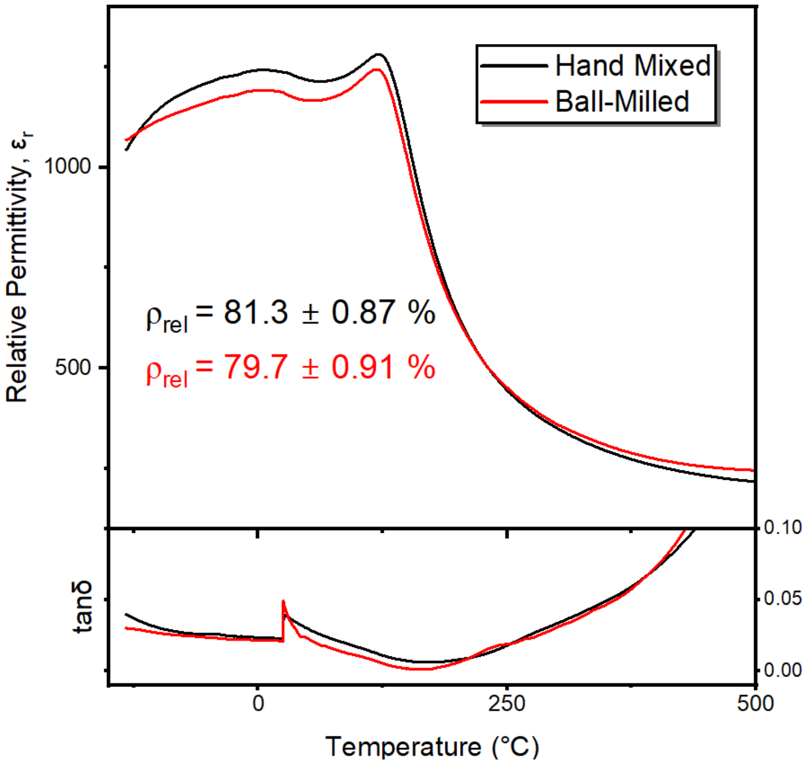

Figure 7.3: A comparison of the dielectric responses of BC7T based composites sintered at 1250 °C when the phase mixture was formed from hand-mixing vs ball milling of the associated components.

A comparison of the dielectric responses of the BC7T composites where pre sintering processing varies between hand mixing (black) and ball-milling (red) of the BC7T and pre-calcined 60NNBT is shown in figure 7.3. The permittivity magnitudes vary slightly, with the ball milled sample offering a room temperature permittivity ~ 50 lower than the hand mixed sample. Both composites exhibit a permittivity magnitude in excess of 1200 at room temperature. The most significant variation in permittivity between the two composites appears towards the low temperature permittivity response, where the depolarisation of the NNBT related permittivity peak is not as sharp in the ball milled sample with respect the hand mixed sample. tan δ is almost identical for both samples. The loss in the hand mixed sample is higher by a maximum ~0.01 compared to the ball-milled sample at temperatures below the T_m associated to the BC7T matrix phase. The high temperature rise, consistent with increasing DC conductivity contributions, is almost identical in both composites.

The TCC response, figure 7.4, shows the profile/shape of the permittivity response, and varies minimally across the X8R temperature range, -55 to 150 °C. Both composites are consistent in achieving the X8R rated TCC specification, with $T_{-15\%}$ equivalent between both composites at 152 °C. The difference in how 'sharp' the depolarisation of the low temperature NNBT-related phase is becomes more apparent from this TCC plot. It is apparent that the high temperature BCT related permittivity peak varies between the two composites, with the ball milled sample exhibiting an associated permittivity peak that is slightly higher with respect to the room temperature permittivity and comparatively more diffuse than the hand mixed sample. The T_m associated to the BCT related permittivity peak also varies between the two composites, with the ball milled sample exhibiting a $T_m \sim 119$ °C, lower than that of the hand mixed sample with ~ 122 °C.

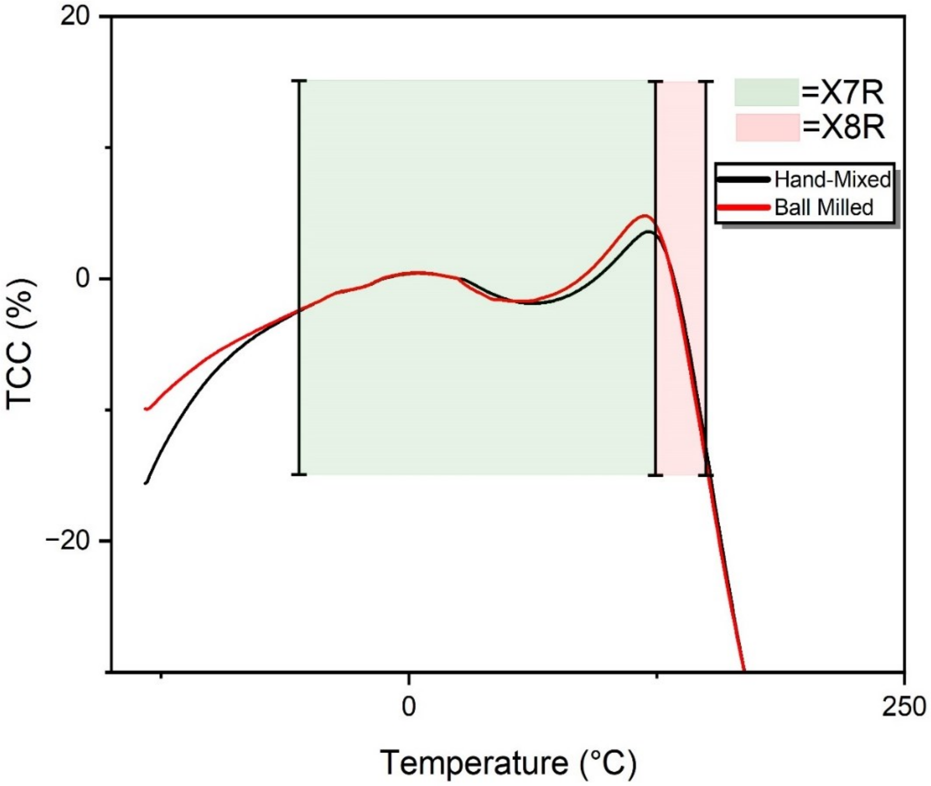

Figure 7.4: The TCC responses of the hand-mixed and ball milled BC7T based composite systems.

7.4 Ball-milled stoichiometric mix of BT, NN and BCT for the synthesis of 60NNBT during sintering

7.4.1 XRD of Ball-Milled BC7T Composites using Pre-Calcined 60NNBT vs Stoichiometric Mix of BC7T, NN & BT

It is next considered whether the 60NNBT used within the composite systems can be synthesised during sintering. This would be achieved from the necessary stoichiometric mix of BC7T, NN and BT (one pot) to yield the same 80:20 wt.% ratio of BC7T:60NNBT, as tabulated in table 7.2.

Table 7.2: The necessary stoichiometry to attain a 15g batch of 80:20 BC7T: 60NNBT, assuming 60NNBT formation during sintering.

Commercial Powder	Mass (g)
BC7T-200	12.00
KCM200 (BT)	1.46
NN	1.54

A comparison of the diffraction patterns for BC7T-60NNBT composites synthesised from ball-milling the BC7T and pre-calcined 60NNBT components in the 80:20 wt.% ratio (black), and ball milling of the stoichiometric mix of BC7T, BT and NN (red), is shown in figure 7.5. The overlaid diffraction patterns show a comparable effect as the comparison between hand mixed and ball milled composites formed with pre-calcined 60NNBT, figure 7.2.

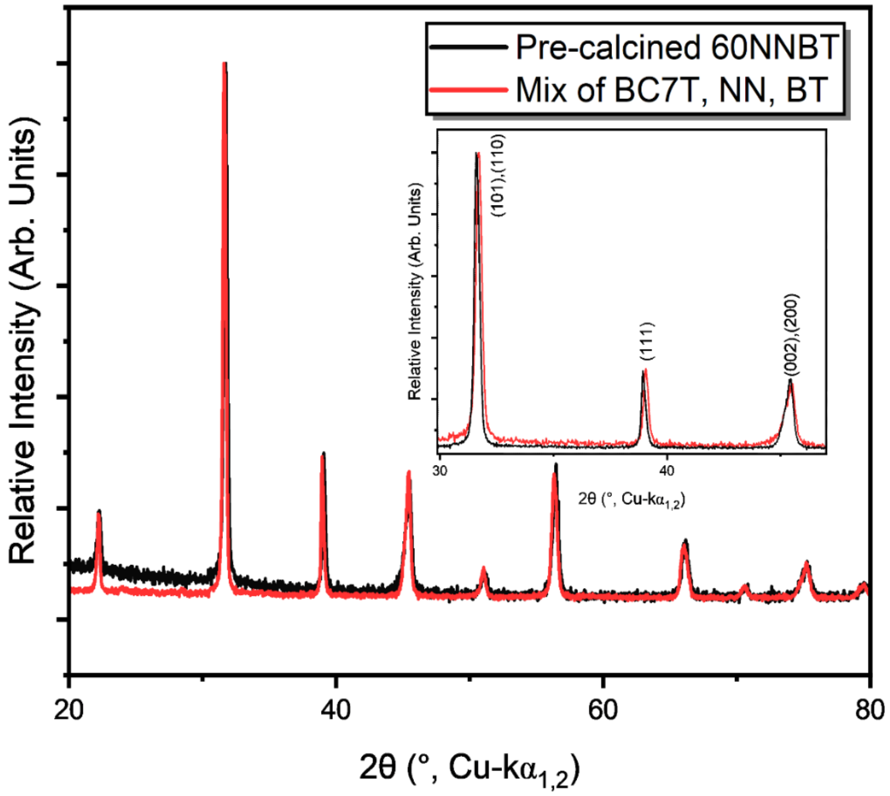

Figure 7.5: The XRD diffraction patterns of the BC7T-60NNBT composites formed from hand mixing and ball milling of BC7T with pre-calcined 60NNBT, and ball milling of the stoichiometric mix of BC7T, NN and BT (table 7.2). 60NNBT in the latter system is assumed to form during sintering.

All reflections share similar 2θ values corresponding to overlapping tetragonal BC7T and pseudo-cubic 60NNBT reflections. 60NNBT appears to have been synthesised during sintering based on this similarity of XRD patterns for the composite formed from the mixed commercial powders with that of pre-calcined 60NNBT. No additional superlattice reflections ~ 26 – 41 ° are evident, which are associated to the in-phase/anti-phase tilting of [NbO_6] octahedra that yield the antiferroelectric orthorhombic ‘P’ room temperature polymorph of NN. This implies the mixed, undoped NN is not retained post sintering. 2θ values do shift between the composites synthesised via these differing routes, indicating the lattice parameters for one or more of the component phases differ. Intensities of peaks are also found to vary according to the synthesis route.

7.4.2 DS Response of Ball-Milled BC7T Composites using Pre-Calcined 60NNBT vs Stoichiometric Mix of BC7T, NN & BT

The dielectric responses of the BC7T-60NNBT composites formed from pre-calcined 60NNBT and from a stoichiometric mixture of BC7T, BT and NN are compared in figure 7.6.

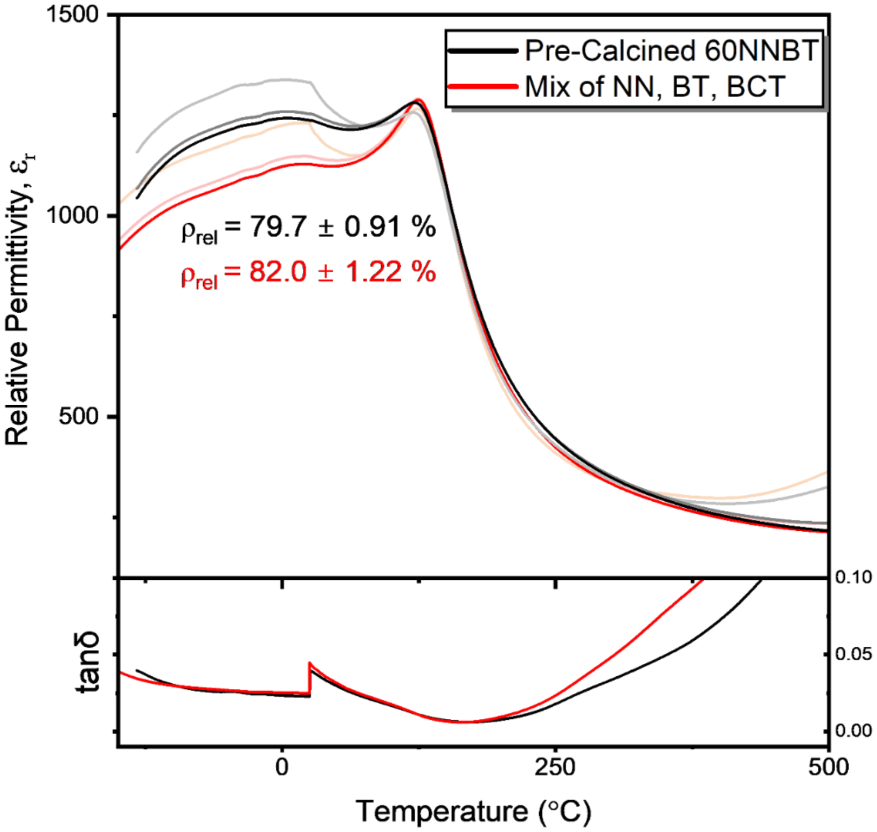

Figure 7.6: A comparison of the dielectric responses BC7T-60NNBT composites sintered at 1250 °C when the phase mixture was formed from ball milling with pre-calcined 60NNBT vs ball milling of the stoichiometric ratio of industrially sought BCT, NN and BT. 60NNBT is intended to be synthesised during sintering for the latter composite.

Similarities exist between the two responses in the permittivity being composed of a low and high temperature response associated with a NNBT and BCT type phase, respectively. The relative intensities of these different permittivity peaks, however, are quite different. The permittivity of the NNBT type low temperature response is much lower in the composite formed from the mixing of oxides compared to that using pre-calcined 60NNBT. The intensity of the BC7T related permittivity peak in both composites is, however, similar. This disparity in relative intensities of the two constituent phases of the composites is better visualised on their corresponding TCC profiles, figure 7.7.

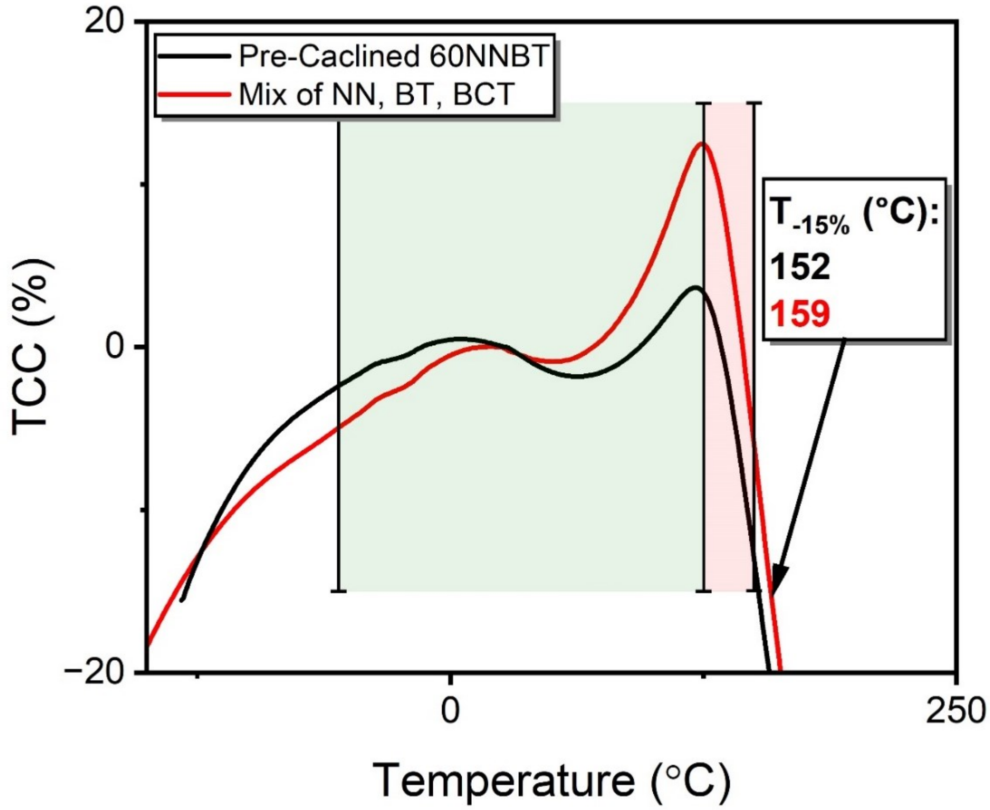

Figure 7.7: The TCC response, at 250 kHz, of the ball milled BC7T based composites formed from pre-calcined 60NNBT and the stoichiometric mix of BT, BCT and NN.

Compared to the composite utilising pre-calcined 60NNBT, the composite formed from the stoichiometric mix of commercial powders exhibits a TCC profile where the high temperature BCT related peak is much higher with respect to the room temperature permittivity and the low temperature response is much lower with respect to the room temperature permittivity. This dissimilarity between low and high temperature permittivity magnitudes destabilises the associated TCC, pushing the composite closer to exceeding the R-type ± 15 % boundaries. The maximum TCC associated with the high temperature BCT related permittivity peak increases from 3.6 % at 122 °C in the hand mixed composite, to 12.4 % at 123 °C in the composite formed of the stoichiometric milling of oxides. Although the depolarisation rates between the two composite systems appear consistent based on the parallel decline of permittivity above T_m, $T_{-15\%}$ is shifted from 152 °C to 159 °C when the composite is formed from the mixing of commercial oxides as opposed to pre calcined 60NNBT.

From figure 7.6, the dielectric loss is identical for temperatures below T_m. Above T_m, tan δ is greatest for the composite formed from the mix of commercial powders, exceeding 0.05 ~ 300 °C. The composite formed of pre-calcined 60NNBT exceeds the same threshold at ~ 350 °C.

An equivalent comparison of the dielectric responses of the BC3T-60NNBT composites formed from ball milling of pre-calcined 60NNBT versus one where 60NNBT is intended to from during sintering of the mixed BC3T, NN and BT, is given in appendix C, figure C1. A comparable dielectric response is observed with the exception that unlike the BC7T analogue, the permittivity magnitude of the composite formed from the mix of commercial BC3T, BT and NN is higher than that of pre-calcined 60NNBT. The intensity of the BC3T related peak is again higher with respect to room temperature than when pre-calcined 60NNBT is used, but not to the same degree as that observed for the BC7T system. TCC, figure C2, is not pushed as close to the +15 % boundary, nor is $T_{-15\%}$ increased by the same degree as in the BC7T system. $T_{-15\%}$ increased by + 2 °C, from 143 to 145 °C. The same relationship of an identical tan δ at sub-T_m temperatures and a higher tan δ above T_m exists between the BC3T composite formed from the mix of commercial powders and that formed of pre-calcined 60NNBT, respectively.

7.5 Addition of Glass to Improve Densification of BCT-60NNBT Composites

Since ball-milling of the composites achieves comparable dielectric response with respect to hand mixing of the BCT and 60NNBT components, the composite has moved closer to having industrial manufacturability. The porosity still remains an issue, quantified with a low ball milled relative density ~ 79.7 ± 0.91 %. The effect of glass as a sintering aid to improve density will be considered next, investigating its role on the dielectric response of the composite. Since BC3T composites were the furthest from X8R specification, comparing the effect of glass on these composites allowed for an additional assessment on its potential influence on $T_{-15\%}$ and X8R attainment for a composite system with high relative permittivity.

7.5.1 XRD analysis of BC3T composites with glass additions

The XRD diffraction patterns of the BC3T-60NNBT composites with varied wt.% of glass added to the pre-sintered mixture, namely 2, 4, 8 and 12 wt.%, are shown in figure 7.8.

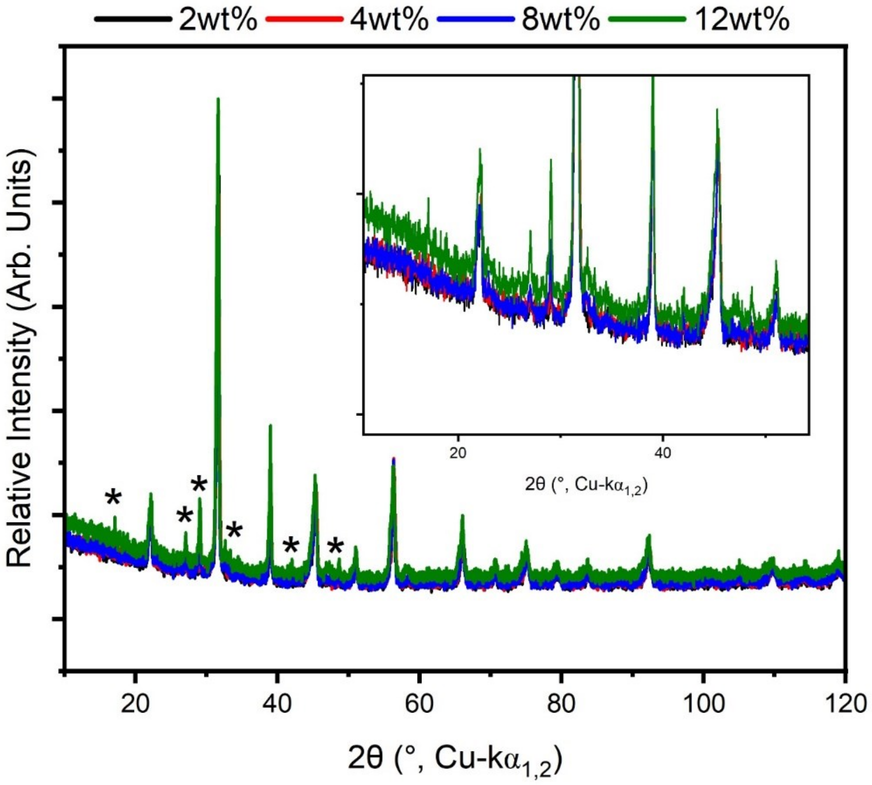

Figure 7.8: The XRD patterns for BC3T-60NNBT composites sintered at 1250 °C for 0.5 hours with increasing glass content. The growth of a $Ba_2TiSi_2O_8$ Fresnoite phase is indicated by the peaks marked with an asterisk, *

The reflections marked with an asterisk correspond to a $Ba_2TiSi_2O_8$ Fresnoite phase, which increase in intensity with increasing glass additions into the composite. The peaks not marked with an asterisk correspond to the perovskite reflections of the tetragonal BC3T and pseudo-cubic 60NNBT phases.

7.5.2 SEM of glass-containing BC3T-composites

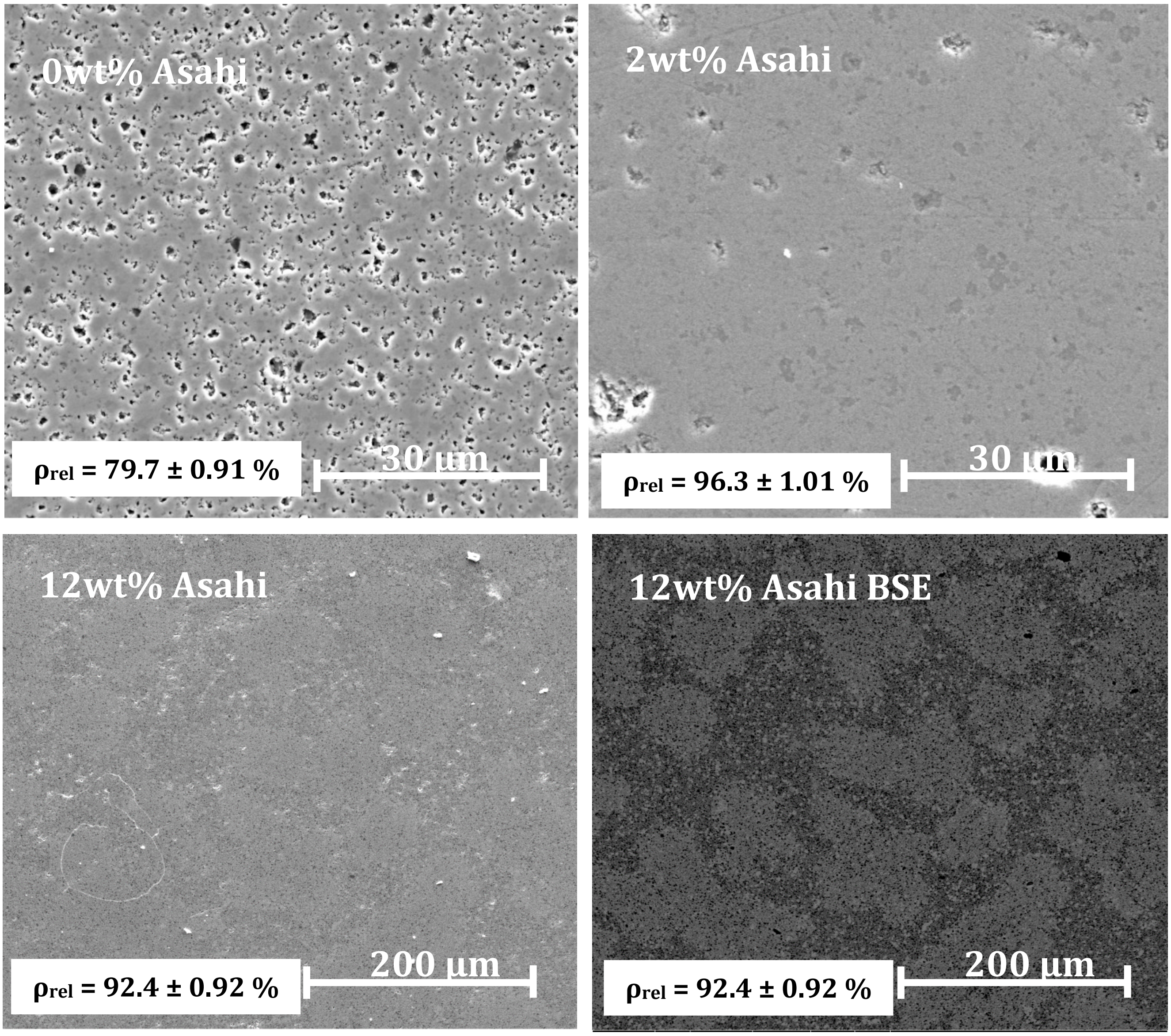

Figure 7.9: The SE and BSE micrographs for the BC3T based composite sintered with 0, 2 and 12 wt.% glass. The growth of Si-rich clusters/islands is clear from the BSE of the 12 wt.% sample.

SEM micrographs for no (0 wt.%), low (2 wt.%) and high (12 wt.%) additions of glass to the BC3T-60NNBT composite are shown in figure 7.9. 2 wt.% results in a significant reduction in porosity, quantified as increasing from 79.7 ± 0.91 to 96.3 ± 1.01 %. Large grains comparatively darker with respect to its surrounding grain structure are clear from the 2 wt.% additions micrograph. These correspond to the 60NNBT related secondary phases that are of lower molecular mass (191.6) compared to the surrounding BC3T (230.3). The 12 wt.% additions of glass appear to increase the porosity from this 2 wt.% additions composite, with noticeable clustering of denser and potentially compositionally variant regions forming a 'leopard print' type microstructure, clear from the BSE image of figure 7.9 shown in the bottom right. The relative density also decreases form 96.3 ± 1.01 to 92.4 ± 0.92 %.

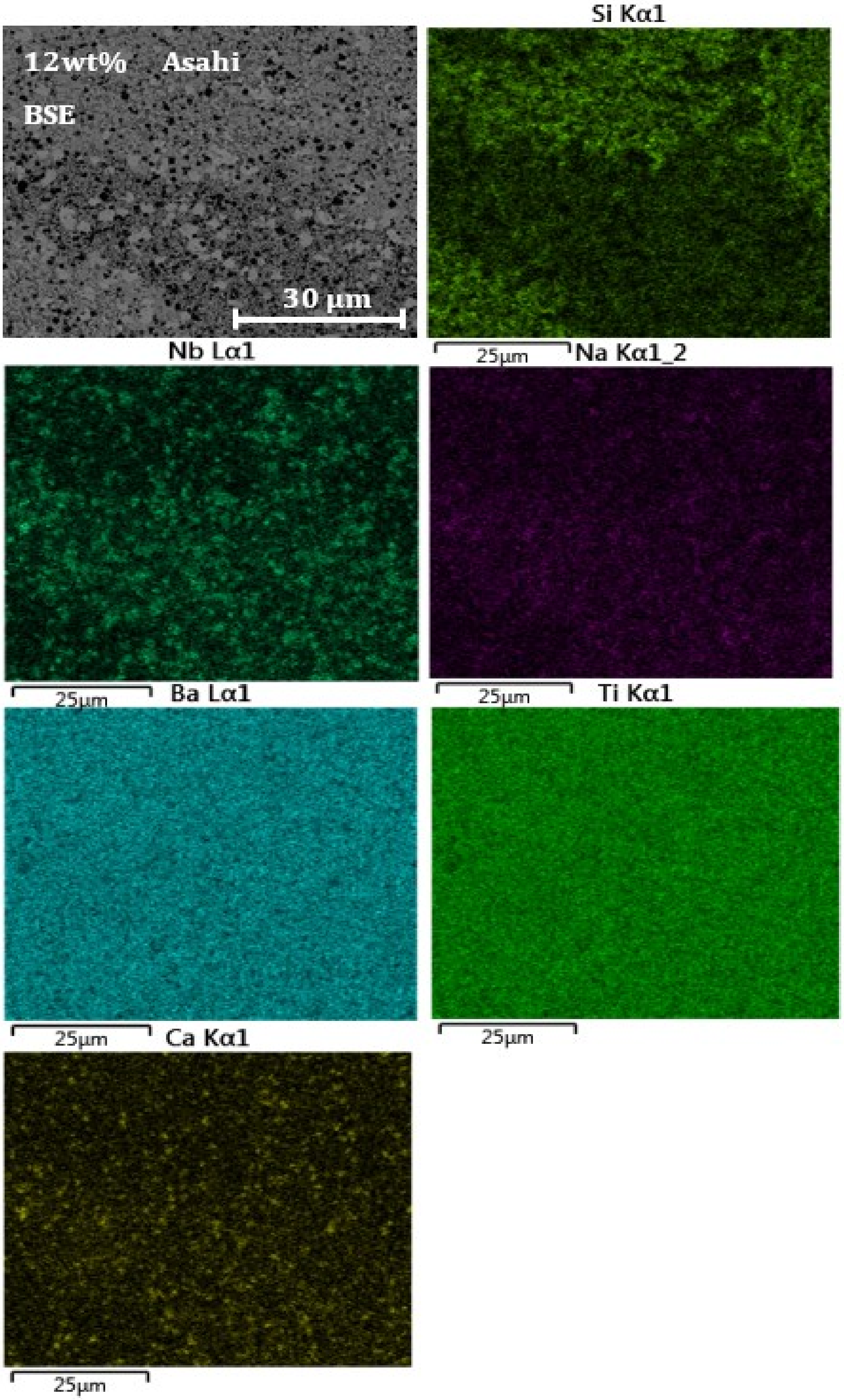

Figure 7.10: EDX elemental maps of the 12 wt.% BC3T based composite, highlighting the edge of one of the Si rich morphological clusters.

EDX analysis of this 12 wt.% BC3T composite, figure 7.10, reveals these clusters to be Si-rich. The lighter shading of these regions makes sense from the comparatively lower atomic mass of Si (~28.1) with respect to the other cations that constitute the composite (with the exception of Na, ~23.0, in the NNBT secondary phases). From the BSE image of figure 7.9, the porosity appears to be greater in the channels between these Si-rich clusters, with this porosity variability another factor influencing the clustering of contrasting intensity across the micrograph. The NNBT type phases that are clear in the EDX analyses as small, micron scaled spots of high Nb and Na concentration, appear to have a higher population density in the areas that are not Si rich. EDX reveals a relatively homogeneous distribution of Ba, Ti within the matrix phase, but the Ca distribution is heterogeneous. This is consistent with the WDS results in results chapter 2 for the glass-free composite, figure 6.5. There appears no preference for Ca-rich areas to form and are distributed relatively homogeneously throughout the area investigated, including the Si-rich regions.

7.5.3 DS of BC3T composites with glass additions

The dielectric response of the BC3T composites with varied glass contents are shown in figure 7.11, whilst their associated TCC responses are plotted in figure 7.12.

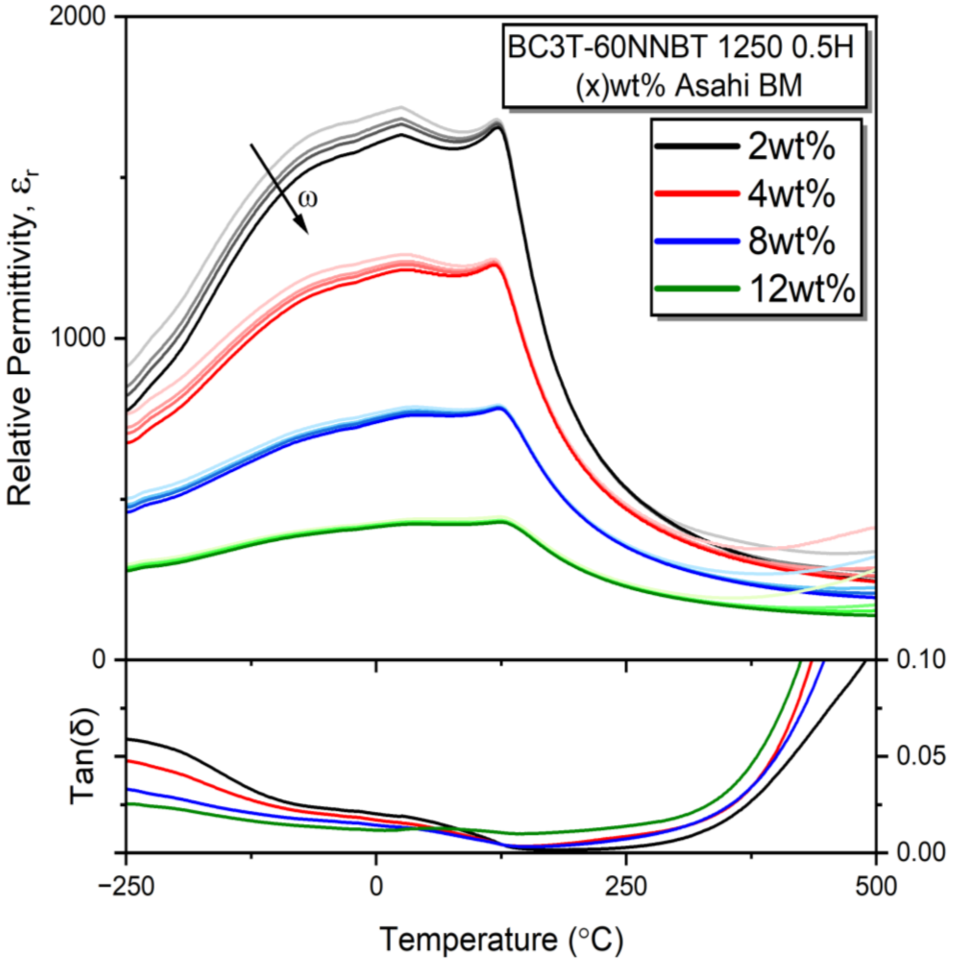

Figure 7.11: The effect of increasing glass content on BC3T based composites sintered at 1250 °C for 0.5 hours. A loss of permittivity magnitude is observed with increasing glass content, whilst the permittivity profile becomes increasingly flattened.

The permittivity magnitude associated to the BC3T based composite decreases with increasing glass content. The frequency dependence at lower temperatures that is associated with the relaxor 60NNBT composition of the composite also decreases with increasing glass content. The low and high temperature depolarisation responses become increasingly diffuse, with this effect more noticeable on the TCC response. $T_{-15\%}$, at 143 °C for the composite without any glass addition from figure 6.9, is shifted to higher temperatures maximising at 164 °C for 12 wt.% glass addition. Across the 2 – 12 wt.% glass addition range, a Δ $T_{-15\%}$ ~ + 12 °C is achieved, as shown in figure 7.12. This BC3T composite that was previously only characterised with X7R rated TCC in the previous chapter now meets X8R rated TCC specification for glass contents of 8 wt.% and above. Based on the shift of $T_{-15\%}$ with glass content, plotted in appendix C figure C3, a glass content of ~ 6.5 wt.% is sufficient to extent $T_{-15\%}$ to the 150 °C 8R-type TCC boundary.

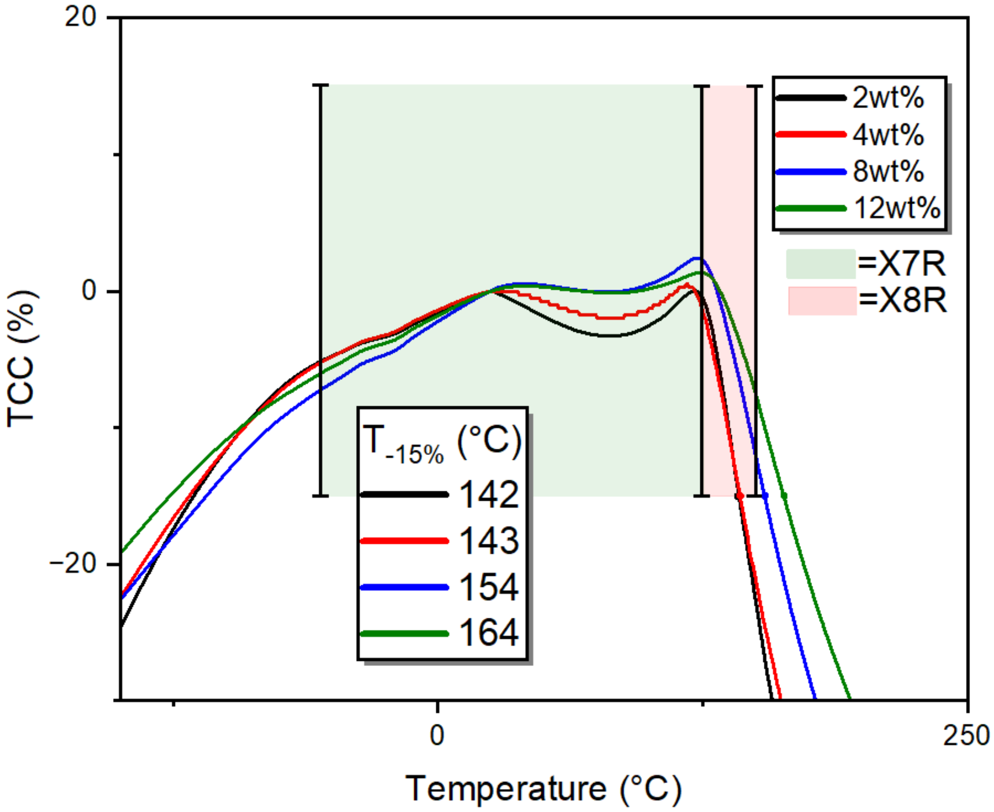

Figure 7.12: The TCC associated to the permittivity responses of BC3T composites sintered at 1250 °C for 0.5 hours with increasing glass content.

The tan δ responses of the composites with varied glass contents are shown in figure 7.11. The sub ambient 'relaxations' in the loss that are clear at 2 wt.% additions (black) are progressively supressed with increasing glass content. This is in line with the comparable suppression in their associated permittivity anomalies with increasing glass addition. The overall tan δ for the sub ambient permittivity response is lower with increasing glass content. Above T_m, the trend appears to be the converse, with 12 wt.% exhibiting the highest losses and 2 wt.% exhibiting the lowest losses. 4 and 8 wt.% appear to show very consistent losses above T_m, and lie between these aforementioned minima and maxima. All composites show a rise in tan δ at temperatures above ~ 375 °C, with the onset of DC conductivity dominating the dielectric losses as opposed to local ac polarisation losses.

7.5.4 The electric field dependence of glass containing BC3T composites

To assess the electric field dependence of these composites, a room temperature polarisation electric-field (PE) analysis of the composites was conducted, with results shown in figure 7.13.

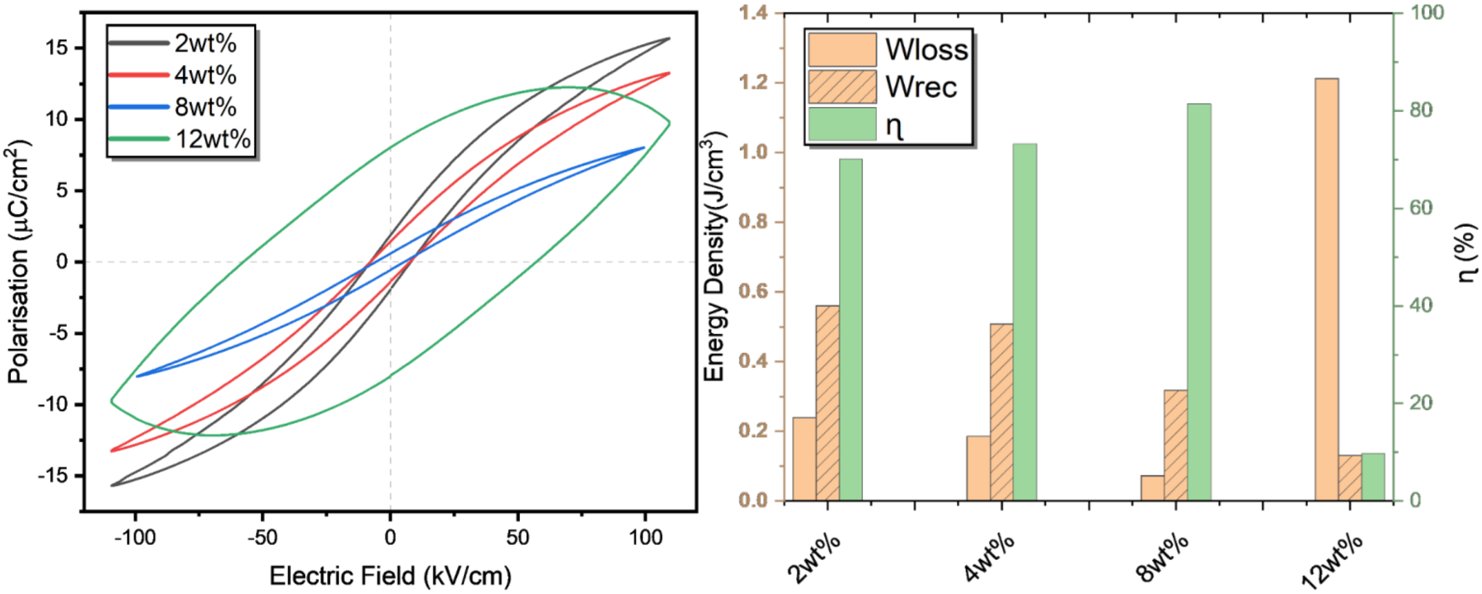

Figure 7.13: The P-E response of the BC3T based composites with varied glass content. The lower graph visualised the recoverable and unrecoverable energy density associated to the polarisation response of the composites, as well as the energy storage efficiency.

All samples were able to sustain a maximum voltage of ~ 110-120 kVcm^{-1}. A glass-free composite is not shown on figure 7.13 for its electric field dependence was unmeasurable. Thus, electric field resistance is significantly improved upon low, 2 wt.%, additions of glass. The maximum polarisation achieved for the composites decreases with glass, which is consistent with the observed reduction in permittivity with increasing glass content.

With increasing glass content, the PE loops appear to transition from a ferroelectric type response at 2 wt.% with the polarisation trending towards saturation at higher fields, to a more linear type response at 8 wt.%, with reduced saturation effects at higher electric fields. The PE response for the 12 wt.% composition is extremely wide, indicating large leakage currents and a transition from dielectric behaviour. Recoverable and irrecoverable energy densities of the composites were quantified according to the integrals stated in figure C4 of appendix C. From 2 – 8 wt.% glass additions, the increasing linearity of response results in a lower irrecoverable energy density. The lower polarisation achieved simultaneously decreases the recoverable energy density, with the maximum recoverable energy density occurring for the 2 wt.% composite at 0.56 Jcm^{-3}, and the lowest occurring in the 12 wt.% composite at 0.13 Jcm^{-3}. However, the recoverable and irrecoverable energy densities do not decrease at the same rate with increasing glass content, and consequently the efficiency in recovering stored energy density increases with glass content between 2 and 8 wt.%. The maximum efficiency is calculated as 81.5 % in the 8 wt.% composite, whilst the lowest efficiency is associated to the 12 wt.% glass composite, with an efficiency of 9.7 %. For the 2 wt.% glass sample that shows no evidence of fresnoite phase formation, an associated energy storage efficiency ~77.1% is achieved.

7.6 Discussion

Figure 7.3 revealed that the X8R rated permittivity response attained for a hand-mixed 3-0 composite of BC7T and pre-calcined 60NNBT could be reproduced with ball milling of its components in the same 80:20 wt.% ratio. This is reflected in permittivity magnitudes that differ minimally with superimposable TCC profiles, figure 7.4, and almost identical tan δ responses. No additional permittivity peaks/anomalies suggest additional phase formation are encouraged by the different milling technique utilised, consistent with the XRD diffraction patterns in figure 7.2 exhibiting the same reflections at relatively equivalent 2θ. This is unsurprising since the same phases were mixed pre-sintering. Ball milling was only conducted for around 6 hours, so limited contamination from the YSZ milling media should have occurred. It is unlikely that the ball milling will have improved upon the homogeneity of the phase distribution as an already homogeneous 3-0 distribution of NNBT secondary phases within the BC7T matrix was evident from the micrographs of figure 6.7 and 6.8, results chapter 2. Since the YSZ milling media were relatively large in size, cylinders 10 mm in diameter and 20 mm in length, the BC7T nano powders and the micron scaled 60NNBT (from solid state synthesis) that are milled are unlikely to reduce in size. Some materials can become susceptible to cold welding effects but since this ball milling is relatively low energy, it is unlikely to be the case. Thus, particle distribution and size are expected to be fairly consistent for the ball-milling and hand-mixed composites. Consequently, comparable interdiffusion rates between the BCT and 60NNBT phases are expected, producing similar compositional distributions and yielding the reproducible dielectric responses observed in figure 7.3. This is significant in transitioning the composite systems from lab-scaled bulk prototyping towards industrial processing, where large batches of ball milled slurries are synthesised prior to tape casting of dielectric layers.

For improved commercial feasibility, synthesising 60NNBT during the sintering stage from a stoichiometric ball milled mixture of BCT, NN and BT (one pot) would be preferable, alleviating the necessity for a calcination stage and expediating manufacture. Figure 7.6 shows that a comparable 'biphasic' BCT based composite permittivity response can be achieved from the stoichiometric mix of nano powders, with X8R rated TCC achieved (figure 7.7). Noticeable differences occur at the low temperature NNBT related permittivity response in figure 7.6. It is logical that this is the region of the permittivity response that varies since it is the only composite component that varies between the two systems investigated. The fact that the shape of the permittivity response at low temperatures appears fairly consistent, just translated to a lower permittivity (by ~ 120) when the 60NNBT phase is synthesised during sintering, suggests compositionally similar NNBT type secondary phase compositions (with similar intragranular compositional gradients to those defined in results chapter 2 via WDS, figure 6.7) are equivalently homogeneously distributed throughout the BCT matrix phase. The XRD diffraction peaks of the two composites are in agreement with this theory, as the two composites share equivalent reflections with comparable diffusivities and asymmetries associated with the overlap of tetragonal (P4mm) BCT and pseudo-cubic (Pm-3m) 60NNBT, with only slightly shifted 2θ, and no evidence of unreacted NN retained after the short sintering dwell. The phase formation of this low temperature NNBT phase is perhaps the most thermodynamically stable configuration, suggested previously from the ability to retain a greater compositional heterogeneity when composites were constituted from BT and a relaxor NNBT pre sintering, figure 5.17.

The morphology of these secondary NNBT-related phases is likely to be the major difference between the two composite systems. The NNBT phases synthesised during sintering will be different in shape and size with respect to those phases formed from pre-calcined 60NNBT, characterised in results chapter 1 and 2. They are potentially smaller as a result of their synthesis from nano powders under short sintering dwell times that limits coarsening effects. Since the permittivity contribution of this relaxor NNBT secondary phase is a product of PNRs, smaller grains on the nanoscale could impede the dynamism and correlated polarisability of these local PNR clusters, reducing the NNBT phase permittivity contribution.

As Ca was found to diffuse into these NNBT phase edges by WDS mappings, figure 6.7, and since these NNBT type phases are possibly smaller and are synthesised during sintering via local interdiffusion between local NN and BT nano particles, where there is also BCT present, it is possible that a higher proportion of the NNBT secondary phase is Ca doped in this nano powder based composite. Should Ca replace Ba in 1:1 charge conserving isovalent substitution, the lower polarisability and off centring of Ca, which may couple to the displacive behaviour of Nb, could lower the NNBT permittivity response as described previously in results chapter 2.

The tan δ response is consistent for composites formed of pre calcined 60NNBT and the milling of nano powders for temperatures below T_m. This is expected as the composites are considered to feature the same components in comparable phase distributions. The high temperature tan δ are clearly different and larger in the composite that utilised a stoichiometric milling of the oxides, figure 7.6. Given the higher surface area of Na containing components within the stoichiometric mix of oxides, NN nano powders as opposed to micron-scaled 60NNBT, there could be greater Na non-stoichiometry imposed into the sintered composite via lattice Na volatilisation. The consequence could be oxygen vacancy formation within the composite, resulting in p-type conductivity upon reoxidation as the composite cools from its 1250 °C sintering temperature. This increase in tan δ could then be the product of an increase in p-type carrier concentration. No impedance has been conducted yet to confirm these higher losses are electronic in nature, nor has atmospheric impedance been conducted to confirm if such losses are p-type.

The overall effect of this lower NNBT related permittivity response in the composite formed from the mixed oxides rather than pre-calcined 60NNBT is a 'anticlockwise rotation' of the TCC response, figure 7.6. The BCT peak has a comparatively higher TCC maximum, ~ 12.4 % compared to ~3.6%, pushing closer to the +15 % R-rated TCC boundary. Since the depolarisation response in both composites appears consistent based on the comparable gradients of their associated permittivity decrease above T_m, it is this higher maximum TCC that pushes $T_{-15\%}$ to higher temperatures. The increase is from 152 to 159 °C when the 60NNBT is synthesised during sintering. The increase in TCC associated to the BCT peak in the composite appears as another mechanism to shift $T_{-15\%}$ to higher temperatures. Increasing the volume fraction of BCT retained post sintering could thereby induce a similar effect and push $T_{-15\%}$ to higher temperatures.

Figure C2 showed that X7R rated TCC for the BC3T-60NNBT composite achieved in results chapter 2 could also be reasonably reproduced when the 60NNBT was synthesised during sintering, as opposed to using pre-calcined 60NNBT. In this case, the permittivity of the stoichiometric mix of oxides yields a higher room temperature permittivity magnitude compared to the composite formed of pre-calcined 60NNBT, however the same anticlockwise TCC rotation induced by lower NNBT phase permittivity contributions is observed. No repeat samples were made for either BC3T or BC7T composite systems made from the stoichiometric mix of oxides, which is a priority of future work to assess how reproducible the observed permittivity magnitudes and associated TCCs are between batches. Again, the maximum TCC associated to the BCT peak increases from ~ 3.4 to 7.9 % from the pre-calcined 60NNBT to mixed oxide composite, with an accompanying shift in $T_{-15\%}$ from 143 to 145 °C. A consistent mechanism is shown in that an increasing TCC associated to the BCT permittivity peak yields a higher $T_{-15\%}$. Could the TCC of the BC3T related permittivity peak be increased to a similar extent shown in the BC7T composite, the $T_{-15\%}$ could be shifted to even higher temperature possibly attaining X8R rated TCC, with an inherently higher permittivity magnitude than that of the BC7T composite based on its lower starting Ca content.

Small 2 wt.% additions of glass are sufficient to induce a large increase in density, clear from the SEM micrographs of figure 7.9. The equivalent 3-0 BC3T-60NNBT composite macrostructure is formed with small nanoscale BC3T related grains and micron scale NNBT phases distributed. The glass appears to mediate densification without inducing mass transport and grain coarsening effects. The resulting retention of compositional heterogeneity is shown in Figure 7.11, which reveals that glass addition does not compromise the biphasic permittivity contribution discussed for all composite structures. Increasing glass content decreases the permittivity magnitude, increases high temperature losses and flattens the depolarisation responses above T_m (and at low temperatures). This pushes $T_{-15\%}$ to higher temperatures, thus BC3T-60NNBT is able to attain X8R rated TCC for estimated glass contents ≥ 6.5 wt.%, figure C3. Simultaneously, the XRD diffraction patterns for these glass containing composites, figure 7.8, reveal increasingly intense additional reflections, marked by an asterisk, associated to the formation of a $Ba_2TiSi_2O_8$ fresnoite phase. Si is far too small for A and even B site occupation of the perovskite lattice, preferring a low coordination typically more covalent in character, such as the tetrahedral sites it occupies within this fresnoite structure, and so it is unsurprising to see it crystallise into this ternary phase with increasing wt.%. Si doping of BT has been found to exhibit a limit ~ 5 mol% [285], above which the formation of this fresnoite phase occurs ~ 800 °C. This phase formation can clearly be seen from the EDX and BSE images, clustering locally and influencing the NNBT phase distributions, figure 7.10. Significant diffraction peaks appear from 4 wt. % additions onwards, consistent with the quantities of silicate glasses added that yield fresnoite formation within literature [280,282]

This additional $Ba_2TiSi_2O_8$ Fresnoite phase forming has an inherently lower relative permittivity than either of the two other materials, often calculated ~ 18 [286,287] at room temperature. The temperature dependence of permittivity for undoped and Ca-doped $Ba_2TiSi_2O_8$ are shown in

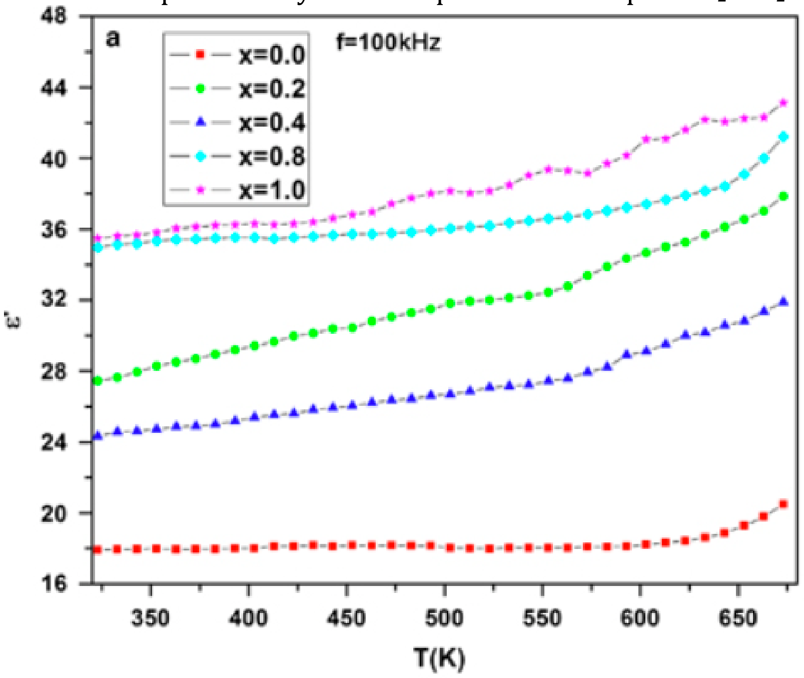

Figure 7.14: The variation of relative permittivity of $Ba_{2-x}Ca_xTiSi_2O_8$ with temperature, at 100 kHz. Reformatted from [286]

figure 7.14 [286]. Given the Ca content that exists within both the glass and the BCT matrix phase of the composite, it is not unreasonable to suggest some Ca will have doped into this ternary fresnoite phase formed. The relative permittivity remains relatively flat across the X8R temperature range, after which it begins to increase in permittivity. This low permittivity contribution from the fresnoite phase forming would lower that of the overall permittivity response of the composite, but based on its increase in permittivity towards higher temperatures, provide an additional polarisation response where the BCT and NNBT are increasingly thermally depolarised. This would explain the flattening of the depolarisation rate of the composite above T_m and the extension of $T_{-15\%}$ to higher temperatures observed in figure 7.13.

Voltage effects on permittivity stability, the so-called voltage coefficient of capacitance (VCC), have been shown to occur within composite core-shell structures when the conductivities of the component phases are sufficiently different [288]. Although the component phases within this composite have variable conductivities, figure 6.16, they are not orders of magnitude apart, nor is the electric field strength incurred by the 100 mV potential difference sufficient to encourage such VCC effects. Thus, the flattening of the TCC is not considered to be a function of local field variations throughout the composite, but more an effect of the fresnoite phase formation.

The breakdown strength of the composites increases with glass addition, quantified as 110-120 $kVcm^{-1}$ for all glass containing composites, where no PE hysteresis loop could be measured for the glass-free composite. The breakdown strength is independent of glass content, suggesting the dielectric breakdown is not induced by the $Ba_2TiSi_2O_8$ that progressively forms with increasing glass content. Breakdown strength would likely be improved for thinner samples where the statistical distribution of failure inducing flaws is lower, such as in tape cast layers of MLCCs. Data frequent within literature also utilise smaller electrode contacts to manipulate field induced breakdown values, preventing arcing between electrode interfaces. This also potentially indirectly probes smaller volumes of the ceramic and reduces the likelihood of breakdown on account of the inherent spreading resistance (depending upon the thickness of the sample and the resulting electrode radius to thickness ratio, s/r) [289,290]. Although we have quantified a breakdown strength, it is highly device and measurement sensitive, with direct comparison not so valid. Instead, this measurement mainly serves to prove the effect of reduced porosity on improving the field strength. Reasonably high energy density efficiencies are achieved, yet this was also quantified for a bipolar measurement as opposed to a unipolar measurement, which offers inherently higher efficiencies. Calculated recoverable energy densities are orders of magnitudes lower compared to publications aimed at high energy density capacitance [19], with the highest being 0.56 Jcm^{-3} in the 2 wt.% glass additions. This could be improved should the breakdown strength be extended. There is, however good recoverable energy density, ~81.5 % under a bipolar electric field application.

7.7 Conclusions

The dielectric response of the X8R achieving hand mixed BC7T composite of results chapter 2 is relatively reproducible when its BC7T and 60NNBT components are ball milled instead of being hand mixed. Subtle differences in the temperature dependence of the permittivity at very low temperatures and higher temperatures exist; however, overall the profiles of these permittivity responses are almost superimposable, with almost identical TCC responses of the composites. Dielectric losses share a similar temperature dependence in both composites despite different milling/mixing mechanisms. The dielectric response of the composite system is therefore relatively insensitive to the pre-sintering processing. This gives promise to the industrial scalability of these composite systems that require larger batch sizes. Similar dielectric responses are achieved when the BCT-60NNBT composite is formed from ball milling of BCT, NN and BT nano powders in the necessary stoichiometry, where 60NNBT is assumed to form during sintering. Variability in 60NNNBT morphology is assumed based on the starting particle sizes and sintering conditions, and is yet to be characterised, but is likely the influential factor inducing a lower 60NNBT related permittivity response in the sintered composite. This influences TCC, pushing it closer to the ± 15 % thresholds, but X8R and X7R specifications are reproduced for BC7T and BC3T based systems, respectively. Higher losses are incurred in composites where 60NNBT is synthesised during sintering, although good dielectric response is achieved for the X8R operating temperature range.

Addition of a low wt.% of glass to the pre-sintered mixture, 2 wt.% being the optimal concentration investigated, has a significant effect on improving the density of the composite systems observed post-sintering, from 79.7 ± 0.91 to 96.3 ± 1.01 %. Higher concentrations of glass become deleterious to the magnitude of the permittivity due to the formation of an inherently low permittivity $Ba_2TiSi_2O_8$ phase, clear from the EDX and XRD analyses of the composites. Although this phase formation and its polarisation contribution towards higher temperatures extends $T_{-15\%}$ to even higher temperatures, the significant loss of permittivity, an increase in dielectric loss and increasing porosity does not appear to be worth this sacrifice.

The dielectric breakdown strength for a ~0.5 mm bulk composite sample is observed for a bipolar electric field application to be ~110-120 kVcm^{-1}, independent of the wt.% of glass added. This compares to the inability to measure any P-E loop for the glass-free sample, with considerable enhancement in breakdown strength observed. Industrially, the BC7T-60NNBT with 2 wt.% glass addition appears to have improved upon the density and breakdown strength concerns without compromising the dielectric properties of the BC7T-composite that achieved X8R rated TCC from results chapter 2.

This is the final results chapter investigating ceramic composites for temperature stable dielectrics. The next, and final, results chapter will transition from utilising heterostructures to homogeneous single phase materials for temperature stable dielectrics. Instead of composites, the fourth results chapter will utilise crystallographic defects, specificially Perovskite A-site vacancies, as a mechanism for flattening the dielectric response of an otherwise temperature dependent dielectric – $NaNbO_3$. This represents a system with a comparably simpler compositional distribution that is inherently less sensitive to its processing conditions, and a potential alternative to composites for X7R or X8R TCC attainement.

7.8 Appendix

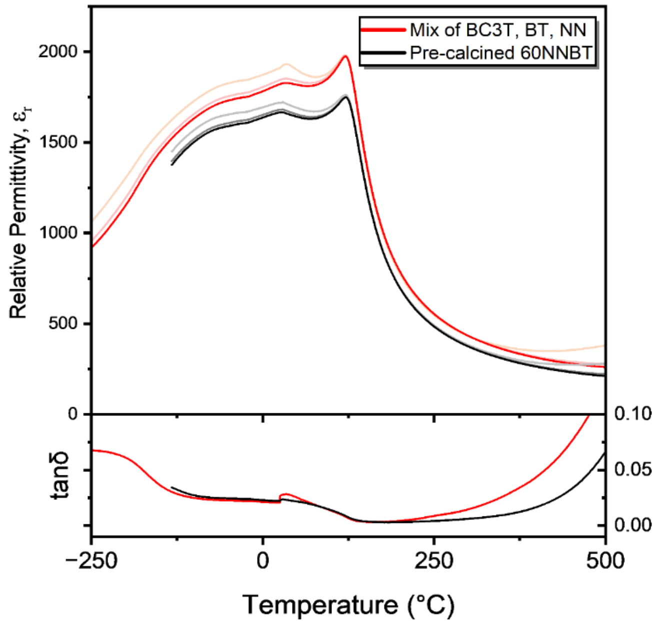

Figure C1: The dielectric response of the ball-milled BC3T-60NNBT composites formed using pre-calcined 60NNBT (black) vs stoichiometric mix of BC3T, NN and BT (red) where 60NNBT is assumed to form during sintering.

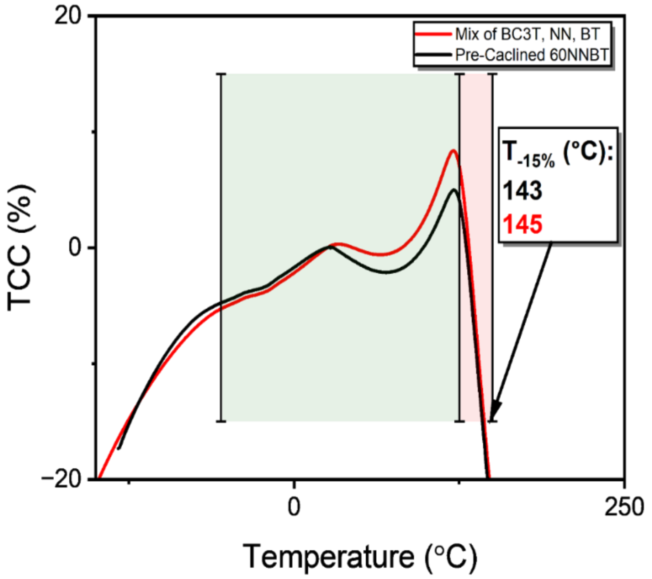

Figure C2: The TCC associated with ball-milled BC3T-60NNBT composites formed at 1250 °C for 0.5 hours, from pre calcined 60NNBT (black) vs a stoichiometric mix of BC3T, NN, BT (red). 60NNBT is assumed to form during sintering for the latter.

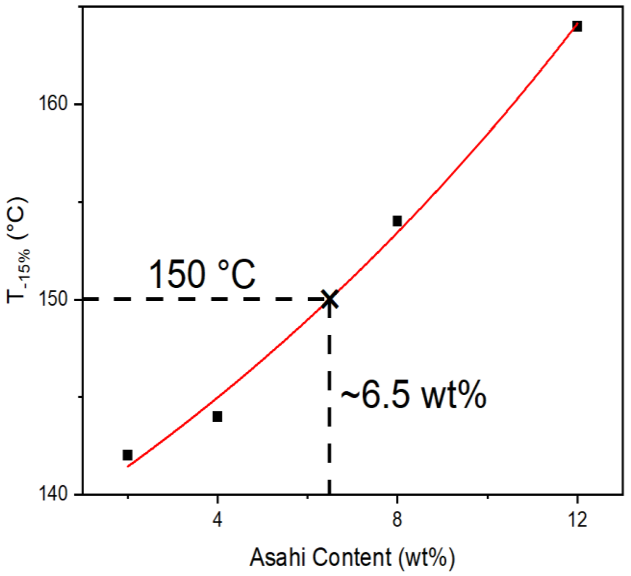

Figure C3: The distribution of $T_{-15\%}$ for the BC3T-60NNBT composite sintered at 1250 °C for 0.5 hours with varied wt.% additions of glass. An estimated 6.5 wt.% of glass is necessary to shift the BC3T composite into X8R rated TCC.

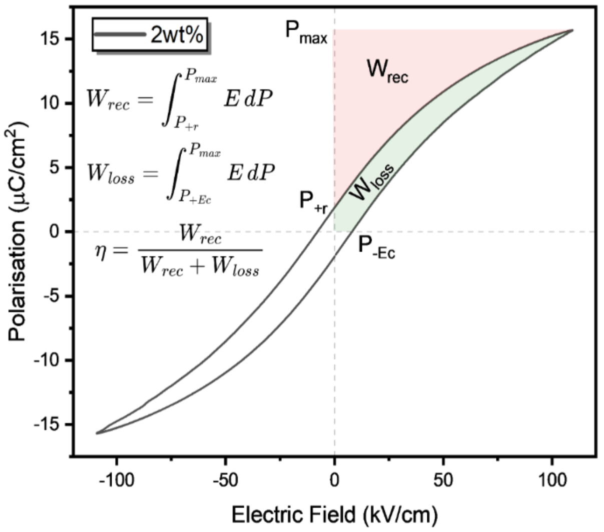

Figure C4: The P-E response for the BC3T-60NNBT composite with 2 wt.% glass, sintered at 1250 °C for 0.5 hours. The plot gives the integrals that are used to quantify the irrecoverable and recoverable energy density associated with the polarisation response of the composite. The efficiency is the ratio of the recoverable energy density to the total energy transferred upon polarisation.

8 Results Chapter 4: The role of A-site vacancies formed in the $La_{1/3}NbO_3$-$NaNbO_3$ perovskite solid solution as a mechanism for improving the temperature invariance of permittivity and energy storage efficiency in dielectrics

8.1 Introduction

Interest in $NaNbO_3$ has recently been renewed for integration as high energy density dielectrics, often a result of stabilising the antiferroelectric room temperature polymorph it exhibits which offers an inherently higher energy storage efficiency with respect to any ferroelectric analogues. More recent reports have summarised an ability for A site vacancies to destabilise the long range ordering of these formerly antiferroelectric materials, inducing order disorder transitions that produce diffuse dielectric responses with relatively high permittivity [194,201,205,291], and consequently, improved energy storage efficiencies with decent recoverable energy densities, >1 Jcm^{-3} [195]. Here, a report on the $NaNbO_3$-$La_{1/3}NbO_3$ binary is made regarding structural, dielectric and electrical properties based on the role of A site vacancies in the $NaNbO_3$ perovskite lattice, formed as charge compensating defects upon the aliovalent La^{3+} substitution for Na^+. The dielectric/electric properties of the materials produced are assessed for different applications, including temperature stable dielectrics and high energy storage efficiency dielectrics.

8.2 Overview

A site vacancies were introduced as charge compensating defects due to the aliovalent nature of trivalent La^{3+} substitution for monovalent Na^+, forming the solid solution $La_xNa_{1-3x}NbO_3$ (xLNN):

$$3Na_{Na}^{X} \rightarrow La_{Na}^{\cdot\cdot} + 2V_{Na}' \quad (8.1)$$

Compositions between the $NaNbO_3$ and $La_{1/3}NbO_3$ end member were made via a solid-state synthesis route according to that shown in section 4.1, with a sintering temperature of 1325 °C for 5 hours used to create dense polycrystalline samples. The compositions made were tabulated in table 4.1 alongside the reagents used. Each sample was characterised structurally using XRD and SEM, followed by DS, IS and PE analysis to characterise the dielectric performance of the solid solution.

8.3 Results

8.3.1 XRD

XRD analysis reveals a series of room temperature polymorphs are accommodated across the solid solution range investigated, with the transitional patterns shown with increasing La content in figure 8.1 a).

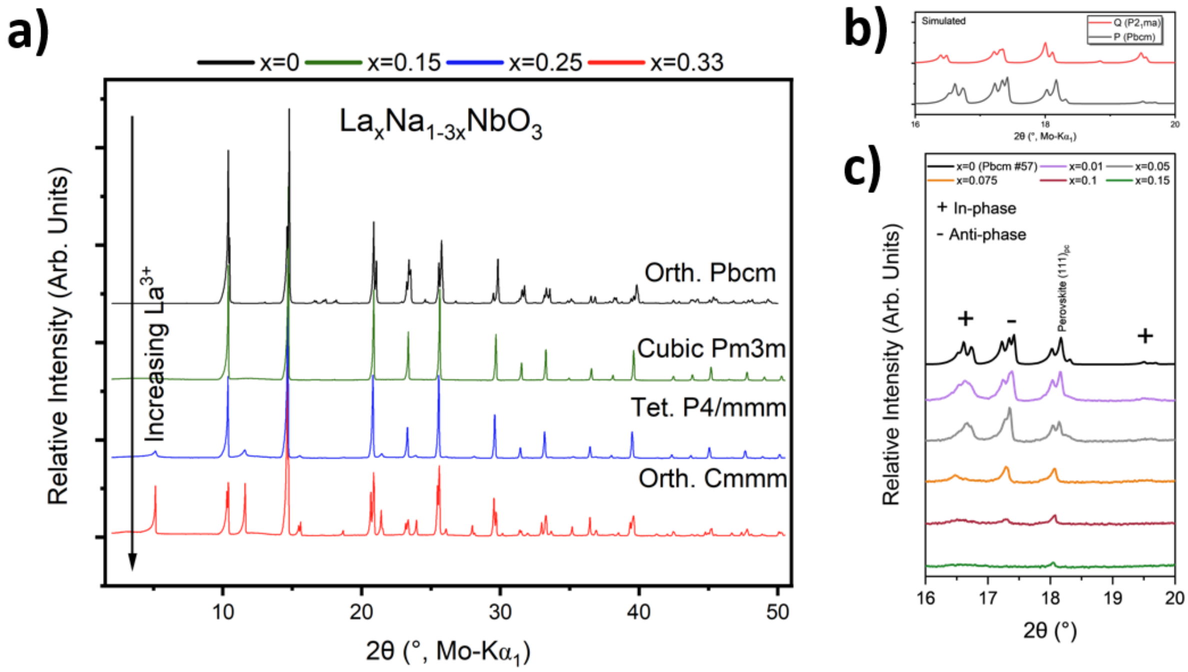

Figure 8.1: The compositionally driven phase transition sequence across the xLNN solid solution.

At low concentrations of La^{3+} (and V_{Na}'), the orthorhombic Pbcm (the antiferroelectric 'P' phase of $NaNbO_3$) phase is stabilised. There is no evidence of a high intensity peak ~ 19.5 ° associated to the (221),(122) planes, characteristic of a doubling of the pseudo-cubic ideal perovskite cell as present for the ferroelectric Q room temperature polymorph of $NaNbO_3$ (see figure 8.1 b) for simulated patterns of the P and Q polymorphs). Instead, a diffuse and low intensity peak associated to the (124)(241)(025) orthorhombic lattice planes, characteristic of the antiferroelectric P room temperature polymorph of $NaNbO_3$ is present. A clear suppression in the superlattice reflections between $16 < 2\theta (°) < 18.5$ is shown in figure 8.1 c). These peaks are associated with the extended periodicity created from in-phase and antiphase octahedral tilt sequences of the P polymorph of $NaNbO_3$ combined with the quadrupling of the pseudo-cubic cell length along [001] with the antiparallel Nb displacements.

Figure 8.1 c) reveals a suppression in these superlattice reflections with increasing La^{3+} content. As the composition transitions towards 15LNN (x = 0.15), all superlattice reflections and peak splitting is lost, and the structure increases in symmetry towards a 'pseudo-cubic' Pm3m symmetry. This high symmetry state is subsequently lost as the material transitions to a tetragonal P4/mmm structure at 25LNN (x = 0.25). At 27LNN (x =0.27), a final room temperature compositionally driven phase transformation occurs to an orthorhombic structure based on space group Cmmm, which is associated with the 2/3 A site deficient $La_{1/3}NbO_3$ end member. No additional reflections that are not characterised by the space groups of each phase are evident in the XRD diffraction patterns across the series. The refinements for each symmetry exhibited are shown in appendix D, figures D1-D4. Tables D1 show the refined lattice parameters and goodness of fit parameters for each composition of the LNN series, whilst tables D2-D11 give their refined structural parameters and associated bond lengths.

Each phase can be reduced to the 'ideal', ABO_3 perovskite pseudo-cubic aristotype cell (a_p) through geometric relationships shown in table 8.1. This is a direct result of their octahedral tilts and cationic displacements increasing the repeat length of the lattice.

Table 8.1: The geometrical relationships between the 'ideal' aristotype pseudo-cubic ABO_3 subcell and the unit cells of the room temperature phases across the $La_xNa_{1-3x}NbO_3$ solid solution.

Space group	Geometric relationship to ideal perovskite cell (with lattice parameter a_p)
Orthorhombic Pbcm	$a = \sqrt{2}a_p, b = \sqrt{2}a_p\ c = 4a_p$
Pseudocubic Pm3m	$a = a_p$
Tetragonal P4mm	$a, b = a_p, c = 2a_p$
Orthorhombic Cmmm	$a = 2a_p, b = 2a_p\ c = 2a_p$

The reduced pseudo-cubic subcell volume can be plotted against La^{3+} content as shown in figure 8.2. A near linear expansion of the subcell occurs with increasing La^{3+} content until ~ 20LNN (x = 0.20). Hereafter, the expansion rate reduces until it reaches the $La_{1/3}NbO_3$ end member.

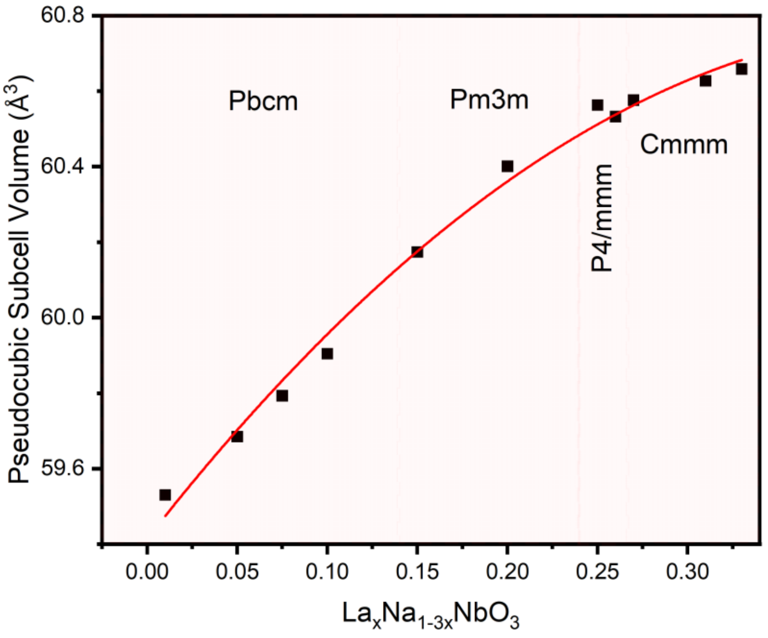

Figure 8.2: The expansion of the aristotype ABO_3 ideal pseudocubic perovskite sub cell which constitutes the unit cells and lattice symmetry of each xLNN room temperature polymorph.

8.3.2 SEM

The micrographs of select compositions across the solid solution are shown in figure 8.3.

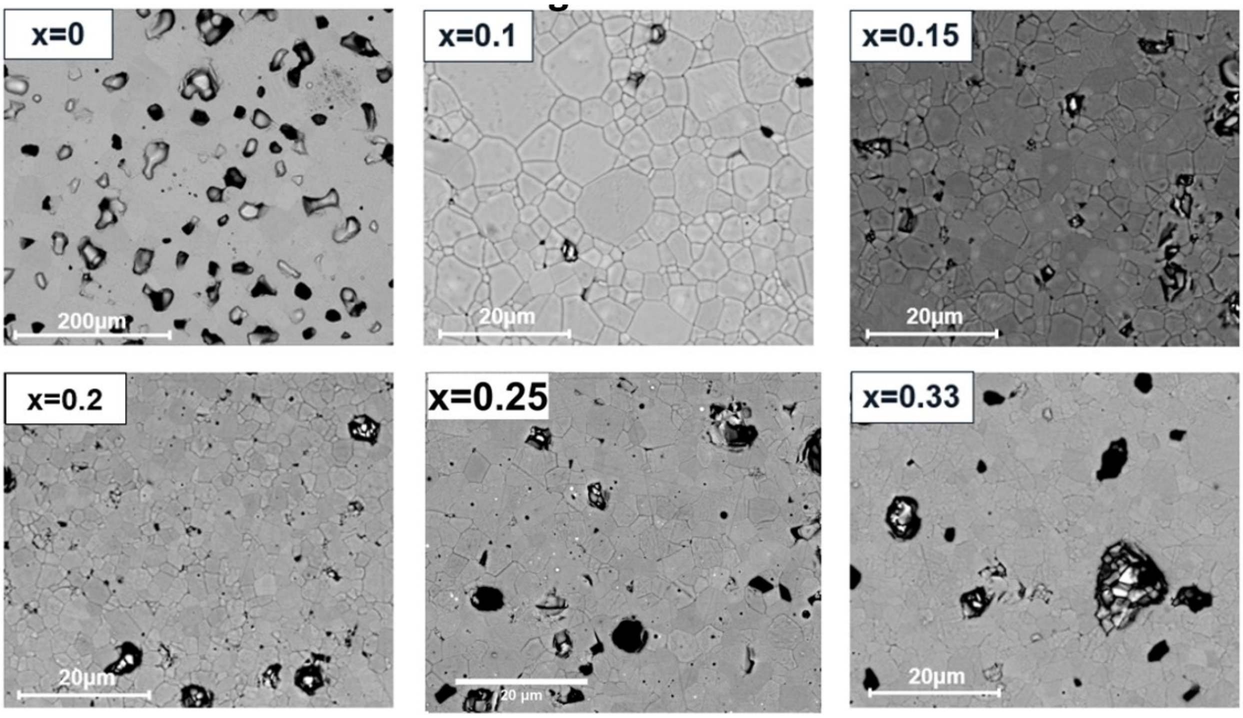

Figure 8.3: The microstructures of a select number of compositions across the xLNN solid solution series. No evidence of secondary phase formation is evident.

All micrographs reveal a grain structure typical of dense ceramics, with grains of truncated octahedra geometry. No areas of abnormal grain morphology appear. In the 15LNN and 33LNN samples, particularly for the latter, a bimodal grain size distribution appears to exist. No obvious contrasting grains appear that may be associated with any additional phase formation outside of the stoichiometry intended for $La_xNa_{1-3x}NbO_3$. White spots do appear on the 25LNN sample, although these appear to be deposited upon the surface, being an artifact of the sample preparation stage.

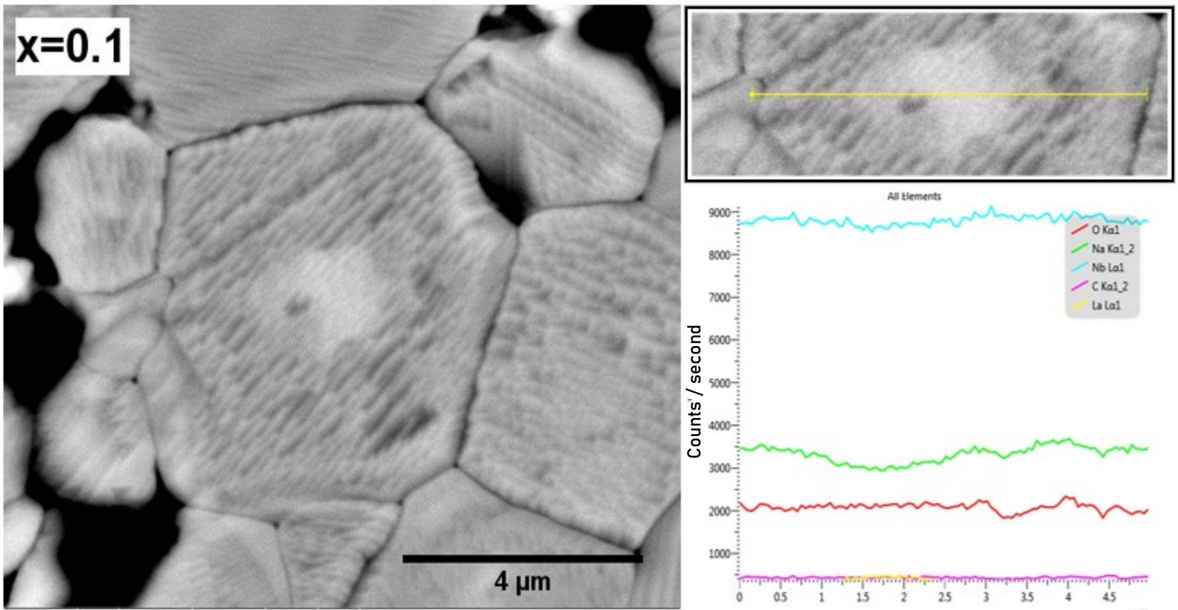

Figure 8.4: A elemental line scan across a 10LNN grain with a contrasting core region, appearing Na deficient towards the centre of the grain.

Intragranular contrast is evident in the BSE micrographs for a significant proportion of grains for compositions up to 20LNN, appearing like a core shell type gradient. A lighter core appears relative to the darker shell region, potentially indicative of a larger atomic mass towards the centre of the grain compared to the outer grain region. A corresponding line scan on the 10LNN sample via EDS analysis, shown in figure 8.4, suggests A site compositional variance, specifically Na deficient grain cores. These cores may be comparatively $La_{1/3}NbO_3$-rich with respect to the shell regions.

8.3.3 Dielectric Spectroscopy

The variation in relative permittivity and dielectric response for a select number of compositions across the solid solution is shown in figure 8.5. Upon low dopant concentrations of La^{3+}, the overall shape and magnitude of the relative permittivity response typical of $NaNbO_3$ is preserved. T_m, corresponding to the paraelectric-antiferroelectric phase transition, is simply lowered by ~ 150 °C between $0 \leq La^{3+}$ (mol%) ≤ 5, from 360 to 210 °C. In this same composition, dielectric losses are reduced with increasing La content to a minimum at 5 mol%, where tan δ < 0.05 across the entire temperature ranged measured, reaching a maximum of 0.017 at 500 °C.

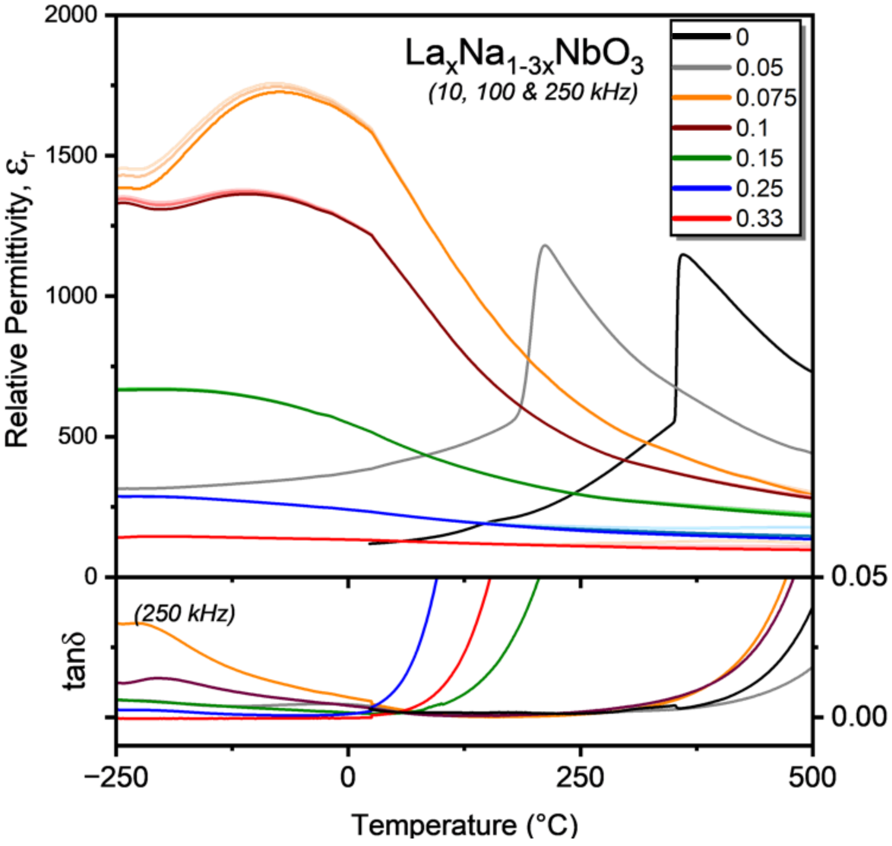

Figure 8.5: The relative permittivity and tan δ for a select number of compositions across the xLNN solid solution. An increasing diffusivity in permittivity response occurs between 5 and 7.5LNN. Dielectric losses increase considerably from 15LNN onwards.

For compositions ≥ 7.5LNN a significant transition in the relative permittivity response is observed. Between 5 and 7.5LNN, T_m drops by 282 °C, with 7.5LNN having T_m at – 72 °C. The corresponding maximum observed permittivity increases, from 1180 in 5LNN to 1730 in 7.5LNN, whilst the diffusivity of the permittivity response increases dramatically. This diffusivity results in a permittivity response around room temperature appearing relatively linear, in 10LNN for example. There is an increase in the frequency dependence of relative permittivity after this transition between 5LNN and 7.5LNN, with lower frequencies offering lower T_m's and higher maximum permittivity's compared to higher frequencies. For 7.5 ≤ La^{3+} (mol%) < 15, tan δ remains low, < 0.05, for a temperature range of -250 to 480 °C, but there is a greater increase in the higher temperature losses with respect to the compositions below 7.5LNN.

For compositions above 7.5LNN, the significant effect that further La^{3+} substitution has on the relative permittivity response is to lower the maximum permittivity observed. Although T_m continues to decrease until the $La_{1/3}NbO_3$ end member, the rate of decrease is much smaller than the initial drop observed between 5LNN and 7.5LNN. The dielectric loss shows a significant transition from dielectric-like behaviour with low losses < 15LNN, to the onset of high losses towards room temperature for compositions above this threshold, indicative of a transition between insulating and conducting materials.

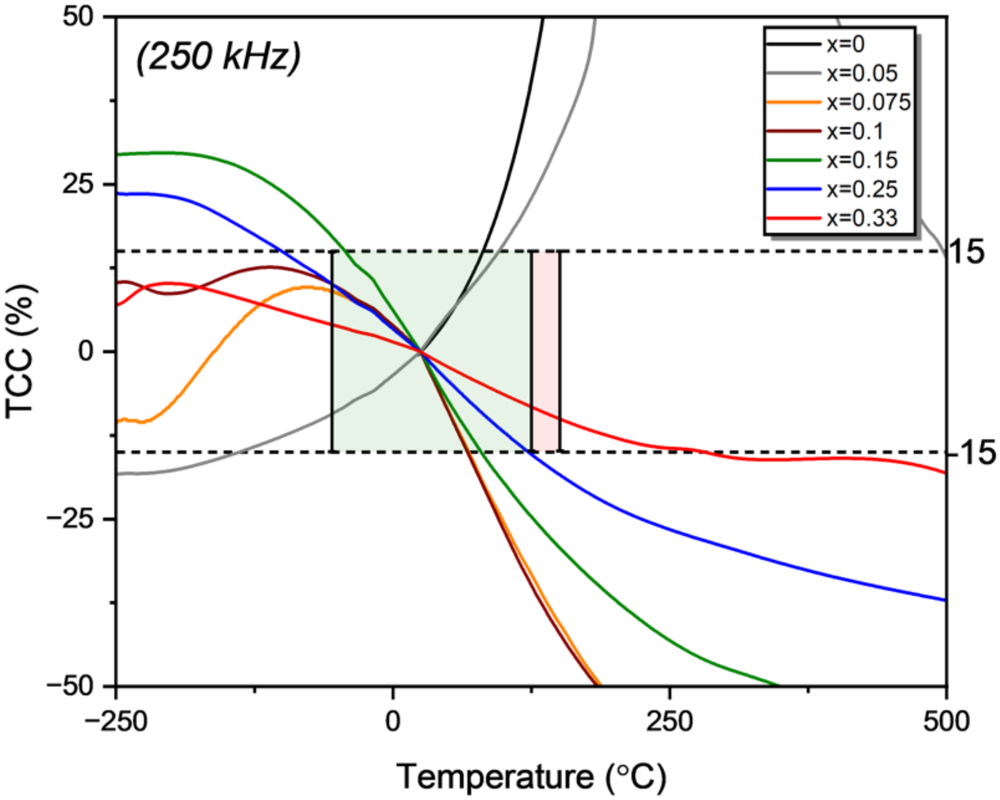

Figure 8.6: The TCC variation across the solid solution, with increasing TCC stabilisation as the solution transitions towards the A site deficient $La_{1/3}NbO_3$ end member.

The TCC variation of these compositions is shown in figure 8.6. A clear suppression in the temperature variance of TCC occurs with increasing La^{3+} content, particularly when the transition between the antiferroelectric 5LNN and diffuse 7.5LNN permittivity responses occurs. Of the compositions investigated, only those above 25LNN exist with a TCC profile that satisfies the X7R TCC window. Of the compositions shown in figure 8.5, only 33LNN meets X8R rated TCC specification, although it far exceeds the 150 °C upper temperature boundary. $T_{-15\%}$ is ~ 280 °C, whilst at the lower temperature regime the ± 15% TCC boundaries are not exceeded, figure 8.6. This composition does show good thermal stability, but only with a maximum permittivity of ~145 occurring at -205 °C observable on figure 8.5. At room temperature, this permittivity drops to 131.

8.3.4 P-E analysis of 10LNN

Since figure 8.5 revealed a near linear-type relative permittivity dependence of 10LNN around room temperature with low dielectric losses, the electric field dependence of polarisation for this composition was measured using a bipolar measurement. This PE dependence of 10LNN is shown in figure 8.7.

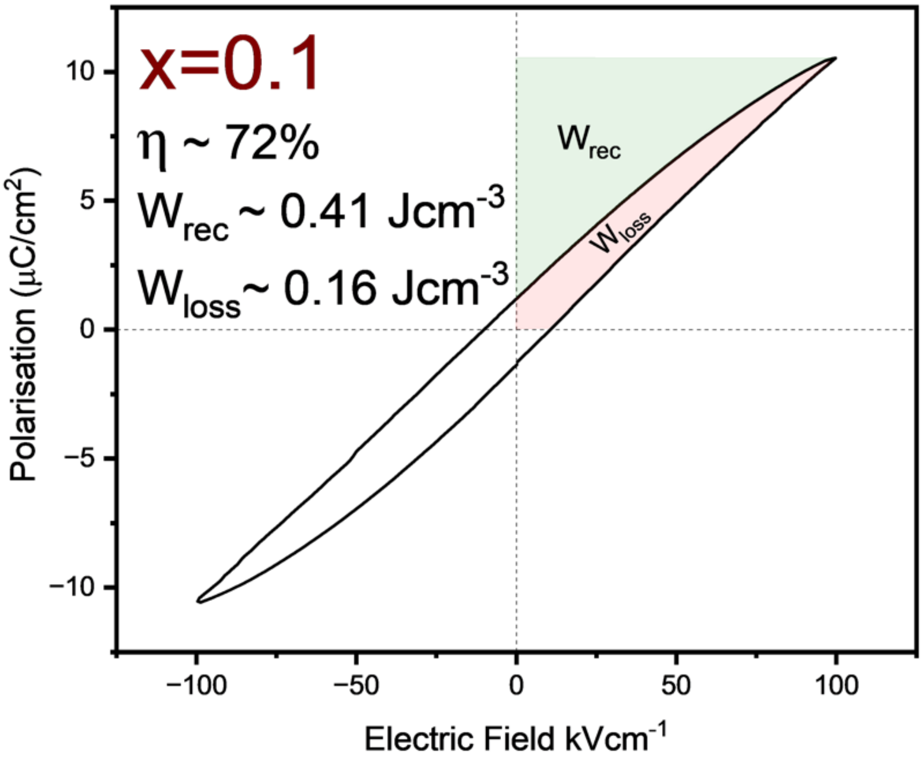

Figure 8.7: The bipolar polarisation-electric field hysteresis of 10LNN showing relatively linear field dependency. Recoverable energy density, irrecoverable energy density and energy storage efficiency are stated on the inset.

There appears no saturation, typical of a ferroelectric or antiferroelectric, and the maximum polarisation achieved is constrained only by the onset of field induced dielectric breakdown strength ~ 100 kVcm^{-1}. By integrating the areas of the curve according to the equations of figure C4 in appendix C (results chapter 3), the recoverable and irrecoverable energy densities, alongside the energy storage efficiency are given in table 8.2.

Table 8.2: The recoverable and irrecoverable energy densities within 10LNN exposed to a maximum bipolar electric field of 100 kVcm^{-1}, alongside the associated energy storage efficiency.

PE characteristics of 10LNN	
W_{rec} (Jcm^{-3})	0.411
W_{loss} (Jcm^{-3})	0.161
η (%)	72

8.3.5 Impedance Spectroscopy

The Z* plots and corresponding Z''/M'' spectroscopic plots for LNN compositions from three distinct regions of the solid solution are shown in figures 8.8-8.10. These include 5LNN (figure 8.8), 25LNN (figure 8.9) and 33LNN (figure 8.10), which correspond to a composition from:

i) 5LNN represents a composition that is consistent with a P-type (AFE) polymorph based on XRD with a corresponding AFE $NaNbO_3$-type dielectric response with low losses.

ii) 25LNN represents the composition after 15LNN where the transition to a high dielectric loss state is maximised. The onset of high dc losses is observable above room temperature.

iii) 33LNN contains no Na but still shows high dielectric loss behaviour associated with a dc conductivity contribution, similar to all compositions above 15LNN. It has been reported in the literature to exhibit La^{3+} ion conduction [169].

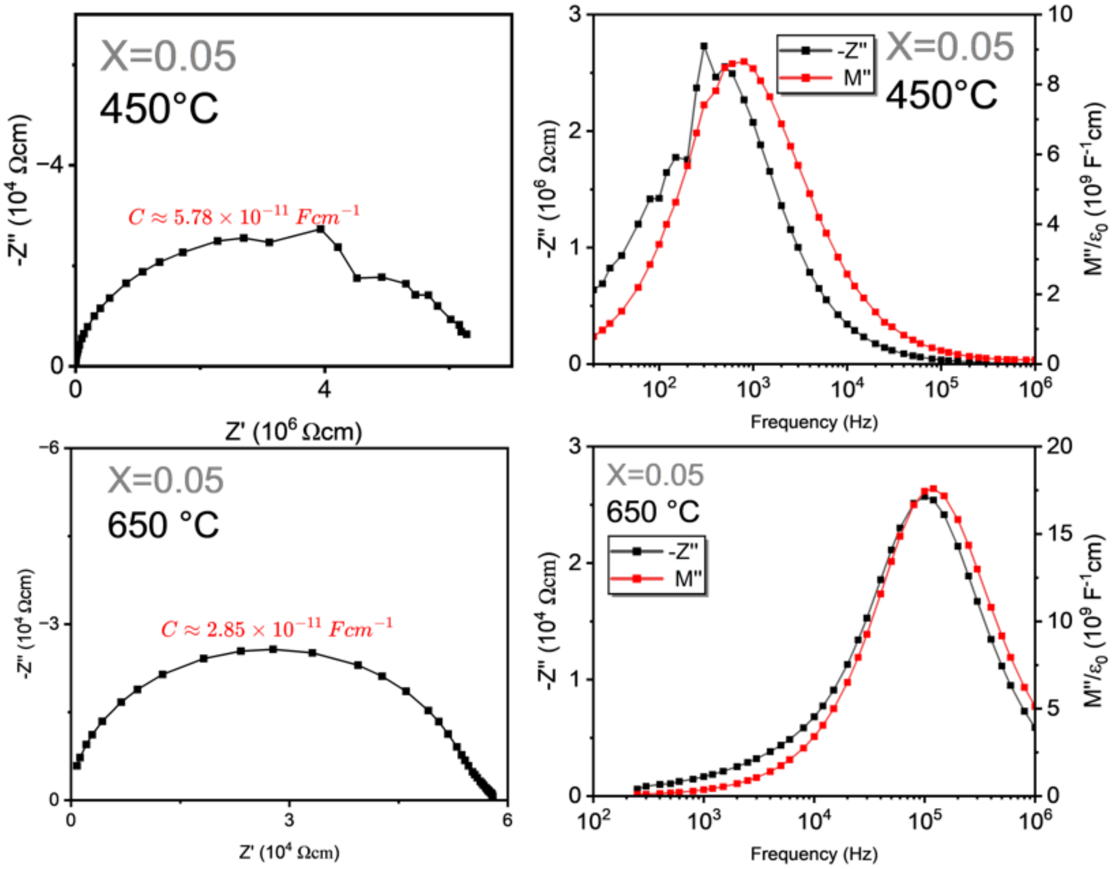

Figure 8.8: The Z* and Z''/M'' spectroscopic plots for 5LNN at 450 and 650 °C. Suggestion of a single parallel RC element representative of the bulk ceramic response. No evidence of ionic conduction.

For all three compositions, Z* and combined Z''/M'' plots are shown at comparatively lower and higher temperatures to observe any evolution in the electrical microstructure with temperature that was inferred by the tan δ responses of figure 8.5. In the low temperature (upper portion) of figures 8.8-8.10, Z''/M'' peaks appear Debye like and share a similar f_{max}, thereby corresponding to the same electroactive region of the sample undergoing relaxation, representable (to a first approximation) by a parallel RC element. Based on the C associated with this RC element, in the order of ~ 10^{-11} Fcm^{-1}, this electroactive parallel RC element in all three compositions is representative of the bulk response. There is no suggestion of a higher capacitance grain boundary or surface component being electrically distinguishable from this bulk response. There is a low frequency response associated with compositions 25 and 33LNN.

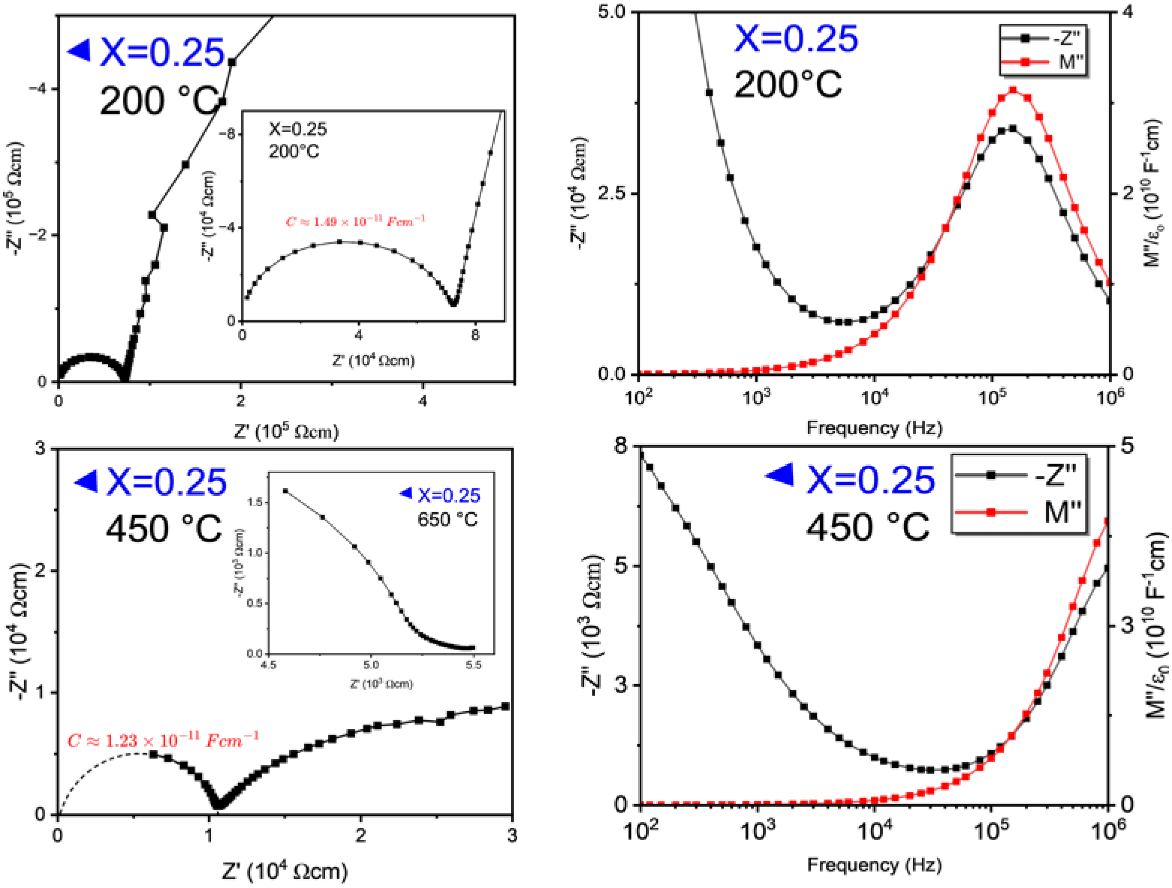

Figure 8.9: The Z* and Z''/M'' spectroscopic plots for 25LNN at 200 and 450 °C. Suggestion of a single parallel RC element representative of the bulk ceramic response, with a low frequency spike representative of ionic conduction that subsequently collapses towards higher temperatures.

Z* plots for all compositions is dominated by a single arc, indicative of a single (albeit not 'ideal') parallel RC element representative of the bulk response of the LNN grains. A low frequency Warburg spike is present in the low temperature responses of 25 and 33LNN, clear in figure 8.9 and figure 8.10, respectively, which is compatible with the low frequency Z'' spectroscopic response in suggesting semi-infinite diffusion of an ionic species is occurring throughout these LNN compositions at these corresponding temperatures.

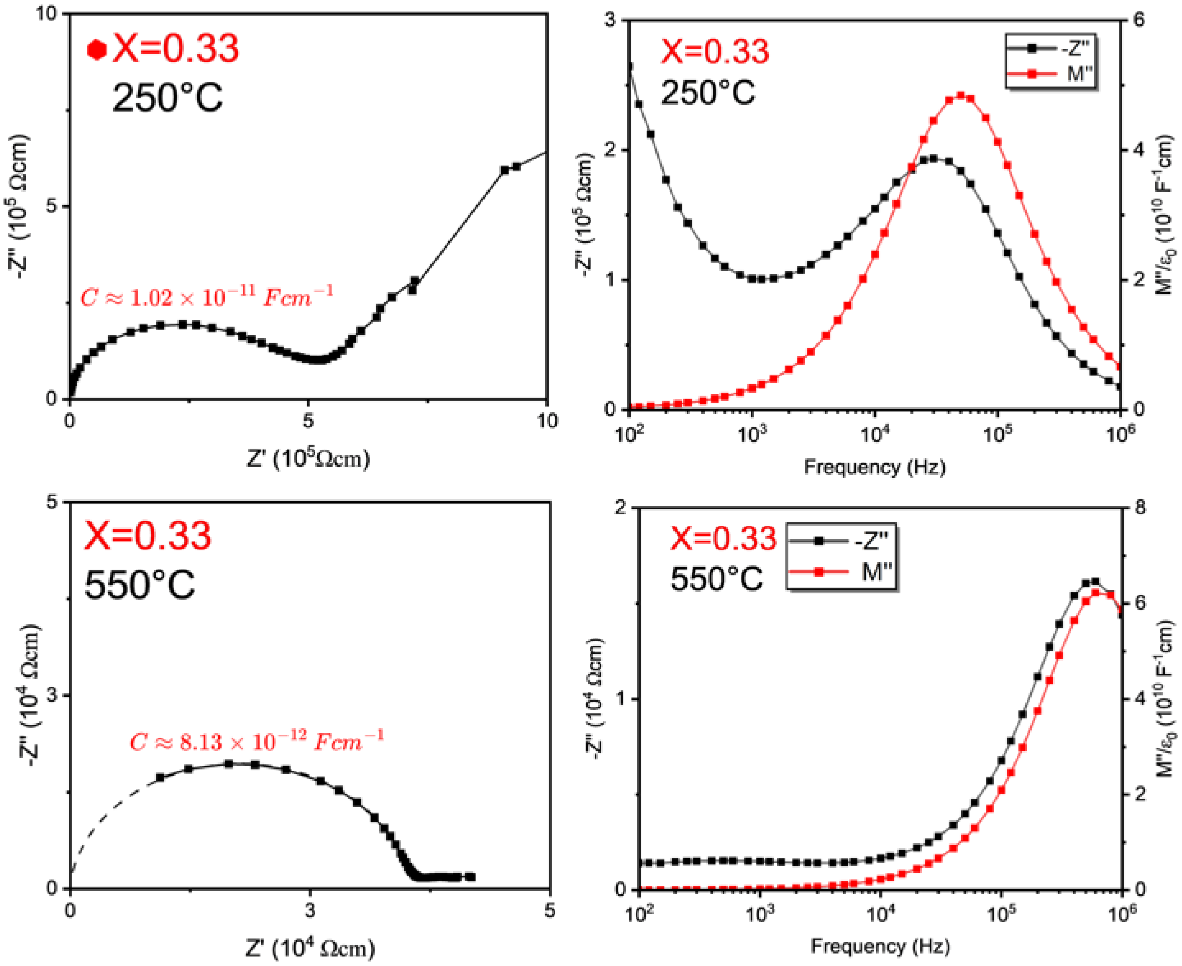

Figure 8.10: The Z* and Z''/M'' spectroscopic plots for 33LNN at 250 and 550 °C. Suggestion of a single parallel RC element representative of the bulk ceramic response, with a low frequency spike representative of ionic conduction that subsequently collapses towards higher temperatures.

For figure 8.8, the Z* plot at comparably higher temperatures still retains a single arc representative of the bulk dominant response. In figures 8.9 and 8.10, the low frequency Warburg spike in the Z* at low temperatures for 25 and 33LNN has collapsed, forming an additional semi-circle. This would suggest a mixed ionic-electronic contribution, where the electronic component is becoming increasingly more dominant than the ionic contribution towards these elevated temperatures. Figure 8.11 shows a plot of LNN compositions total dc conductivity, calculated from the inverse of the diameter of the bulk arc in the Z* plots against temperature. All compositions show a linear, Arrhenius type conductivity, although the activation energy associated (which is tabulated in table 8.3) changes between samples and for distinct temperature regions. For 0 ≤ La^{3+} (mol%) < 15, a single linear fit can be made to the conductivity values. These compositions fall into Region I on figure 8.11. The activation energy associated with this total dc conductivity, calculated from the gradient of the linear dependency, is between 1.10 ± 0.01 and 1.38 ± 0.03 eV. This linearity corresponds to compositions that do not show any evidence of a low frequency Warburg spike in Z* plots as shown for 5LNN in figure 8.8, and are therefore electronically conductive only.

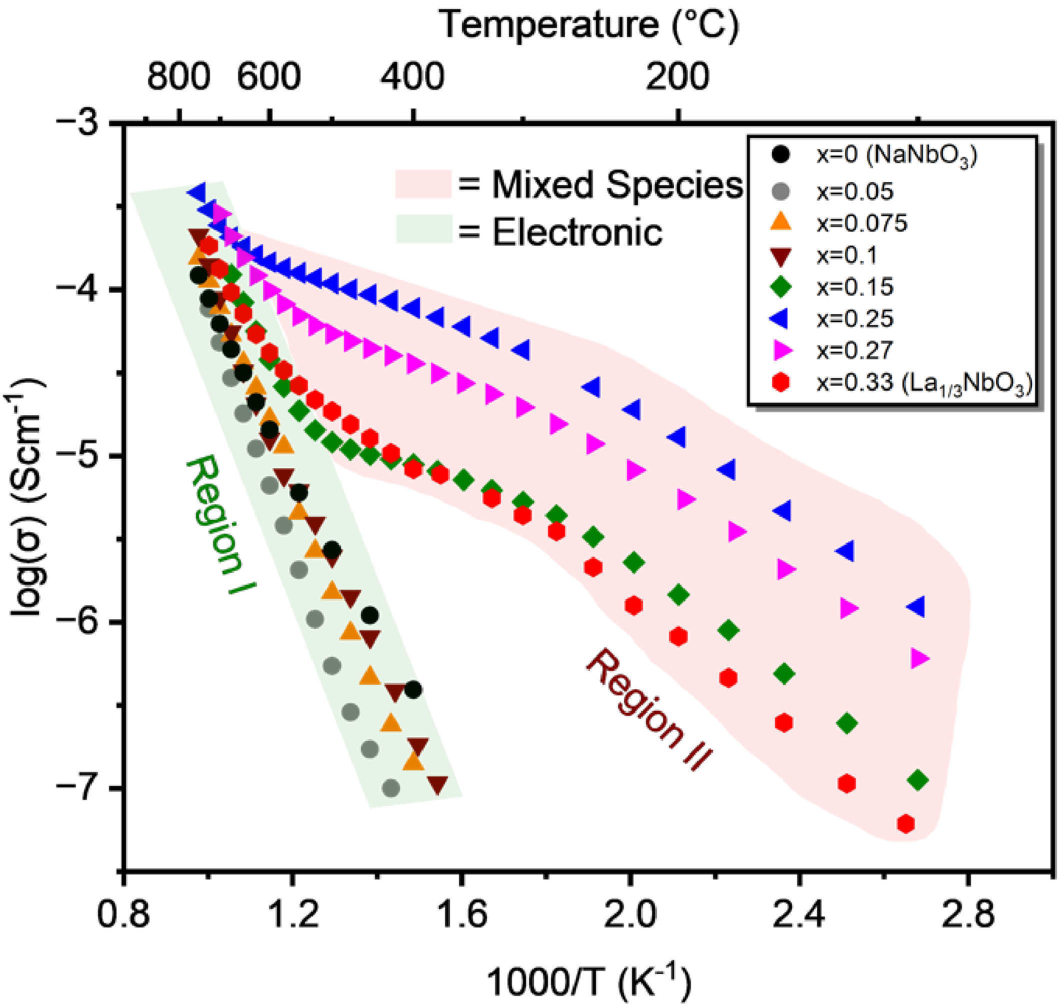

Figure 8.11: The temperature dependence of total dc conductivity for a select number of compositions across the xLNN solid solution. Compositions can be separated into two regions: Region I refers to compositions with electronic DC conductivity. Region II groups compositions with low temperature ionically dominant DC conduction and high temperature electronic dominant DC conduction.

For compositions ≥ 15LNN, the temperature dependence of conductivity can be associated to a second region (Region II in figure 8.11), where activation energy transitions from a low energy state, ~ 0.34 ± 0.07 eV in 25LNN, to a higher energy state at higher temperatures. This higher temperature state shows an activation energy closer to band I compositions, visually manifested in the bending of the conductivity profiles towards a gradient more consistent with region I materials. This transition in activation energies corresponds to a collapse in the Z* low frequency response. Thus, the lower temperature activation energy is associated to the ionically dominant contribution in LNN materials, and the higher temperature higher activation energy state reflects a transition to electronically dominant dc conductivity.

Table 8.3: The activation energies for the distinct conduction regimes present across the LNN solid solution, as calculated from the linear gradient fit to the temperature dependence of total dc conductivity in figure 8.11.

Activation Energy calculated from the gradient of the linear fit (eV)		
Composition (XLNN)	Low Temperature domain	High Temperature domain
$NaNbO_3$	(N/A, Region I composition)	1.10 ± 0.01
5LNN	(N/A, Region I composition)	1.38 ± 0.03
7.5LNN	(N/A, Region I composition)	1.23 ± 0.02
10LNN	(N/A, Region I composition)	1.34 ± 0.05
15LNN	0.38 ± 0.006	1.02 ± 0.03
25LNN	0.34 ± 0.007	0.77 ± 0.04
27LNN	0.33 ± 0.005	0.86 ± 0.05
33LNN	0.43 ± 0.006	0.95 ± 0.03

The high temperature activation energies for the mixed ionic-electronic conductors (≥ 15LNN) are shown in red in table 8.3, emphasising their value must be considered with caution. The high temperature gradients are inherently difficult to extrapolate from figure 8.11 since there is bending of the conduction profiles associated to the transition between dominant ionic and electronic conduction states at such temperatures.

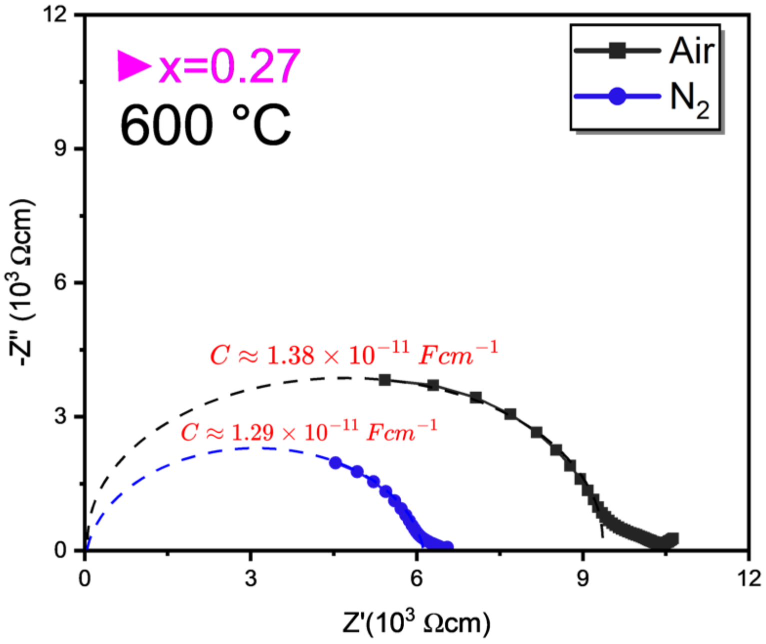

Figure 8.12: The Z* responses for 27LNN under air and N_2 atmospheres at 600 °C. A decrease in conductivity is observed under the latter based on the smaller diameter of the arc.

To isolate the type of electronic species being conducted, 27LNN was measured under air and an inert N_2 atmosphere, at 600 °C. This reflected a temperature high enough for the electronic contribution to total conductivity to be significant, whilst not too high that a bulk parallel RC contribution exceeded the 1 MHz upper frequency limit of the impedance analyser. Figure 8.12 shows the change in Z* between these two different atmospheres. An increase in conductivity under a N_2 atmosphere is apparent from the reduction in the diameter of the Z* plot compared to air. This suggests that the electronic component is n-type.

8.3.6 Galvanostatic Cycling of a symmetrically electrode Na|25LNN|Na cell

To determine the conducting ionic species in the LNN compositions, a coin cell featuring the most conductive 25LNN sample was constructed with symmetric Na electrodes. This cell was cycled (via a galvanostatic cycling (GSC) operation) with a progressively increasing target current at 60 °C. The current-voltage plot of the cell under cyclic voltage loading is shown in figure 8.13.

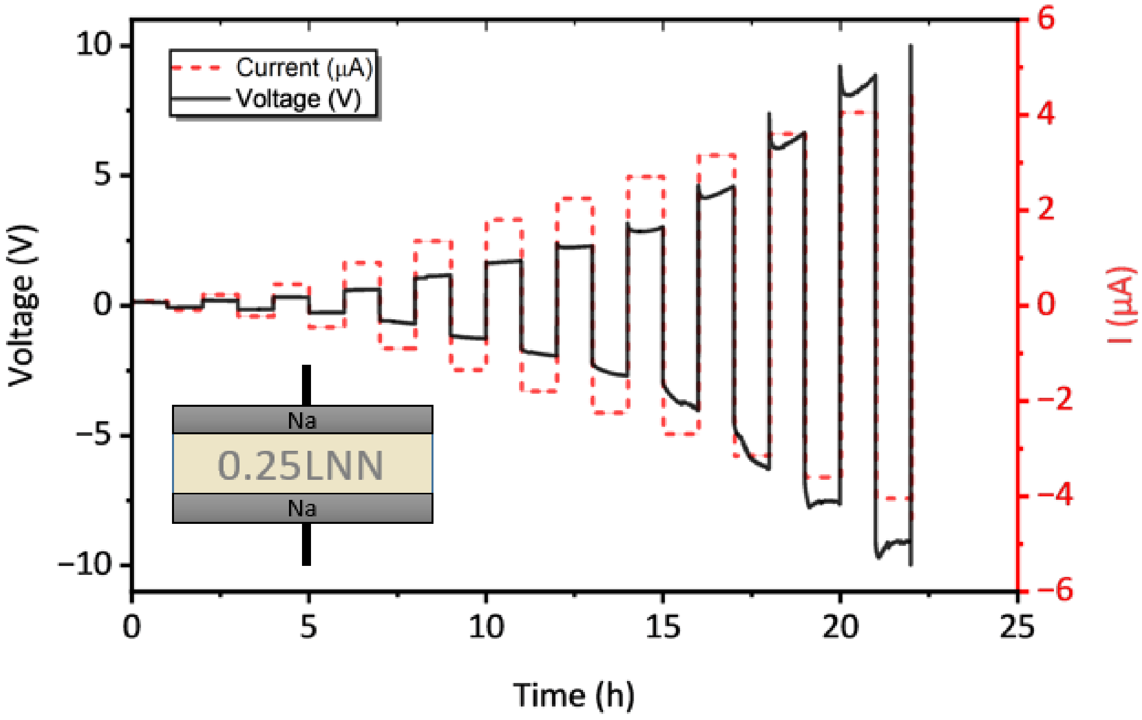

Figure 8.13: The galvanostatic cycling of the Na|25LNN|Na symmetric cell at 60 °C. The ability to run current through the sample indicates Na^+ conductivity at lower temperatures.

The fact that a voltage could be established across the cell when a small current was applied suggests the Na from the electrodes is capable of migrating through the ceramic, and that the ionic species that is observed to conduct through the sample at lower temperatures, producing the Warburg spike evident in the Z* plot of figure 8.9, are Na^+ ions.

8.4 Discussion

XRD diffraction patterns in figure 8.1 and SEM micrographs in figure 8.3 suggest the intended $La_xNa_{1-3x}NbO_3$ stoichiometry is formed, with no discernible secondary phase formation occurring. La^{3+} substitution into the A site sublattice is accommodated for by formation of V_{Na}'. The linear expansion of the pseudo-cubic sub-cell with increasing La^{3+} content is in agreement with this notion, in accordance with Vegard's law, although deviation from linearity is observed towards the $La_{1/3}NbO_3$ end member, beyond 20LNN. This can be attributed to the progressive ordering of La^{3+}/V_{Na}' into alternating (002) planes, doubling the c axis in the tetragonal P4/mmm and orthorhombic Cmmm symmetries with respect to the pseudo-cubic ideal ABO_3 perovskite unit cell. Superlattice reflections associated with this cell doubling along [001] are clear when comparing the 15LNN and 25LNN diffraction patterns in figure 8.1 a), with peaks of the (h k odd) type appearing, such as the (001) singlet at 5.2 °. The expansion of the pseudo-cubic sub-cell with increasing La^{3+} and thus V_{Na}' concentration is a direct result of increasing anionic repulsion effects with reduced average A site occupancy, rather than a size effect of competing A site cations since $La^{3+}_{(XII)}$ has a smaller radius (1.36 Å) than $Na^{+}_{(XII)}$ (1.39 Å). As the La^{3+}/V_{Na}' are able to order within the tetragonal and orthorhombic symmetries at higher concentrations, this anionic repulsion effect is increasingly screened, and cell expansion rates are reduced.

Peaks in the range $16 < 2\theta$ (°) < 20 for compositions below 15LNN, magnified in figure 8.1 c), are reflections associated with both the independent and combinatorial effect of the in-phase and antiphase tilting of the $[NbO_6]$ octahedra, as well as the antiparallel Nb displacements. These peaks can be indexed as being (h k odd) type, which correspond to quarter integer $\frac{1}{4}(001)_{pc}$ reflections, implying the quadrupling of the unit cell along the c axis compatible with the P-type room temperature polymorph of $NaNbO_3$. From comparison of the superlattice reflections with the simulated patterns of both the P and Q phases of figure 8.1 b), similarity between the LNN samples and the P polymorph is clear. The most obvious difference is observed at ~ 19.5 °, where the experimental peak intensity is relatively weak compared to that expected of the (014) peak associated with the antiphase tilting in the ferroelectric Q room temperature polymorph of $NaNbO_3$. Thus, La^{3+} doping stabilises the antiferroelectric P phase at room temperature. This is similar to $CaZrO_3$ substitution into $NaNbO_3$ which has been reported to stabilise the antiferroelectric P polymorph [210,292], but contrasts to Sr^{2+} doped $NaNbO_3$, where the Q phase stabilisation is achieved [201,204,291]. Since Ca and Sr both introduce one vacancy per mole dopant, a good comparison between cation size and polymorphic stabilisation in doped $NaNbO_3$

can be inferred. The P phase appears to be stabilised by a reduction in tolerance factor based on the A-site cation difference (ignoring vacancy radii), for which this La-based system is in agreement with.

Cation size, by virtue of this phase stabilisation preference, is also found to prefer the suppression of certain tilt systems, unsurprising since tilt systems act to reduce the volume of the A site interstice and improve cation coordination. For both this La-based system and the Ca-based system, increasing V_{Na}' begins to inhibit both the in-phase and anti-phase tilt sequences that create the antiferroelectric symmetry to the same extent. No preference for the suppression of a particular sense of tilt is apparent since all superlattice reflections in the range 16 < 2θ (°) < 20 reduce in intensity to the same degree with composition. This is unlike the Bi^{3+} doped system, which appears to predominantly favour the suppression of anti-phase tilting [194], or Sr^{2+} doped $NaNbO_3$ which exhibits a preference for in-phase octahedral tilt suppression [201].

It is important to distinguish that the pseudo-cubic symmetry observed between 15LNN and 25LNN reflects the average structure of the compositions near the midpoint of the solid solution. There is evidence of diffuse scattering between the (100) and (110) peak between 10 – 15 ° manifesting as a 'curvature' of the background intensity, corresponding to the same d-space region as the (101) ordering peak that appears in 25LNN. This could suggest a local ordering of La^{3+}/V_{Na}' (and local tetragonal symmetry) is present within the pseudo-cubic compositions, with insufficient periodicity to create a Bragg type reflection. After 25 LNN, a threshold V_{Na}' concentration of 50 mol% drives a macroscopic ordering of A site cations and V_{Na}' into alternating (001) planes, however diffusivity around these ordering peaks remains and indicates a clear competing long range vs short range structural ordering effect. Such local structure is better probed through characterisation techniques such as total scattering/pair distribution function analysis. Such local structural techniques had revealed the clustering of Bi^{3+} and V_{Na}' in the Bi analogue, which had driven the order-disorder transition described at ~ 10 mol% Bi^{3+} doping.

The core-shell type microstructure that is evident in figure 8.3 for compositions below 25LNN is relatively minor as EDS elemental line distributions shown in figure 8.4 for 10LNN reveal only a small decrease in [Na], whilst other elements including La appear relatively invariant. This could be a result of Na volatility, with core Na migrating towards the grain boundaries to compensate the loss of volatilisation of Na that may occur during sintering. However, given the inherent limitations of EDS at quantitatively defining the elemental distributions of light elements, and the low concentration drop suggested by the EDS line scans, the observed Na deficiencies may only truly be confirmed by a more resolute, WDS quantification in the future.

The dielectric responses show interesting and variable behaviour across the solid solution. Small La^{3+}/V_{Na}' concentrations stabilise the typical $NaNbO_3$ profile, with limited influence on the antiparallel Nb displacements that yield the polarisation response but rather a reduction in the length scale of domain formation that occurs. This contrasts to Bi doped $NaNbO_3$ where the same number of vacancies are generated per mole of A-site dopant, yet for 5 mol% T_m drops below 100 °C and shows large tan δ [195]. In that system there is an additional influence from the stereochemically active $6s^2$ lone pair which will add additional disruption to the polar ordering, whilst Bi (as well as Na) is volatile at the sintering temperature utilised, and additional non-stoichiometries could be introduced imparting the higher dielectric losses observed. The sudden drop in T_m and diffusivity enhancement of the dielectric permittivity response between 5LNN and 7.5LNN characterises an order-disorder transition associated to the cooperative/correlated Nb cation displacements. This type of transition has been observed in a wide variety of A-site deficient $NaNbO_3$ systems, in Bi-, Sr- and Ca-$NaNbO_3$ [194,195,201,205], occurring universally at $[V_{Na}'] \sim$ 15-20 mol%. Levin et al [194] directly observed clustering of the vacancies associated with this transition, inducing a short scale ordering effect common in relaxor materials and inducing the diffuse frequency dependent permittivity response observed here. It is expected that a similar effect occurs universally for these A-site deficient $NaNbO_3$ materials. The progressive decrease in permittivity magnitude beyond 7.5LNN reflects a reduction in size and frequency of these polar clusters (PNRs) that are embedded within a macroscopically non-polar matrix. A permittivity ~ 180 for the $La_{1/3}NbO_3$ end member is higher than that expected of the atomic polarisability of its component ions. This is likely a result of Nb displacements that occur away from the A site vacant planes of $La_{1/3}NbO_3$, enhancing the local dipole moments that form [167].

The enhanced diffusivity associated with this order-disorder transition between 5LNN and 7.5LNN reduces the TCC, clear from figure 8.6. This, however, is only sufficient for X7R or X8R class II MLCCs near 25LNN, at which point the permittivity is maximised at the -55 °C minimum operating bound and is below 300 for all compositions. Not only is this permittivity magnitude unreasonably small for class II dielectrics but high dielectric losses associated with ionic conduction render these materials redundant for dielectric applications. Only those between 7.5LNN and 15LNN would find use in temperature stable dielectrics, and would need to be utilised within an appropriate dielectric architecture, such as a multilayer lamination or composite structure, to satisfy any useful TCC criteria.

10LNN does show a linear-type permittivity variation, producing a linear type PE response whose maximum polarisation is limited by its breakdown strength rather than saturation effects. The magnitude of recoverable energy density is not competitive with respect to other A-site deficient $NaNbO_3$ compositions [195], although many of these materials have energy density quantification towards much higher electric field applications ~ 200 kVcm^{-1}. However, the role of A site vacancies in linearising the field dependency of polarisation is clear. This is achieved without the need for a multitude of dopants, as is often the case [293,294]. There is also a clear window for improving field strength, through reduction in sample thickness and the statistical reduction in breakdown nucleating flaws, by improving the density of the sample, or manipulating grain size. The use of a more polarisable dopant species in the solid solution, such as Bi^{3+} which whose stereochemical lone pair enhances off centring of the cation and improves dipole moment magnitudes, could work well for such an application, and is likely a reason such a system offered a recoverable energy density over twice greater than that reported here [195]. The composition for the LNN series with respect to energy density application was not optimised and compositions closer to the 7.5LNN order-disorder transition with less vacancies may offer greater polarisability and higher recoverable energy density.

At compositions ≥ 15LNN, Na^+ ionic conduction becomes clear from the presence of a low frequency Warburg diffusion element in the Z* plots, combined with the GSC data for the symmetric Na|25LNN|Na cell constructed. This is a sensible result since a monovalent ion can migrate though channels that begin to percolate through the structure with increasing vacancy concentration, shown for perovskite compositions in the $LiNbO_3$-$La_{1/3}NbO_3$ binary system [177]. This ionic conductivity is of course not desirable from a dielectric perspective, but optimises at 25LNN with a value of 8.0 x 10^{-5} Scm^{-1} at 400 °C. This may be a consequence of a morphotropic type phase boundary where local coexistence of disordered and ordered vacancy states exist between a tetragonal and pseudo-cubic state, providing an optimal level of migration pathways. This may be combined with a favourable balance of columbic attractions between positively charged La^{3+}/ (mobile) Na^+ cations and the relatively negatively charged V_{Na}', as well as an optimal number of Na^+ species available for migration.

A review of this same composition [190] found a total conductivity ~ 1.06 x 10^{-5} Scm^{-1} at 30 °C with a comparable activation energy ~ 0.32 eV, suggesting similar Na^+ dominant ionic conductivity. Extrapolating this to 400 °C would give a conductivity two orders of magnitude greater than the one reported in this thesis, ~ 8.8 x 10^{-3} Scm^{-1}. There was, however, variability in processing between this report by Kong et al [190] and that presented here. 15 wt.% additional Na_2C0_3 was added by Kong et al [190] to limit Na volatilisation effects during sintering at a comparatively lower temperatures of 1250 °C. The SEM micrographs are limited and do not show a large distribution of grains, nor are EDX results presented. Electrical heterogeneity is clear within the Z* plots, with a grain bulk, grain boundary and an additional uncharacterised arc present, unlike the Z* plots shown in figure 8.9. XRD diffraction patterns presented by Kong et al [190] also show broad and asymmetric peaks not consistent with tetragonal symmetry, and so this discrepancy in total conductivity is likely a product of a unique multiphasic distribution of phases in the reported literature work.

Should the ionic conductivity be strongly linked to the coexistence of disordered and ordered states of V_{Na}' at the pseudo-cubic/tetragonal phase boundary, variation in the B site cation could have a significant influence on the maximum achievable Na^+ ionic conductivity. Since the room temperature polymorph of $La_{1/3}TaO_3$ is tetragonal P4/mmm as opposed to Orthorhombic Cmmm, the onset of an disorder-order condition between tetragonal and pseudo-cubic cells (~25LNN in the Nb based system) will possibly occur at a different Na content. Since Nb and Ta are of similar size, bottleneck sizes considered to be the main potential barrier for migration are expected to be similar and thus a different Na concentration could yield improved diffusion coefficients.

For the $La_{1/3}NbO_3$ end member, the low frequency response in the Z* plots reveal a low temperature ionic contribution to the conductivity. Its activation energy is similar, but different to Na containing compositions, whilst the temperature dependence of the conductivity appears more convoluted, with multiple gradients and transition states yielding an often-curved temperature dependence. Of course, the species being conducted at low temperatures in $La_{1/3}NbO_3$ can no longer be Na^+. This leaves three possibilities to consider:

i) Proton (H^+) conduction (due to adsorbed water near RT)
ii) O^{2-} conduction
iii) La^{3+} conduction

The species being conducted has not been identified to date, although ongoing efforts are in progress. There is a lack of any observable increase in resistivity above RT as a sample is heated as any (potential) H^+ ions are evaporated as water. For O^{2-} ions, it is not likely that La^{3+} would have acceptor doped into the B site on account of its large size, nor is there any volatile Na to induce non-stoichiometry. The formation of $V_O^{\cdot\cdot}$ is difficult to rationalise on this basis, and no La containing secondary phases are present within the microstructure from XRD or SEM analyses. O^{18} time of flight secondary ion mass spectrometry measurements are being conducted (Prof Roger de Souza, Aachen University) to determine if oxygen ions are mobile or not. La^{3+} has been proposed to migrate through $La_{1/3}NbO_3$ in early work [169] however had been discredited on the basis of a lack of in-depth phase analysis on a post electrolysis sample, from which oxide ion conductivity was inferred. Furthermore, no effort was made to discredit protonic conductivity.

8.5 Conclusions

A complete solid solution is formed between $NaNbO_3$ and $La_{1/3}NbO_3$, with A site vacancies formed as charge compensating defects. No additional phases were evident in XRD or SEM analyses. The increasing structural strain imposed by A site vacancies and smaller La^{3+} cation doping for Na^+ is relaxed through a series of room temperature phase transitions, driven by $[NbO_6]$ tilt variation, Nb displacements and disordering of the A site species. These structural variations are reflected in the range of dielectric behaviours exhibited across the solid solution series. At low concentrations of La^{3+}/V_{Na}' below 7.5LNN, antiferroelectric dielectrics are obtained, and the A site vacancies introduced simply act as T_m shifters. Dielectric losses remain low across a wide temperature range, up to 480 °C, but TCC remains highly temperature sensitive.

For materials between 7.5 and 15LNN, an order-disorder transition occurs and relaxor-antiferroelectric dielectrics are observed. TCC is improved and dielectric behaviour is retained, although the TCC achieved is insufficient for X7R or X8R classification. Linear type polarisation-electric field dependence is achieved through this reduction in polar correlation lengths, with decent energy storage efficiencies achieved but limited recoverable energy densities. For the $15 < La^{3+}$ (mol%) < 33 range, the materials can be characterised as mixed n-type electronic/Na^+ conducting materials. These compositions are Na^+ dominant at low and intermediate temperatures, and electronically dominant at high temperatures. Na^+ ionic conductivity is optimised for 25LNN. Ionic conductivity is achieved for the $La_{1/3}NbO_3$ end member, for which the mobile species is currently being investigated.

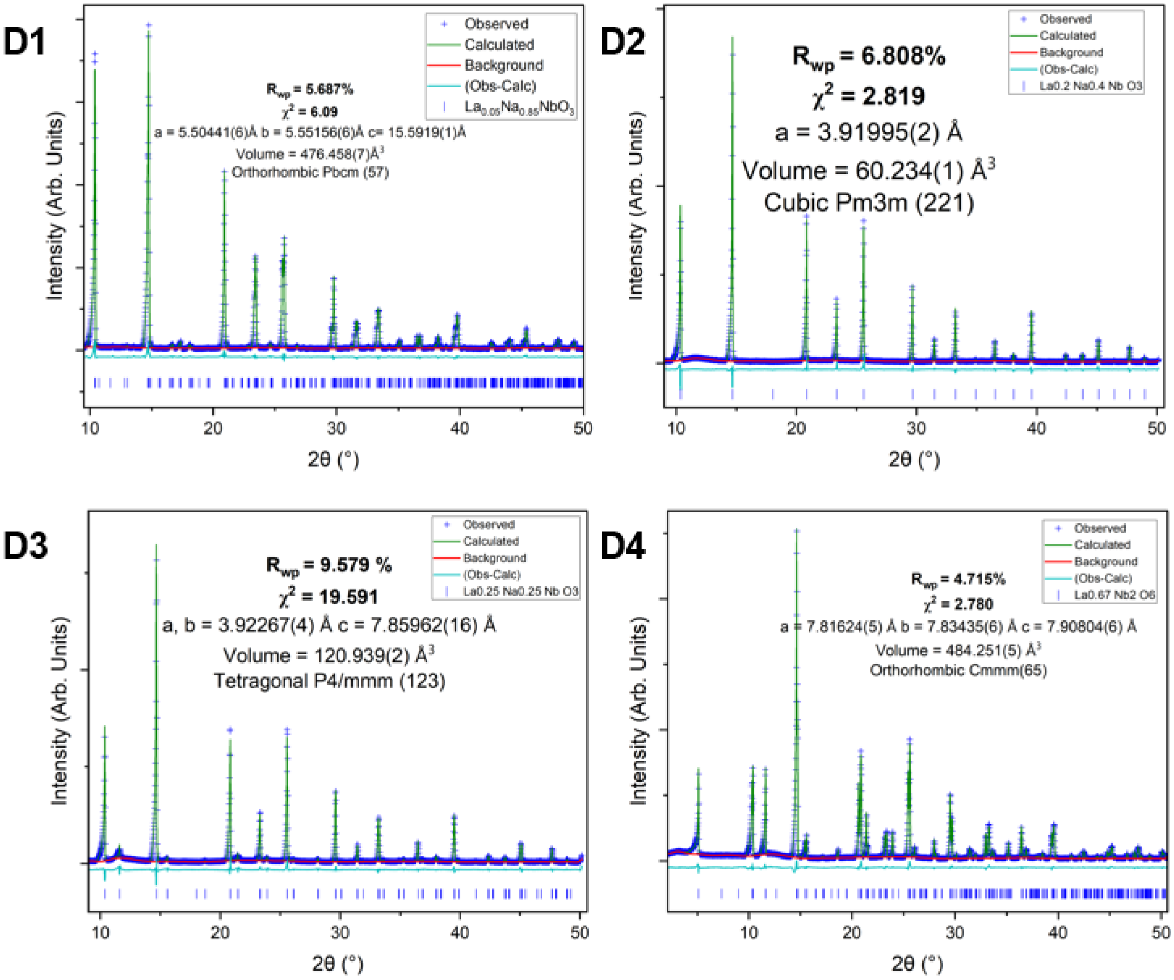

Figure D1-D4: The Rietveld Refinements for x=0.05, 0.2, 0.25 & 0.33, Showing the 4 symmetries observed across the $La_xNa_{1-3x}NbO_3$ solid solution

Table D1: The refined lattice parameters and volumes, with associated goodness of fit parameters, for each of the refined $La_xNa_{1-3x}NbO_3$ components.

			$La_xNa_{1-3x}NbO_3$			
x	a	b	c	volume	Rwp	χ2
0	5.50074(7)	5.56398(7)	15.5157(1)	474.875(6)	6.431	7.91
0.05	5.50441(6)	5.55156(6)	15.59188(15)	476.458(7)	5.687	6.09
0.075	5.5293(1)	5.5388(1)	15.6214(2)	478.425(6)	5.666	4.732
0.1	5.5323(8)	5.5318(8)	15.6388(9)	478.614(4)	5.479	3.814
0.15	3.91583(1)			60.045(1)	5.629	4.824
0.2	3.9199(2)			60.234(1)	6.805	2.816
0.25	3.92267(4)		7.85962(16)	120.939(2)	9.579	19.591
0.27	7.82741(11)	7.83491(13)	7.88474(5)	483.548(5)	4.940	4.338
0.31	7.81532(4)	7.83636(6)	7.90122(5)	483.914(6)	5.143	4.607
0.33	7.81624(5)	7.83435(7)	7.90804(6)	484.251(5)	4.715	2.780

0LNN

Site	x	y	z	Fraction	Uiso
Na(1)	0.2278(14)	0.25	0	0.985(5)	0.0115(19)
Na(2)	0.2303(16)	0.2200(9)	0.250	0.998(6)	0.0173(24)
Nb	0.2530(3)	0.7318(2)	0.1245(2)	1	0.0077(1)
O(1)	0.680(2)	0.250	0	1	0.0076(33)
O(2)	0.2023(26)	0.7623(17)	0.25	1	0.0193(37)
O(3)	0.4737(12)	0.4600(16)	0.1407(9)	1	0.0262(26)
O(4)	0.0325(11)	0.0328(12)	0.1096(9)	1	0.0189(24)

Microstrain	Equatorial: 1287(38), axial: 501(20)
Crystallite Size (μm)	1.88(12)
Nb-O(1,2,3,4)	1.9695(8),1.9741(2),1.9829(2),2.0804(4)
Na(1)-O($1_{a,b}$, 3,4)	2.8278(6)$_a$/2.4869(9)$_b$, 2.8309(3), 2.3471(9)
Na(2)-O($2_{a,b}$, $3_{a,b}$ 4)	3.0211(3)$_a$/2.5514(5)$_b$, 2.7611(9)$_a$/2.5395(6)$_b$, 2.6481(6)

5LNN

Site	x	y	z	Fraction	Uiso
La(1)	0.234(75)	0.25	0	0.054(2)	0.040(45)
Na(1)	0.237(19)	0.25	0	0.831(4)	0.004(13)
La(2)	0.250(25)	0.176(17)	0.250	0.031(2)	0.018(24)
Na(2)	0.233(3)	0.232(2)	0.250	0.861(5)	0.005(7)
Nb	0.2509(4)	0.7365(2)	0.1249(4)	1	0.00996(9)
O(1)	0.698(4)	0.250	0	1	0.0179(7)
O(2)	0.2083(41)	0.758(2)	0.25	1	0.0179(7)
O(3)	0.476(1)	0.473(2)	0.140(1)	1	0.0179(7)
O(4)	0.0289(14)	0.032(1)	0.112(1)	1	0.0179(7)

Microstrain	713 (35)
Crystallite Size (μm)	2.47(44)
Nb-O(1,2,$3_{a,b}$,4)	1.9690(9),1.9679(2),2.0100(7)$_a$/1.9310(4)$_b$,2.0574(6)
Na(1)-O($1_{a,b}$, $3_{a,b}$, 4)	2.7981(8)$_a$/2.5406(9)$_b$, 3.1038(2)$_a$/2.8306(6)$_b$, 2.4130(5)
La(1)-O($1_{a,b}$ $3_{a,b}$, 4)	2.7999(5)$_a$/2.5544(2)$_b$, 3.1107(9)$_a$/2.8444(4)$_b$, 2.4130(5)
Na(2)-O($2_{a,b}$, $3_{a,b}$ 4)	3.0758(8)$_a$/2.9260(6)$_b$, 2.7466(9)$_a$/2.5499(7)$_b$, 2.6697(3)
La(2)-O($2_{a,b}$, $3_{a,b}$ 4)	3.2436(11)$_a$/2.3274(54)$_b$, 2.6834(1)$_a$/2.5413(4)$_b$, 2.5973(8)

7.5LNN

Site	x	y	z	Fraction	Uiso
La(1)	0.237(18)	0.25	0	0.071(5)	0.011(28)
Na(1)	0.246(13)	0.25	0	0.773(4)	0.004(15)
La(2)	0.275(6)	0.264(7)	0.250	0.076(4)	0.009(78)
Na(2)	0.218(4)	0.230(4)	0.250	0.752(6)	0.011(5)
Nb	0.2516(2)	0.7473(6)	0.1256(4)	1	0.0105(1)
O(1)	0.683(4)	0.250	0	1	0.021(7)
O(2)	0.260(5)	0.778(6)	0.25	1	0.011(4)
O(3)	0.491(4)	0.484(6)	0.139(1)	1	0.024(7)
O(4)	0.0078(41)	0.023(5)	0.111(2)	1	0.039(8)

Microstrain	1762 (135)
Crystallite Size (µm)	10(27)
Nb-O(1,2,3$_{a,b}$,4)	1.9946(4),1.9515(8),1.9771(7)$_a$/1.9522(8)$_b$,2.0499(6)
Na(1)-O(1$_{a,b}$, 3$_{a,b}$, 4)	2.7963(5)$_a$/2.4172(5)$_b$, 3.0073(6)$_a$/2.8778(2)$_b$, 2.5195(5)
La(1)-O(1$_{a,b}$ 3$_{a,b}$, 4)	2.8039(8)$_a$/2.4690(1)$_b$, 3.0326(9)$_a$/2.8778(2)$_b$, 2.4928(5)
Na(2)-O(2$_{a,b}$, 3$_{a,b}$ 4)	3.0453(2)$_a$/2.8954(2)$_b$, 2.7223(4)$_a$/2.6852(1)$_b$, 2.7121(3)
La(2)-O(2$_{a,b}$, 3$_{a,b}$ 4)	2.8520(2)$_a$/2.5665(5)$_b$, 2.6516(7)$_a$/2.4220(3)$_b$, 2.9422(8)

10LNN

Site	x	y	z	Fraction	Uiso
La(1)	0.244(60)	0.25	0	0.108(3)	0.0058(38)
Na(1)	0.244(50)	0.25	0	0.693(3)	0.021(7)
La(2)	0.275(5)	0.259(10)	0.250	0.098(3)	0.015(11)
Na(2)	0.231(7)	0.241(11)	0.250	0.687(8)	0.014(10)
Nb	0.2513(3)	0.7479(6)	0.1252(2)	1	0.0119(1)
O(1)	0.703(6)	0.250	0	1	0.0276(6)
O(2)	0.274(5)	0.781(6)	0.25	1	0.0276(6)
O(3)	0.479(3)	0.485(5)	0.140(1)	1	0.0276(6)
O(4)	0.018(4)	0.015(7)	0.120(1)	1	0.0276(6)

Microstrain	844 (29)
Crystallite Size (µm)	4.7(15)
Nb-O(1,2,3$_{a,b}$,4)	1.9743(4),1.9662(3),1.9733(1)$_a$/1.9322(8)$_b$,2.0560(9)
Na(1)-O(1$_{a,b}$, 3$_{a,b}$, 4)	2.8114(7)$_a$/2.4332(6)$_b$, 3.0311(11)$_a$/2.6114(2)$_b$, 2.5221(8)
La(1)-O(1$_{a,b}$ 3$_{a,b}$, 4)	2.8114(6)$_a$/2.4778(2)$_b$, 3.0145(8)$_a$/2.8812(4)$_b$, 2.5233(7)
Na(2)-O(2$_{a,b}$, 3$_{a,b}$ 4)	3.0335(1)$_a$/2.9022(3)$_b$, 2.7341(5)$_a$/2.7231(9)$_b$, 2.7633(10)
La(2)-O(2$_{a,b}$, 3$_{a,b}$ 4)	2.8931(10)$_a$/2.6613(5)$_b$, 2.63112(5)$_a$/2.4451(2)$_b$, 2.8113(7)

15LNN

Site	x	y	z	Fraction	Uiso
La	0	0	0	0.147(8)	0.0034(13)
Na	0	0	0	0.544(3)	0.0234(34)
Nb	0.5	0.5	0.5	1	0.0104(1)
O	0	0.5	0.5	1	0.0341(6)
Microstrain			546 (27)		
Crystallite Size (μm)			2.74(48)		
Nb-O			1.95792(1)		
La,Na-O			2.76891(1)		

20LNN

Site	x	y	z	Fraction	Uiso
La	0	0	0	0.108(3)	0.015(11)
Na	0	0	0	0.693(3)	0.011(13)
Nb	0.5	0.5	0.5	0.098(3)	0.0131(2)
O	0	0.5	0.5	0.687(8)	0.0290(8)
Microstrain			384 (18)		
Crystallite Size (μm)			10(2)		
Nb-O			1.95998(1)		
La,Na-O			2.77983(1)		

25LNN

Site	x	y	z	Fraction	Uiso
La	0	0	0	0.216(8)	0.0107(14)
Na	0	0	0	0.393(5)	0.0113(4)
La(2)	0	0	0.5	0.295(1)	0.0074(22)
Na(2)	0	0	0.5	0.100(11)	0.0118(11)
Nb	0.5	0.5	0.2552(2)	1	0.0126(2)
O(5)	0.5	0.5	0	1	0.0179(67)
O(6)	0.5	0.5	0.5	1	0.0303(74)
O(7)	0	0.5	0.2409(7)	1	0.0234(34)
Microstrain			Equatorial: 988(38) Axial: 1035(111)		
Crystallite Size (μm)			3.477(62)		
Nb-O(5,6,7)			2.0061(6),1.9237(9),1.9645(2)		
La,Na-O(5,7)			2.7737(3),2.7266(5)		
La,Na(2)-O(6,7)			2.7737(6),2.8268(8)		

27LNN

Site	x	y	z	Fraction	Uiso
La	0	0.2463(11)	0	0.502(1)	0.0053(2)
Na	0	0.2657(28)	0	0.372(5)	0.0284(4)
La(2)	0	0.2560(18)	0.5	0.041(1)	0.0119(25)
Nb	0.2507(7)	0	0.2601(1)	1	0.0117(1)
O(3)	0.2494(5)	0	0	1	0.0231(17)
O(4)	0.2705(19)	0	0.5	1	0.0177(17)
O(5)	0	0	0.2458(38)	1	0.0169(57)
O(6)	0	0.5	0.2073(20)	1	0.0202(44)
O(7)	0.25	0.25	0.2425(19)	1	0.0094(26)
Microstrain		S400: 266(32), S040: 468(53), S004: 409(31), S220: -49(21), S202: -100(34), S022: 547(67)			
Crystallite Size (μm)		0.778(26)			
Nb-O(3,4,5,6,7)		2.0615(11), 1.9017(11), 1.9594(55), 1.9875(58), 1.9684(8)			
La-O($3_{a,b}$4,5,6)		2.9014(8)$_{a}$/2.635(8)$_{b}$, 2.700(6), 2.5921(8), 2.8044(9)			
Na-O($3_{a,b}$4,5,6)		2.926(3)$_{a}$/2.653(2)$_{b}$, 3.080(30)2.311(3), 2.722(7)			

31LNN

Site	x	y	z	Fraction	Uiso
La	0	0.2462(2)	0	0.611 (5)	0.0047(29)
Na	0	0.2945(48)	0	0.122(4)	0.038(4)
Nb	0.2507(7)	0	0.2601(1)	1	0.0119(1)
O(3)	0.2296(14)	0	0	1	0.014(5)
O(4)	0.2701(14)	0	0.5	1	0.014(5)
O(5)	0	0	0.2575(15)	1	0.014(5)
O(6)	0	0.5	0.2103(14)	1	0.014(5)
O(7)	0.25	0.25	0.235(1)	1	0.014(5)
Microstrain		744 (41)			
Crystallite Size (μm)		1.12(33)			
Nb-O(3,4,5,6,7)		2.0615(11), 1.9017(11), 1.9594(55), 1.9875(58), 1.9684(8)			
La-O($3_{a,b}$4,5,6)		2.9014(8)$_{a}$/2.635(8)$_{b}$, 2.700(6), 2.5921(8), 2.8044(9)			
Na-O($3_{a,b}$4,5,6)		2.926(3)$_{a}$/2.653(2)$_{b}$, 3.080(30)2.311(3), 2.722(7)			

33LNN

Site	x	y	z	Fraction	Uiso
La	0	0.2455(3)	0	0.668(1)	0.0059(2)
Nb	0.2505(5)	0	0.2604(1)	1	0.0109(1)
O(3)	0.2308(13)	0	0	1	0.0103(5)
O(4)	0.2711(12)	0	0.5	1	0.0103(5)
O(5)	0	0	0.248(2)	1	0.0103(5)
O(6)	0	0.5	0.2102(4)	1	0.0103(5)
O(7)	0.25	0.25	0.238(1)	1	0.0103(5)

Microstrain	650(28)
Crystallite Size (μm)	3.44(86)
Nb-O(1,2,3,4,5)	2.06575(2), 1.90093(1), 1.96066(2), 1.98978(2), 1.96610(0)
La-O($1_{a,b}$ 3,4,5)	2.89819(1)$_a$/2.63751(1)$_b$, 2.75077(1), 2.59576(1), 2.71763(2)

Table D2-D11: The refined site coordinates, fractions, Uiso, microstrain and crystallite sizes for each LNN material synthesised. The A-O and B-O bond lengths are also tabulated.

A-O$_{a,b}$ refers to (a) long and (b) short cation-oxygen bonds between the crystallographically distinct sites.

Oxygen Uiso and are held equivalent for 33, 31, 10 & 5LNN. Oxygen site fractions are held at 1 for all samples with the exception of 20LNN. These are done for the purpose of maintaining a stable refinement.

9 Conclusions

The composites investigated show desirable dielectric properties for a materials system with prospective use within temperature stable class II MLCCs. For a system considered for X7R TCC specification, a relative permittivity of ~2000 can be obtained with low dielectric losses ($\tan \delta < 0.05$) for a temperature range far exceeding the interested -55 to 125 °C X7R boundaries. BT and 60NNBT can be mixed together under a short period, using both hand mixing (0.5 hours) and ball milling (6 hours) methods, to achieve a reproducible dielectric response. With small additions of sintering glass, the density can be improved and the dielectric breakdown strength is a reasonable ~ 110 $\mathrm{kVcm^{-1}}$ for composites. If X8R TCC specification is required, doping of ~ 7 mol% calcium into the A site of the BT matrix phase, forming BCT, results in the necessary extension of temperature stability. This comes at a cost of a reduction in permittivity magnitude, by almost half, and so thinner dielectric layers in an MLCC (thinner by roughly half) are necessary with these BCT composites relative to the BT composites to achieve an equivalent device capacitance. Based on the reasonable resistance to field induced dielectric breakdown, BCT composites with ≤ 2 wt.% glass addition could operate in the inherently higher electric field conditions imposed.

Although results chapter 3 focused on enhancing the industrial scalability of the composite systems, there are still more questions to be answered before true industrial feasibility can be ascribed. Firstly, the sintering conditions used were all under air. For an MLCC formulation to be attractive industrially, its electrodes would need to be base metal (BME) for their lower cost (relative to inert Au, Pt or Ag-Pd types often used), and thus susceptible to oxidation under air sintering. This means that sintering of the dielectric must be performed under reduced atmospheres, and with the absence of any type of acceptor dopant within the system, it is likely that the dielectric behaviour of the composites would be lost. This is unless Ca is able to act as an amphoteric dopant and locate onto the B site of the matrix phase, however this would impart a significant reduction of T_m associated to the matrix BCT phase which is essential to yielding X8R rated TCC in the composite. Low pO_2 conditions would also be observed in an organic burn off stage during manufacture, where components of the slurry used to ensure mechanical compliance with the casting methods used are removed. A reoxidation stage upon cooling would be necessary.

Based on the Na content, and the Ellingham diagram for Ni and Na, Ni would act as a reducing agent for Na, causing the precipitation of Na metal and the oxidation of Ni. The two are thermodynamically incompatible at the processing conditions utilised for MLCCs and the 1250 °C sintering temperature used here. Cu is a BME more thermodynamically compatible with Na and offers an inherent advantage over Ni in its comparably lower associated impedance. Its processing conditions do, however, necessitate a lower sintering temperature than what has been used within this thesis, < 1000 °C, based on its lower melting point compared to Ni. This could be achieved with the addition of glass or different commercial sintering additives, on thinner tapes as opposed to bulk samples. Further studies on the sintering conditions of the all nano-powder BCT, BT and NN mix used in results chapter 3 could yield a sufficiently lower sintering temperature for dense composite dielectric layers. This would, of course, necessitate further investigation. The lower firing temperature associated with the Cu BME could also reduce the potential for reduction, inhibiting the transition to semiconducting behaviour possible under lower pO_2.

Thus, the composite system shows a good, reproducible and industrially non-disruptive architecture to achieving temperature stable dielectric permittivity response from materials that independently cannot meet X7R or X8R TCC specification. The composite system represents a more competitive NNBT based macrostructure compared to multilayer systems suggested by preceding work [149,231,232] on an account of a lack of need for interfacial interdiffusion barriers, nor will it carry the same concerns of interlayer delamination and the additional manufacturing complexities that sequential layer lamination imposes. It does not, however, at this point represent a system that is capable of displacing BT core shell type formulations unless its processing window can be better understood. Should it be Cu compatible with lower associated sintering temperatures compared to existing conditions, it may become a more attractive formulation. There is a lack of rare earths in this composite system that are often used in industrial $BaTiO_3$ on account of their amphoteric doping nature and core-shell inducing diffusion properties, which are undesirable for cost and geopolitically related availability insecurities. However, as discussed previously, this system has not sintered under industrial conditions and the behaviour without similar amphoteric dopants is unknown.

For the LNN system, dielectric behaviour is only observed for a select compositional window in the solid solution, specifically $0 \leq La^{3+}$ (mol%) < 15 substitutions into the A site sublattice. For this window, TCC is only improved for compositions of an even smaller compositional space, above the order-disorder transition at 7.5LNN. Despite ‘flattening’ of TCC, its variance still exceeds the ± 15 % boundaries required for an R type class II dielectric, and at much lower temperatures than the -55 to 125/150 °C operational window. These dielectrics would not be appropriate for class II temperature stable MLCCs.

The variation in electrical properties with increasing La^{3+}/V_{Na}' concentration is, however, a more interesting property of the solid solution. A transition between a dielectric-antiferroelectric, linear-dielectric and a mixed ionic-electronic conductor can be achieved solely by changing the

V_{Na}' concentration in the system and mediating structural transitions/order-disorder states. The linear dielectric response exhibits moderate energy storage efficiency and density, and should a more polarisable/breakdown resistant composition be found, promises higher recoverable energy densities suitable for energy density applications.

There is certainly plenty of scope for enhancing the Na^+ conductivity within the A-site deficient $NaNbO_3$ perovskite window. Different sized rare earth A-site cations would be a first start. Addition of 6+ valence states into the perovskite B site, such as W or Mo doping of LNN, could encourage further A site vacancy concentration per Na/La ratio. This may represent another avenue for Na^+ conductivity optimisation. Should this conductivity be improved, the mixed conductivity nature of the LNN sample could find itself with prospective integration as an electrode material. The Na-$Ce_{1/3}NbO_3$ analogues, for example, showed zero strain [295], a property appropriate for anode materials in batteries and a property potentially shared by this isostructural LNN series. Alternatively, additional dopants can be used to minimise the electronic contribution to the conductivity and isolate the Na^+ ionic conductivity, leaving this as a solid-state electrolyte instead. The $La_{1/3}NbO_3$ composition brings additional interesting complexities, for the ionic conduction that is clearly present must be a different but unknown migrating species. This solid solution represents a hugely diverse compositional space that clearly offers a basis for optimisation for a series of differing applications, all through the variation in V_{Na}'.

10 Future Work

For the composite system, future work will predominantly relate to enhancing the industrial/commercial feasibility of the system with respect to MLCC integration. For the system formed of a stoichiometric mix of commercial NN, BT and BCT nano powders, characterisation of the NNBT phase grain size and morphology using SEM, whilst analysing intragranular compositional heterogeneity via EDX and/or WDS, is necessary to understand the lower permittivity contribution such phases offer with respect to composites formed of pre-calcined 60NNBT. Should the lower permittivity be associated with smaller grain sizes, work should proceed on modifying the sintering conditions to facilitate grain coarsening and an increase in the polar correlation lengths without compromising the compositional heterogeneity between the BCT matrix and NNBT secondary phases. There was no data obtained for the reproducibility of this 'industrial mix' of commercial nano powders, thus, it is unknown at this stage whether or not this variability of permittivity response observed for a composite formed of commercial nano powders is a function of the starting materials used in the pre-sintered mixture or not.

Additional studies on the ability to lower the sintering temperature should be conducted. The addition of glass as a sintering aid, and the transient liquid phase formed during sintering, should mediate densification at reduced sintering temperatures. The composites with glass addition should be sintered at temperatures below 1250 °C and close to 1000 °C, with the prospect of utilising Cu electrodes in prototype MLCCs. The dwell time may need to be increased from 0.5 hours to accommodate for the lower temperature at sintering. Should bulk densities be achievable at these sufficiently lower sintering temperatures, a prototype MLCC utilising the BC7T-60NNBT mixtures discussed in results chapter 2 should be constructed using Cu internal electrodes. This will need to be sintered under an inert/reducing atmosphere, likely N_2, and reoxidised during an annealing stage at a temperature below sintering under a higher pO_2. Dielectric spectroscopy will be important to understand if the dielectric properties of the composite have been retained, considering no acceptor dopants have been used within the formulation.

For the LNN system, local structure analysis, potentially using neutron diffraction and pair distribution analyses or HRTEM, will be necessary to describe the difference in local structure from macrostructure which is evident from the diffusivity of some diffraction pattern reflections. Vacancy ordering and octahedral tilting cooperation is confined to incommensurate microdomains within the $La_{1/3}NbO_3$ end member, and incur the diffusivity in the Bi doped $NaNbO_3$ system [194]. It will be analogous within this A site deficient LNN system, where the complete solid solution formed will offer a greater range of compositions to investigate these structural intricacies. Furthermore, the effect of local structure on optimal conductivity within these A site deficient $NaNbO_3$ systems has not been described since other compositions, such as Ca, Sr or Bi, are unable to exceed the 20 mol% doping concentration on account of secondary phase formation. There is a large scope for conductivity optimisation within this family of $RE_xNa_{1-3x}NbO_3$ A site deficient perovskites. Donor doping of the B site with W^{6+} or Mo^{6+} could increase the number of A-site vacancies introduced, or co doping of larger Ba^{2+} with W^{6+} can expand the O4 bottleneck within the vacancy ordered 25LNN sample to improve the diffusion coefficient of Na^+ without compromising the number of A site vacancies formed.

11 References

[1] M.R.F. https://www.marketresearchfuture.com, Multilayer Ceramic Capacitor Market Size, Report Trends 2032, (n.d.). https://www.marketresearchfuture.com/reports/multilayer-ceramic-capacitor-market-7738 (accessed September 3, 2024).

[2] Multilayer Ceramic Capacitor (MLCC) Market Size & Share, Growth Analysis 2036, (n.d.). https://www.researchnester.com/reports/multilayer-ceramic-capacitor-mlcc-market/5199 (accessed September 3, 2024).

[3] J. Lee, High Voltage Ceramic Capacitors for Electric Vehicles, (n.d.). https://www.kyocera-avx.com/docs/techinfo/CeramicCapacitors/high-voltage-mlcc-in-electric-vehicles.pdf (accessed August 28, 2024).

[4] R. Fiore, Circuit Designers Notebook: Understanding Temperature Coefficient of Capacitance, (n.d.). https://rfs.kyocera-avx.com/userFiles/uploads/pdfs/temp_coef.pdf (accessed September 3, 2024).

[5] C. Hammond, The Basics of Crystallography and Diffraction, Fourth Edition, IUCr International Union of Crystallography, Oxford Science Publications, University of Leeds, 2015.

[6] M.F.C. Ladd, R.A. Palmer, Structure Determination by X-ray Crystallography, Third Edition, Plenum Press, London, New York, n.d.

[7] A.R. West, Solid State Chemistry and its Applications, Second Edition, John Wiley & Sons, University of Sheffield, 2016.

[8] H. Burzlaff, H. Zimmermann, 3.3. Space-group symbols and their use, International Tables for Crystallography (2016). Vol. A, ch. 3.3, pp. 777-791, doi:10.1107/97809553602060000931

[9] J.K. Cockcroft, A Hypertext Book of Crystallographic Space Group Diagrams and Tables, (1997). http://img.chem.ucl.ac.uk/sgp/mainmenu.htm (accessed September 3, 2024).

[10] M.E. Lines, A.M. Glass, Principles and Applications of Ferroelectrics and Related Materials, Oxford Classic Texts in the Physical Sciences, Oxford, New York, 2009.

[11] R.K. Pandey, Fundamentals of Electroceramics: Materials, Devices, and Applications, Wiley, 2019.

[12] D. Damjanovic, Ferroelectric, dielectric and piezoelectric properties of ferroelectric thin films and ceramics, Rep. Prog. Phys. 61 (1998) 1267. https://doi.org/10.1088/0034-4885/61/9/002.

[13] A.J. Moulsen, J.M. Herbert, Electroceramics: Materials, Properties, Applications, Second Edition, John Wiley & Sons, 2003.

[14] B.T. Matthias, New Ferroelectric Crystals, Phys. Rev. 75 (1949) 1771–1771. https://doi.org/10.1103/PhysRev.75.1771.

[15] W.J. Merz, Double Hysteresis Loop of $BaTiO_3$ at the Curie Point, Phys. Rev. 91 (1953) 513–517. https://doi.org/10.1103/PhysRev.91.513.

[16] K. Yao, S. Chen, M. Rahimabady, M.S. Mirshekarloo, S. Yu, F.E.H. Tay, T. Sritharan, L. Lu, Nonlinear dielectric thin films for high-power electric storage with energy density comparable with electrochemical supercapacitors, IEEE Trans. Ultrason. Ferroelectr. Freq. Control 58 (2011) 1968–1974. https://doi.org/10.1109/TUFFC.2011.2039.

[17] N.H. Fletcher, A.D. Hilton, B.W. Ricketts, Optimization of energy storage density in ceramic capacitors, J. Phys. Appl. Phys. 29 (1996) 253. https://doi.org/10.1088/0022-3727/29/1/037.

[18] Z. Chen, S. Mao, L. Ma, G. Luo, Q. Feng, Z. Cen, F. Toyohisa, X. Peng, L. Liu, H. Zhou, C. Hu, N. Luo, Phase engineering in $NaNbO_3$ antiferroelectrics for high energy storage density, J. Materiomics 8 (2022) 753–762. https://doi.org/10.1016/j.jmat.2022.03.004.

[19] G. Wang, Z. Lu, Y. Li, L. Li, H. Ji, A. Feteira, D. Zhou, D. Wang, S. Zhang, I.M. Reaney, Electroceramics for High-Energy Density Capacitors: Current Status and Future Perspectives, Chem. Rev. 121 (2021) 6124–6172. https://doi.org/10.1021/acs.chemrev.0c01264.

[20] R. Mitchell, Perovskites: Modern and Ancient, Almaz Press, 2002.

[21] M.A. Green, A. Ho-Baillie, H.J. Snaith, The emergence of perovskite solar cells, Nat. Photonics 8 (2014) 506–514. https://doi.org/10.1038/nphoton.2014.134.

[22] A.M. Glazer, Simple ways of determining perovskite structures, Acta Crystallogr. Sect. A 31 (1975) 756–762. https://doi.org/10.1107/S0567739475001635.

[23] A.S. Bhalla, R. Guo, R. Roy, The perovskite structure—a review of its role in ceramic science and technology, Mater. Res. Innov. 4 (2000) 3–26. https://doi.org/10.1007/s100190000062.

[24] M.A. Peña, J.L.G. Fierro, Chemical Structures and Performance of Perovskite Oxides, Chem. Rev. 101 (2001) 1981–2018. https://doi.org/10.1021/cr980129f.

[25] H.D. Megaw, Crystal structure of double oxides of the perovskite type, Proc. Phys. Soc. 58 (1946) 133. https://doi.org/10.1088/0959-5309/58/2/301.

[26] V.V.M. Goldschmidt, Die Gesetze der Krystallochemie, Naturwissenschaften Springer (1926) 477–485.

[27] Z. Li, M. Yang, J.-S. Park, S.-H. Wei, J.J. Berry, K. Zhu, Stabilizing Perovskite Structures by Tuning Tolerance Factor: Formation of Formamidinium and Cesium Lead Iodide Solid-State Alloys, Chem. Mater. 28 (2016) 284–292. https://doi.org/10.1021/acs.chemmater.5b04107.

[28] K. Hong, T. Hyung Lee, J. Min Suh, S.-H. Yoon, H. Won Jang, Perspectives and challenges in multilayer ceramic capacitors for next generation electronics, J. Mater. Chem. C 7 (2019) 9782–9802. https://doi.org/10.1039/C9TC02921D.

[29] H. Thurnauer, J. Deaderick, Insulating Material, US2429588A, 1941. https://patents.google.com/patent/US2429588A/en.

[30] A. Von Hippel, R.G. Breckenridge, F.G. Chesley, L. Tisza, High dielectric constant ceramics, Ind. Eng. Chem. 38 (1946) 1097–1109. https://doi.org/10.1021/ie50443a009.

[31] W.J. Merz, The Electric and Optical Behavior of $BaTiO_3$ Single-Domain Crystals, Phys. Rev. 76 (1949) 1221–1225. https://doi.org/10.1103/PhysRev.76.1221.

[32] M.-J. Pan, C.A. Randall, A brief introduction to ceramic capacitors, IEEE Electr. Insul. Mag. 26 (2010) 44–50. https://doi.org/10.1109/MEI.2010.5482787.

[33] A. Von Hippel, Ferroelectricity, Domain Structure, and Phase Transitions of Barium Titanate, Rev. Mod. Phys. 22 (1950) 221–237. https://doi.org/10.1103/RevModPhys.22.221.

[34] W. Cochran, Crystal Stability and the Theory of Ferroelectricity, Phys. Rev. Lett. 3 (1959) 412–414. https://doi.org/10.1103/PhysRevLett.3.412.

[35] P.C. Kwok, P.B. Miller, Free Energy of Displacive Ferroelectrics, Phys. Rev. 151 (1966) 387–400. https://doi.org/10.1103/PhysRev.151.387.

[36] W. Cochran, Crystal stability and the theory of ferroelectricity part II. Piezoelectric crystals, Adv. Phys. 10 (1961) 401–420. https://doi.org/10.1080/00018736100101321.

[37] B. Ravel, E.A. Stern, R.I. Vedrinskii, V. Kraizman, Local structure and the phase transitions of $BaTiO_3$, Ferroelectrics 206 (1998) 407–430. https://doi.org/10.1080/00150199808009173.

[38] D. Hennings, R. Waser, Defect Chemistry of $BaTiO_3$ and $SrTiO_3$: Practical Aspects and Application to Electronic Ceramics, in: J. Nowotny, W. Weppner (Eds.), Non-Stoichiom. Compd. Surf. Grain Boundaries Struct. Defects, Springer Netherlands, Dordrecht, 1989: pp. 137–153. https://doi.org/10.1007/978-94-009-0943-4_10.

[39] W. Heywang, Resistivity Anomaly in Doped Barium Titanate, J. Am. Ceram. Soc. 47 (1964) 484–490. https://doi.org/10.1111/j.1151-2916.1964.tb13795.x.

[40] G.H. Jonker, Some aspects of semiconducting barium titanate, Solid-State Electron. 7 (1964) 895–903. https://doi.org/10.1016/0038-1101(64)90068-1.

[41] G.V. Lewis, C.R.A. Catlow, R.E.W. Casselton, PTCR Effect in $BaTiO_3$, J. Am. Ceram. Soc. 68 (1985) 555–558. https://doi.org/10.1111/j.1151-2916.1985.tb11523.x.

[42] A.B. Alles, V.R.W. Amarakoon, V.L. Burdick, Positive Temperature Coefficient of Resistivity Effect in Undoped, Atmospherically Reduced Barium Titanate, J. Am. Ceram. Soc. 72 (1989) 148–151. https://doi.org/10.1111/j.1151-2916.1989.tb05970.x.

[43] W. Heywang, Semiconducting barium titanate, J. Mater. Sci. 6 (1971) 1214–1224. https://doi.org/10.1007/BF00550094.

[44] A.B. Alles, V.L. Burdick, Grain Boundary Oxidation in PTCR Barium Titanate Thermistors, J. Am. Ceram. Soc. 76 (1993) 401–408. https://doi.org/10.1111/j.1151-2916.1993.tb03798.x.

[45] F.D. Morrison, D.C. Sinclair, A.R. West, Characterization of Lanthanum-Doped Barium Titanate Ceramics Using Impedance Spectroscopy, J. Am. Ceram. Soc. 84 (2001) 531–538. https://doi.org/10.1111/j.1151-2916.2001.tb00694.x.

[46] F.D. Morrison, D.C. Sinclair, J.M.S. Skakle, A.R. West, Novel Doping Mechanism for Very-High-Permittivity Barium Titanate Ceramics, J. Am. Ceram. Soc. 81 (1998) 1957–1960. https://doi.org/10.1111/j.1151-2916.1998.tb02575.x.

[47] F.D. Morrison, D.C. Sinclair, A.R. West, Electrical and structural characteristics of lanthanum-doped barium titanate ceramics, J. Appl. Phys. 86 (1999) 6355–6366. https://doi.org/10.1063/1.371698.

[48] D. Makovec, Z. Samardžija, U. Delalut, D. Kolar, Defect Structure and Phase Relations of Highly Lanthanum-Doped Barium Titanate, J. Am. Ceram. Soc. 78 (1995) 2193–2197. https://doi.org/10.1111/j.1151-2916.1995.tb08635.x.

[49] F.D. Morrison, A.M. Coats, D.C. Sinclair, A.R. West, Charge Compensation Mechanisms in La-Doped $BaTiO_3$, (n.d.).

[50] C.L. Freeman, J.A. Dawson, H.-R. Chen, L. Ben, J.H. Harding, F.D. Morrison, D.C. Sinclair, A.R. West, Energetics of Donor-Doping, Metal Vacancies, and Oxygen-Loss in A-Site Rare-Earth-Doped $BaTiO_3$, Adv. Funct. Mater. 23 (2013) 3925–3928. https://doi.org/10.1002/adfm.201203147.

[51] C.-J. Peng, H.-Y. Lu, Compensation Effect in Semiconducting Barium Titanate, J. Am. Ceram. Soc. 71 (1988) C-44-C–46. https://doi.org/10.1111/j.1151-2916.1988.tb05780.x.

[52] G.V. Lewis, C.R.A. Catlow, Defect studies of doped and undoped barium titanate using computer simulation techniques, J. Phys. Chem. Solids 47 (1986) 89–97. https://doi.org/10.1016/0022-3697(86)90182-4.

[53] N.-H. Chan, D.M. Smyth, Defect Chemistry of Donor-Doped $BaTiO_3$, J. Am. Ceram. Soc. 67 (1984) 285–288. https://doi.org/10.1111/j.1151-2916.1984.tb18849.x.

[54] F.D. Morrison, D.C. Sinclair, A.R. West, An Alternative Explanation for the Origin of the Resistivity Anomaly in La-Doped $BaTiO_3$, J. Am. Ceram. Soc. 84 (2001) 474–76. https://doi.org/10.1111/j.1151-2916.2001.tb00684.x.

[55] J.M. Herbert, Thin ceramic dielectrics combined with nickel electrodes, Proc. Inst. Electr. Eng. 112 (1965) 1474. https://doi.org/10.1049/piee.1965.0237.

[56] O. Saburi, Properties of Semiconductive Barium Titanates, J. Phys. Soc. Jpn. 14 (1959) 1159–1174. https://doi.org/10.1143/JPSJ.14.1159.

[57] G.Y. Yang, G.D. Lian, E.C. Dickey, C.A. Randall, D.E. Barber, P. Pinceloup, M.A. Henderson, R.A. Hill, J.J. Beeson, D.J. Skamser, Oxygen nonstoichiometry and dielectric evolution of $BaTiO_3$. Part II—insulation resistance degradation under applied dc bias, J. Appl. Phys. 96 (2004) 7500–7508. https://doi.org/10.1063/1.1809268.

[58] J.B. MacCHESNEY, P.K. Gallagher, F.V. DiMARCELLO, Stabilized Barium Titanate Ceramics for Capacitor Dielectrics, J. Am. Ceram. Soc. 46 (1963) 197–202. https://doi.org/10.1111/j.1151-2916.1963.tb19771.x.

[59] D.A. Payne, Concerning the Physics of Failure of Barium Titanate Capacitors, in: 6th Annu. Reliab. Phys. Symp. IEEE, 1967: pp. 257–264. https://doi.org/10.1109/IRPS.1967.362419.

[60] H. Chazono, H. Kishi, dc-Electrical Degradation of the BT-Based Material for Multilayer Ceramic Capacitor with Ni internal Electrode: Impedance Analysis and Microstructure, Jpn. J. Appl. Phys. 40 (2001) 5624. https://doi.org/10.1143/JJAP.40.5624.

[61] J. Rödel, G. Tomandl, Degradation of Mn-doped $BaTiO_3$ ceramic under a high d.c. electric field, J. Mater. Sci. 19 (1984) 3515–3523. https://doi.org/10.1007/BF02396925.

[62] N.-H. Chan, R. k. Sharma, D. m. Smyth, Nonstoichiometry in Undoped $BaTiO_3$, J. Am. Ceram. Soc. 64 (1981) 556–562. https://doi.org/10.1111/j.1151-2916.1981.tb10325.x.

[63] M. Vollman, R. Waser, Grain Boundary Defect Chemistry of Acceptor-Doped Titanates: Space Charge Layer Width, J. Am. Ceram. Soc. 77 (1994) 235–243. https://doi.org/10.1111/j.1151-2916.1994.tb06983.x.

[64] Y.-M. Chiang, T. Takagi, Grain-Boundary Chemistry of Barium Titanate and Strontium Titanate: I, High-Temperature Equilibrium Space Charge, J. Am. Ceram. Soc. 73 (1990) 3278–3285. https://doi.org/10.1111/j.1151-2916.1990.tb06450.x.

[65] R. Waser, T. Baiatu, K.-H. Härdtl, dc Electrical Degradation of Perovskite-Type Titanates: I, Ceramics, J. Am. Ceram. Soc. 73 (1990) 1645–1653. https://doi.org/10.1111/j.1151-2916.1990.tb09809.x.

[66] Y. Tsur, T.D. Dunbar, C.A. Randall, Crystal and Defect Chemistry of Rare Earth Cations in $BaTiO_3$, J. Electroceramics 7 (2001) 25–34. https://doi.org/10.1023/A:1012218826733.

[67] K. Kinoshita, A. Yamaji, Grain-size effects on dielectric properties in barium titanate ceramics, J. Appl. Phys. 47 (1976) 371–373. https://doi.org/10.1063/1.322330.

[68] G. Arlt, D. Hennings, G. De With, Dielectric properties of fine-grained barium titanate ceramics, J. Appl. Phys. 58 (1985) 1619–1625. https://doi.org/10.1063/1.336051.

[69] T. Hoshina, K. Takizawa, J. Li, T. Kasama, H. Kakemoto, T. Tsurumi, Domain Size Effect on Dielectric Properties of Barium Titanate Ceramics, Jpn. J. Appl. Phys. 47 (2008) 7607. https://doi.org/10.1143/JJAP.47.7607.

[70] D. Ghosh, A. Sakata, J. Carter, P.A. Thomas, H. Han, J.C. Nino, J.L. Jones, Domain Wall Displacement is the Origin of Superior Permittivity and Piezoelectricity in $BaTiO_3$ at Intermediate Grain Sizes, Adv. Funct. Mater. 24 (2014) 885–896. https://doi.org/10.1002/adfm.201301913.

[71] M.T. Buscaglia, M. Viviani, V. Buscaglia, L. Mitoseriu, A. Testino, P. Nanni, Z. Zhao, M. Nygren, C. Harnagea, D. Piazza, C. Galassi, High dielectric constant and frozen macroscopic polarization in dense nanocrystalline $BaTiO_3$ ceramics, Phys. Rev. B 73 (2006) 064114. https://doi.org/10.1103/PhysRevB.73.064114.

[72] P. Zheng, J.L. Zhang, Y.Q. Tan, C.L. Wang, Grain-size effects on dielectric and piezoelectric properties of poled $BaTiO_3$ ceramics, Acta Mater. 60 (2012) 5022–5030. https://doi.org/10.1016/j.actamat.2012.06.015.

[73] G. Arlt, N.A. Pertsev, Force constant and effective mass of 90° domain walls in ferroelectric ceramics, J. Appl. Phys. 70 (1991) 2283–2289. https://doi.org/10.1063/1.349421.

[74] J.L. Jones, E.B. Slamovich, K.J. Bowman, Domain texture distributions in tetragonal lead zirconate titanate by x-ray and neutron diffraction, J. Appl. Phys. 97 (2005) 034113. https://doi.org/10.1063/1.1849821.

[75] Effect of the Ba/Ti Ratio on the Microstructures and Dielectric Properties of Barium Titanate-Based Glass–Ceramics - Chen - 2009 - Journal of the American Ceramic Society - Wiley Online Library, (n.d.). https://ceramics.onlinelibrary.wiley.com/doi/full/10.1111/j.1551-2916.2009.03028.x (accessed September 6, 2024).

[76] D. Hennings, A. Schnell, G. Simon, Diffuse Ferroelectric Phase Transitions in $Ba(Ti_{1-y}Zr_y)O3$ Ceramics, J. Am. Ceram. Soc. 65 (1982) 539–544. https://doi.org/10.1111/j.1151-2916.1982.tb10778.x.

[77] H.-Y. Lu, J.-S. Bow, W.-H. Deng, Core-Shell Structures in ZrO_2-Modified $BaTiO_3$ Ceramic, J. Am. Ceram. Soc. 73 (1990) 3562–3568. https://doi.org/10.1111/j.1151-2916.1990.tb04258.x.

[78] D. Hennings, G. Rosenstein, Temperature-Stable Dielectrics Based on Chemically Inhomogeneous $BaTiO_3$, J. Am. Ceram. Soc. 67 (1984) 249–254. https://doi.org/10.1111/j.1151-2916.1984.tb18841.x.

[79] C.A. Randall, S.F. Wang, D. Laubscher, J.P. Dougherty, W. Huebner, Structure property relationships in core-shell $BaTiO_3$–LiF ceramics, J. Mater. Res. 8 (1993) 871–879. https://doi.org/10.1557/JMR.1993.0871.

[80] S.-C. Jeon, B.-K. Yoon, K.-H. Kim, S.-J.L. Kang, Effects of core/shell volumetric ratio on the dielectric-temperature behavior of $BaTiO_3$, J. Adv. Ceram. 3 (2014) 76–82. https://doi.org/10.1007/s40145-014-0096-y.

[81] H. Kishi, Y. Okino, M. Honda, Y. Iguchi, M. Imaeda, Y. Takahashi, H. Ohsato, T. Okuda, The Effect of MgO and Rare-Earth Oxide on Formation Behavior of Core-Shell Structure in $BaTiO_3$, Jpn. J. Appl. Phys. 36 (1997) 5954. https://doi.org/10.1143/JJAP.36.5954.

[82] H. Kishi, N. Kohzu, J. Sugino, H. Ohsato, Y. Iguchi, T. Okuda, The effect of rare-earth (La, Sm, Dy, Ho and Er) and Mg on the microstructure in $BaTiO_3$, J. Eur. Ceram. Soc. 19 (1999) 1043–1046. https://doi.org/10.1016/S0955-2219(98)00370-7.

[83] S.-C. Jeon, C.-S. Lee, S.-J.L. Kang, The Mechanism of Core/Shell Structure Formation During Sintering of 3-Based Ceramics, J. Am. Ceram. Soc. 95 (2012) 2435–2438. https://doi.org/10.1111/j.1551-2916.2012.05111.x.

[84] M.T. Buscaglia, M. Viviani, Z. Zhao, V. Buscaglia, P. Nanni, Synthesis of $BaTiO_3$ Core−Shell Particles and Fabrication of Dielectric Ceramics with Local Graded Structure, Chem. Mater. 18 (2006) 4002–4010. https://doi.org/10.1021/cm060403j.

[85] H. Chazono, M.F.M. Fujimoto, Sintering Characteristics and Formation Mechanisms of "Core-Shell" Structure in $BaTiO_3$-Nb_2O_5-Co_3O_5 Ternary System, Jpn. J. Appl. Phys. 34 (1995) 5354. https://doi.org/10.1143/JJAP.34.5354.

[86] R.D. Shannon, Revised effective ionic radii and systematic studies of interatomic distances in halides and chalcogenides, Acta Crystallogr. Sect. A 32 (1976) 751–767. https://doi.org/10.1107/S0567739476001551.

[87] W.J. Merz, The Effect of Hydrostatic Pressure on the Curie Point of Barium Titanate Single Crystals, Phys. Rev. 78 (1950) 52–54. https://doi.org/10.1103/PhysRev.78.52.

[88] R.E. Cohen, Origin of ferroelectricity in perovskite oxides, Nature 358 (1992) 136–138. https://doi.org/10.1038/358136a0.

[89] G. Durst, M. Grotenhuis, A.G. Barkow, Solid Solubility Study of Barium, Strontium, and Calcium Titanates, J. Am. Ceram. Soc. 33 (1950) 133–139. https://doi.org/10.1111/j.1151-2916.1950.tb12775.x.

[90] R.C. DeVRIES, R. Roy, Phase Equilibria in the System $BaTiO_3$—$CaTiO_3$, J. Am. Ceram. Soc. 38 (1955) 142–146. https://doi.org/10.1111/j.1151-2916.1955.tb14918.x.

[91] M. McQUARRIE, F.W. Behnke, Structural and Dielectric Studies in the System (Ba, Ca) (Ti, Zr)O_3, J. Am. Ceram. Soc. 37 (1954) 539–543. https://doi.org/10.1111/j.1151-2916.1954.tb13986.x.

[92] T. Mitsui, W.B. Westphal, Dielectric and X-Ray Studies of $Ca_xBa_{1-x}TiO_3$ and $Ca_xSr_{1-x}TiO_3$, Phys. Rev. 124 (1961) 1354–1359. https://doi.org/10.1103/PhysRev.124.1354.

[93] D.A. Berlincourt, F. Kulcsar, Electromechanical Properties of $BaTiO_3$ Compositions Showing Substantial Shifts in Phase Transition Points, J. Acoust. Soc. Am. 24 (1952) 709–713. https://doi.org/10.1121/1.1906961.

[94] L. Zhang, O.P. Thakur, A. Feteira, G.M. Keith, A.G. Mould, D.C. Sinclair, A.R. West, Comment on the use of calcium as a dopant in X8R BaTiO3-based ceramics, Appl. Phys. Lett. 90 (2007) 142914. https://doi.org/10.1063/1.2720305.

[95] D.C. Sinclair, J. Paul Attfield, The influence of A-cation disorder on the Curie temperature of ferroelectric $ATiO_3$ perovskites, Chem. Commun. (1999) 1497–1498. https://doi.org/10.1039/a903680f.

[96] I. Levin, V. Krayzman, J.C. Woicik, Local-structure origins of the sustained Curie temperature in (Ba,Ca)TiO_3 ferroelectrics, Appl. Phys. Lett. 102 (2013) 162906. https://doi.org/10.1063/1.4802996.

[97] D. Fu, M. Itoh, S. Koshihara, T. Kosugi, S. Tsuneyuki, Anomalous Phase Diagram of Ferroelectric (Ba,Ca)TiO_3 Single Crystals with Giant Electromechanical Response, Phys. Rev. Lett. 100 (2008) 227601. https://doi.org/10.1103/PhysRevLett.100.227601.

[98] J.A. Dawson, D.C. Sinclair, J.H. Harding, C.L. Freeman, A-Site Strain and Displacement in $Ba_{1-x}Ca_xTiO_3$ and $Ba_{1-x}Sr_xTiO_3$ and the Consequences for the Curie Temperature, Chem. Mater. 26 (2014) 6104–6112. https://doi.org/10.1021/cm502158n.

[99] Z.Q. Zhuang, M.P. Harmer, D.M. Smyth, R.E. Newnham, The effect of octahedrally-coordinated calcium on the ferroelectric transition of $BaTiO_3$, Mater. Res. Bull. 22 (1987) 1329–1335. https://doi.org/10.1016/0025-5408(87)90296-0.

[100] Y. Sakabe, K. Minai, K. Wakino, High-Dielectric Constant Ceramics for Base Metal Monolithic Capacitors, Jpn. J. Appl. Phys. 20 (1981) 147. https://doi.org/10.7567/JJAPS.20S4.147.

[101] X.W. Zhang, Y.H. Han, M. Lal, D.M. Smyth, Defect Chemistry of $BaTiO_3$ with Additions of $CaTiO_3$, J. Am. Ceram. Soc. 70 (1987) 100–103. https://doi.org/10.1111/j.1151-2916.1987.tb04937.x.

[102] P. Vousden, A study of the unit-cell dimensions and symmetry of certain ferroelectric compounds of niobium and tantalum at room temperature, Acta Crystallogr. 4 (1951) 373–376. https://doi.org/10.1107/S0365110X5100115X.

[103] B.T. Matthias, J.P. Remeika, Dielectric Properties of Sodium and Potassium Niobates, Phys. Rev. 82 (1951) 727–729. https://doi.org/10.1103/PhysRev.82.727.

[104] P. Vousden, The structure of ferroelectric sodium niobate at room temperature, Acta Crystallogr. 4 (1951) 545–551. https://doi.org/10.1107/S0365110X51001768.

[105] C. Kittel, Theory of Antiferroelectric Crystals, Phys. Rev. 82 (1951) 729–732. https://doi.org/10.1103/PhysRev.82.729.

[106] H.D. Megaw, M. Wells, The space group of $NaNbO_3$ and $(Na_{0.995}K_{0.005})NbO_3$, Acta Crystallogr. 11 (1958) 858–862. https://doi.org/10.1107/S0365110X58002437.

[107] K.E. Johnston, C.C. Tang, J.E. Parker, K.S. Knight, P. Lightfoot, S.E. Ashbrook, The Polar Phase of $NaNbO_3$: A Combined Study by Powder Diffraction, Solid-State NMR, and First-Principles Calculations, J. Am. Chem. Soc. 132 (2010) 8732–8746. https://doi.org/10.1021/ja101860r.

[108] M.-H. Zhang, L. Fulanović, C. Zhao, J. Koruza, Review on field-induced phase transitions in lead-free $NaNbO_3$-based antiferroelectric perovskite oxides for energy storage, J. Materiomics 9 (2023) 1–18. https://doi.org/10.1016/j.jmat.2022.09.008.

[109] J. Koruza, J. Tellier, B. Malič, V. Bobnar, M. Kosec, Phase transitions of sodium niobate powder and ceramics, prepared by solid state synthesis, J. Appl. Phys. 108 (2010) 113509. https://doi.org/10.1063/1.3512980.

[110] A.C. Sakowski-Cowley, K. Łukaszewicz, H.D. Megaw, The structure of sodium niobate at room temperature, and the problem of reliability in pseudosymmetric structures, Acta Crystallogr. B 25 (1969) 851–865. https://doi.org/10.1107/S0567740869003141.

[111] L.E. Cross, B.J. Nicholson, LV. The optical and electrical properties of single crystals of sodium niobate, Lond. Edinb. Dublin Philos. Mag. J. Sci. 46 (1955) 453–466. https://doi.org/10.1080/14786440508520582.

[112] M.-H. Zhang, C. Zhao, L. Fulanović, J. Rödel, N. Novak, A. Schökel, J. Koruza, Revealing the mechanism of electric-field-induced phase transition in antiferroelectric $NaNbO_3$ by in situ high-energy x-ray diffraction, Appl. Phys. Lett. 118 (2021) 132903. https://doi.org/10.1063/5.0043050.

[113] E.A. Wood, R.C. Miller, J.P. Remeika, The field-induced ferroelectric phase of sodium niobate, Acta Crystallogr. 15 (1962) 1273–1279. https://doi.org/10.1107/S0365110X62003357.

[114] M.-H. Zhang, L. Fulanović, S. Egert, H. Ding, P.B. Groszewicz, H.-J. Kleebe, L. Molina-Luna, J. Koruza, Electric-field-induced antiferroelectric to ferroelectric phase transition in polycrystalline $NaNbO_3$, Acta Mater. 200 (2020) 127–135. https://doi.org/10.1016/j.actamat.2020.09.002.

[115] Y. Shiratori, A. Magrez, J. Dornseiffer, F.-H. Haegel, C. Pithan, R. Waser, Polymorphism in Micro-, Submicro-, and Nanocrystalline $NaNbO_3$, J. Phys. Chem. B 109 (2005) 20122–20130. https://doi.org/10.1021/jp052974p.

[116] J. Koruza, P. Groszewicz, H. Breitzke, G. Buntkowsky, T. Rojac, B. Malič, Grain-size-induced ferroelectricity in $NaNbO_3$, Acta Mater. 126 (2017) 77–85. https://doi.org/10.1016/j.actamat.2016.12.049.

[117] R.A. Shakhovoy, S.I. Raevskaya, L.A. Shakhovaya, D.V. Suzdalev, I.P. Raevski, Yu.I. Yuzyuk, A.F. Semenchev, M. El Marssi, Ferroelectric Q and antiferroelectric P phases' coexistence and local phase transitions in oxygen-deficient $NaNbO_3$ single crystal: micro-Raman, dielectric and dilatometric studies, J. Raman Spectrosc. 43 (2012) 1141–1145. https://doi.org/10.1002/jrs.3140.

[118] Y. Shiratori, A. Magrez, W. Fischer, C. Pithan, R. Waser, Temperature-induced Phase Transitions in Micro-, Submicro-, and Nanocrystalline $NaNbO_3$, J. Phys. Chem. C 111 (2007) 18493–18502. https://doi.org/10.1021/jp0738053.

[119] L.A. Reznichenko, L.A. Shilkina, E.S. Gagarina, I.P. Raevskii, E.A. Dul'kin, E.M. Kuznetsova, V.V. Akhnazarova, Structural instabilities, incommensurate modulations and P and Q phases in sodium niobate in the temperature range 300–500 K, Crystallogr. Rep. 48 (2003) 448–456. https://doi.org/10.1134/1.1578130.

[120] W. Li, X. Xia, J. Zeng, L. Zheng, G. Li, Significant differences in $NaNbO_3$ ceramics fabricated using Nb_2O_5 precursors with various crystal structures, Ceram. Int. 46 (2020) 3759–3766. https://doi.org/10.1016/j.ceramint.2019.10.098.

[121] M.-H. Zhang, N. Hadaeghi, S. Egert, H. Ding, H. Zhang, P.B. Groszewicz, G. Buntkowsky, A. Klein, J. Koruza, Design of Lead-Free Antiferroelectric $(1 - x)NaNbO_3$–$xSrSnO_3$ Compositions Guided by First-Principles Calculations, Chem. Mater. 33 (2021) 266–274. https://doi.org/10.1021/acs.chemmater.0c03685.

[122] A.M. Glazer, The classification of tilted octahedra in perovskites, Acta Crystallogr. Sect. B 28 (1972) 3384–3392. https://doi.org/10.1107/S0567740872007976.

[123] C.J. Howard, H.T. Stokes, Group-Theoretical Analysis of Octahedral Tilting in Perovskites, Acta Crystallogr. B 54 (1998) 782–789. https://doi.org/10.1107/S0108768198004200.

[124] L. Jiang, D.C. Mitchell, W. Dmowski, T. Egami, Local structure of $NaNbO_3$: A neutron scattering study, Phys. Rev. B 88 (2013) 014105. https://doi.org/10.1103/PhysRevB.88.014105.

[125] A.M. Glazer, K. Ishida, Cation displacements and octahedral tilts in $NaNbO_3$ Part I—Determination from x-ray difference reflections, Ferroelectrics 6 (1973) 219–224. https://doi.org/10.1080/00150197408243971.

[126] A.M. Glazer, H.D. Megaw, Studies of the lattice parameters and domains in the phase transitions of $NaNbO_3$, Acta Crystallogr. Sect. A 29 (1973) 489–495. https://doi.org/10.1107/S0567739473001245.

[127] M. Ahtee, A.M. Glazer, H.D. Megaw, The structures of sodium niobate between 480° and 575°C, and their relevance to soft-phonon modes, Philos. Mag. J. Theor. Exp. Appl. Phys. 26 (1972) 995–1014. https://doi.org/10.1080/14786437208226972.

[128] H.D. Megaw, The thermal expansion of interatomic bonds, illustrated by experimental evidence from certain niobates, Acta Crystallogr. Sect. A 24 (1968) 589–604. https://doi.org/10.1107/S0567739468001294.

[129] H.D. Megaw, The seven phases of sodium niobate, Ferroelectrics 7 (1974) 87–89. https://doi.org/10.1080/00150197408237956.

[130] I. Lefkowitz, K. Łukaszewicz, H.D. Megaw, The high-temperature phases of sodium niobate and the nature of transitions in pseudosymmetric structures, Acta Crystallogr. 20 (1966) 670–683. https://doi.org/10.1107/S0365110X66001592.

[131] I.P. Raevskii, L.A. Reznichenko, V.G. Smotrakov, V.V. Eremkin, M.A. Malitskaya, E.M. Kuznetsova, L.A. Shilkina, A new phase transition in sodium niobate, Tech. Phys. Lett. 26 (2000) 744–746. https://doi.org/10.1134/1.1307831.

[132] A. Hussain, A. Gadelmawla, J.G. Maier, G.E. Eyoum, H. Miyazaki, K. Kimura, K. Hayashi, K.G. Webber, Effect of A-site non-stoichiometry in $NaNbO_3$ ceramics, Scr. Mater. 255 (2025) 116384. https://doi.org/10.1016/j.scriptamat.2024.116384.

[133] H. Guo, H. Shimizu, Y. Mizuno, C.A. Randall, Domain configuration changes under electric field-induced antiferroelectric-ferroelectric phase transitions in $NaNbO_3$-based ceramics, J. Appl. Phys. 118 (2015) 054102. https://doi.org/10.1063/1.4928153.

[134] R.M. Glaister, Solid Solution Dielectrics Based on Sodium Niobate, J. Am. Ceram. Soc. 43 (1960) 348–353. https://doi.org/10.1111/j.1151-2916.1960.tb13669.x.

[135] P. Baxter, N.J. Hellicar, B. Lewis, Effect of Additives of Limited Solid Solubility on Ferroelectric Properties of Barium Titanate Ceramics, J. Am. Ceram. Soc. 42 (1959) 465–470. https://doi.org/10.1111/j.1151-2916.1959.tb13558.x.

[136] P.Y. Foeller, Novel materials and routes for rare-earth-free $BaTiO_3$-based ceramics for MLCC applications., Thesis, University of Sheffield, 2017.

https://etheses.whiterose.ac.uk/18954/1/Thesis%20Philip%20Y%20Foeller.pdf (accessed April 21, 2023).

[137] D.-K. Kwon, Y. Goh, D. Son, B.-H. Kim, H. Bae, S. Perini, M. Lanagan, Temperature- and Frequency-Dependent Dielectric Properties of Sol–Gel-Derived $BaTiO_3$-$NaNbO_3$ Solid Solutions, J. Electron. Mater. 45 (2016) 631–638. https://doi.org/10.1007/s11664-015-4162-1.

[138] J.T. Zeng, K.W. Kwok, H.L.W. Chan, Ferroelectric and Piezoelectric Properties of $Na_{1-x}Ba_xNb_{1-x}Ti_xO_3$ Ceramics, J. Am. Ceram. Soc. 89 (2006) 2828–2832. https://doi.org/10.1111/j.1551-2916.2006.01172.x.

[139] H. Abdelkefi, H. Khemakhem, G. Vélu, J.C. Carru, R. Von der Mühll, Dielectric proprieties of ferroelectric ceramics derived from the system $BaTiO_3NaNbO_3$-based solid solutions, Solid State Sci. 6 (2004) 1347–1351. https://doi.org/10.1016/j.solidstatesciences.2004.07.012.

[140] R.E. Newnham, D.P. Skinner, L.E. Cross, Connectivity and piezoelectric-pyroelectric composites, Mater. Res. Bull. 13 (1978) 525–536. https://doi.org/10.1016/0025-5408(78)90161-7.

[141] M.T. Benlahrache, N. Benhamla, S. Achour, Dielectric properties of $BaTiO_3$–$NaNbO_3$ composites, J. Eur. Ceram. Soc. 24 (2004) 1493–1496. https://doi.org/10.1016/S0955-2219(03)00577-6.

[142] S.K. Sarkar, M.L. Sharma, Dielectric strength and dielectric constant of $BaTiO_3$-$NaNbO_3$ composites at room temperature, J. Mater. Sci. Lett. 8 (1989) 1365–1367. https://doi.org/10.1007/BF00720188.

[143] I.P. Raevskii, L.M. Proskuryakova, L.A. Reznichenko, E.K. Zvorykina, L.A. Shilkina, Obtaining solid solutions in the $NaNbO_3$-$BaTiO_3$ system and investigation of its properties, Sov. Phys. J. 21 (1978) 259–261. https://doi.org/10.1007/BF00898503.

[144] R. Zuo, H. Qi, J. Fu, J.-F. Li, L. Li, Multiscale identification of local tetragonal distortion in $NaNbO_3$-$BaTiO_3$ weak relaxor ferroelectrics by Raman, synchrotron x-ray diffraction, and absorption spectra, Appl. Phys. Lett. 111 (2017) 132901. https://doi.org/10.1063/1.4995009.

[145] H. Abdelkefi, H. Khemakhem, A. Simon, J. Darriet, X-ray diffraction study of $Ba_{0.985}Na_{0.015}Ti_{0.985}Nb_{0.015}O_3$, $Ba_{0.6}Na_{0.4}Ti_{0.6}Nb_{0.4}O_3$ and $Ba_{0.3}Na_{0.7}Ti_{0.3}Nb_{0.7}O_3$ compositions, J. Alloys Compd. 463 (2008) 423–427. https://doi.org/10.1016/j.jallcom.2007.09.031.

[146] R.B. Zampiere, G.S. Dias, L.F. Cótica, I.A. Santos, Enhanced ferroism in mechanically processed and environmentally friendly $Ba_{0.30}Na_{0.70}Ti_{0.30}Nb_{0.70}O_3$ ceramics, Scr. Mater. 66 (2012) 542–545. https://doi.org/10.1016/j.scriptamat.2011.12.031.

[147] K. Ćwikiel, E. Nogas-Ćwikiel, Dielectric and pyroelectric properties of the $Ba_{0.3}$ $Na_{0.7}$ $Ti_{0.3}$ $Nb_{0.7}$ O_3 ceramics obtained by sol-gel method, Phase Transit. 80 (2007) 141–146. https://doi.org/10.1080/01411590601090575.

[148] R. Zuo, H. Qi, J. Fu, J. Li, M. Shi, Y. Xu, Giant electrostrictive effects of $NaNbO_3$-$BaTiO_3$ lead-free relaxor ferroelectrics, Appl. Phys. Lett. 108 (2016) 232904. https://doi.org/10.1063/1.4953457.

[149] G.W. Kerridge, Resource efficient development of combinatorial materials for future Multilayer Ceramic Capacitor applications, PhD, University of Sheffield, 2022. https://etheses.whiterose.ac.uk/30435/ (accessed June 25, 2024).

[150] Y. Fan, X. Wang, H. Li, A. Feteira, D. Wang, G. Wang, D.C. Sinclair, I.M. Reaney, Pb, Bi, and rare earth free X6R barium titanate–sodium niobate ceramics for high voltage capacitor applications, Appl. Phys. Lett. 122 (2023) 143901. https://doi.org/10.1063/5.0142200.

[151] H. Wang, E. Li, M. Xing, C. Zhong, Achieving ultrahigh energy storage density and efficiency in 0.90$NaNbO_3$–0.10$BaTiO_3$ ceramics *via* a composition modification strategy, Dalton Trans. 51 (2022) 10085–10094. https://doi.org/10.1039/D2DT01265K.

[152] P.N. Iyer, A.J. Smith, Double oxides containing niobium, tantalum, or protactinium. III. Systems involving the rare earths, Acta Crystallogr. 23 (1967) 740–746. https://doi.org/10.1107/S0365110X67003639.

[153] W.L. Kehl, R.G. Hay, D. Wahl, The Structure of Tetragonal Tungsten Trioxide, J. Appl. Phys. 23 (1952) 212–215. https://doi.org/10.1063/1.1702176.

[154] H.A. Evans, Y. Wu, R. Seshadri, A.K. Cheetham, Perovskite-related ReO_3-type structures, Nat. Rev. Mater. 5 (2020) 196–213. https://doi.org/10.1038/s41578-019-0160-x.

[155] L. Carrillo, M.E. Villafuerte-Castrejón, G. González, L.E. Sansores, L. Bucio, J. Duque, R. Pomés, Superstructure determination of the perovskite $\beta La_{0.33}NbO_3$, J. Mater. Sci. 35 (2000) 3047–3052. https://doi.org/10.1023/A:1004863715548.

[156] Y. Sakai, D. Urushihara, T. Asaka, K. Fukuda, Z. Yang, N. Tanibata, H. Takeda, M. Nakayama, Octahedral Tilting and Modulation Structure in Perovskite-Related Compound $La_{1/3}NbO_3$, Phys. Status Solidi B n/a (2022) 2100561. https://doi.org/10.1002/pssb.202100561.

[157] J. Bouwma, K.J. de Vries, A.J. Burggraaf, Non-stoichiometry, defect structure, and dielectric relaxation in lanthana-substituted $SrTiO_3$, Phys. Status Solidi A 35 (1976) 281–290. https://doi.org/10.1002/pssa.2210350130.

[158] M. Abe, K. Uchino, X-ray study of the deficient perovskite $La_{2/3}TiO_3$, Mater. Res. Bull. 9 (1974) 147–155. https://doi.org/10.1016/0025-5408(74)90194-9.

[159] B.J. Kennedy, C.J. Howard, Y. Kubota, K. Kato, Phase transition behaviour in the *A*-site deficient perovskite oxide $La_{1/3}NbO_3$, J. Solid State Chem. 177 (2004) 4552–4556. https://doi.org/10.1016/j.jssc.2004.08.047.

[160] C.J. Howard, Z. Zhang, Structures and phase transition in the layered perovskite $La_{0.6}Sr_{0.1}TiO_3$: a new orthorhombic structure solved from high-resolution diffraction in combination with group theoretical analysis, J. Phys. Condens. Matter 15 (2003) 4543. https://doi.org/10.1088/0953-8984/15/26/304.

[161] Z. Zhang, C.J. Howard, B.J. Kennedy, K.S. Knight, Q. Zhou, Crystal structure of $Ln_{1/3}NbO_3$ (Ln=Nd, Pr) and phase transition in $Nd_{1/3}NbO_3$, J. Solid State Chem. 180 (2007) 1846–1851. https://doi.org/10.1016/j.jssc.2007.03.029.

[162] H.T. Stokes, E.H. Kisi, D.M. Hatch, C.J. Howard, Group-theoretical analysis of octahedral tilting in ferroelectric perovskites, Acta Crystallogr. B 58 (2002) 934–938. https://doi.org/10.1107/S0108768102015756.

[163] X. Gao, C.A.J. Fisher, Y.H. Ikuhara, Y. Fujiwara, S. Kobayashi, H. Moriwake, A. Kuwabara, K. Hoshikawa, K. Kohama, H. Iba, Y. Ikuhara, Cation ordering in A-site-deficient Li-ion conducting perovskites $La_{(1-x)/3}Li_xNbO_3$, J. Mater. Chem. A 3 (2015) 3351–3359. https://doi.org/10.1039/C4TA07040B.

[164] D. Kepaptsoglou, J.D. Baran, F. Azough, D. Ekren, D. Srivastava, M. Molinari, S.C. Parker, Q.M. Ramasse, R. Freer, Prospects for Engineering Thermoelectric Properties in $La_{1/3}NbO_3$ Ceramics Revealed via Atomic-Level Characterization and Modeling, Inorg. Chem. 57 (2018) 45–55. https://doi.org/10.1021/acs.inorgchem.7b01584.

[165] Z. Yang, R.E. Ward, N. Tanibata, H. Takeda, M. Nakayama, T. Asaka, Arrangement in $La_{1/3}NbO_3$ Obtained by First-Principles Density Functional Theory with Cluster Expansion and Monte Carlo Simulation, J. Phys. Chem. C 124 (2020) 9746–9754. https://doi.org/10.1021/acs.jpcc.0c01350.

[166] Z. Yang, M. Nakayama, Materials Simulation for the Modulated Arrangement in A-Site Deficient Perovskite-Type Lithium Doped Lanthanum Niobate as Solid Electrolytes for All Solid-State Li Ion Batteries, J. Phys. Soc. Jpn. 91 (2022) 091010. https://doi.org/10.7566/JPSJ.91.091010.

[167] A.N. Salak, N.P. Vyshatko, D.D. Khalyavin, O. Prokhnenko, V.M. Ferreira, Low-temperature structural and dielectric phenomena in $La_{1/3}NbO_3$ and $La_{1/3}TaO_3$: Comparative study, Appl. Phys. Lett. 93 (2008) 162903. https://doi.org/10.1063/1.3006331.

[168] A. Mikonis, J. Macutkevic, R. Grigalaitis, J. Banys, R. Adomavicius, A. Krotkus, A.N. Salak, N.P. Vyshatko, D.D. Khalyavin, BROADBAND DIELECTRIC SPECTROSCOPY OF $La_{1/3}NbO_3$ CERAMICS, Integr. Ferroelectr. 109 (2009) 55–60. https://doi.org/10.1080/10584580903432551.

[169] A.M. George, A.N. Virkar, Mixed iono-electronic conduction in β-$LaNb_3O_9$, J. Phys. Chem. Solids 49 (1988) 743–751. https://doi.org/10.1016/0022-3697(88)90023-6.

[170] G. Adachi, N. Imanaka, S. Tamura, Ionic Conducting Lanthanide Oxides, Chem. Rev. 102 (2002) 2405–2430. https://doi.org/10.1021/cr0103064.

[171] Trivalent Ionic Conductivity of Perovskite-Type $Y_x(Ta_{3x}W_{1-3x})O_3$, (n.d.). https://www.jstage.jst.go.jp/article/electrochemistry/68/6/68_504/_article/-char/ja/ (accessed September 16, 2024).

[172] A.G. Belous, G.N. Novitskaya, S.V. Polyanetskaya, Yu.I. Gornikov, Investigation into complex oxides of $La_{2/3-x}Li_{3x}TiO_3$ composition, Izv Akad Nauk SSSR Neorg Mater 23 (1987) 470–472.

[173] Y. Inaguma, C. Liquan, M. Itoh, T. Nakamura, T. Uchida, H. Ikuta, M. Wakihara, High ionic conductivity in lithium lanthanum titanate, Solid State Commun. 86 (1993) 689–693. https://doi.org/10.1016/0038-1098(93)90841-A.

[174] P. Knauth, Inorganic solid Li ion conductors: An overview, Solid State Ion. 180 (2009) 911–916. https://doi.org/10.1016/j.ssi.2009.03.022.

[175] S. Stramare, V. Thangadurai, W. Weppner, Lithium Lanthanum Titanates: A Review, Chem. Mater. 15 (2003) 3974–3990. https://doi.org/10.1021/cm0300516.

[176] Y. Kawakami, H. Ikuta, M. Wakihara, Ionic conduction of lithium for Perovskite-type compounds, $Li_xLa_{(1-x)/3}NbO_3$ and $(Li_{0.25}La_{0.25})1-xSr_{0.5x}NbO_3$, J. Solid State Electrochem. 2 (1998) 206–210. https://doi.org/10.1007/s100080050089.

[177] S. García-Martín, J.M. Rojo, H. Tsukamoto, E. Morán, M.A. Alario-Franco, Lithium-ion conductivity in the novel $La_{1/3-x}Li_{3x}NbO_3$ solid solution with perovskite-related structure, Solid State Ion. 116 (1999) 11–18. https://doi.org/10.1016/S0167-2738(98)00266-5.

[178] A. Belous, E. Pashkova, O. Gavrilenko, O. V'yunov, L. Kovalenko, Solid electrolytes based on lithium-containing lanthanum metaniobates, J. Eur. Ceram. Soc. 24 (2004) 1301–1304. https://doi.org/10.1016/S0955-2219(03)00501-6.

[179] Y. Fujiwara, K. Hoshikawa, K. Kohama, Growth of solid electrolyte $Li_xLa_{(1-x)/3}NbO_3$ single crystals by the directional solidification method, J. Cryst. Growth 433 (2016) 48–53. https://doi.org/10.1016/j.jcrysgro.2015.09.033.

[180] Y. Kawakami, M. Fukuda, H. Ikuta, M. Wakihara, Ionic conduction of lithium for perovskite type compounds, $(Li_{0.05}La_{0.317})1-xSr_{0.5x}NbO_3$, $(Li_{0.1}La_{0.3})1-xSr_{0.5x}NbO_3$ and $(Li_{0.25}La_{0.25})_{1-x}M_{0.5x}NbO_3$ (M=Ca and Sr), Solid State Ion. 110 (1998) 187–192. https://doi.org/10.1016/S0167-2738(98)00131-3.

[181] L. Latie, G. Villeneuve, D. Conte, G. Le Flem, Ionic conductivity of oxides with general formula $Li_xLn_{1/3}Nb_{1-x}Ti_xO_3$ (Ln = La, Nd), J. Solid State Chem. 51 (1984) 293–299. https://doi.org/10.1016/0022-4596(84)90345-1.

[182] M. Itoh, Y. Inaguma, W.-H. Jung, L. Chen, T. Nakamura, High lithium ion conductivity in the perovskite-type compounds $Ln_{1/2}Li_{1/2}TiO_3$(Ln=La,Pr,Nd,Sm), Solid State Ion. 70–71 (1994) 203–207. https://doi.org/10.1016/0167-2738(94)90310-7.

[183] Y. Inaguma, Y. Matsui, J. Yu, Y.-J. Shan, T. Nakamura, M. Itoh, EFFECT OF SUBSTITUTION AND PRESSURE ON LITHIUM ION CONDUCTIVITY IN PEROVSKITES $Ln_{1/2}Li_{1/2}TiO_3$ (Ln = La, Pr, Nd AND Sm), J. Phys. Chem. Solids 58 (1997) 843–852. https://doi.org/10.1016/S0022-3697(96)00226-0.

[184] S. García-Martín, M.Á. Alario-Franco, Modulated Structure of $La_{1/3-x}Li_{3x}NbO_3$ $0 \leq x \leq 0.06$ Perovskite-Related Materials, J. Solid State Chem. 148 (1999) 93–99. https://doi.org/10.1006/jssc.1999.8377.

[185] X. Gao, C.A.J. Fisher, T. Kimura, Y.H. Ikuhara, H. Moriwake, A. Kuwabara, H. Oki, T. Tojigamori, R. Huang, Y. Ikuhara, Lithium Atom and A-Site Vacancy Distributions in Lanthanum Lithium Titanate, Chem. Mater. 25 (2013) 1607–1614. https://doi.org/10.1021/cm3041357.

[186] J. Ibarra, Influence of composition on the structure and conductivity of the fast ionic conductors $La_{2/3-x}Li_{3x}TiO_3$ $(0.03 \leq x \leq 0.167)$, Solid State Ion. 134 (2000) 219–228. https://doi.org/10.1016/S0167-2738(00)00761-X.

[187] M. Catti, Ion Mobility Pathways of the Li+ Conductor $Li_{0.125}La_{0.625}TiO_3$ by Ab Initio Simulations, J. Phys. Chem. C 112 (2008) 11068–11074. https://doi.org/10.1021/jp803345y.

[188] A.P. Pivovarova, V.I. Strakhov, V.P. Popov, Phase Relations in the $LaNb_3O_9$ – $NaNbO_3$ System in the Temperature Range of 20 TO 800°C, Refract. Ind. Ceram. 42 (2001) 285–287. https://doi.org/10.1023/A:1012718529213.

[189] A.P. Pivovarova, V.I. Strakhov, V.P. Popov, Dielectric Properties of Perovskite Solid Solutions Based on Sodium Metaniobate in the $NaNbO_3$ – $LaNb_3O_9$ System, Refract. Ind. Ceram. 43 (2002) 36–39. https://doi.org/10.1023/A:1015807631947.

[190] Y. Kong, Y. Liu, G. Hu, Synthesis and sodium ionic conductivity for perovskite-structured $Na_{0.25}La_{0.25}NbO_3$ ceramic, Ceram. Int. 48 (2022) 36136–36139. https://doi.org/10.1016/j.ceramint.2022.08.168.

[191] D.O. Mishchuk, O.I. V?yunov, O.V. Ovchar, A.G. Belous, Structural and dielectric properties of solid solutions of sodium niobate in lanthanum and neodymium niobates, Inorg. Mater. 40 (2004) 1324–1330. https://doi.org/10.1007/s10789-005-0019-y.

[192] M.D. Peel, S.P. Thompson, A. Daoud-Aladine, S.E. Ashbrook, P. Lightfoot, New Twists on the Perovskite Theme: Crystal Structures of the Elusive Phases R and S of $NaNbO_3$, Inorg. Chem. 51 (2012) 6876–6889. https://doi.org/10.1021/ic3006585.

[193] J.J. Bian, Y.Z. Li, Structural evolution and microwave dielectric properties of A-site deficient perovskite $La_{(1-x)/3}Na_xNbO_3$ ($0.0<x\leq 0.4$), Mater. Chem. Phys. 122 (2010) 617–622. https://doi.org/10.1016/j.matchemphys.2010.03.056.

[194] I. Levin, F. Yang, R. Maier, W.J. Laws, D.S. Keeble, G. Cibin, D.C. Sinclair, Displacive Order–Disorder Behavior and Intrinsic Clustering of Lattice Distortions in Bi-Substituted $NaNbO_3$, Adv. Funct. Mater. 30 (2020) 2001840. https://doi.org/10.1002/adfm.202001840.

[195] L. Zhang, Z. Yan, T. Chen, H. Luo, H. Zhang, T. Khanom, D. Zhang, I. Abrahams, H. Yan, Tunable phase transitions in $NaNbO_3$ ceramics through bismuth/vacancy modification, J. Mater. Chem. C 9 (2021) 4289–4299. https://doi.org/10.1039/D0TC05969B.

[196] X. Lei, Z. Peng, P. Liang, D. Wu, X. Chao, Z. Yang, Realizing oxygen ion conduction in perovskite structure $NaNbO_3$ by A-site Bismuth doping, J. Alloys Compd. 924 (2022) 166506. https://doi.org/10.1016/j.jallcom.2022.166506.

[197] W.G. Mumme, I.E. Grey, B. Edwards, C. Turner, J. Nino, T.A. Vanderah, $BiNb_3O_9$, a metastable perovskite phase with Bi/vacancy ordering: Crystal structure and dielectric properties, J. Solid State Chem. 200 (2013) 323–327. https://doi.org/10.1016/j.jssc.2013.01.052.

[198] X. Hu, M. Valant, D. Suvorov, Phase transitions and dielectric properties of the $Ag_{1-x}Bi_{x/3}NbO_3$ system, J. Appl. Phys. 99 (2006) 124109. https://doi.org/10.1063/1.2209552.

[199] S.K. Mishra, R. Mittal, V.Yu. Pomjakushin, S.L. Chaplot, Phase stability and structural temperature dependence in sodium niobate: A high-resolution powder neutron diffraction study, Phys. Rev. B 83 (2011) 134105. https://doi.org/10.1103/PhysRevB.83.134105.

[200] R.H. Mitchell, B.J. Kennedy, K.S. Knight, The crystal structure of lueshite at 298 K resolved by high-resolution time-of-flight neutron powder diffraction, Phys. Chem. Miner. 45 (2018) 77–83. https://doi.org/10.1007/s00269-017-0905-2.

[201] T. E. Hooper, D. C. Sinclair, Structural, dielectric, and conduction behaviour of A-site deficient $Sr_xNa_{1-2x}NbO_3$ ceramics, J. Mater. Chem. C 12 (2024) 12992–13001. https://doi.org/10.1039/D4TC02433H.

[202] 唐棣生, 梁敬魁, 石庭俊, 张玉苓, 田静华, 李文秀, $SrNb_2O_6$-$NaNbO_3$-$LiNbO_3$赝三元系相图的研究, 物理学报 28 (2005) 62–77. https://doi.org/10.7498/aps.28.62.

[203] S.I. Raevskaya, L.A. Reznichenko, I.P. Raevski, V.V. Titov, S.V. Titov, J.-L. Dellis, Lead-Free Niobate Ceramics with Relaxor-Like Properties, Ferroelectrics 340 (2006) 107–112. https://doi.org/10.1080/00150190600889114.

[204] A. Torres-Pardo, R. Jiménez, J.M. González-Calbet, E. García-González, Room Temperature Ferroelectricity in $Na_{1-x}Sr_{x/2}\square_{x/2}NbO_3$ through the Introduction of Cationic Vacancies, Chem. Mater. 20 (2008) 6957–6964. https://doi.org/10.1021/cm802101r.

[205] S. Aso, H. Matsuo, Y. Noguchi, Reversible electric-field-induced phase transition in Ca-modified $NaNbO_3$ perovskites for energy storage applications, Sci. Rep. 13 (2023) 6771. https://doi.org/10.1038/s41598-023-33975-6.

[206] G. Shirane, R. Newnham, R. Pepinsky, Dielectric Properties and Phase Transitions of $NaNbO_3$ and $(Na,K)NbO_3$, Phys. Rev. 96 (1954) 581–588. https://doi.org/10.1103/PhysRev.96.581.

[207] V.J. Tennery, K.W. Hang, Thermal and X-Ray Diffraction Studies of the NaNbO3–KNbO3 System, J. Appl. Phys. 39 (1968) 4749–4753. https://doi.org/10.1063/1.1655833.

[208] M. Wells, H.D. Megaw, The Structures of $NaNbO_3$ and $Na_{0.975}K_{0.025}NbO_3$, Proc. Phys. Soc. 78 (1961) 1258. https://doi.org/10.1088/0370-1328/78/6/124.

[209] M.D. Peel, S.E. Ashbrook, P. Lightfoot, Unusual Phase Behavior in the Piezoelectric Perovskite System, Li $_x$ Na $_{1-x}$ NbO $_3$, Inorg. Chem. 52 (2013) 8872–8880. https://doi.org/10.1021/ic401061t.

[210] H. Guo, H. Shimizu, C.A. Randall, Microstructural evolution in NaNbO3-based antiferroelectrics, J. Appl. Phys. 118 (2015) 174107. https://doi.org/10.1063/1.4935273.

[211] J.F. Tressler, S. Alkoy, A. Dogan, R.E. Newnham, Functional composites for sensors, actuators and transducers, Compos. Part Appl. Sci. Manuf. 30 (1999) 477–482. https://doi.org/10.1016/S1359-835X(98)00137-7.

[212] S. Luo, Y. Shen, S. Yu, Y. Wan, W.-H. Liao, R. Sun, C.-P. Wong, Construction of a 3D-$BaTiO_3$ network leading to significantly enhanced dielectric permittivity and energy storage density of polymer composites, Energy Environ. Sci. 10 (2017) 137–144. https://doi.org/10.1039/C6EE03190K.

[213] H. Tang, H.A. Sodano, Ultra High Energy Density Nanocomposite Capacitors with Fast Discharge Using $Ba_{0.2}Sr_{0.8}TiO_3$ Nanowires, Nano Lett. 13 (2013) 1373–1379. https://doi.org/10.1021/nl3037273.

[214] E.J. Barshaw, J. White, M.J. Chait, J.B. Cornette, J. Bustamante, F. Folli, D. Biltchick, G. Borelli, G. Picci, M. Rabuffi, High Energy Density (HED) Biaxially-Oriented Poly-Propylene (BOPP) Capacitors For Pulse Power Applications, IEEE Trans. Magn. 43 (2007) 223–225. https://doi.org/10.1109/TMAG.2006.887682.

[215] Status quo and future prospects for metallized polypropylene energy storage capacitors, (n.d.). https://xplorestaging.ieee.org/document/1178232?denied= (accessed September 27, 2024).

[216] A. Jain, P. K. J., A.Kr. Sharma, A. Jain, R. P.n, Dielectric and piezoelectric properties of PVDF/PZT composites: A review, Polym. Eng. Sci. 55 (2015) 1589–1616. https://doi.org/10.1002/pen.24088.

[217] K. Zou, Y. Dan, Y. Yu, Y. Zhang, Q. Zhang, Y. Lu, H. Huang, X. Zhang, Y. He, Flexible dielectric nanocomposites with simultaneously large discharge energy density and high energy efficiency utilizing $(Pb,La)(Zr,Sn,Ti)O_3$ antiferroelectric nanoparticles as fillers, J. Mater. Chem. A 7 (2019) 13473–13482. https://doi.org/10.1039/C9TA01299K.

[218] V. Tomer, E. Manias, C.A. Randall, High field properties and energy storage in nanocomposite dielectrics of poly(vinylidene fluoride-hexafluoropropylene), J. Appl. Phys. 110 (2011) 044107. https://doi.org/10.1063/1.3609082.

[219] C. R. Bowen, H. A. Kim, P. M. Weaver, S. Dunn, Piezoelectric and ferroelectric materials and structures for energy harvesting applications, Energy Environ. Sci. 7 (2014) 25–44. https://doi.org/10.1039/C3EE42454E.

[220] M. Amin Karami, D.J. Inman, Powering pacemakers from heartbeat vibrations using linear and nonlinear energy harvesters, Appl. Phys. Lett. 100 (2012) 042901. https://doi.org/10.1063/1.3679102.

[221] D.A. van den Ende, H.J. van de Wiel, W.A. Groen, S. van der Zwaag, Direct strain energy harvesting in automobile tires using piezoelectric PZT–polymer composites, Smart Mater. Struct. 21 (2011) 015011. https://doi.org/10.1088/0964-1726/21/1/015011.

[222] R. Kar-Gupta, T.A. Venkatesh, Electromechanical response of piezoelectric composites: Effects of geometric connectivity and grain size, Acta Mater. 56 (2008) 3810–3823. https://doi.org/10.1016/j.actamat.2008.04.031.

[223] C.R. Bowen, V.Yu. Topolov, Piezoelectric sensitivity of $PbTiO_3$-based ceramic/polymer composites with 0–3 and 3–3 connectivity, Acta Mater. 51 (2003) 4965–4976. https://doi.org/10.1016/S1359-6454(03)00283-0.

[224] H. Kara, R. Ramesh, R. Stevens, C.R. Bowen, Porous PZT ceramics for receiving transducers, IEEE Trans. Ultrason. Ferroelectr. Freq. Control 50 (2003) 289–296. https://doi.org/10.1109/TUFFC.2003.1193622.

[225] T.R. Armstrong, L.E. Morgens, A.K. Maurice, R.C. Buchanan, Effects of Zirconia on Microstructure and Dielectric Properties of Barium Titanate Ceramics, J. Am. Ceram. Soc. 72 (1989) 605–611. https://doi.org/10.1111/j.1151-2916.1989.tb06182.x.

[226] K. Bi, M. Bi, Y. Hao, W. Luo, Z. Cai, X. Wang, Y. Huang, Ultrafine core-shell $BaTiO_3@SiO_2$ structures for nanocomposite capacitors with high energy density, Nano Energy 51 (2018) 513–523. https://doi.org/10.1016/j.nanoen.2018.07.006.

[227] Z.-M. Dang, J.-K. Yuan, J.-W. Zha, T. Zhou, S.-T. Li, G.-H. Hu, Fundamentals, processes and applications of high-permittivity polymer–matrix composites, Prog. Mater. Sci. 57 (2012) 660–723. https://doi.org/10.1016/j.pmatsci.2011.08.001.

[228] T. Zakri, J.-P. Laurent, M. Vauclin, Theoretical evidence for `Lichtenecker's mixture formulae' based on the effective medium theory, J. Phys. Appl. Phys. 31 (1998) 1589. https://doi.org/10.1088/0022-3727/31/13/013.

[229] M.T. Sebastian, H. Jantunen, Polymer–Ceramic Composites of 0–3 Connectivity for Circuits in Electronics: A Review, Int. J. Appl. Ceram. Technol. 7 (2010) 415–434. https://doi.org/10.1111/j.1744-7402.2009.02482.x.

[230] N. Jayasundere, B.V. Smith, Dielectric constant for binary piezoelectric 0-3 composites, J. Appl. Phys. 73 (1993) 2462–2466. https://doi.org/10.1063/1.354057.

[231] P.Y. Foeller, J.S. Dean, I.M. Reaney, D.C. Sinclair, Design of a bilayer ceramic capacitor with low temperature coefficient of capacitance, Appl. Phys. Lett. 109 (2016) 082904. https://doi.org/10.1063/1.4961616.

[232] G. Kerridge, D.C. Sinclair, J.S. Dean, Resource efficient exploration of ternary phase space to develop multi-layer ceramic capacitors, Acta Mater. 207 (2021) 116690. https://doi.org/10.1016/j.actamat.2021.116690.

[233] J.R. Connolly, Diffraction Basics, Introduction to X-Ray Powder Diffraction, (n.d.). https://www.cigs.unimore.it/CigsDownloads/labs/xrdp/manuali_letture/05-Diffraction-Basics.pdf (accessed September 3, 2024).

[234] S. Mitchell, J. Perez-Ramirez, X ray diffraction. Materials characterization .pptx, Advanced Catalysis Engineering, (2024). https://www.slideshare.net/slideshow/x-ray-diffraction-materials-characterization-pptx/266860367 (accessed October 12, 2024).

[235] Lecture 7: Systematic Absences, Crystallography Supplementary Subject, (n.d.). http://goodwin.chem.ox.ac.uk/goodwin/TEACHING_files/l7_handout.pdf (accessed September 4, 2024).

[236] USGS OFR01-041: X-Ray Diffraction Primer, A Laboratory Manual for X-Ray Powder Diffraction, USGS Costal Mar. Geol. Program (n.d.). https://pubs.usgs.gov/of/2001/of01-041/htmldocs/xrpd.htm (accessed September 3, 2024).

[237] B.D. Cullity, S.R. Stock, Elements of X-Ray Diffraction, Third Edition, Pearson Education Limited, 2016. https://www.eng.uc.edu/~beaucag/Classes/AdvancedMaterialsThermodynamics/Books/B.D.%20Cullity,%20S.R.%20Stock%20-%20Elements%20of%20X-Ray%20Diffraction-Pearson%20Education%20Limited%20(2014).pdf (accessed September 3, 2024).

[238] X-ray Transition Energies Database, (n.d.).

[239] N. Döbelin, Lesson 1 X-rays & Diffraction, (n.d.). https://profex.doebelin.org/wp-content/uploads/2014/02/Lesson-1-X-rays-and-Diffraction.pdf.

[240] Scanning Electron Microscopy | Electrons in SEM - UK, ThermoFisher Scientific, ThermoFisher Sci. (n.d.). https://www.thermofisher.com/uk/en/home/materials-science/learning-center/applications/sem-electrons.html (accessed September 4, 2024).

[241] J.I. Goldstein, D. Newbury, J.R. Michael, N.W.M. Ritchie, J.H.J. Scott, D.C. Joy, Scanning Electron Microscopy and X-Ray Microanalysis, Fourth Edition, Springer, 2018. https://link.springer.com/book/10.1007/978-1-4939-6676-9.

[242] S.J.B. Reed, Electron Microprobe Analysis and Scanning Electron Microscopy in Geology, Second Edition, Cambridge University Press, 2009. https://www.cambridge.org/core/books/electron-microprobe-analysis-and-scanning-electron-microscopy-in-geology/A7BD5CF9A6E6D9E2360E4F378C81D002.

[243] H. Kanter, Contribution of Backscattered Electrons to Secondary Electron Formation, Phys. Rev. 121 (1961) 681–684. https://doi.org/10.1103/PhysRev.121.681.

[244] H. Seiler, Secondary electron emission in the scanning electron microscope, J. Appl. Phys. 54 (1983) R1–R18. https://doi.org/10.1063/1.332840.

[245] G.E. Lloyd, Atomic number and crystallographic contrast images with the SEM: a review of backscattered electron techniques, Mineral. Mag. 51 (1987) 3–19. https://doi.org/10.1180/minmag.1987.051.359.02.

[246] G. Love, Quantitative Methods in Electron Microscopy, University of Bath, 1978. https://researchportal.bath.ac.uk/en/studentTheses/quantitative-methods-in-electron-microscopy (accessed April 9, 2024).

[247] L. Corbari, M.-A. Cambon-Bonavita, G.J. Long, F. Grandjean, M. Zbinden, F. Gaill, P. Compère, Iron oxide deposits associated with the ectosymbiotic bacteria in the hydrothermal vent shrimp *Rimicaris exoculata*, Biogeosciences 5 (2008) 1295–1310. https://doi.org/10.5194/bg-5-1295-2008.

[248] S.J.B. Reed, Introduction to Energy Dispersive X-ray Spectrometry (EDS), (1995). https://cfamm.ucr.edu/media/126/download, (accessed September 1, 2024).

[249] McSwiggen & Associates, -Tech Note: WDS vs EDS, (n.d.). http://mcswiggen.com/TechNotes/WDSvsEDS.htm (accessed September 4, 2024).

[250] J.T.S. Irvine, D.C. Sinclair, A.R. West, Electroceramics: Characterization by Impedance Spectroscopy, Adv. Mater. 2 (1990) 132–138. https://doi.org/10.1002/adma.19900020304.

[251] D.C. Sinclair, Characterization of Electro-materials using ac Impedance Spectroscopy, 34 (1994).

[252] J. Ramírez-González, D.C. Sinclair, A.R. West, Impedance and Dielectric Spectroscopy of Functional Materials: A Critical Evaluation of the Two Techniques, J. Electrochem. Soc. 170 (2023) 116504. https://doi.org/10.1149/1945-7111/ad09fa.

[253] A.K. Jonscher, The ‘universal’ dielectric response, Nature 267 (1977) 673–679. https://doi.org/10.1038/267673a0.

[254] A.K. Jonscher, A new understanding of the dielectric relaxation of solids, J. Mater. Sci. 16 (1981) 2037–2060. https://doi.org/10.1007/BF00542364.

[255] K.S. Cole, R.H. Cole, Dispersion and Absorption in Dielectrics I. Alternating Current Characteristics, J. Chem. Phys. 9 (1941) 341–351. https://doi.org/10.1063/1.1750906.

[256] D.P. Almond, A.R. West, Impedance and modulus spectroscopy of “real” dispersive conductors, Solid State Ion. 11 (1983) 57–64. https://doi.org/10.1016/0167-2738(83)90063-2.

[257] D. McLean, Dielectric Materials and Capacitor Miniaturization, IEEE Trans. Parts Mater. Packag. 3 (1967) 163–169. https://doi.org/10.1109/TPMP.1967.1135735.

[258] J.I. Roscow, C.R. Bowen, D.P. Almond, Breakdown in the Case for Materials with Giant Permittivity?, ACS Energy Lett. 2 (2017) 2264–2269. https://doi.org/10.1021/acsenergylett.7b00798.

[259] C.B. Sawyer, C.H. Tower, Rochelle Salt as a Dielectric, Phys. Rev. 35 (1930) 269–273. https://doi.org/10.1103/PhysRev.35.269.

[260] B. Ando, S. Graziani, Basic measurements for the characterization of ferroelectric devices, IEEE Trans. Instrum. Meas. 54 (2005) 1054–1060. https://doi.org/10.1109/TIM.2005.847232.

[261] T.E. Hooper, High Voltage Coefficient Piezoelectric Materials for Underwater Transducer Applications, University of Leeds, 2020. https://etheses.whiterose.ac.uk/27188/1/Tom_Hooper_High_Voltage_Coefficient_Piezoelectric_Materials_For_Underwater_Transducer_Applications_June_2020.pdf.

[262] C. Chauvet, C. Laurent, Weibull statistics in short-term dielectric breakdown of thin polyethylene films, IEEE Trans. Electr. Insul. 28 (1993) 18–29. https://doi.org/10.1109/14.192236.

[263] B.H. Toby, R.B. Von Dreele, GSAS-II: the genesis of a modern open-source all purpose crystallography software package, J. Appl. Crystallogr. 46 (2013) 544–549. https://doi.org/10.1107/S0021889813003531.

[264] S. Saha, T.P. Sinha, A. Mookerjee, Electronic structure, chemical bonding, and optical properties of paraelectric $BaTiO_3$, Phys. Rev. B 62 (2000) 8828–8834. https://doi.org/10.1103/PhysRevB.62.8828.

[265] N. Bein, B. Kmet, T. Rojac, A.B. Golob, B. Malič, J. Moxter, T. Schneider, L. Fulanovic, M. Azadeh, T. Frömling, S. Egert, H. Wang, P. Van Aken, J. Schwarzkopf, A. Klein, Fermi energy, electrical conductivity, and the energy gap of $NaNbO_3$, Phys. Rev. Mater. 6 (2022) 084404. https://doi.org/10.1103/PhysRevMaterials.6.084404.

[266] S.H. Wemple, Polarization Fluctuations and the Optical-Absorption Edge in $BaTiO_3$, Phys. Rev. B 2 (1970) 2679–2689. https://doi.org/10.1103/PhysRevB.2.2679.

[267] G. Gouget, M. Duttine, E. Durand, A. Villesuzanne, V. Rodriguez, F. Adamietz, T. Le Mercier, M.-D. Braida, A. Demourgues, Isolating the Two Room-Temperature Polymorphs of $NaNbO_3$: Structural Features, Optical Band Gap, and Reactivity, ACS Appl. Electron. Mater. 1 (2019) 513–522. https://doi.org/10.1021/acsaelm.8b00125.

[268] R. Gerson, T.C. Marshall, Dielectric Breakdown of Porous Ceramics, J. Appl. Phys. 30 (1959) 1650–1653. https://doi.org/10.1063/1.1735030.

[269] Y.J. Wu, Y.H. Huang, N. Wang, J. Li, M.S. Fu, X.M. Chen, Effects of phase constitution and microstructure on energy storage properties of barium strontium titanate ceramics, J. Eur. Ceram. Soc. 37 (2017) 2099–2104. https://doi.org/10.1016/j.jeurceramsoc.2016.12.052.

[270] J. Hostaša, F. Picelli, S. Hříbalová, V. Nečina, Sintering aids, their role and behaviour in the production of transparent ceramics, Open Ceram. 7 (2021) 100137. https://doi.org/10.1016/j.oceram.2021.100137.

[271] W.D. Kingery, Densification during Sintering in the Presence of a Liquid Phase. I. Theory, J. Appl. Phys. 30 (1959) 301–306. https://doi.org/10.1063/1.1735155.

[272] Y. Ye, S.C. Zhang, F. Dogan, E. Schamiloglu, J. Gaudet, P. Castro, M. Roybal, M. Joler, C. Christodoulou, Influence of nanocrystalline grain size on the breakdown strength of ceramic dielectrics, in: Dig. Tech. Pap. PPC-2003 14th IEEE Int. Pulsed Power Conf. IEEE Cat No03CH37472, 2003: pp. 719-722 Vol.1. https://doi.org/10.1109/PPC.2003.1277809.

[273] E.K. Beauchamp, Effect of Microstructure on Pulse Electrical Strength of MgO, J. Am. Ceram. Soc. 54 (1971) 484–487. https://doi.org/10.1111/j.1151-2916.1971.tb12184.x.

[274] T. Tunkasiri, G. Rujijanagul, Dielectric strength of fine grained barium titanate ceramics, J. Mater. Sci. Lett. 15 (1996) 1767–1769. https://doi.org/10.1007/BF00275336.

[275] A. Young, G. Hilmas, S.C. Zhang, R.W. Schwartz, Effect of Liquid-Phase Sintering on the Breakdown Strength of Barium Titanate, J. Am. Ceram. Soc. 90 (2007) 1504–1510. https://doi.org/10.1111/j.1551-2916.2007.01637.x.

[276] K.R. Chowdary, E.C. Subbarao, Liquid phase sintered $BaTiO_3$, Ferroelectrics 37 (1981) 689–692. https://doi.org/10.1080/00150198108223523.

[277] S.K. Sarkar, M.L. Sharma, Liquid phase sintering of $BaTiO_3$ by boric oxide (B_2O_3) and lead borate (PbB_2O_4) glasses and its effect on dielectric strength and dielectric constant, Mater. Res. Bull. 24 (1989) 773–779. https://doi.org/10.1016/0025-5408(89)90038-X.

[278] T. Wang, L. Jin, L. Shu, Q. Hu, X. Wei, Energy storage properties in $Ba_{0.4}Sr_{0.6}TiO_3$ ceramics with addition of semi-conductive $BaO–B_2O_3–SiO_2–Na_2CO_3–K_2CO_3$ glass, J. Alloys Compd. 617 (2014) 399–403. https://doi.org/10.1016/j.jallcom.2014.08.038.

[279] Q. Zhang, L. Wang, J. Luo, Q. Tang, J. Du, Improved Energy Storage Density in Barium Strontium Titanate by Addition of $BaO–SiO_2–B_2O_3$ Glass, J. Am. Ceram. Soc. 92 (2009) 1871–1873. https://doi.org/10.1111/j.1551-2916.2009.03109.x.

[280] D. Zhang, T.W. Button, V.O. Sherman, A.K. Tagantsev, T. Price, D. Iddles, Effects of glass additions on the microstructure and dielectric properties of barium strontium titanate (BST) ceramics, J. Eur. Ceram. Soc. 30 (2010) 407–412. https://doi.org/10.1016/j.jeurceramsoc.2009.05.003.

[281] Z. Jiwei, Y. Xi, C. Xiaogang, Z. Liangying, H. Chen, Direct-current field dependence of dielectric properties in B_2O_3-SiO_2 glass doped $Ba_{0.6}Sr_{0.4}TiO_3$ ceramics, J. Mater. Sci. 37 (2002) 3739–3745. https://doi.org/10.1023/A:1016525712077.

[282] P. v. Divya, V. Kumar, Crystallization Studies and Properties of $(Ba_{1-x}Sr_x)TiO_3$in Borosilicate Glass, J. Am. Ceram. Soc. 90 (2007) 472–476. https://doi.org/10.1111/j.1551-2916.2006.01452.x.

[283] P.V. Divya, G. Vignesh, V. Kumar, Crystallization studies and dielectric properties of $(Ba_{0.7}Sr_{0.3})TiO_3$ in bariumaluminosilicate glass, J. Phys. Appl. Phys. 40 (2007) 7804–7810. https://doi.org/10.1088/0022-3727/40/24/032.

[284] B.R. Priya Rani, M.T. Sebastian, The effect of glass addition on the dielectric properties of barium strontium titanate, J. Mater. Sci. Mater. Electron. 19 (2008) 39–44. https://doi.org/10.1007/s10854-007-9224-6.

[285] S. Xiao, X. Yan, Preparation and characterization of Si-doped barium titanate nanopowders and ceramics, Microelectron. Eng. 86 (2009) 387–391. https://doi.org/10.1016/j.mee.2008.11.042.

[286] S.K. Barbar, M. Roy, Synthesis, Structural, and Electrical Properties of Ca-Modified $Ba_2TiSi_2O_8$ Ceramics, J. Am. Ceram. Soc. 94 (2011) 843–848. https://doi.org/10.1111/j.1551-2916.2010.04187.x.

[287] M.C. Foster, D.J. Arbogast, R.M. Nielson, P. Photinos, S.C. Abrahams, Fresnoite: A new ferroelectric mineral, J. Appl. Phys. 85 (1999) 2299–2303. https://doi.org/10.1063/1.369541.

[288] R.C. D'Silva Green, G. Dale, G. McLaughlin, M. Strawhorne, D.C. Sinclair, J.S. Dean, Application of Johnson's approximation in finite element modeling for electric field-dependent materials, Int. J. Appl. Ceram. Technol. (2024). https://doi.org/10.1111/ijac.14824.

[289] R.A. Veazey, A.S. Gandy, D.C. Sinclair, J.S. Dean, Finite element modeling of resistive surface layers by micro-contact impedance spectroscopy, J. Am. Ceram. Soc. 103 (2020) 2702–2714. https://doi.org/10.1111/jace.16981.

[290] H. Ma, D.C. Sinclair, J.S. Dean, Modifications to the spreading resistance equation when using micro-contact impedance spectroscopy to measure resistive surface layers. Solid State Ion. 414 (2024) 116652. https://doi.org/10.1016/j.ssi.2024.116652.

[291] A. Torres-Pardo, R. Jiménez, J.M. González-Calbet, E. García-González, Induction of Relaxor Behavior in $Na_{1-x}Sr_{x/2}\square_{x/2}NbO_3$ through the Introduction of Cationic Vacancies, Chem. Mater. 21 (2009) 2193–2200. https://doi.org/10.1021/cm9000834.

[292] H. Shimizu, H. Guo, S.E. Reyes-Lillo, Y. Mizuno, K.M. Rabe, C.A. Randall, Lead-free antiferroelectric: $xCaZrO_3$-$(1 - x)NaNbO_3$ system $(0 \leq x \leq 0.10)$, Dalton Trans. 44 (2015) 10763–10772. https://doi.org/10.1039/C4DT03919J.

[293] D. Wang, Z. Fan, D. Zhou, A. Khesro, S. Murakami, A. Feteira, Q. Zhao, X. Tan, I.M. Reaney, Bismuth ferrite-based lead-free ceramics and multilayers with high recoverable energy density, J. Mater. Chem. A 6 (2018) 4133–4144. https://doi.org/10.1039/C7TA09857J.

[294] H. Ji, D. Wang, W. Bao, Z. Lu, G. Wang, H. Yang, A. Mostaed, L. Li, A. Feteira, S. Sun, F. Xu, D. Li, C.-J. Ma, S.-Y. Liu, I.M. Reaney, Ultrahigh energy density in short-range tilted NBT-based lead-free multilayer ceramic capacitors by nanodomain percolation, Energy Storage Mater. 38 (2021) 113–120. https://doi.org/10.1016/j.ensm.2021.01.023.

[295] G. Liang, L. Yang, X. Xiong, K. Pei, X. Zhao, C. Wang, W. You, X. Liu, X. Zhang, R. Che, Interfacial Space Charge Enhanced Sodium Storage in a Zero-Strain Cerium Niobite Perovskite Anode, Adv. Funct. Mater. 32 (2022) 2206129. https://doi.org/10.1002/adfm.202206129.